Theoretical Modelling of Low Latitude Current system

By

GEETA VASANT JADHAV

UNDER THE SUPERVISION OF

PROF. R. RAJARAM

INDIAN INSTITUTE OF GEOMAGNETISM,

COLABA, MUMBAI - 400 005

MAHARASTRA, INDIA

SEPTEMBER 2001

A THESIS

SUBMITTED TO THE DEPARTMENT OF PHYSICS,

UNIVERSITY OF MUMBAI, MUMBAI

FOR THE DEGREE OF

DOCTOR OF PHILOSOPHY IN PHYSICS

Dedicated to

Aai and Baba

Statement required under 0.770 Statement No. 1

I hereby declare that the work described in this thesis has not been submitted previously to this or any other university for Ph. D. or any other degree.

Statement required under 0.771 Statement No. 2

"*Whether the work is based on the discovery of new facts by the candidate or of new relations of facts observed by others, and how the work tends to the general advancement of knowledge.*"

Chapter I gives the necessary background for orienting the work presented in this thesis. Chapters II, III, IV, V, VI, VII and VIII are based on the original research carried out by the candidate. It includes new results about the global picture of low latitude currents obtained from satellite measurements, and ionospheric modulation of compressible hydromagnetic waves. Further, this is backed up by a theoretical model to account for the observed global pattern. Chapter IX summarizes the conclusions of the present study. The important findings that contribute to the advancement of knowledge, obtained as the outcome of the research done are summarized below:

1. A new approach in satellite data analysis is introduced, which considers day to day variability of the equatorial electrojet (EEJ) signature in different longitude zones and this has been obtained through an objective analysis of the satellite data.
2. In the present dissertation, study of the zonal variation of EEJ parameters such as peak current intensity (J_0), total current (I_+), EEJ width and position of EEJ axis (centre of EEJ) has been carried out. The study shows that the EEJ axis follows the dip equator at

altitude of 106 km. and undergoes diurnal variation; the deviation of EEJ axis from dip equator is a minimum at noon. Zonal variation of the amplitude of EEJ is in agreement with earlier results and depicts that the peaks in different longitudes are not same at all local times. Average EEJ amplitude undergoes expected diurnal variation.

3. Correlation between the strength of EEJ in different longitudinal regions shows that the correlation between neighbouring longitudinal zones does not necessarily to be good. Further for the first time the principal component analysis of the equatorial geomagnetic variations from satellite data has been carried out and it reveals the importance of tidal components.
4. An attempt is made to prove the reverse EEJ signature at satellite is the indication of counter electrojet (CEJ). Seasonal variation of CEJ occurrence frequency, which has been done for the first time using satellite data follows the earlier ground based observations. The percentage of occurrence of CEJ is highest in the longitude region between 300^0 to 330^0 E. Theoretical work has been done to account for the anomaly observed in this longitude zone.
5. The day side ionosphere introduces significant phase delays for frequencies in excess of about 20 mHz. The phase delay increases with frequency and with increase in the conductivity of the ionosphere. There is also an increase in the amplitude of the wave above equatorial dayside ionosphere. The uniformly excellent coherence between the satellite and ground oscillations and systematically good correlation between the filtered time series at the two levels suggests that the compressible hydromagnetic waves are phase coherent over a wide range of latitudes.

6. The local time dependence of the frequency and latitudinal structures of the equatorial enhancement of short period fluctuations in the period range covering the pc5-6 region has been studied using African ground data. Coherence and cross phase analysis has been used to examine the nature of phase shifts and polarization changes introduced by the equatorial ionospheric conductivity.
7. A complete numerical model for the calculation of atmospheric tides has been generated, which includes the determination of thermal sources and the calculation of the atmospheric response to the excitation. Thus it calculates equivalent depths for diurnal, semidiurnal, symmetric and antisymmetric cases, calculates Hough coefficients for above cases and calculates wind velocity & phase at all heights.
8. A standard conductivity model has been generated and further conductivity profile based on real data has also been generated.
9. A new numerical model of low latitude current system has been developed. The model takes into account the fact that the ionospheric conductivities are dependent on the geomagnetic field strength and configuration, as well as on the ionization density, as parameterized by the solar activity level and zenith angle. In addition, the model also considers different tidal modes to solve $\nabla \cdot J = 0$.

Statement required under 0.771 Statement No. 3

"*The source from which the information is derived and the extent to which he has based his work on the others, and shall indicate which portion or portions of this thesis he claims as original.*"

The sources from which the information is derived are the investigations carried out by the candidate. Some of the results have been reported in the following research papers published in International journals:

Chapter II:

(1) **Geeta Jadhav**, M. Rajaram and R. Rajaram, Equatorial Electrojet: Main field control of the Equatorial Electrojet: A preliminary study from Oersted data, J. of Geodynamics (in press).

Chapter III :

(2) **Geeta Jadhav**, M. Rajaram and R. Rajaram, Identification of External Current variations in Oersted Data, Proc. of 3rd Oersted International Science Team Meeting,2000.

(3) **Geeta Jadhav**, Mita Rajaram and R. Rajaram, Detailed study of Equatorial Electrojet phenomenon using Oersted satellite observations, J. of Geophy. Res. (in press)

Chapter IV :

(4) **Geeta Jadhav** and R. Rajaram, Study of Reverse equatorial electrojet signature observed in Oersted satellite data, J. of Geophy. Res. (to be communicated)

Chapter V :

(5) **Geeta Jadhav**, Mita Rajaram, and R. Rajaram, Modification of daytime compressional waves by the ionosphere: First results from Oersted, J. of Geophy. Res. Lett., Vol. 28, No.1, p.103-107, 2001.

Chapter I is a general introduction covering briefly the already known aspects for the study in the thesis. The candidate was fully involved in the data analysis and interpretation of the

results presented in Chapters II, III, IV and V. The satellite data used is taken from Oersted Science Centre at the Danish Meteorological Institute, and ground data of the Japanese stations & Dst indices from WDC-C2, Kyoto. The work presented in chapters VI, VII & VIII is fully carried out by the candidate. The atmospheric model and conductivity model calculations are basically extension of earlier models. Full references are given in the dissertation for any material drawn from other published work. The work and the results obtained are original.

The development of computer programs for the various computations used in this thesis, have been formulated by the candidate. The discussions as well as the presentations of the results in different chapters are also done by the candidate.

Statement required under 0.771 Statement No. 4

"*Where a candidate presents joint work, he shall clearly state the portion which his own contribution as distinguished from the portion contributor by his collaborators.*"

In the joint work on which chapter II, III, and IV are based, the analysis of the data, the computations and the presentation of the results are entirely by the candidate. Discussions with the collaborators have helped. The candidate is benefited by guidance and suggestions of the guiding teacher.

(Prof. R. Rajaram)
Guiding Teacher

(Geeta Jadhav)
Candidate

SYNOPSIS SUBMITTED BY GEETA JADHAV FOR THE DEGREE OF DOCTOR OF PHILOSOPHY OF THE UNIVERSITY OF MUMBAI IN PHYSICS.

NAME OF THE CANDIDATE	**: GEETA JADHAV**
TITLE OF THE THESIS	**: THEORETICAL MODELLING OF LOW LATITUDE CURRENT SYSTEM.**
DEGREE	**: DOCTOR OF PHILOSOPHY**
SUBJECT	**: PHYSICS**
NAME OF THE GUIDE	**: PROF. R. RAJARAM**
INSTITUTE WHERE RESEARCH WAS DONE	**: INDIAN INSTITUTE OF GEOMAGNETISM, COLABA, MUMBAI- 400 005**
NUMBER AND DATE OF REGISTRATION	**: IIG/No.10/ 06-02-1998**
SIGNATURE OF STUDENT	**:**
SIGNATURE OF GUIDE	**:**

SYNOPSIS

The atmosphere is the gaseous envelope of the earth. The radiation from the sun heats the atmosphere, dissociates its molecules, and liberates free electrons. Ionosphere can be defined as that part of a planetary atmosphere where ions and electrons are present in quantities sufficient to affect the propagation of radio waves. Conventionally, it extends from 60 km to about 2000 km above the earth's surface. The magnetic field near the earth is due to the sources inside the earth and sources external to it. In his historic article on “Terrestrial Magnetism” in the Encyclopaedia Britannica, Balfour Stewart (1882) discussed the origin of the diurnal, seasonal and sunspot cycle geomagnetic variations. He suggested the existence of the electric current in the upper atmosphere. The action described by Stewart is like a dynamo action in which the earth is the magnet, the moving air is the armature, and the convected conducting ionosphere represents the windings. Thus, the neutral atmosphere and the ionosphere play a fundamental role in geomagnetic variations through their role in the charge separation processes, electrical conductivities and currents.

At the dip equator (I = 0), the earth's magnetic field is exactly horizontal and because of the small magnitude of the vertical earth's magnetic field the effective conductivity is very large. This leads to various geomagnetic and ionospheric phenomena, many of which are unique to that region. The establishment of a geomagnetic observatory at Huancayo, near the dip equator, indicated an abnormally large amplitude of diurnal variation in the horizontal component H. It was discovered later, that this enhancement occurs everywhere on the earth near the dip equator, resulting in the so called 'Equatorial Electrojet' (EEJ). EEJ is the major current system in the equatorial region that controls the dynamics and

electrodynamics of the ionospheric plasma at low latitudes. The relationship between the electrojet and ionospheric parameters was discovered by Matsushita(1951) for the first time. Ionospheric drift measurements at Thumba were found to be very closely associated with the electrojet, both on a short term and long term basis (Chandra et al. 1971). This shows that the study of EEJ is essential in order to get clearer insight into the understanding of the upper atmosphere. Since India comes under this region, the study of EEJ current system gives valuable information about the dynamics and electrodynamics involved in her space.

The better theoretical model of the current system associated with low latitudes should explain most of the observed features related to the phenomenon. If we examine the global area influenced by the EEJ phenomenon, we observe that around 90% of area is covered by oceans and forests where, the continuous recording of ground based magnetic observations are not possible. Hence, the study of the phenomenon using only ground-based data is not sufficient. Since satellite data does not have the above problem, it can span the entire globe. Here, we have made use of the scalar magnetic field measurements obtained from Oersted satellite, which has polar orbit with local time varying from forenoon to afternoon hours. Earlier, POGO satellite series (OGO-2, OGO-4 & OGO-6) had measurements of EEJ as a part of their objectives. Cain and Sweeney (1973) have studied scalar magnetic field from the POGO satellite which had altitude range of 400 to 800 km. Onwumechili & Agu (1980,1981a,1981b,1982), Agu & Onwumechili (1981a,1981b) studied the POGO data in more detail and discussed general features of the magnetic field associated with EEJ. But their method of analysis did not consider the day to day variability of EEJ. Magsat satellite

had passes during dawn and dusk times but despite this restriction it did establish the presence of the meridional current system associated with EEJ. EEJ is basically daytime event, hence Magsat could not contribute significantly to the understanding of the day to day variability of the EEJ. Under these circumstances, the study of EEJ using Oersted satellite is of great importance. A method of analysis, which takes into account the day to day variability, has been used in the present study. The excellent correlation between satellite and ground observations indicates that the satellite data and the method adopted for the analysis is quite reliable. The global picture obtained from this study certainly improves the understanding of the phenomenon.

From a theoretical point of view, it was noted that in the region between 70 and 140 km, the ion-neutral collision frequency is larger than the ion cyclotron frequency ($\nu_i > \omega_i$), although electron-neutral collision frequency is less than the electron cyclotron frequency ($\nu_e < \omega_e$). Thus the ions will move with the neutral air, but the electrons are controlled by the magnetic field. At the equator, where the electric field during the daytime is primarily eastward and the magnetic field is northward, the electrons within 70-140 km drift upward relative to ions and produce the Hall polarization electric field. This in turn produces additional Hall conductivity in the east direction.

Baker and Martyn (1953) provided the first theoretical model of the electrical fields and currents in low latitudes, assuming the dynamo region to be a thin sheet and that north-south electric fields were absent. Untiedt (1967) removed the restriction of complete inhibition of polarisation currents and described a self-consistent model assuming a

meridional current flowing towards the magnetic equator below 120 km and away from it above this height. Suguira and Poros (1969) modified Untiedt's model by extending the meridional current loop to 10^0 magnetic latitude. Richmond (1973) further extended the model by including the effect of neutral air winds and two-stream instability. Reddy and Devasia (1978) treated the electrojet by an equivalent-electric-circuit method to facilitate the interpretation of neutral-wind effects on the electrojet structures. Forbes and Lindzen (1976) investigated the localtime, latitude and height structure of the electrojet by solving the full three-dimensional equations within a 14^0 latitude belt along the magnetic equator. They ensured a degree of self-consistency between the global Sq current system, global and local winds, conductivities and the eastward equatorial polarization field through boundary conditions at the boundary of the electrojet region. Takeda and Maeda (1980) and Takeda (1982) have developed a basic self-consistent 3-dimensional model of the ionospheric dynamo, which is numerically solvable as a boundary value problem. Singh and Cole (1987) have developed a method for numerically solving a suitably formulated ionospheric-wind dynamo equation for the electrostatic potential and field. They further derived the three dimensional electric current density in a magnetic meridional plane in the equatorial and low-latitude ionosphere. In the present thesis, we have tried to solve three dimensional ionospheric dynamo equation numerically and different combination of atmospheric tides have been introduced which could account for the observed global picture of EEJ obtained from Oersted data.

Thus, in the present studies, we have used ground as well as satellite data base to study the current system at low latitudes and further a theoretical model has been put forward in order to back up the observational results.

Studies of the magnetic field fluctuations of shorter periods are also important in order to understand the electrodynamics involved in ionosphere. The first observations of ultra-low-frequency (ULF) fluctuations (periods ranging from seconds to minutes) of magnetic fields were made on the ground by Stewart in 1861. These geomagnetic pulsations are manifestations of hydromagnetic waves generated through a combination of mechanical and electromagnetic forces. They originate mainly in the magnetosphere but are observed both on the surface of the earth and at satellite altitudes at various radial distances. These oscillations are generally either transverse Alfven waves or compressional magneto-acoustic waves. Both these types of pulsations have been observed on the ground as also in different regions of the plasmasphere and magnetosphere. As these waves pass through the ionosphere, the electrons and ions take part in their motions so that energy is shared between the fields of the waves and the kinetic energy of the charged particles. Thus the study of small period oscillations gives better insight into the dynamics of space. In the present study, we have also studied the response of the ionosphere to the compressible hydromagnetic waves.

The major objectives of the present studies are as follows:

(1) To study the global pattern of the low latitude current system and obtain different modes responsible for the global variation.

(2) To examine the temporal and zonal variation of different parameters associated with the low latitude ionospheric current system.

(3) To study the current system associated with counter electrojet using satellite and ground data.

(4) To examine and model the ionospheric response for the short period oscillations.

(5) To obtain the theoretical model for low latitude current system.

The present thesis contains 9 chapters. Each chapter has been discussed briefly below.

Chapter 1 briefly introduces the spatial variation of the Earth's magnetic field, spherical harmonic analysis of main geomagnetic field, International Geomagnetic Reference Field Model (IGRF), ionosphere, magnetosphere, production and loss of the ionospheric plasma, electrical conductivity of the ionosphere, solar quiet time and equatorial electrojet currents. It also includes description of results of rocket measurements of ionospheric currents and few empirical models of the low latitude current systems such as constant current ribbon model and band with parabolic distribution given by Chapman. It discusses in greater detail, the model given by Onwumechili (1967) which allows a westward current outside the main positive eastward current region. It also introduces data analysis techniques such as spectral analysis, coherence and cross phase analysis, principal component analysis etc, which are used later in this thesis.

Chapter 2 talks about the main field control of the low latitude current system. It is observed that EEJ is sensitive to the strength and distribution of the earth's main magnetic

field. The Oersted initial field model along with the earlier IGRF models have been used to provide insight into the secular changes in the global patterns of the position and strength of the EEJ. A northward drift in the location of the dip equator (hence the position of the axis of the EEJ) to the extent of 1^0 per decade is seen around 300^0. In contrast, in the Pacific, east of Australia, there is practically no drift. It is also observed that the largest secular variation in the Cowling conductivity occurs in the South American sector with a possible 4% increase per decade for the same level of ionisation in the E-region. The Oersted main field model does not suggest any changes or reversal of these trends. A very significant result is that the magnetic field at the dip equator need not be perpendicular to the line of zero dip and this deviation from the idealized scenario can lead to a significant contribution of the EEJ to the declination component.

Quiet day scalar field data from Oersted provides greater insight into the relative importance of the geomagnetic field structure and tidal control. This is obtained through a study of the day to day variability of the equatorial electrojet and its longitudinal variations. We find that the EEJ can be clearly identified on almost all the passes and the centre of EEJ is sensitive to the main field. There is a clear indication of zonal variation in the electrojet strength at satellite height. The largest amplitude is found in the American sector where the Cowling conductivity attains its maximum value. The electrojet strength at the satellite height also exhibits other maxima at around 100^0E and 190^0E longitude consistent with the earlier observations of Pogo. Variations at these longitudes could perhaps be linked with different tidal components of migrating tides or with non-migrating tides. The width of the electrojet at satellite height also seems to show a maximum in the South American sector.

Chapter 3 is mainly observation based and discusses global picture of low latitude currents obtained from statistical study of Oersted satellite data. Detailed analysis of the scalar magnetic field data from Oersted satellite for quiet days for epoch April'1999 to March'2000, have revealed many important aspects of Equatorial electrojet phenomenon. Earlier methods of satellite data analysis failed in considering day to day variability associated with EEJ. In the present studies, we have introduced a new approach in satellite data analysis, which considers EEJ signature on each day independently. To check the reliability of the data and our method of analysis, we made use of ground magnetic field data. The scatter plots and correlation analysis between satellite and ground based observations show excellent correlation. This definitely encourages us further to get global picture of EEJ. In that regard, we first studied the zonal variation of EEJ parameters such as peak current intensity (J_0), total current (I_+), EEJ width and position of EEJ axis (centre of EEJ). The studies show that the EEJ axis follows the dip equator at altitude of 106 km. and undergoes diurnal variation; the deviation of EEJ axis from dip equator shows a minimum at noon. Zonal variation of the amplitude of EEJ is in agreement with earlier results and depicts additional feature of temporal dependence of peaks. Average EEJ amplitude undergoes expected diurnal variation. For the first time, it has been possible to get correlation matrix for all longitude zones on the day to day variability basis. This brings out an interesting aspect of longitudinal correlation of EEJ- that the correlation between neighbouring longitudinal zones does not necessarily have to be good. Principal component analysis of the equatorial geomagnetic variations from satellite data has been carried out for the first time. It clearly points out the first component as migrating component, which

contributes 33% in the global variation of the EEJ and other components are due to different tidal modes. Thus, the present studies suggest that besides conductivity, atmospheric tidal modes play important role in the longitudinal dependence of the EEJ current system.

In **Chapter 4**, we have studied reverse EEJ signature seen in the Oersted satellite data. An attempt has been made to prove the reverse EEJ signature at satellite is an indication of counter electrojet (CEJ). We observe that reverse signature at satellite is supported by the counter electrojet in the Indian ground data. Seasonal variation of CEJ occurrence frequency, which has been done for the first time using satellite data is in agreement with earlier ground based studies. Satellite based studies have advantage of studying the longitudinal variation of CEJ occurrences. The percentage of occurrence of CEJ is highest in the longitude region between 300^0 to 330^0 E. If we examine the angle between magnetic field and gradient vector of dip angle (∇ I) at the dip equator, we find that the angle is maximum in the above longitude zone. All earlier models considered this angle to be zero. Here, we have put forward a model, which takes into account the above situation. The modified conditions may be linked with the peculiarities of the electrojet features in this region.

Chapter 5 discusses the ionospheric response to short period oscillations. Ionospheric modulation of compressional hydromagnetic waves has been examined using the scalar magnetic field data obtained from the Oersted satellite and ground magnetic data from the Japanese sector. It is shown that the dayside ionosphere introduces significant phase delays

for frequencies in excess of about 20 mHz. The phase delay increases with frequency and with increase in the conductivity of the ionosphere. There is also an increase in the amplitude of the wave above equatorial dayside ionosphere. The uniformly excellent coherence between the satellite and ground oscillations and systematically good correlation between the filtered time series at the two levels suggests that the compressional hydromagnetic waves are phase coherent over a wide range of latitudes.

During the International Equatorial Electrojet Year (IEEY), chain of 10 geomagnetic observatories were operated in the West African region, covering dip latitudes from 7^0 N to 6^0 S, for the period between November'1992 and November'1994. This data with sampling rate of one minute has been used to study the local time dependence of the frequency and latitudinal structures of the equatorial enhancement of short period fluctuations in the period range covering the pc5-6 region. Coherence and cross phase analysis is used to examine the nature of phase shifts introduced by the equatorial ionospheric conductivity, is also presented in this chapter.

Chapter 6 discusses the classical theory of atmospheric tides. Atmospheric solar tides are global-scale waves with periods that are harmonics of a 24 hour day. Migrating tidal components propagate westward with the apparent motion of the sun, so their zonal wavenumbers are identical to their frequency (in units of "tide maxima per day"). Numerical calculation of tides involves the investigation of the sources of periodic excitation and the calculation of the atmospheric response to the excitation. We have considered thermal source of excitation, which primarily includes the heat absorption due to O_3 & O_2 and Rayleigh scattering (Nicolet, 1984) and absorption due to water in the

troposphere. In the wavelength region 116.3 nm to 202.5 nm, it considers O_2 & O_3 absorption and Rayleigh scattering and no multiple scattering, while in the wavelength region of 202.5 nm to 850 nm, it also considers multiple scattering. The calculations are done for any given day of the year and at latitude, longitude and time at heights varying from 0 km to 100 km. Grove's method has been used for the calculation of the tropospheric heat absorption due to water.

The classical solution simplifies the differential equations that describe the tidal motions, in order to make the problem more tractable for analytic approaches. The exclusion of dissipative terms, background winds and latitudinal gradients in the background atmosphere makes the system of differential equations separable. Eliminating the derivatives with respect to time and longitude and simplifying yields a single, separable partial differential equation for the perturbation in terms of altitude and latitude. To solve latitude dependent equation, also known as Laplace's equation, we used method given by Hough (1897,1898), which makes use of expansion in associated Legendre polynomials; while vertical equation has been solved using finite difference method. Fortran program has been developed to calculate equivalent depths and Hough coefficients for diurnal, semidiurnal, symmetric and antisymmetric cases and determines wind velocity & phase at all heights. The tidal amplitude increases exponentially with height because of the exponential decrease in the background atmospheric density, hence at ionospheric heights, tides play very important role; but the tides could be either propagating upwards or evanescent depending on the mode selected. Tides computed are used in chapter 8 for the calculation of ionospheric currents..

Chapter 7 discusses atmospheric electrical conductivity models. In the numerical model given by A. D. Richmond (1972), he computed the densities of electrons & ions by balancing photoionization rates with chemical loss rates in infinite plane atmosphere. For neutral densities of N_2, O_2, O, Richmond used values given by Jacchia model (1971). In his model he did not consider electron-ion collision frequency. In 1976, J. M. Forbes took into account the electron-ion density and obtained the conductivity profile. Many workers use standard conductivity profiles by either Richmond or Forbes.

This chapter looks for more realistic conductivity profile, which uses electron & ion number densities from International Reference Ionosphere model (IRI) and neutral densities from Mass Spectrometer and Incoherent Scatter Extended Atmospheric model (MSIS) model for a given latitude, longitude, height and at a given time and day of a year. The computation utilizes modified formula for O-O+ collision frequency given by Pesnell et al (1993). The low latitude current system processes involve the electrical conductivity of the lower ionosphere, which is highly anisotropic with respect to the geomagnetic field. Hence more accurate and realistic conductivity model is expected to improve the calculations.

Chapter 8 provides a basic theoretical framework for interpreting the observational results presented in Chapters III, IV and V. the major part of this chapter is devoted to the solution of the dynamo equation for current $\bar{J}$, expressed as,

$$\bar{J} = \tilde{\sigma} \cdot \left[\bar{E} + \bar{V} \times \bar{B}\right] \qquad (1)$$

where, $\bar{V}$ is the neutral wind velocity associated with the atmospheric tides, which has been discussed in detail in chapter VI and $\tilde{\sigma}$ is a conductivity tensor computed in chapter VII of the thesis. $\bar{B}$ is the ambient magnetic field and $\bar{E}$ is the electrostatic field introduced in the ionosphere through the action of the tidal forces. In reality, $\bar{B}$ should be derived from IGRF, but the numerical code becomes complicated then. Many of the results based on the statistical analysis can be recovered using simple dipole model for the main geomagnetic field. We adopt a scheme based on dipole field but we take into consideration the fact that the dipole axis is inclined to the geographic axis. This enables us to examine some of the asymmetries observed in the statistical analysis of EEJ signatures obtained from satellite, in chapter III.

To calculate $\bar{J}$ from equation (1), we have to obtain the distribution of $\bar{E} = -\nabla\Phi$, where Φ is the electrostatic potential. This can be achieved by solving second order differential equation in Φ, obtained by putting divergence of $\bar{J}$ equal to zero. We adopt a scheme suggested by Singh and Cole(1987) to obtain the numerical solutions for Φ. The boundary conditions used demands that the cross field component of the meridional current integrated over field line vanishes at inner boundary defined by the neutral atmosphere and the outer boundary defined by the assumed high latitude limit of the Sq current system. Distribution of electrostatic field and currents has been evaluated and results are discussed with reference to the observations.

In the last part of the chapter, a simple numerical model is presented for the calculation of the modulation of hydromagnetic waves by the day time ionosphere, essentially using a formalism presented by Fedorov et.al.(1999).

Chapter 9 summarizes the main conclusions of the present work and outlines some suggestions for the future work. It is believed that the observational results obtained in this thesis give a clearer global picture of the current system associated with low latitudes. The results along with theoretical model will improve the understanding of the ionosphere in the Indian region.

References

Agu, C. E. and C. A. Onwumechili, J. Atmos. Terr. Phys.,43,801-807,1981a.

Agu, C. E. and C. A. Onwumechili, J. Atmos. Terr. Phys.,43,809-816,1981b.

Baker, W. G. and D. F. Martyn, Phil. Trans. Roy. Soc. Lond, A246,281-294, 1953.

Cain, J. C. and R. E. Sweeney, J. Atmos. Terr. Phys.,35,1231-1247,1973.

Chandra, H., R. K. Misra and R. G. Rastogi, Plan. Space Sci.,19,1497-1503,1971.

Fedorov, E.,V. Pilipenko, V. Surkov, D.R.K. Rao and K. Yumoto, J. Geo. Res.,104,A3,4329-4336,1999.

Forbes, J. M. and R. S. Lindzen, J. Atmos. Terr. Phys.,38,911-920,1976.

Hough, S. S., Phil. Trans. Roy. Soc. A,189,201-257,1897.

Hough, S. S., Phil. Trans. Roy. Soc. A,191,139-185,1898.

Jaccjia, L. G., Smithson. Astrophys. Obs. Spec. Rept. No.332,1971.

Matsushita, S.,J. Geomagn. Geoelectr.,3,44-46,1951.

Nicolet, M., Planet space Sci.,32,1467-1468,1984.

Onwumechili, A., pp. 425-507,Academic press, New York,1967.

Onwumechili, C. A. and C. E. Agu, Planet Space Sci.,28,1125-1130,1980.

Onwumechili, C. A. and C. E. Agu, Planet Space Sci.,29,627-634,1981a.

Onwumechili, C. A. and C. E. Agu, J. Atmos. Terr. Phys.,43,573-578,1981b.

Onwumechili, C. A. and C. E. Agu, Ann. Geophys.,38,307-313,1982.

Pesnell, W. D., Omidvar K., and W. R. Hoegy, *Geophys. Res. Lett.*, 20, 1343-1346, 1993

Reddy, C. A. and C. V. Devasia, Nature 273,195-199,1978.

Richmond, A. D., Report AFCRL-72-0668, ERP 421,Air Force Cambridge Res. Lab., Hanscom AFB, Bedford, Mass.,1972.

Richmond, A. D., J. Atmos. Terr. Phys. 35,1083-1103,1973.

Singh, A. and K. D. Cole, J. Atmos. Terr. Phys. 49,512-527,1987;

J. Atmos. Terr. Phys. 49,529-537,1987,

J. Atmos. Terr. Phys. 49,539-547,1987.

Stewart, B., Terrestrial magnetism, Encyclopedia Britannica, 9th edn.,1882.

Sugiura, M. and D. J. Poros, J. Geophys. Res.,74,4025-4034,1969.

Takeda, M.,J.Atmos. Terr.Phys.,44,187,1982.

Takeda, M. and H. Maeda, J. Geo. Res.,85,6895,1980.

Untiedt, J., J. Geophys. Res.,72,5799-5810,1967.

(Prof. R. Rajaram)
Guiding Teacher

(Geeta Jadhav)
Candidate

Acknowledgements

I am very much indebted to Prof. R. Rajaram, the supervisor of my Ph.D. work. Without his guidance and moral support, this work would have been impossible. This thesis is the output of the training and encouragement given by him. The countless discussions with him have certainly helped me to understand the subject and to improve the programming skills. I express my deep sense of gratitude to him for all his efforts in getting good work done out of me.

I express my sincere thanks to Prof. G. S. Lakhina, Director, Indian Institute of Geomagnetism, Colaba, where this Ph. D. work has been completed, for the facilities, help and cooperation provided during the course of this work.

Thanks are due to Dr. (Mrs.) Mita Rajaram for her valuable suggestions and help extended at various stages during the course of the thesis.

I am also grateful to all senior academic staff for their encouragement and fruitful discussions at various times .

I express special thanks to Mr. A. K. Sinha, who helped me to understand the subject through number of discussions. His cooperation in sharing the computer facility helped me to complete my work efficiently.

I would like to thank my colleagues Mr. Kakad, and Mr. S. P. Anand for their extensive cooperation in preparing the thesis.

I am extremely grateful to the Oersted Science Data Centre at the Danish Meteorological Institute for providing me with valuable magnetic field data used for the present dissertation.

I am very thankful to WDC-C2, Kyoto, for making available the Dst indices and magnetic field data at Huancayo on their Internet site.

I am grateful to Prof. G. K. Rangarajan for guiding me in the acquisition of magnetic data at Fuquene and Jose William Arias for providing Fuquene observatory magnetic data. He also provided me with up to date collection of

references on the subject, which proved to be very useful during the course of studies.

I express my thanks to Dr. Jacques Vassal for providing magnetic field data of West African region during IEEY'93.

Thanks are due to all the library and documentation staff for their excellent support as and when required.

I appreciate the excellent Xerox work done by Mr. Vilas and Smt. Rutha on many occasions.

I also thank to all Watchmen, who were very caring during my late night stay at the Institute for the completion of the manuscript.

Last but not the least, I must thank to my family members, whose moral support, patience and cooperation made this goal possible. The strength given by them has proved to be of tremendous value in the completion of the thesis.

Geeta Jadhav

September' 2001.

CONTENTS

Chapter 1
Introduction

1.1 Earth's Magnetic Field:

The existence of the Earth's magnetic field has been known since ancient times. The fact that a magnet free to move about its mass-centre in a horizontal plane or in a vertical plane, comes to rest along a particular direction shows that the earth behaves as a magnet and has a magnetic field all around it. Instruments sent out in Sputniks have revealed that the magnetic field of the earth extends to about 66,000 miles from its surface. In order to have a clear understanding of the state of the earth's magnetism; it is necessary to know the intensity, direction and variation of this magnetic force over the whole of the earth's surface.

The magnetic force at any point can be specified in several ways. One of which could be geographic rectangular coordinate system X, Y, Z, where X is along the geographic north in the horizontal plane and is reckoned positive if northward, negative if southward. Y is the horizontal component transverse to *X* component, and is reckoned positive if eastward, negative if westward. *Z* is the vertical component, also known as vertical intensity, reckoned positive if downward, negative if upward.

Another common way of specifying the magnetic force is by means of *H*, *D*, and *I*, defined as follows: H is the magnitude of the horizontal component, considered positive irrespective of its direction and is called the horizontal intensity. *D* is the azimuth of the horizontal component, reckoned positively from the geographical north towards the east, from 0^0 to 360^0, or negatively westwards from the north, it is called the magnetic declination. *I* is the angle made by the direction of the whole magnetic force with the horizontal, and is reckoned positive if the force is inclined downwards, or negative if upwards, it is

called the magnetic dip or magnetic inclination; *D* and *I* are measured in degrees and minutes of arc. The intensity of the whole magnetic force is denoted by *F* and called as the total intensity.

Therefore we can write

$$I = \tan^{-1}\left(\frac{Z}{H}\right) \qquad \text{and}$$

$$D = \tan^{-1}\left(\frac{Y}{X}\right)$$

When the magnetic elements are determined all over the earth' s surface, it is found that they vary in magnitude from place to place at a given time, and are also different at different times at a given location. It is found that many places have the same value of a magnetic element. The magnetic state of the earth is, therefore best shown by constructing charts upon which lines are drawn through place, having the same value of a magnetic element. Such maps or charts are called Isomagnetic charts. The line joining points where the dip is zero, is called the magnetic equator, while points where the dip is 90^0, or the dip needle is vertical, are called magnetic poles. The lines of equal inclination are roughly parallel to the magnetic equator.

If the Earth is considered to be a sphere, then

$X = -B_\theta$,

$Y = B_\phi$,

$Z = -B_r$

Where in spherical coordinate system, θ is co-latitude, ϕ is longitude and r is radius.

Let us consider Maxwell's equations,

$$\overline{\nabla} \times \overline{B} = \mu_0 \overline{J} \qquad (1.1)$$

$$\overline{\nabla} \cdot \overline{B} = 0 \qquad (1.2)$$

where, $\overline{B}$ is the main geomagnetic field. The current density $\overline{J}$ is certainly negligible between the surface of the Earth and the ionosphere, so that the field

may be taken to be curl free. This immediately allows representation of $\overline{B}$ as the gradient of a scalar potential *V*,

$$\overline{B} = -\overline{\nabla} V$$

Hence equation (1.2), shows that *V* must satisfy the Laplace equation,

$$\nabla^2 V = 0$$

This can be written in spherical coordinates as

$$\frac{1}{r}\frac{\partial(rV)}{\partial r^2} + \frac{1}{r^2 \sin\theta}\frac{\partial}{\partial\theta}\left(\sin\theta \frac{\partial V}{\partial\theta}\right) + \frac{1}{r^2 \sin^2\theta}\frac{\partial^2 V}{\partial\phi^2} = 0$$

If *a* is the mean radius of the earth' s surface, the general solution after normalization is

$$V(r,\theta,\phi) = a\sum_{n=1}^{\infty}\sum_{m=0}^{n} \{[g_n^m \cos m\phi + h_n^m \sin m\phi]\left(\frac{a}{r}\right)^{n+1} + [q_n^m \cos m\phi + s_n^m \sin m\phi]\left(\frac{r}{a}\right)^{n}\} P_{n,m}(\cos\theta) \quad (1.3)$$

where $P_{n,m}$ are associated Legendre functions.

A series representation of a function in terms of spherical harmonics, such as above equation, is called a spherical harmonic expansion and the quantities g_n^m, h_n^m, q_n^m and s_n^m are called spherical harmonic coefficients. In our notation n is called the degree and m the order of $P_{n,m}(\theta)$. Terms in $(a/r)^{n+1}$ go to zero as r goes to infinity and describe fields from sources inside r = a; terms in (r/a) go to zero as r goes to zero and describe fields from sources outside r = a. The term for n = 0 corresponds to a magnetic monopole and violates equation (1.2), which is normally omitted from the analysis.

Thus using equation (1.3), we compute the components in the spherical coordinate system as

$$B_r = \frac{-\partial V}{\partial r} = \sum_{n=1}^{\infty}\sum_{m=0}^{n} \{(n+1)\left[g_n^m \cos m\phi + h_n^m \sin m\phi\right]\left(\frac{a}{r}\right)^{n+2} - n\left[q_n^m \cos m\phi + s_n^m \sin m\phi\right]\left(\frac{r}{a}\right)^{n-1}\} P_n^m(\theta) \tag{1.4}$$

$$B_\theta = \frac{-\partial V}{r\partial \theta} = -\sum_{n=1}^{\infty}\sum_{m=0}^{n} \{\left[g_n^m \cos m\phi + h_n^m \sin m\phi\right]\left(\frac{a}{r}\right)^{n+2} + \left[q_n^m \cos m\phi + s_n^m \sin m\phi\right]\left(\frac{r}{a}\right)^{n-1}\} \frac{dP_n^m(\theta)}{d\theta} \tag{1.5}$$

$$B_\phi = \frac{-1}{r\sin\theta}\frac{\partial V}{\partial \phi} = \frac{1}{\sin\theta}\sum_{n=1}^{\infty}\sum_{m=0}^{n} m\{\left[g_n^m \sin m\phi - h_n^m \cos m\phi\right]\left(\frac{a}{r}\right)^{n+2} + \left[q_n^m \sin m\phi - s_n^m \cos m\phi\right]\left(\frac{r}{a}\right)^{n-1}\} P_n^m(\theta) \tag{1.6}$$

1.2 International Geomagnetic Reference Field Model (IGRF) :

It is now well known that the magnetic field at any location near the Earth is a combination of field due to three sources viz. Earth' s core, crust and Earth' s ionosphere and beyond. Among theses three sources, field from Earth' s core also known as main field, is largest in magnitude, which is around 99% of the total magnetic field. Its temporal or secular variation is slow, with a maximum of about 1% per year.

In order to study the main field, a method of measuring magnetic intensity in absolute units was found by Gauss in 1832. Measurements from different observatories were soon providing a synoptic picture over some of that portion of the globe covered by landmasses. Each value of X, Y and Z furnishes an equation between the coefficients. To minimize the effects of measurement errors and the effect of neglecting higher orders in the expansion, Gauss considered a series of measurements, well distributed over the entire globe, of much greater

number than the number of unknown coefficients to be determined, which are further solved by the method of least squares. But large number of unknowns and equations make the method impractical; hence there was a need of more practical method. New method requires X, Y and Z data at fixed parallels of co-latitude, θ_i , $i = 1,2,...k$ and at regularly spaced intervals of longitude ϕ. For each parallel of co-latitude, each component of data is Fourier analyzed to give

$$X(\theta_i,\phi) = \sum_{m=0}^{N} \alpha_{mx}(\theta_i)\cos m\phi + \beta_{mx}(\theta_i)\sin m\phi \qquad (1.7)$$

$$Y(\theta_i,\phi) = \sum_{m=0}^{N} \alpha_{my}(\theta_i)\cos m\phi + \beta_{my}(\theta_i)\sin m\phi \qquad (1.8)$$

$$Z(\theta_i,\phi) = \sum_{m=0}^{N} \alpha_{mz}(\theta_i)\cos m\phi + \beta_{mz}(\theta_i)\sin m\phi \qquad (1.9)$$

Equating coefficients of $\cos m\phi$ and $\sin m\phi$ between equations (1.7) and (1.5), (1.8) and (1.6), and (1.9) and (1.4) for each θ_i gives:

$$\begin{Bmatrix} \alpha_{mx}(\theta_i) \\ \beta_{mx}(\theta_i) \end{Bmatrix} = \sum_{n=m}^{N} \begin{Bmatrix} g_n^m + q_n^m \\ h_n^m + s_n^m \end{Bmatrix} \frac{dP_n^m(\theta_i)}{d\theta},$$

$$\begin{Bmatrix} \alpha_{my}(\theta_i) \\ \beta_{my}(\theta_i) \end{Bmatrix} = \sum_{n=m}^{N} \begin{Bmatrix} -(h_n^m + s_n^m) \\ (g_n^m + q_n^m) \end{Bmatrix} \frac{mP_n^m(\theta_i)}{\sin\theta_i},$$

$$\begin{Bmatrix} \alpha_{mz}(\theta_i) \\ \beta_{mz}(\theta_i) \end{Bmatrix} = -\sum_{n=m}^{N} \begin{Bmatrix} (n+1)g_n^m - nq_n^m \\ (n+1)h_n^m - ns_n^m \end{Bmatrix} P_n^m(\theta_i).$$

Thus, each component yields k equations relating the spherical harmonic coefficients g_n^m, h_n^m, q_n^m and s_n^m to the Fourier coefficients, α and β. These equations are then solved by least squares for the spherical harmonic coefficients.

The International Geomagnetic Reference Field (IGRF) model is the empirical representation of the Earth' s magnetic field recommended for scientific use by the International Association of Geomagnetism and Aeronomy (IAGA). The IGRF model represents the main (core) field without external sources. The model employs the usual spherical harmonics expansion of the scalar potential in

geocentric coordinates. The IGRF model coefficients are based on all available data sources including geomagnetic measurements from observatories, ships, aircrafts and satellites.

1.3 Ionosphere:

Ionosphere can be defined as that part of a planetary atmosphere where ions and electrons are present in quantities sufficient to affect the propagation of radio waves. Conventionally, it extends from 60 km to about 2000 km above the earth' s surface. The ionization of the atmosphere is not uniform but is stratified. This stratification results because of differences in the chemical composition and physical properties of the atmosphere at different heights and also because of unequal abilities of different gases in absorbing solar radiation of different wavelengths. There are three prominent layers during daytime viz. D, E and F regions, and under certain conditions the F layer splits into F1 and F2. Figure (1.1) shows a typical daytime profile of electron concentration on which are marked the different layers of the ionosphere and the neutral atmosphere. A typical temperature profile is also shown. The earth' s magnetic field affects the electrons' motion at all heights but with greater height, its importance increases; that part of the ionosphere where it exerts a predominant influenced is called the magnetosphere.

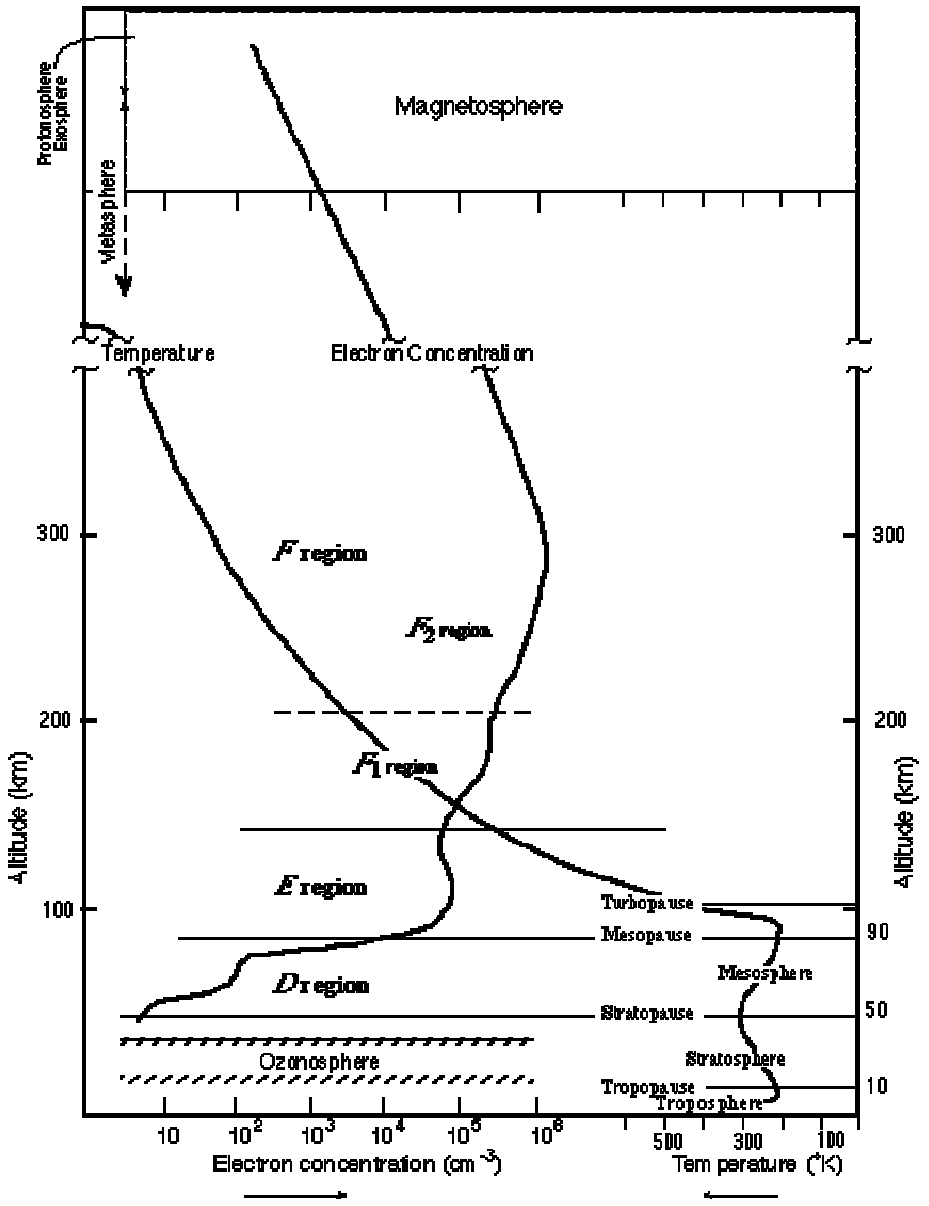

Figure 1.1 The electron concentration profile

(Source: http://ion.le.ac.uk/ionosphere/profile.html)

1.3.1 Production and loss of the ionospheric plasma:

In any gas, ionized by vertically incident radiation, electrons are produced most rapidly at a height where the number of molecules in a unit column is equal to the reciprocal of the ionization cross-section. If the concentrations of different ionizable gases are known as functions of height, it is then possible to deduce the

height at which different wavelengths would produce electrons most rapidly if they were incident vertically. The electrons are produced in the E region by the ionization of N_2, O_2 and O; in the F region by N_2 and O. The part of the spectrum, that penetrate to the D-region, have wavelengths greater than 102.7 nm (X-radiation). The enhanced X-radiation during a solar flare leads to an increased rate of production in the D region. Most of the longer-wave radiation that could ionize gases in the D region is absorbed at greater heights.

When electrons are produced, their equilibrium distribution is determined at the smaller heights by photochemical processes and at the greater heights by diffusion. If the rate of production is q and the rate of loss is L, then photochemical equilibrium is set up when $q = L$. A free electron can disappear by reactions of the following three different types:

Recombination with an atomic positive ion accompanied by radiation of a photon as represented by

$$e^- + X^+ \rightarrow X + h\upsilon \qquad \text{(radiative combination)}$$

Recombination accompanied by dissociation of a molecular positive ion as represented by

$$e^- + XY^+ \rightarrow X + Y \qquad \text{(dissociative recombination)}$$

Attachment to a neutral particle to form a negative ion as represented by

$$e^- + Z \rightarrow Z^- \qquad \text{(attachment)}$$

For the heights considered here, the attachment reaction to form negative ions are rapidly detached by other reactions, so that loss of electrons by attachment can be neglected. However, in the lowest ionosphere the loss of electrons by attachment can be important.

When electrons disappear by first two types of reactions, the rate of loss from unit volume is given by

$$L = -\frac{d[e]}{dt} = -\alpha[e][P^+]$$

where, α is the recombination coefficient and $[P^+]$ is the concentration of the (atomic or molecular) positive ion. If there are no negative ions, we can write [e] = $[P^+]$ and

$$-\frac{d[e]}{dt} = -\alpha[e]^2$$

Since dissociative recombination involves two material particles, whereas radiative recombination involves only one (and a photon), the need to conserve energy and momentum is more easily satisfied in dissociative reaction. The calculated magnitude of the radiative recombination coefficient is about $10^{-18} m^3 s^{-1}$ whereas that of the dissociative recombination coefficient is very much larger, about $10^{-13} m^3 s^{-1}$.

1.3.2 Ionospheric Temperature:

Photoionization of the upper atmosphere by solar ultraviolet absorption gives rise to photoelectrons and releases photoelectron energy due to its interaction with the neutrals, ions, and electrons. Inelastic collisions with neutral particles are efficient in removing energy from the more energetic photoelectrons, resulting in some additional ionization, although most of the energy absorbed in such collisions is radiated away or utilized in subsequent chemical reactions.

Elastic collisions of photoelectrons with ambient electrons and ions heat these gases above the neutral gas temperature. Since in the process of photoionization, electrons are ejected from the parent molecules with energies greater than the thermal energy of the ambient gas, the electron temperature (T_e) and ion temperature (T_i) can differ from each other and from neutral temperature (Tn). Because the momentum transfer from photoelectrons is faster to electrons than to ions and faster to neutral particles from ions than from electrons, the three gas temperatures usually satisfy the relationships $T_e > T_i > T_n$. Below 120 km, the collision frequencies are so large that the three gas temperatures are nearly equal, but above this altitude in sunlight, T_e increases rapidly up to approximately 200

km, which is level of peak electron-production, where it is usually about twice the neutral temperature. The detailed behaviour of T_e above 200 km depends strongly on the electron concentration height profile, and in general T_e varies inversely with the electron concentration. Due to the large ion-neutral collision frequency, the ion temperature remains close to the neutral temperature up to approximately 200km, but above this altitude T_i begins to increase until ultimately $T_i \approx T_e$.

At night, photoionization ceases and the three gas temperatures all tend toward the same value. This equilibrium proceeds rapidly at low altitudes and latitudes, but considerable heat can be stored in the plasma contained on the high-latitude magnetic-field lines that extend far out into space (several earth radii). It takes some time to conduct all this heat away, and lack of thermal equilibrium is observed at high altitudes and latitudes long after sunset. In addition, even though the atmosphere may be locally in darkness, the atmosphere at the opposite, or conjugate, end of the local magnetic field lines may not be. When this is the case, direct impingement of photoelectrons released in the opposite hemisphere can heat the local plasma; this direct heating is augmented by thermal conduction along the magnetic tube from the hot sunlit conjugate ionosphere.

1.3.3 Electrical Conductivity of the Ionosphere:

Above about 85 km, electrons start playing an important role in determining the conductivity of the medium. Electrons are produced mainly through the ionization of the molecules by solar UV radiation as seen in section 1.4. In the narrow belt characterized by auroral activity there exists another source of ionization associated with downward precipitating ions and electrons; a source that is highly variable and geomagnetic activity dependent.

Conductivity relates the ionospheric currents to the electric field. The conductivity along magnetic field is known as parallel or longitudinal

conductivity (σ_0). If electric and magnetic fields are perpendicular to each other, the conductivity along electric field is known as Pederson conductivity (σ_1), while conductivity perpendicular to both the fields is called Hall conductivity (σ_2).

Since ionozation is due to the solar rays and the electrons generated are also continuously lost through recombination, the electron density changes with the position of the sun. It has a definite diurnal pattern of variation with electron density peaking near local noon. The lower part of the ionosphere disappears at night as there is no production of electrons and the loss processes are strong. Thus, in the sunlit ionosphere the conductivity is due predominantly to solar radiation and is fairly uniform, varying gradually with solar zenith angle, undergoing through a diurnal pattern.

1.4 Geomagnetic variation:

1.4.1 Quiet Day Geomagnetic variation:

The variation in the magnetic field at a given station can be seen to be fairly repetitive with clear pattern related to the movement of the sun between sunrise and sunset. Very often they follow a smooth pattern conventionally called ' quiet day' pattern. On occasions this is violently disturbed, called geomagnetically ' disturbed days' . When the small but persistent effects due to lunar motion are removed, the changes are called Sq for solar quiet variations.

Systematic monitoring of the magnetic field variations on ground was carried out in the nineteenth century and the diurnal variation of the field was clearly identified. The latitude profile of the diurnal (24 hour) variation of the magnetic elements in local time, show a reversal in H near about 35^0N or 35^0S latitude. Between 35^0N and 35^0S latitude, H increases after sunrise and attains its maximum value and then goes to night time level little after sunset, while beyond these latitudes, the diurnal pattern is reversed. The vertical component changes sign across the magnetic equator and so does the declination

component. Since the magnetic field has to be related to some current and we know currents therein the ionosphere, we can construct an equivalent current system in the ionosphere that will reproduce the ground observations. A typical pattern of the daytime equivalent currents in the ionosphere under equinoctial conditions is shown in figure 1.2. This current system seem to be consisting of two loops, one in the northern hemisphere centered at its focus at about 35^0N flowing anti clockwise and other in the southern hemisphere flowing clockwise with the equator as the separating region. These current loops are confined largely to the daylight hemisphere and are fixed in space relative to the sun. As earth rotates under the current system the diurnal variations in H, Z & D are registered. They are called solar quiet day or Sq current system. These currents are produced by atmospheric dynamo in which currents are driven by the movement of the neutral air and their magnitudes depend on the conductivity of the ionized medium in which they flow (principally E region).

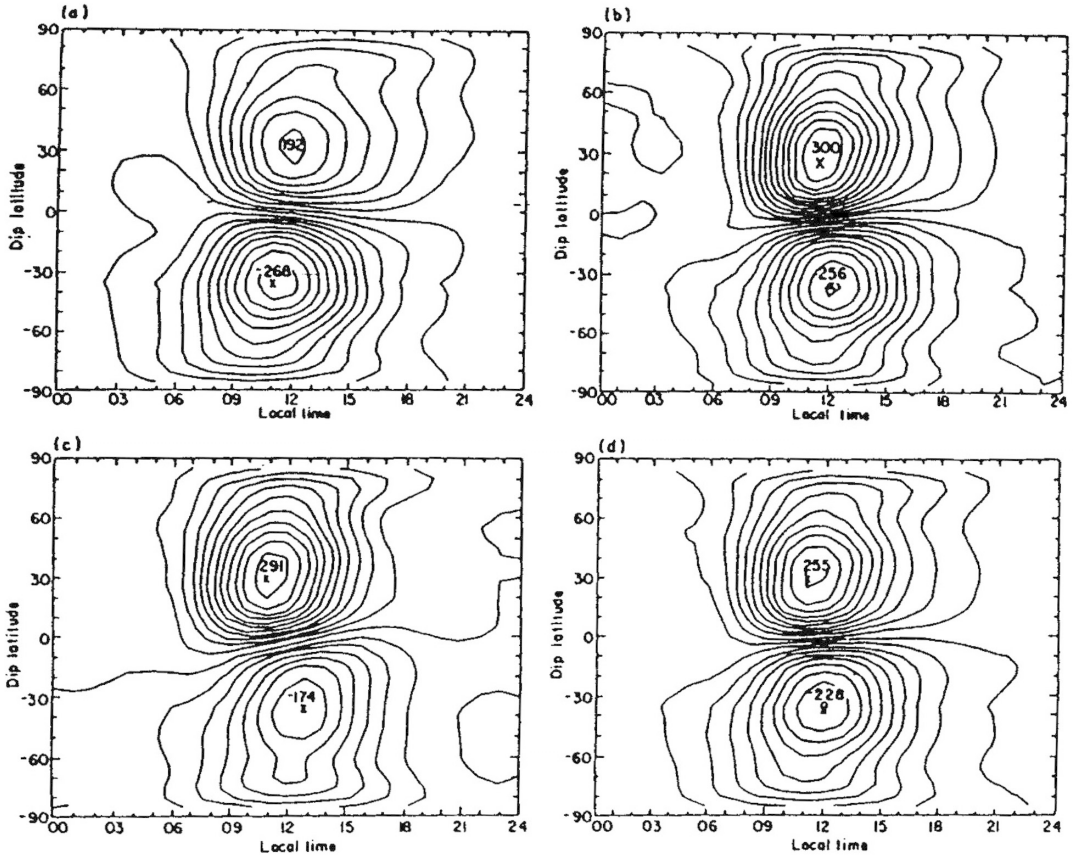

Figure 1.2 : The Sq ionospheric current system plotted for D months (top left);E months (top right); J months (bottom left); and annual average (bottom right) when the average of 21 to 3 hr is taken as the zero level. Currents flow anticlockwise in the northern hemisphere and clockwise in the southern hemisphere. The current intensity between consecutive lines is $25\times10^3 A$.
(after Matsushita [1968])

1.4.2 Equatorial electrojet (EEJ):

A special feature of the ionospheric currents in the ionosphere is an enhancement within a few degrees of the dip equator. This diurnally varying eastward jet of currents is known as the Equatorial Electrojet (EEJ) and is one of the exciting areas of research in equatorial dynamics, which has been studied in the present thesis. The EEJ is the high concentration of ionospheric current flowing from west to east in a narrow belt flanking the dip equator in the sunward hemisphere. This is related to the fact that in the region of the dip equator, the magnetic lines of force are horizontal and as a consequence a large vertical

polarization electric field, mainly responsible for the enhanced eastward currents, can be set up. Thus it should be noted that the enhancement at the dip equator is merely associated with the special field line geometry of the geomagnetic field around the dip equator. Both the Sq and EEJ variations are driven by the atmospheric tides (primarily associated with differential solar heating and having a smaller contribution from lunar gravitational forcing) and their variability from day to day should be linked with the tidal variability.

1.4.3 Disturbed Day Geomagnetic variation:

The increased amount of solar wind, which is basically protons and electrons, coming to earth causes the changes in the quiet day variation of geomagnetic field, this is called as Disturbed day geomagnetic variation and the disturbances are called as geomagnetic storms. Generally, the storm starts with a sudden commencement, (SSC) that occurs almost simultaneously (within minutes) everywhere on the earth. This is caused by the shock wave at the magnetosphere formed by the arrival of the fast solar wind plasma. SSC may be followed by an increase in the magnetic northward field as an initial phase, a compression effect can continue up to several hours. This is followed by the main phase, in which northward field decreases and shows major fluctuations for a longer time. Finally in a recovery phase, it tries to return gradually to an undisturbed level, which takes quite a long time as several days.

The spectrum on disturbed day shows number of peaks and the amplitude increases with increasing period, unlike that for quiet day variations. Geomagnetic pulsations are generally referred to shorter period variations below few minutes. It has been divided into two groups called continuous (Pc) and irregular (Pi) pulsations, corresponding to their appearance on a timeseries. Further they are numbered as indicated in Table 1.1, according to the frequency range.

Table : 1.1

	Period (sec.)	**Frequency**
Pc1	0.2-5	0.2-5 Hz
Pc2	5-10	0.1-0.2 Hz
Pc3	10-45	22-100 mHz
Pc4	45-150	7-22 mHz
Pc5	150-600	2-7 mHz
Pi1	1-40	0.025-1 Hz
Pi2	40-150	2-25 mHz

1.5 Measurement of Ionospheric currents and electric fields:

Upper atmospheric electric fields and currents can be estimated from the following:

1. Surface geomagnetic variations
2. Surface electric field and air-earth current measurements:.
3. Stratospheric balloon based horizontal electric field measurements.
4. Rocket or satellite based measurements.
5. Ionospheric radars.

Surface geomagnetic variations:

Surface geomagnetic observatory measurements provide continuous and relatively cheap estimates of parameters of the ionospheric components. The biggest shortcoming of the surface geomagnetic measurements is they can provide an estimate of the height-integrated contribution of the ionospheric currents.

Surface electric field and air-earth current measurements:

The Solar Quiet Day (Sq) current system introduces a potential difference, Φ, of

5-15 kV between the equatorial and mid-latitude ionosphere. We note that the low latitude ionosphere can be considered to be at a uniform voltage only to this degree of approximation. The conductivity of the middle and lower atmosphere is small but not zero. There is therefore a leakage of currents through the lower atmosphere to the ground. This has the effect that large scale horizontal electric fields are mapped down to altitudes of 25 km almost without any change. Plastic balloon floating at 30 km altitude have provided excellent data of Sq electric field.

Electric Fields from Stratospheric Balloons:

The atmosphere below the ionosphere has finite though relative to the medium above a lower conductivity. On the other hand the earth is a near perfect conductor. One of the consequences of this is that the horizontal electric fields in the ionosphere get mapped down to an altitude of around 30 km. with almost no attenuation. At the height of 30 km. thunderstorm related field is still vertical but considerably attenuated. The electric fields of ionospheric origin are horizontal and can therefore be distinguished from the electric field of thunderstorm origin though smaller in magnitude. It is thus possible to get the ionospheric electric fields by monitoring the horizontal electric fields at 30 –35 km altitude.

The electric fields at balloon altitudes are measured using the double Langmuir probe. Stratospheric plastic balloons, which can float at around a fixed height of 25-35 km from a few hours to days, have provided very valuable measurements of the electric fields in the ionosphere. While the rocket provides only a few minutes of data, the balloon can generate continuous data for hours and even days.

Rocket or satellite based measurements:

Space borne magnetometers are a valuable diagnostic tool for monitoring ionospheric current systems. Unlike the surface magnetic field measurements that can only monitor the height integrated currents, the space borne magnetometers can give the exact structure of the current system they are cutting through. The currents are computed from the curl of the magnetic field, which requires that the satellite/rocket should cut across the current sheet and the magnetometer should be able to measure the component of the magnetic field variation tangential to the current sheet. In general vector measurements are required but in the special case of the equatorial electrojet, the scalar measurements are adequate.

Almost all the knowledge we have on the vertical structure of the equatorial electrojet currents has been derived from rocket scalar magnetic field data. The magnetic field at the magnetic equator is horizontal and the horizontally stratified EEJ currents flow perpendicular to the ambient field and produces only changes in the magnitude of the magnetic field. Thus a vertical rocket launch with a simple proton magnetometer payload can provide all the information required to obtain the vertical structure of the EEJ measurements at ionospheric heights will require accuracies of the order of arc seconds in attitude measurements, a feat accomplished only by highly expensive and sophisticated satellites specially designed for vector magnetic field measurements. It is not surprising that a few vector measurements attempted through rockets have not been really successful.

Polar orbiting low altitude satellites with magnetometer or electric field probes are very useful for obtaining information on ionospheric currents and electric fields. If the altitude of the satellite is well above the current system, the magnetometer on board the satellite can be used only to monitor the height

integrated EEJ currents. What the satellite records will be a mirror image of what a ground-based array will record. Even in this case the satellite does offer some advantages like global coverage and relatively smaller noise due to sub-surface conductivity anomalies. The importance of the former can be gauged from the fact that more than 70% of the EEJ regions are not accessible as they lie in the oceans.

Satellite with lower altitudes can be used to monitor the vertical current loop associated with the EEJ. We have noted that the EEJ currents are strongly controlled by the vertical electric fields, only part of which is directly related to the horizontal potential gradients. Thus, even if the Cowling conductivity is known, the horizontal field cannot be directly estimated. The vertical current loop also contributes to the vertical polarization field and hence the EEJ currents. Magsat, a special satellite flown with tri-axial magnetometer and an accurate attitude determining system, was able to monitor these currents in spite of the fact that the satellite orbit was confined to the dawn and dusk sectors where the EEJ is weak. Tri-axial magnetometers in polar orbiting satellites are ideally suited to monitor the field-aligned currents. Almost all the information we have on Birkeland currents is based on these measurements.

The biggest problem with satellite-based measurements is the limited spatial coverage. A number of satellite passes are required to produce synoptic or global maps. This can be attained either through radar based monitoring or through a process of assimilative modeling described later.

Radar based monitoring:

The geomagnetic field in the upper part of the ionosphere can be taken, for most practical purposes as a perfect conductor. An electric field $\overline{E}$ perpendicular to the ambient magnetic field $\overline{B}$, will thus produce a drift $\overline{V}_D = \overline{E} \times \overline{B} / B^2$ which is perpendicular both to the ambient magnetic field as well as the imposed electric

field. If one can detect the plasma drift, one can estimate the electric field. The neutral wind induced plasma drifts would then be regarded as noise and reliable estimates of the electric field patterns is restricted to regions where neutral collisions are not important. In the absence of collisions the electric field parallel to the ambient magnetic field becomes negligible. The electric fields at middle and low latitudes range from 0.1 mV/meter to a few mV/meter. These fields produce cross field $\overline{E} \times \overline{B}$ plasma drifts from few meters per second to tens of meters/second and these drifts can be picked up by the back scatter radar. HF and VHF radars have been most effectively used for the said purpose, both in the coherent and in the in-coherent mode. Over a period of time a number of mid-latitude stations have contributed in setting up of a database, some of which have been incorporated into empirical models of the electric field distribution.

At the dip equator the horizontal electric fields are very small being only a fraction of mV/meter. But because of the special geometry of the ambient magnetic field, they can set up in the height region of 105 km. or so vertical polarization fields of the order of 10 mV/meter. At these height the electrons do not experience any collisions and therefore the electron density irregularities experience the $\overline{E} \times \overline{B}$ eastward drift that has been systematically monitored at Thumba using the coherent back scatter set up there. This has proved a very effective method for monitoring the vertical electric fields. The primary horizontal field responsible for setting up the equatorial electrojet can only be inferred indirectly using appropriate models.

The most important development in the area of large-scale electric field mapping using the radar technique has been the implementation multi-national Super Dual Auroral Radar Network (Super DARN) system. The network consists of networks of HF coherent backscatter radars, which measure ionospheric Line Of

Sight (LOS) Doppler velocities over a large portion of northern and southern hemispheres.

1.6 Empirical models of the equatorial electrojet current:

Just after the discovery of Equatorial electrojet phenomenon, Chapman put forward different current model to study the EEJ. Let the centre of the current system at an altitude of *h* km be at the origin of the coordinate system (x,y,z), point to the north, east & downward, respectively.

1.6.1 Line Current Model:

It is one-dimensional and the current $\bar{I}$, carried by the line at a fixed distance $x = d\ km$ and fixed altitude $h\ km$ is given by

$$\bar{I} = I_c \hat{y}$$

is constant along the line $x = d,\ z = 0$, where $\bar{I}_c$ is a constant.

1.6.2 Current Ribbon of Constant Intensity Model:

It is a one-dimensional model and current intensity is given by

$$\bar{J} = J_c \hat{y} \quad cons\tan t \ \ for - w \le x \le w$$
$$\bar{J} = 0 \quad for\ x < -w\ and\ x > w$$

where, $w\,(km)$ is the half width of the current and $\bar{J}_c$ is a constant. It is unidirectional and essentially a step function. It has zero thickness and no current density.

1.6.3 Current Ribbon of Parabolic Intensity Model:

It is one-dimensional and current intensity is given by

$$\bar{J} = J_0\left(1 - x^2 / w^2\right)\hat{y} \quad for - w \le x \le w$$
$$\bar{J} = 0 \quad for \ \ x^2 > w^2$$

where J_0 is the peak intensity at $x = 0$. It is unidirectional and does not have thickness.

1.6.4 Current Ribbon of Fourth degree intensity Model:

Fambitkoye and Mayaud [1976] introduced this one dimensional and its current density given by

$$\bar{J} = J_0\left(1-\frac{x^2}{w^2}\right)\hat{y} \qquad for \quad -w \le x \le w.$$

1.6.5 Onwumechili' s model of EEJ

We discuss this model in great detail as we are going to use it extensively to deduce currents from satellite measurements of electric field. To get current which causes quiet day geomagnetic variations, one need to have a simple function with the smallest number of parameters. Three major considerations arise:

(a) The main part of the currents is believed to flow in the ionosphere; from the altitude distribution of ionospheric conductivity, the current is greatest at some altitude,

(b) It is known that the current is limited in altitude but it is unlikely that it assumes the terminal zero value abruptly, and

(c) Every current must have a path such that the forward current equals the return current.

One of the simplest function that incorporates the above three points is

$$\overline{C} = \overline{C}_o \frac{b^2\left(b^2+\beta z^2\right)}{\left(b^2+z^2\right)^2} \qquad (1.10)$$

where, $\overline{C}$ & $\overline{C}_o(x,y)$ are vector current densities in amp-km^2

b is a constant length, β is a dimensionless constant and the axes of the Cartesian coordinate system as described above.

Here our main interest is the equatorial electrojet that flows from west to east for most of the daytime, & therefore we concentrate on the eastward component of current density, $\bar{j}$. The latitudinal distribution of the Sq current can be represented with a function similar to equation (1.10), because the current has an axis near the equator, it decreases gradually away from the axis; and at least part of the return current is a function of latitude.

Therefore, we can write,

$$\bar{j} = \bar{j}_o \frac{a^2\left(a^2 + \alpha x^2\right)}{\left(a^2 + x^2\right)^2} \cdot \frac{b^2\left(b^2 + \beta z^2\right)}{\left(b^2 + z^2\right)^2} \cdot f(y) \qquad (1.11)$$

where,

$f(y)$ is a function of longitude or time, a is a constant length,

$\bar{j}_o$ is the current density at (0,y,0) and α is a dimensionless constant.

If for simplicity we put $f(y)=1$, then

$$\bar{j} = \bar{j}_o \frac{a^2\left(a^2 + \alpha x^2\right)}{\left(a^2 + x^2\right)^2} \cdot \frac{b^2\left(b^2 + \beta z^2\right)}{\left(b^2 + z^2\right)^2} \qquad (1.12)$$

This makes the density constant along any line parallel to the y-axis & depicts the current lines as infinitely long in the eastward or y-direction.

This equation assumes (a) that the current axis is a straight line instead of the expected arc, (b) that the axis $x = z = 0$ is also an axis of symmetry and (c) that the variables are separable.

Height integrated eastward current intensity at a distant x from the origin, $\bar{J}_x$ is given by $\bar{J}x = \bar{J}_{xo} \cdot \frac{a^2\left(a^2 + \alpha x^2\right)}{\left(a^2 + x^2\right)^2}$ (1.13)

Next, we discuss about the direction of flow of the current represented by equation (1.12).

Near the y-axis, the current always flows parallel to that axis and retains that direction everywhere as shown in figure (1.3b) if both α and β are positive or zero. But if α and β are not both positive, the current at some distance from the y-axis becomes antiparallel to that axis, see figure (1.3a) and thus provides for return current without requiring the current lines to turn.

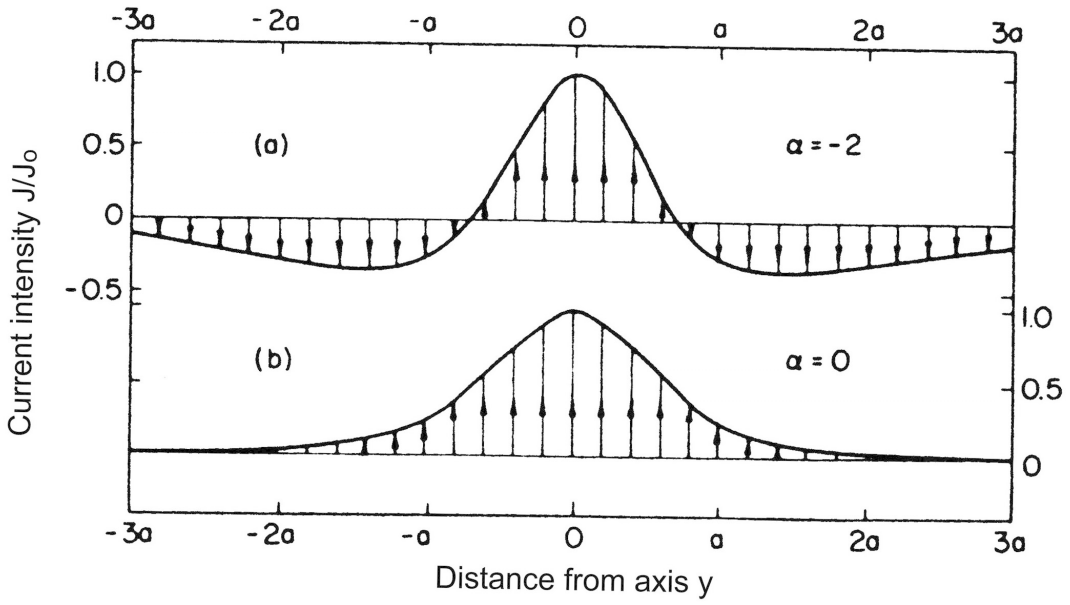

Figure 1.3 : An illustration of two kinds of current flow (a) For negative α, (b) For positive and zero α. (after Matsushita [1968])

In this case, as we move away from the axis the strength of the positive (forward) current decreases gradually to zero. The direction of the return (negative) current increases to a maximum & then gradually decreases to zero toward infinity.

Dropping the subscription in equation (1.13), we write,

$$\bar{J} = \bar{J}_o \frac{a^2\left(a^2 + \alpha x^2\right)}{\left(a^2 + x^2\right)^2} \qquad (1.14)$$

This embodies three distinct types of current distribution.

(1) $\alpha < 0$

$\Rightarrow$ The intensity is zero at $x^2 = -\frac{a^2}{\alpha}$

At x = 0, J = J_o = maximum value

and at $x^2 = \frac{a^2}{\alpha}(\alpha - 2)$, $J = \frac{1}{4} J_o \cdot \frac{\alpha^2}{(\alpha - 1)}$

i.e. at $x = \pm\sqrt{\frac{a^2}{\alpha}(\alpha - 2)}$ J= minimum value

(2) $0 \le \alpha \le 2$, There is only one maximum of value $\bar{J}_o$ at x = 0

(3) $\alpha > 2$

There are two equal maxima of value

$J_m = \frac{1}{4} \quad J_o \cdot \frac{\alpha^2}{(\alpha - 1)}$ at $x^2 = \frac{a^2}{\alpha}(\alpha - 2)$

The variation of the eastward intensity with distance from the axis is shown in Figure (1.4).

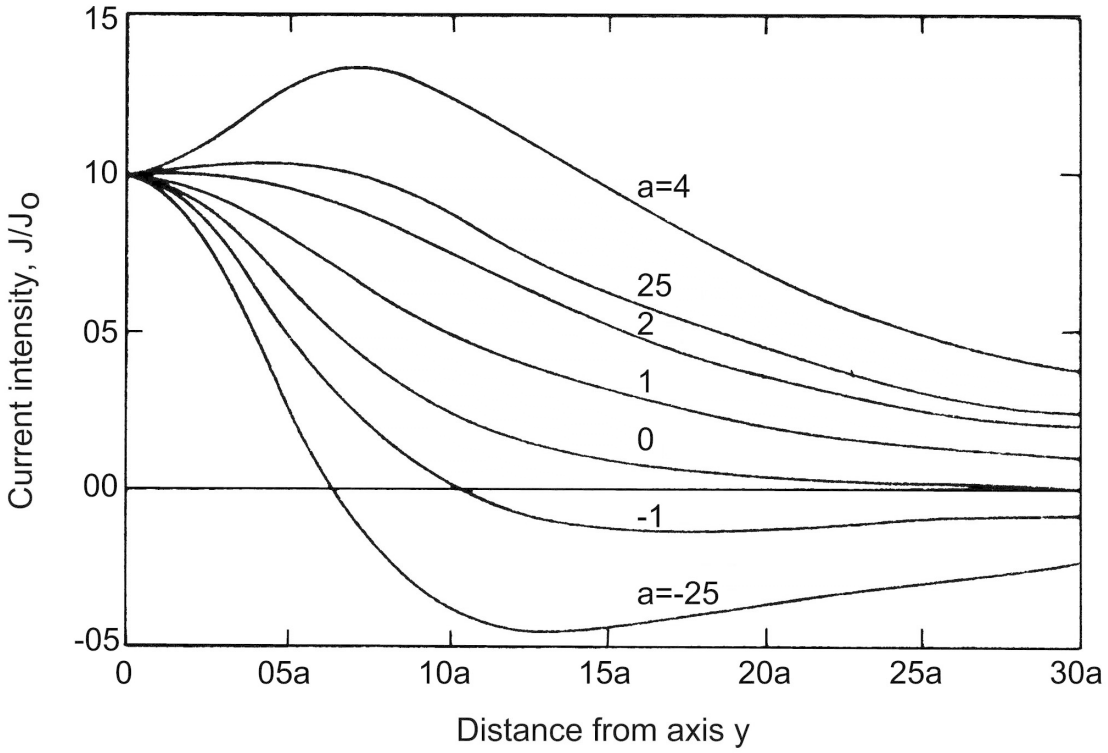

Figure 1.4 : Current intensity as a function of distance from the axis for different values of α. *(after Matsushita [1968])*

Fitting the observed data determines the sign of α. If α is negative, then return currents contribute to the observed field; otherwise, the data should lead to positive α. Two other ranges of α may however, be mentioned, even though they are not likely to fit the Sq and the electrojet. For negative values of α much larger than –5, the minimum current intensity may be numerically much larger than the maximum $\bar{J}_o$, at the axis. Similarly, for positive values of α much larger than 2, the maximum on either side of the axis is larger than the numerical value of J_o at the axis. In short, this model includes a variety of distributions, and the structure of the current system is not finally decided until the observed data are used to fix the distribution constants α and β.

Width and Thickness

We define the width of a current as the distance between the two points where the density is zero along the x -axis and define the thickness similarly along the z-axis. This assumes that the measurements are taken along the axes of symmetry of the current with the origin at the point of maximum current density and the z-axis is downward. If we denote the half-width with w and half the thickness by d, then from equation (1.12),

$$w = \frac{a}{\sqrt{-\alpha}} \qquad (1.15)$$

$$d = \frac{b}{\sqrt{-\beta}} \qquad (1.16)$$

It is clear that w and d are real only when α and β are negative. When they are not real, the lateral extent may be discussed in terms of the apparent width $2a$ and the vertical extent in terms of the apparent thickness $2b$.

Magnetic field produced by the current as given by the model:

The most successful of the current models so far used to fit the magnetic field of the equatorial electrojet is that discussed above. According to equation (1.12), the

density of the current, is independent of y and therefore depicts a current system flowing east-west with constant density along any line lying east-west. Thus, the current is assumed infinitely long in that direction, and the return current is provided not by the turning of the forward current but by the flow of parallel and oppositely directed current at some distance from the axis. Such a model produces no field in the Y-direction. We shall therefore, be dealing with the field components X and Z only. Moreover, the curvature of the earth is disregarded in the integration, and therefore the current is assumed to be flowing in a plane rather than in a spherical shell. It is therefore more appropriate for a narrow current like the electrojet.

The magnetic field to the first approximation produced by this current at point (x,z) is,

$$(sg.z)X = \frac{1}{2}Ka\frac{(v+\alpha v+2\alpha a)u^2+(v+\alpha v+2a)(v+a)^2}{\left[u^2+(v+a)^2\right]^2} \tag{1.17}$$

$$-(sg.x)Z = \frac{1}{2}Ka\frac{u\{(1+\alpha)u^2+(v+\alpha v+3a-\alpha a)(v+a)\}}{\left[u^2+(v+a)^2\right]^2} \tag{1.18}$$

where,

$$sg.z=\frac{z}{|z|},\qquad sg.x=\frac{x}{|x|},\qquad u=|x|,\qquad v=|z|,\qquad K=0.2\pi J_{xo}$$

x and z are distances from the center of the current system which is at 110 km of altitude.

If b is not negligible,

$$(sg.z)X = \frac{1}{2}k(1+\beta)ab\frac{(v+\alpha v+2\alpha a)(u+b)^2(v+\alpha v+2a)(v+a)^2}{\left[(u+b)^2+(v+a)^2\right]^2} \tag{1.19}$$

$$-(sg.x)Z = \frac{1}{2}k\frac{(1+\beta)ab.(u+b)\left[(1+\alpha)(u+b)^2+(v+\alpha v+3a-\alpha a)(v+\alpha)\right]}{\left[(u+b)^2+(v+a)^2\right]^2} \tag{1.20}$$

where, $k = 0.1\pi^2 j_0$

1.7 Principal components analysis:

The most widely used multivariate method, is principal components analysis (PCA), which is a classical statistical method. PCA is a transformation, which transforms a number of (possibly) correlated variables into a (smaller) number of uncorrelated variables called 'principal components' (PC' s). This linear transform has been widely used in data analysis and compression. The objectives of this analysis are to reduce the dimensionality of the data set and to identify new meaningful underlying variables.

The basic idea of the principal component analysis is to describe the dispersion of an array of n points in p-dimensional space by introducing a new set of orthogonal linear coordinates so that the sample variance of given points with respect to these derived coordinates are in decreasing order of magnitude.

The mathematical technique used in PCA is called eigen analysis: we solve for the eigenvalues and eigenvectors of a square symmetric matrix of covariance. The eigenvector associated with the largest eigenvalue has the same direction as the first principal component and contains the most variance in the data. The eigenvector associated with the second largest eigenvalue determines the direction of the second principal component and contains the most variance when the first component is removed from the data. The sum of the eigenvalues equals the trace of the square matrix and the maximum number of eigenvectors equals the number of rows (or columns) of this matrix.

If one standardizes each coordinate by dividing with its sample standard deviation, then the covariance matrix of the standardized variables is just the correlation matrix of the original variables. Thus the above treatment can be applicable to correlation matrix also. Since PC' s based on covariance matrix are

not invariant under linear transformation, including separate scaling of the original coordinates, the PC' s of the covariance matrix are not the same as those of the correlation matrix. However PC' s based on correlation matrix are invariant under separate scaling of the original variables. For this reason, as well as for numerical computations, correlation matrix is a better choice for PCA.

Thus a common way to find the Principal Components of a data set is by calculating the eigenvectors of the data correlation matrix. These vectors give the directions in which the data cloud is stretched most. The projections of the data on the eigenvectors are the Principal Components. The corresponding eigenvalues give an indication of the amount of information the respective Principal Components represent. Principal Components corresponding to large eigenvalues, represent much information in the data set and thus tell us much about the relations between the data points.
This technique of analysis has been used to study day to day variability of EEJ strength in the present investigation. The detailed procedure has been discussed in chapter 3.

1.8 Coherency and Phase:

The geometric mean serves as the measure of the theoretical top limit of the common power at any given frequency *f* in the two single channel time series. In order to attain this top limit, the power at that frequency must have a fixed phase relationship for the two single channel time series in question. If this top limit is indeed attained at a given frequency, we say that the two time series are coherent at that frequency. However, it is usually the case that the phase relationships at a given frequency are changing in a random fashion. If the changes were completely random, the theoretical bottom limit, namely, zero, of the common power would be reached, and the two time series would be completely incoherent. In most observed cases, in time series analysis, the coherency is somewhere between these two theoretical extremes.

Let $M_{jk}(f)$ be the geometric mean of two series denoted by $j(t)$ and $k(t)$.

The coefficient of coherency is defined as

$$K_{jk}(f) = \left|K_{jk}(f)\right| e^{-i\theta_{jk}(f)} = \frac{SP_{jk}(f)}{M_{jk}(f)} = \frac{C_{jk}(f) - iQ_{jk}(f)}{M_{jk}(f)}$$

where $SP_{jk}(f) =$ Cross-spectral density

$C_{jk}(f) =$ Co-spectral density

$Q_{jk}(f) =$ Quadrature-spectral density

The magnitude of the coherency is

$$\left|K_{jk}(f)\right| = \frac{\sqrt{C^2{}_{jk}(f) + Q^2{}_{jk}(f)}}{M_{jk}(f)} = \left|K_{kj}(f)\right|$$

And the phase-lag of the coherency is

$$\theta_{jk}(f) = \tan^{-1}\left(\frac{Q_{jk}(f)}{C_{jk}(f)}\right) = -\theta_{kj}(f)$$

The magnitude of the coherency lies between the limits, 0 corresponding to the completely incoherent case and 1 corresponding to the coherent case.

i.e. $0 \le \left|K_{jk}(f)\right| \le 1.$

The concepts of coherency and cross phase have been used extensively in chapter 5 for the interpretation of the observed results.

1.9 Scope of the Thesis:

As a consequence of the discussion so far made, it is clear that the ionospheric current system plays vital role in the dynamics of the space. The Equatorial Electrojet (EEJ) is a worldwide enhancement of the solar quiet day (Sq) diurnal variation in the geomagnetic field near the dip equator. Thus EEJ is a special ionospheric phenomenon due to the field line geometry at the dip equator. Since the dip equator passes through India, we are the one among very few countries, who get an opportunity to study the phenomenon in detail. The study of the EEJ is essential in order to explore the electrodynamics involved in its space.

Around 90% of area influenced by the EEJ phenomenon is covered by oceans and forests where, the continuous recording of ground based magnetic observations are not possible. Hence, the study of the phenomenon using only ground-based data proves to be inadequate. Since satellite data does not have the above restriction, it can take observations for the entire globe. Here, we have made use of the scalar magnetic field measurements obtained from Oersted satellite, which has polar orbit with local time varying from forenoon to afternoon hours. Oersted has some advantages over earlier satellites such as Pogo and Magsat, e.g. Magsat had dawn-dusk orbit, hence could not throw much light on the daytime phenomenon of EEJ, while Pogo could not bring out the day to day variability of the phenomenon. Under these circumstances, study of Oersted data is valuable. In the present study, we have developed a new method for the analysis, which can take into account the day to day variability. The excellent correlation between satellite and ground observations indicates that the data and the method adopted for the analysis is quite authentic. Orbital period of Oersted is around 100 minutes and it has around 15 daytime passes in a day, covering entire globe. The zonal variation of the EEJ strength obtained from satellite data seems to give new dimension to the traditional models of EEJ. The global picture obtained from this study certainly improves the understanding of the phenomenon.

The study of the main field control of the EEJ brings out the anomaly of longitude zone 300^0 to 330^0E. We find that the angle between the magnetic field and the line of zero dip deviates by around 13^0 in this longitude sector. We have evaluated this angle explicitly for different longitude zones to bring out the importance of including this parameter in future electrojet models. In all earlier theoretical EEJ models this is tacitly assumed to be 90^0.

In the present thesis, we have also studied reverse equatorial electrojet signature seen at the Oersted satellite. An attempt is made to prove the reverse EEJ signature at satellite as an indication of counter electrojet (CEJ). The reverse

signature seen during 0 to 13 UT is well supported by the ground data from Indian sector. For the UT' s greater than 13 hr, the CEJ is not identifiable at Indian stations due to nighttime. We find that whenever, the satellite is in the longitude belt of the ground station observing the CEJ, the satellite also sees the CEJ. The satellite-based analysis performed in this thesis indicates that the CEJ is never seen beyond two successive passes. This suggests that the longitudinal width is not more than 3 hours, at least for the pre-noon CEJ. This result of narrow longitudinal extent is consistent with the findings of Rastogi [1974a,b]. However, the satellite does not see the CEJ if satellite and ground differ in longitude by 30^0 or more. This gives different insight into the longitudinal variation of the CEJ occurrence on a given day.

Seasonal and local time variation of CEJ occurrence frequency, which has been done for the first time using satellite data is in agreement with earlier ground based studies. The longitudinal variation of the centre of the CEJ current system depicts that, the centre lies south of the dip equator for Indian sector and north of the dip equator of American sector. This shows that the centre of CEJ appears to be shifted away from the dip equator towards the geographic equator in both the hemispheres. The higher percentage of occurrence of CEJ in the longitude region between 300^0 to 330^0 E, may be linked with the maximum departure of magnetic field from the dip equator vector in that region.

Investigations of the magnetic field fluctuations of shorter periods are also important in order to understand the electrodynamics involved in ionosphere. We have made use of Oersted and ground data from Japanese stations to study the compressible oscillations in the frequency range of 10-80 mHz. It suggests that the phase differences introduced by the ionosphere have local time and frequency dependence. The study also indicates the equatorial enhancement of the amplitude of the pulsation, but these aspects of pulsations could not be verified as no equatorial station was working during that period. We tried to

examine this possibility using a ground array across the EEJ. However, we could acquire data from West Africa at one-minute sampling interval and therefore, the study looks at a different frequency regime (1-4 mHz).

The main results emerging from the study of short period fluctuations are as follows.

(1) The daytime ionosphere introduces a shift in phase of the hydromagnetic wave impinging on it. The phase shift is greater for higher frequencies and higher conductivity of the ionosphere.

(2) Secondly there are significant phase differences in the oscillations recorded at the centre of the electrojet and below the fringes of the electrojet.

(3) The equatorial enhancement is in general higher for lower frequencies as compared to the higher frequencies.

Thus we find that the studies based on different data sets bring out the important role of equatorial ionosphere in modelling the propagation of the fluctuations.

Thus our basic understanding of the low latitude currents comes from the ground observations and further polished by the rocket and satellite measurements. So the model for low latitude current system should mainly account for the ground, rocket and satellite measurements. The analysis based on satellite data demands few modifications in the earlier models of EEJ. The computations based on Oersted data clearly identify the four peaks in the average strength of EEJ on ground viz. at 0^0, 110^0, 190^0 and 275^0E longitudes. Traditional conductivity model is unable to account for these longitudinal variations of EEJ strength. So there is a need to have a model, which could explain this longitudinal dependence. The model should provide insight into day-to-day variability of EEJ. The analysis based on Oersted data points out that around 70% of day-to-day variability in electrojet strength are due to asymmetry of the dip equator with respect to geographic equator. Hence EEJ model should accommodate this asymmetry in its formalism. We have also discussed the

anomaly in the 300^0 - 330^0 E longitude zone and we expect that EEJ model should account for this.

For the numerical estimates of the EEJ, one needs to compute the conductivity and tidal models. The model should be able to examine the conductivity and neutral wind influence on the day-to-day variability of EEJ. In the present thesis we have devoted separate chapters for these computations, where detailed study has been carried out. We have generated a new conductivity model, which uses modified collision frequency for O^+-O given by Pesnell et al [1993]. We have also computed the traditional conductivity models of Richmond and Forbes and compared these with our model. We have made an attempt to derive these models using more realistic databases. The tidal model computed in this thesis uses classical method to solve the tidal equations and for the computation of heating sources, it adopts more recent methodology. The program and the method of solution adopted here, is such that it can perform tidal computations for different modes, e.g. two-wave, planetary scale waves etc., provided the corresponding heating terms are available. This facilitates the examination of response of EEJ model to different tidal modes.

Ultimately, the main aim of the thesis is to put forward theoretical model for equatorial electrojet, which could account for the above-mentioned features. The basic aspects of the model presented in this thesis are as follows:
The model considers the asymmetry of geomagnetic equator with respect to geographic equator and assumes the dipole geomagnetic field geometry. The tidal calculations that are in geographic coordinate system are transformed into geomagnetic system. The tidal winds were calculated for different modes and hence the sensitivity of the EEJ model to different modes could be examined. To solve 3 dimensional dynamo equations, we adopt a scheme suggested by Singh and Cole [1987]. The boundary conditions used demands that the cross field component of the meridional current integrated over field line vanishes at inner

boundary defined by the neutral atmosphere and the outer boundary defined by the assumed high latitude limit of the Sq current system.

The conclusions of the investigations based on the results discussed in various chapters have been brought out in chapter 9. This chapter also describes the improvement that can be made in the model of EEJ as part of future studies.

Chapter 2

Main Field Control of the Equatorial Electrojet

2.1 Introduction:

There are very few phenomena in the upper atmosphere, that are sensitive to the strength and distribution of the earth' s core field and equatorial electrojet (EEJ) is one of those. The EEJ arises as a direct consequence of the structure of the main geomagnetic field. The latitudinal position of the electrojet axis is dictated by the position of the dip equator at that longitude; while the Hall conductivity that is the main source of the enhanced strength of the EEJ is sensitive to the magnitude of the magnetic field. These features are fairly well brought out by ground based and satellite observations [Rastogi, 1962, Cain and Sweeny, 1973]. In this chapter our aim is to see how the main field models change in different epochs and how the EEJ is sensitive to the main field model. A detailed study of the longitudinal structure of the main field in relation to the strength and position of the EEJ is essential for understanding the phenomenon and its long-term variability. Furthermore, there is a need to examine the idealized scenario assumed by models in context of the actual geometry of the geomagnetic field in different longitudes. For example, models assume that the electrojet currents flow primarily along the dip equator and are at the same time perpendicular to the direction of the horizontal component of the earth' s magnetic field. A close look at the dip equator positions and declination maps [cf. Figure 1.3 in Onwumechili, 1997] will show that around 300^0E to 330^0E longitude zone, the declination (or the angle that the horizontal field makes with the north) changes rapidly from 8^0W to 20^0W. The dip equator orientation changes very little through this region. The angle between the geomagnetic field and the line of zero dip cannot remain constant (and hence cannot be 90^0 everywhere). The angle between the magnetic field and the line of zero dip is evaluated explicitly for different longitude zones

to bring out the importance of including this parameter in future electrojet models.

Finally, the EEJ strength is also subject to day-to-day variability and strongly influenced by the tidal forces and enhancements in the ionization due to the solar radiation. The tidal motions are ordered with respect to the geographic equator while, the electrical conductivity of the ionosphere is controlled mainly by the dip equator. The understanding of the equatorial electrojet is very essential if it has to be used as diagnostic tool for the systematic study of upper atmospheric motions. At the same time the effective use of the equatorial electrojet for the study of the sub-surface conductivity also requires a clear understanding of the spatial structure of the electrojet.

The combination of geomagnetic and geographically controlled dynamic forces or the geometry of the geomagnetic field lines can be expected to lead to longitudinal variations in the EEJ. More than 70% of the area covered by the dip equator lies in the oceanic region; thus Global coverage of the EEJ is possible only by satellite data. The satellite must collect magnetic field data at relatively low altitude and must also have near noon global coverage. The Oersted satellite meets this unique requirement and constitutes a very valuable set of data for studies of the EEJ. Amongst the first papers dealing with the studies of the EEJ from satellite data is the work using the POGO satellite scalar data undertaken by Cain and Sweeney [1973] and one of the early papers that review the satellite measurements of the EEJ is by Onwumechili [1985]. The Magsat collected valuable vector and scalar magnetic field data at low altitudes; despite the restriction imposed by the fact that its orbit was in the dawn dusk sector; nevertheless, the vector data from this satellite has made major contributions to EEJ studies [eg. Langel et al, 1993] and it established the presence of the meridional current system [Maeda et al, 1985].

The Oersted satellite was launched on 23 February 1999 with an apogee of about 849 km, and a perigee of around 638 km. The satellite instrumentation consists of an Overhauser proton magnetometer for scalar magnetic field measurements with absolute accuracy better than 0.5 nT (nanoTesla) and a compact coil fluxgate magnetometer for vector magnetic field measurements with the same intrinsic accuracy. The Oersted satellite orbit is a near polar one, with a small drift with respect to the local time. In the period from April to December 1999, it covers local time ranging from 14:00 hours to 10:00 hours in the day-side hemisphere and constitutes a very unique data-set for studies of the EEJ.

In the present chapter, the IGRF models are used to infer the broad features as well as the secular variations that could be expected in the EEJ strength and position. We also investigate the orientation of the horizontal magnetic field (H) with respect to the dip equator as in all theoretical EEJ models this is tacitly assumed to be 90^0.

2.2 Basic models of the EEJ:

The basic model of the equatorial electrojet given by Baker and Martyn [1953], which inhibits vertical currents that can describe the equatorial enhancement of the diurnal variations of the global current system at the dip equator is well known. In a co-ordinate system that has X-axis along the ambient magnetic field and Y-axis pointing eastward, the net eastward current J_y at the dip equator can be expressed as

$$J_Y = \left(\frac{\sigma_2^2}{\sigma_1} + \sigma_1 \right) E_y = \sigma_3 E_y ,$$

where E_y is the eastward electric field which is a part of the global current system, σ_1 is the Pedersen conductivity, σ_2 is the Hall conductivity and σ_3 is referred to as the Cowling conductivity in literature. The Pedersen conductivity is essentially dependent on ion-neutral collision frequency while Hall

conductivity is inversely proportional to B, the strength of the geomagnetic field. In the dynamo region of the ionosphere, Hall conductivity is larger than the Pedersen conductivity and Cowling conductivity becomes inversely proportional to B^2. Note that the enhancement of the currents at the dip equator presented above is made possible by the build up of a large vertical polarization electric field. Since the geomagnetic field lines are highly conducting this is possible only at the dip equator, as away from the dip equator the charges will leak away along the field lines. Thus the position of the axis of the equatorial electrojet in any longitude zone should be at the position of the dip equator in that longitude while the strength of the current system will vary from longitude to longitude roughly as inverse of B^2. We examine these dependencies on the strength and position of the equatorial electrojet and its secular variation.

There have been improvements in the basic model of the equatorial electrojet that include the vertical currents at the equator, the latitudinal variations in the inclination of the geomagnetic field etc. and these are extensively discussed in literature [Onwumechilli, 1997]. But two basic ingredients remain in all the models:

1. The principal electrojet current flows along the dip equator and
2. The ambient magnetic field is perpendicular to the dip equator.

2.3 Main Field Models and the EEJ:

We first examine how the secular variation in the main field as represented by the different models produces a secular variation in the position and strength of the EEJ. We therefore examine the Oersted Initial Main Field Model, OIFM [Olsen et al, 2000] generated from the Oersted data in the context of long term changes in the longitudinal pattern of the equatorial electrojet. To study the effect of the main field models on the location of the peak of the electrojet, we calculate the location of the dip equator (where the vertical component of the geomagnetic field is zero) from the different IGRF models from 1965 to 1995 epochs and OIFM

2000. Figure 2.1a plots the location of the dip equator (Geographic latitude) in the different longitude sector, on ground, as derived from the four different IGRF models from 1965 to 1995 and from OIFM 2000. This is basically similar to the average latitude of EEJ centres observed by POGO at various longitudes [Cain and Sweeney, 1973]. From this plot we find that the dip equator swings from North to South around 190^0E longitude and swings back north at around 320^0E, also seen by Rangarajan [1994]. It is also observed that from epoch 1965 to 2000, the minimum variation in location of the dip equator is in the longitude zone 155^0 to 215^0E; whereas, the maximum shift lies in the longitude zone from 290^0 to 360^0E and extends to 10^0E (see Figure 2.1a). The most significant feature is the drift of the location of the dip equator (hence the position of the axis of the EEJ) to the extent of 1^0 per decade around 300^0E. In the Indian zone, the dip equator is migrating southward and this supports the observation of Rangarajan and Dekka [1991] while in the South American sector it is migrating northwards. As noted earlier, the main driving force of the EEJ comes from the Cowling conductivity that varies as $(1/B^2)$. To check it's longitude variation, in figure 2.1b a plot is made of $(1/B^2)$ at the dip equator, calculated from the main field models at different epochs, as a function of longitude. Clearly this has a high in the South American sector with a maximum around 290^0E and a low around the Indian zone as also observed in the EEJ variations on ground [Rastogi, 1962]. Further, the secular variation in this term is practically negligible up to around 180^0 and a maximum in this secular variation is from 210^0 to 300^0E with the magnitude of $1/B^2$ increasing continuously. It is also observed that the largest secular variation in the Cowling conductivity occurs in the South American sector with a possible 4.0% increase per decade for the same level of ionisation in the E-region. It is significant to note that the Oersted main field model [Olsen et al, 2000], does not suggest any major changes or reversals of the secular trends in the electrojet. There is some indication of the slowing down of the secular changes in the location of the dip equator and the Cowling conductivity as one approaches the European zone from the Atlantic.

We next examine how far the horizontal geomagnetic field direction deviates from the ' ideal' direction that is perpendicular to the dip equator in different longitude zones. From figure 2.1a, we get the location of the dip equator in different longitudes. It is a straightforward problem to identify the vector along

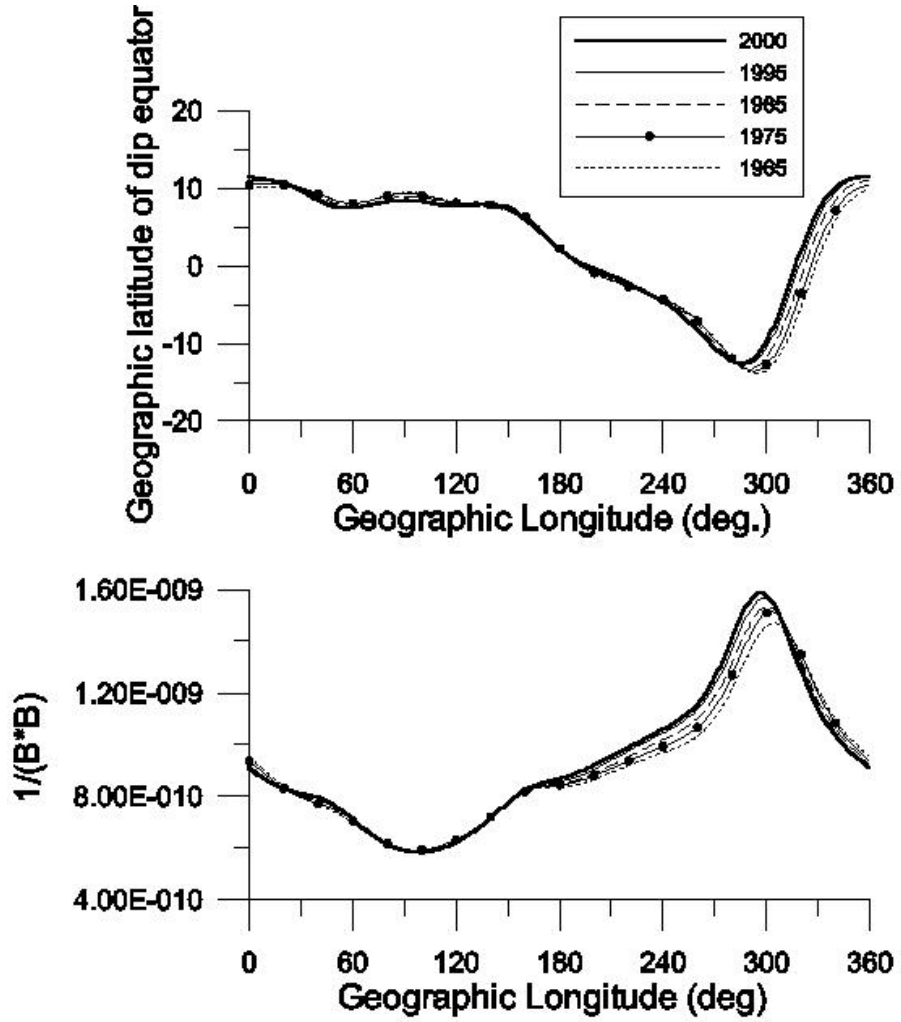

Figure 2.1 : Longitudinal variations of parameters derived from the four different IGRF models from 1965 to 1995 and OIFM 2000
a) Geographic latitude (deg.) of the location of the dip equator (above)
b) (1/B²) in nT⁻² at the dip equator (bottom).

the line of zero dip at each longitude. One can also determine, at the dip equator, the direction of the magnetic field (which is horizontal by the definition of the dip equator). We can then compute, α, the angle between the two directions. We define the ' ideal' direction as 0^0 and define the deviation of the magnetic field

direction as 90-α. This deviation is plotted in Figure 2.2 for two epochs namely 1965 and 2000. Note that in the zone east of 300^0 E longitude, the deviation is around 12^0, which would mean that if the electrojet flows along the dip equator its contribution to the eastward declination component could be almost 20% of the H variations. This is significantly larger than the D components associated with the phenomenon. Exact estimates would require augmentation of the model for this sector.

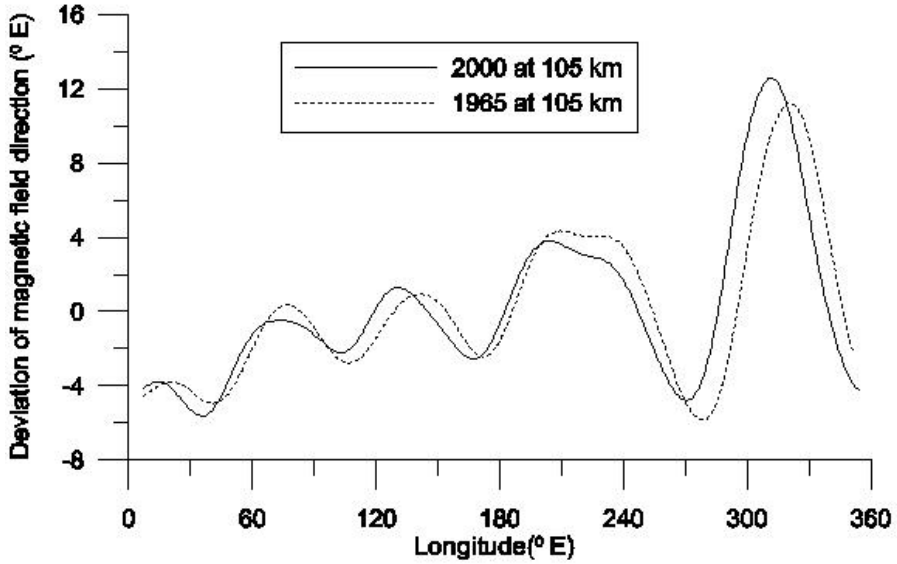

Figure 2.2 : Deviation of the direction (° E) of the M.F. at the dip equator, from the normal to the line of zero dip for the epochs 1965 and 2000. (Electrojet models assume that the M.F. is normal to the line of zero dip everywhere.)

We also note that the deviations can be east or west of the ' ideal'direction depending on the longitude under consideration. There is also a westward drift of the pattern as a whole from 1965 to 2000 AD. This can bring about significant secular longitudinal drift in the ' anomaly' . A closely spaced network of electrojet stations would be of considerable use. Since a major part of the zone lies outside land, vector observations of Oersted satellite will also be invaluable in any such investigation.

2.4 Data Analysis:

A typical EEJ signature at satellite height is a minimum at the dip equator accompanied by ' shoulders' of increased field on either sides [Cain & Sweeney, 1973; Onwumechili, 1985]. Such a signature is also consistent with empirical models of the equatorial electrojet [Onwumechilli, 1997] and is therefore used for identifying the EEJ in the Oersted data.

In the present analysis only data collected during magnetically quiet days (Ap ≤ 4) are used. Only satellite total field data between dip latitude 20^0N and 20^0S is considered. Retrieval of the EEJ signature from the satellite data requires the removal of the variations due to the main field. This is achieved using the OIFM [Olsen et al, 2000] which gives main field contribution up to degree and order 19 for internal, and 2 for external, source fields; it also includes 3 coefficients that account for the Dst dependent part of the external dipole. The secular variation coefficients are also as used by Olsen et al [2000] (provided to us by personal communication). Since the OIFM takes care of ring current contribution through the use of Dst index, the residual magnetic field contains only ionospheric contributions from the Sq and equatorial electrojet current systems. The latter is confined to the equatorial region only. Three distinct situations are encountered:

(1) In many of the cases considered, the residual field showed the typical EEJ signature.

(2) In some cases only one of the shoulders and a minimum around the dip equator appear. In these cases the latitude of the shoulder was identified as the edge of the EEJ. Field values obtained for latitudes on either side of the dip equator with magnitudes greater than the latitude of this shoulder maximum were then used to obtain a quadratic fit that was removed from the latitudinal profile of the field.

(3) In some cases only a minimum was obtained around the dip equator. In this case field values for 20^0N to 15^0 N and 15^0S to 20^0S were used for a quadratic fit that was subtracted out from the latitudinal profile.

These residual plots were generated for the five IQ (International Quiet) days of the months April to December, 1999 during which the satellite passes covered day-side local times ranging from afternoon to forenoon. For each day the satellite covers on an average 15 longitude sectors in the day-side sector. In this chapter, four such IQ days including 57 satellite orbital passes, covering different local times (LT) and satellite radial distance from the Earth (at the equatorial crossing), are presented. Figure 2.3 is a plot of the variation of electrojet as a function of dip latitude between -20^0 and $+20^0$, spanning the entire globe for different longitude sectors (marked in brackets). The four representative quiet days include: a) 11 May 1999 (LT≈13.3 hours; altitude ≈ 660 km); b) 4 July, 1999 (LT≈12.45 hrs; altitude ≈ 870 km); c) 14 August, 1999 (LT≈11.8 hrs; altitude ≈ 730 km); d) 25 September, 1999 (LT≈11.2 hrs; altitude ≈710 km).

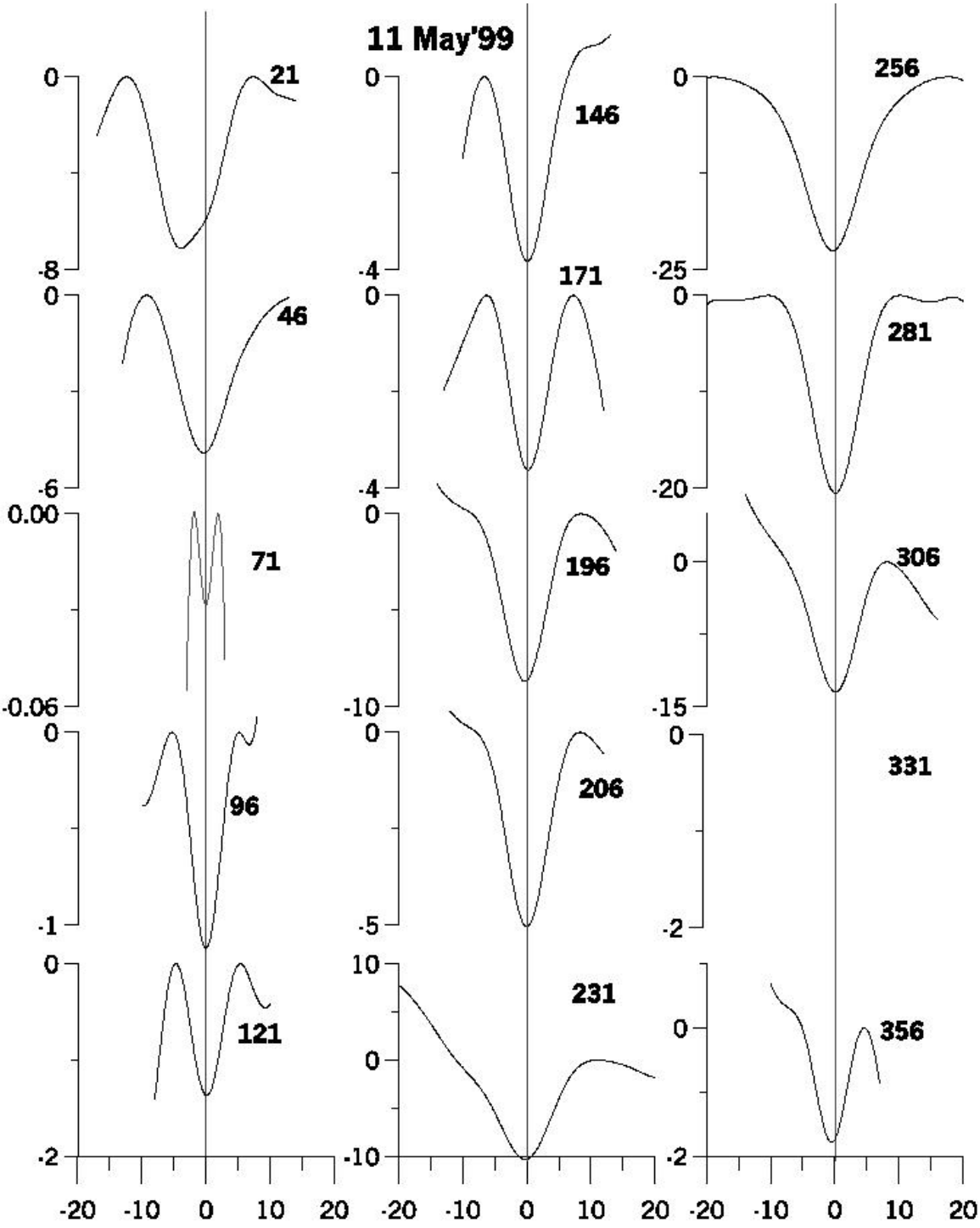

Figure 2.3 : Plot of the equatorial Electrojet strength (in nT) as a function of dip latitude over different longitude zones (shown in brackets) for Oersted day-side passes on following IQ days: a) 11 May 1999 *continued...*

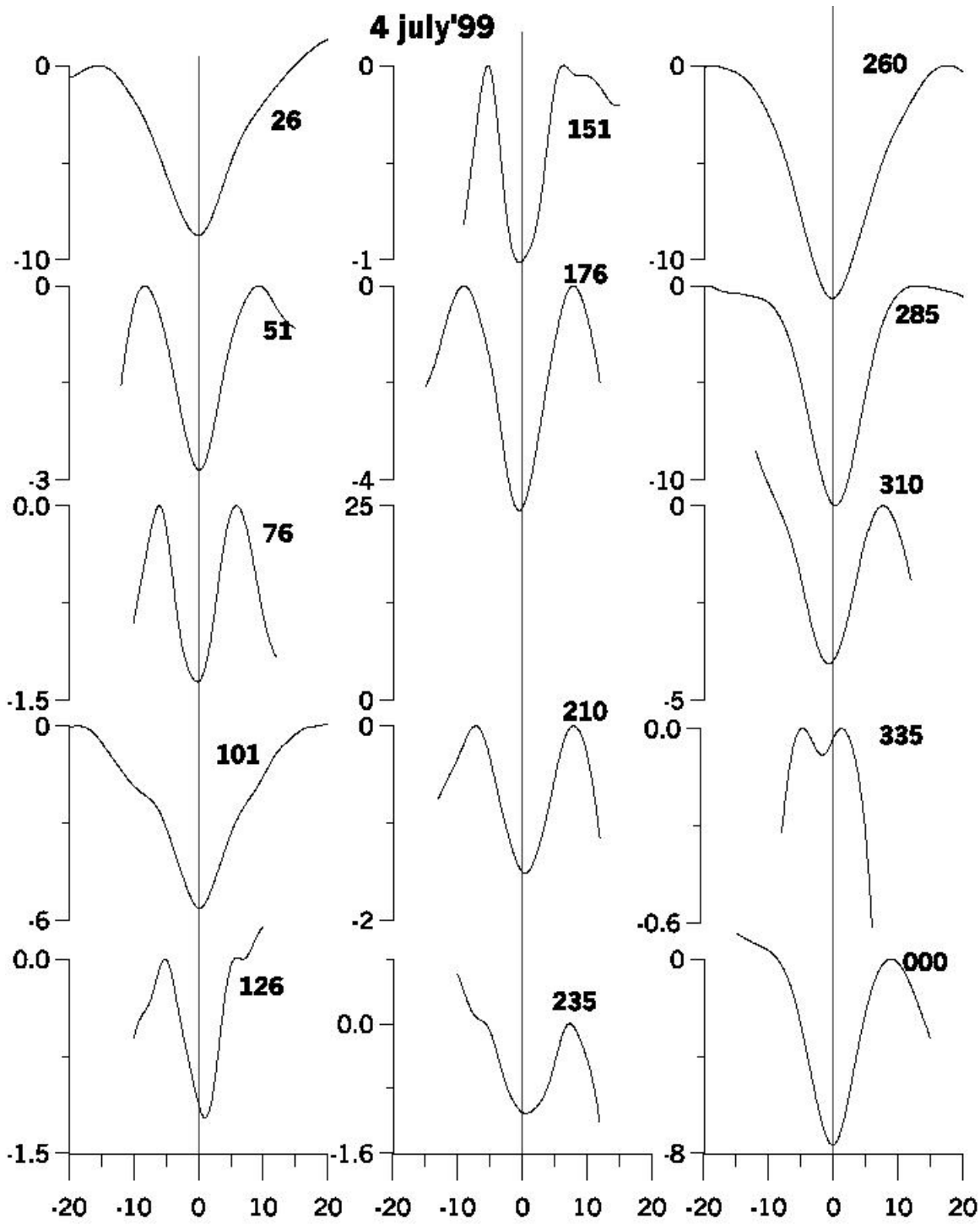

Figure 2.3b : 4 July, 1999 *continued* .....

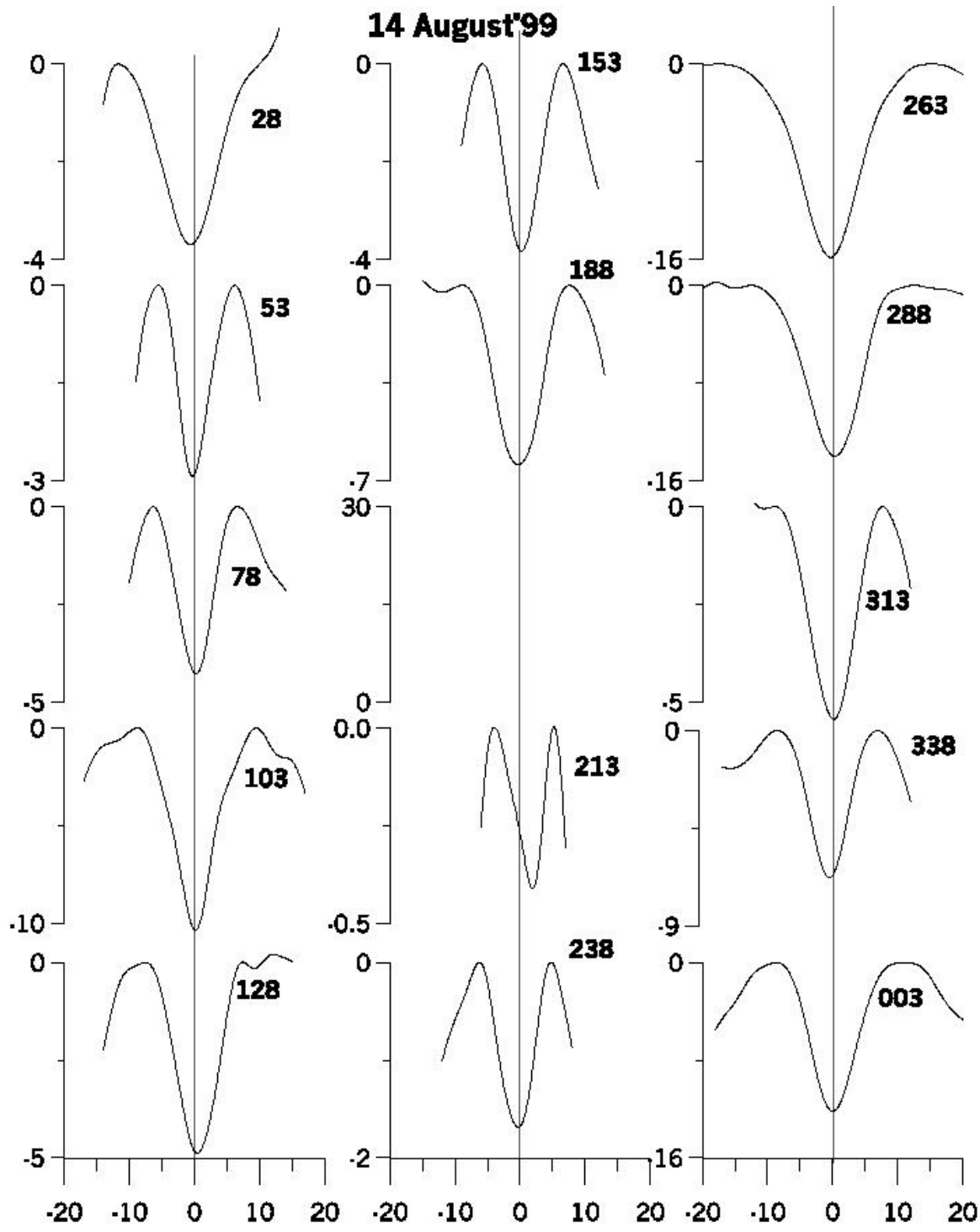

Figure 2.3c : 14 August, 1999 *continued....*

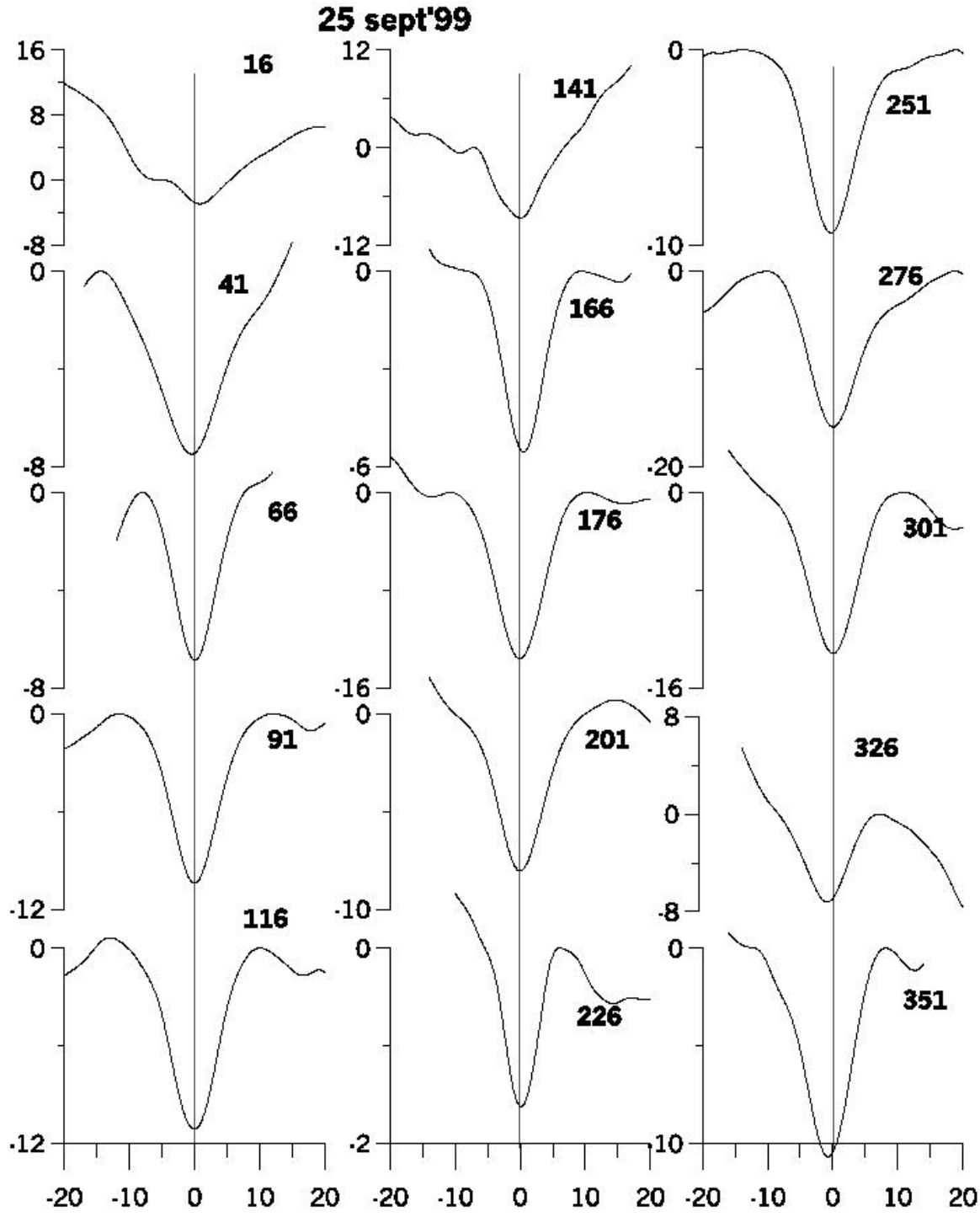

Figure 2.3d : 25 September, 1999.

EEJ can be clearly identified on almost all the passes; in contrast to the ground observation where one sees a peak, at satellite height it appears as a minimum at the dip equator accompanied by two maxima (hump) on either side. In some

cases, one of the humps is not distinct, instead, a distinct change in the slope of the latitudinal variation is observed. In all the plots, the minimum corresponding to the centre of the electrojet is seen to lie on the dip equator, quite consistently. It may be pointed out that the distance of the centre of the EEJ with respect to the dip equator, depends upon the main field model used; we find that by using OIFM, the centre of the EEJ generally falls very close to the dip equator. The electrojet peak seen in the Oersted data are sharp and latitudinal shift of 1^0 to 2^0 are discernible. To verify this, we also simulated the expected shift in the electrojet peak as seen at the satellite altitude for a 1^0 to 2^0 shift in the center of electrojet current system at 106 km and found that the shift was clearly discernible.

2.5 Results and Discussion:

There is a clear indication of zonal variation in the electrojet strength; largest amplitude is found in the American sector. It is because of this large variation in amplitude that we are forced to use different scales for the plots in the different longitude sectors. And as a consequence it is difficult to directly visualize the longitudinal variations from the figure. We therefore calculate S, the strength of the EEJ in nT, as observed at the satellite height for each day and longitude sector. Here, S is taken as the deviation of the value of the field at the dip equator from that at the hump or change in slope. It may be added here that the actual EEJ current strength can only be calculated based on a model specifically chosen for the EEJ. Figure 2.4 is a plot of the variations in the EEJ strengths, S, as a function of longitude on the different days. It may also be noted that the Oersted provides a unique data set in which on a given day, the satellite height at the equatorial crossing does not vary significantly. The electrojet signatures at different longitudes can be directly compared without resorting to specific models. This was not possible using the POGO data.

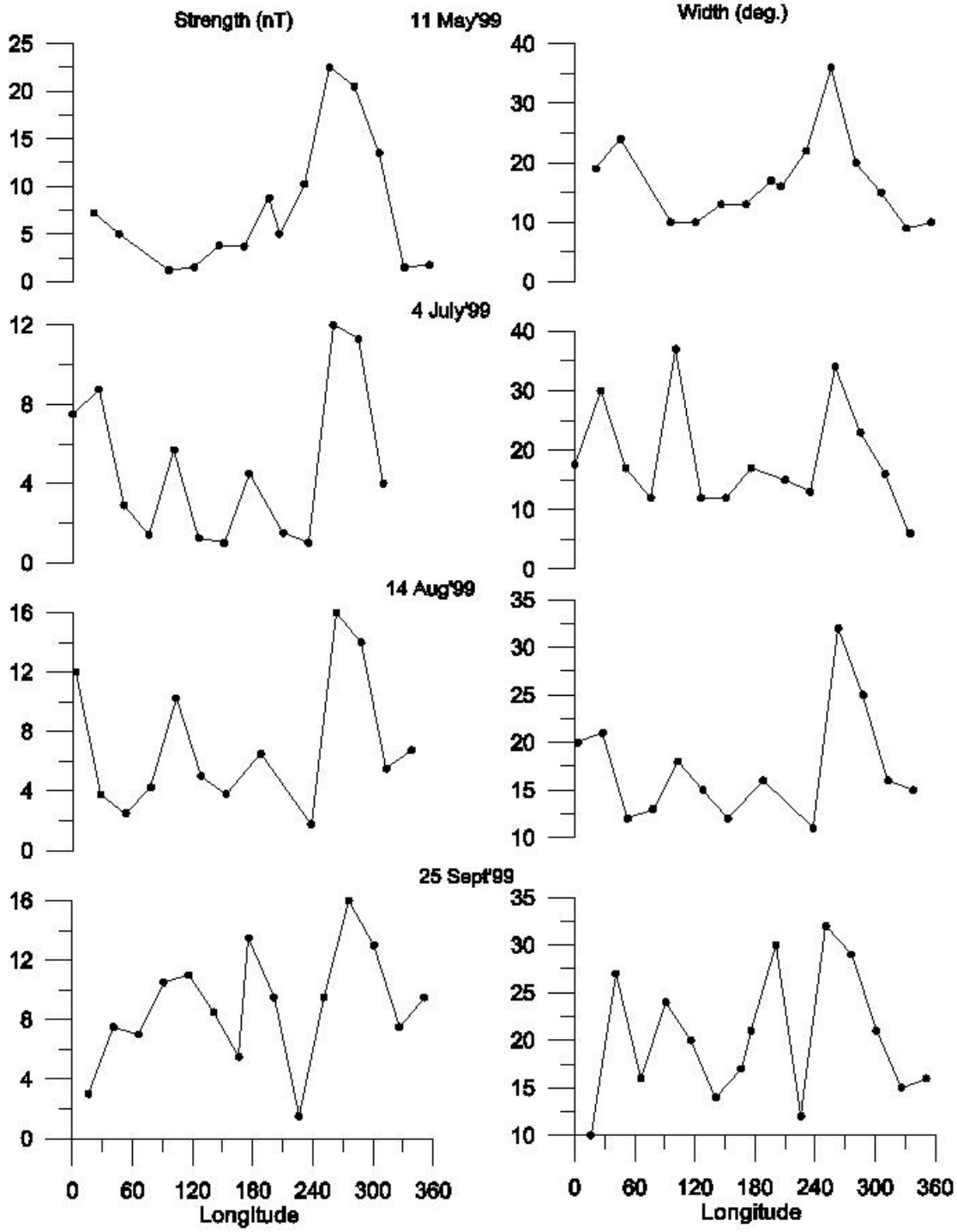

Figure 2.4 : A plot of the variations in the EEJ strengths, S in nT, at satellite height (left) and W in 0 , width of the EEJ, at satellite height (right), both as a function of longitude on the different days

We find that the EEJ strength, S, at the satellite height, on all the four days plotted, shows a stable maximum distinctly higher than the rest, in the longitude zone around 290^0E, in the South American sector. There exist other subsidiary maximum typically around 190^0E and 100^0E. The amplitudes associated with these show considerable day-to-day variability on all the four days presented, with the peak at 100^0E appearing as a crest on 11^{th} of May and as a very well defined maximum on the 25^{th} of September. The position of these peaks are consistent with Onwumechilli's [1985] observation of the peak eastward intensity $J_{0,}$ and total eastward current having maxima around 100^0E and 280^0E longitude with subsidiary maximum at around 190^0E. We also observe a peak around the Greenwich meridian on all the days. The high degree of day-to-day variability in the peaks other than the principal peak at 290^0E, suggests that these maybe due to the external tidal parameters which are likely to be more variable. Onwumechilli [1985] has suggested that a possible explanation may come from regional prevailing winds and possible gradients at electrojet altitudes. A standard migratory tide usually adopted in EEJ modeling, however, cannot produce such longitudinal differences. We are led to the conclusion that variable background winds or non-migrating tides may be likely candidates. It may be pointed out that non-migratory tides have been observed in the mesosphere and lower thermosphere and are currently topic of extensive investigations [Hagan et al, 1997].

In the same figure 2.4 is also plotted the width, W in degrees, of the EEJ at satellite height, as a function of longitude for various days. Here the width, W, is defined as the distance in degrees between the two humps (on figure 2.3) and does not represent the actual width of the current system in the ionosphere but may be related to it. We find that the width also shows a maximum in the South American sector, around 290^0E longitude. There is also a subsidiary peak around 190^0E; the other peaks vary from day-to-day in location and amplitude and may not have any real significance.

2.6 Conclusions:

Using the Oersted initial field model along with the earlier IGRF models, the possible long-term secular changes that could have occurred in the global patterns of the position and strength of the EEJ have been examined. The most significant feature that appears through the analysis is the northward drift of the location of the dip equator (hence the position of the axis of the EEJ) to the extent of 1.0^0 per decade around 300^0E. In contrast, in the Pacific, east of Australia, there is practically no drift. It is also observed that the largest secular variation in the Cowling conductivity occurs in the South American sector with a possible 4% increase per decade for the same level of ionisation in the E-region. A very significant result is that the magnetic field at the dip equator need not be perpendicular to the dip equator itself and this deviation from the idealized scenario of the equatorial electrojet can result in significant contribution of the equatorial electrojet to the declination component. An augmentation of the existing models and a more detailed study of ground and satellite data in 300^0E sector is called for to examine the consequences of this apparent anomaly.

The EEJ has also been studied using the scalar data of the individual passes of the Oersted satellite. Global data from four International quiet days in the day-lit side that included data from satellite orbital passes covering the different longitude sectors has been used to show that the EEJ peak coincides with the dip equator. The strength of the EEJ, at satellite height, shows a very stable maximum in the South American sector on all days emphasizing the importance of control of the geomagnetic field. Secondary peaks are also seen around 0^0, 100^0 and 190^0E. These peaks exhibit day-to-day variability and could be related to variable migratory tides. The longitudinal differences in the EEJ will have implications on the modeling of global subsurface conductivity probing in induction studies.

Only the results of a preliminary analysis of the Oersted data has been presented here to bring out the immense possibilities of utilizing the Oersted data for a comprehensive study of the equatorial electrojet. A more comprehensive study using a larger database along with a model to bring out the electrojet parameters is presented in next chapter.

Chapter 3

A Detailed study of EEJ using Oersted satellite

3.1 Introduction:

Extensive studies of the equatorial electrojet phenomenon have been carried out for many years using ground observations [Rasogi, 1989]. Study of EEJ using satellite is also not new to the scientific community [Cain and Sweeny, 1973]. Satellite based studies have a distinct advantage in that they can cover inaccessible regions occupied by oceans, mountains or forest areas. POGO satellite series (OGO-2, OGO-4 & OGO-6) had measurements of EEJ as a part of their objectives. Cain and Sweeney [1973] have studied scalar magnetic field from the POGO satellite, which covered an altitude range of 400 to 800 km. Following this a number of investigations have been carried out using the POGO data in more detail [cf. Onwumechilli, 1997 and references there in] and general features of the magnetic field of EEJ have been discussed. These investigations showed that the longitudinal variation of EEJ strength could not be entirely accounted for by the longitudinal changes in the Hall conductivity associated with the variations in the strength of the ambient magnetic field. There have also been important studies using the Magsat vector magnetic data [Maeda et. al, 1982; Ravat & Hinze, 1993; Langel et. al., 1993]. Despite the fact that the Magsat orbits were restricted to the dawn and dusk sectors where the EEJ is very weak, these studies brought out many important features of the equatorial electrojet. The most important of these being the clear identification of the meridiaonal currents associated with the EEJ and establishing the dawn/dusk and seasonal asymmetries associated with it.

In the present chapter, we have reported the results obtained from a statistical study of the scalar magnetic field data from Oersted satellite. The Oersted collects magnetic field data at relatively low altitudes and has global coverage

during day lit hours when the electrojet is strong. The Equatorial Electrojet with its axis always located close to the dip equator can be clearly identified on almost all the passes which is seen in the previous chapter [Jadhav et al., 2001]. The altitude of the satellite for the passes during the day varies very little and it becomes possible to get the electrojet strength at different longitude zones on the same day. The Oersted satellite thus constitutes a very valuable set of data for studies of the EEJ. In our earlier study [Jadhav et. al., 2001], we had looked into the extent of geomagnetic main field control over the EEJ. In this chapter, we extend our earlier, essentially preliminary study, to make a more quantitative estimate of the EEJ parameters and its day to day variability as seen in the satellite data.

In section 3.2, the preliminary treatment required for isolating the EEJ signature is laid out. In next section, we have discussed empirical model used for the analysis of EEJ, method of analysis and different EEJ parameters that are obtained in present study. In section 3.4, the validation of the identified parameters through comparison with ground magnetic observations is discussed. In section 3.5, longitudinal variations of the EEJ parameters derived from the satellite data are discussed in detail. Section 3.6 examines the longitudinal variation of the surface geomagnetic field variations derived for the satellite parameters, while in section 3.7 we examine, in depth, the problem of the variability of the EEJ from day to day. Discussion and conclusions have been accommodated in section 3.8.

3.2 Preliminary Treatment of the Oersted Data:

3.2.1 Selection of data:

Oersted satellite has polar elliptical orbit with altitude range of 500-850 km. The orbital period is approximately 100 minutes; hence it can have around 15 orbits per day which leads to approximately 15 daytime passes and 15 nighttime

passes. The longitude and local time increment is -25^0 per orbit and -0.88 min per day respectively. Hence for a given date, all the daytime passes have almost the same local time. In this chapter, we have analyzed 12 months of scalar magnetic field data from April'1999 to March'2000 with LT varying from 13.6 hrs to 9.5 hrs. Table 3.1 gives the typical local times of the passes from month to month.

Table 3.1: Local times of the passes in different months.

MONTH	LT(hr)
1999	
April	13.6
May	13.
June	12.7
July	12.5
August	12
September	11.5
October	11
November	10.5
December	10.
2000	
January	9.5
February	9
March	8.5

The satellite data can, in principle, be used to study the equatorial electrojet in physically in-accessible regions. But the satellite-based analysis does have its own problems. The signature of the EEJ becomes progressively weaker as the height of the satellite orbit increases. At the typical orbit of Oersted, signatures of the EEJ are of the order of only a few nT. On the other hand, fluctuations of magnetospheric origin, like geomagnetic pulsations associated with storm time disturbances, are as large at these heights as they are on ground and therefore have amplitudes comparable to the EEJ signatures one is looking for. The analysis has therefore to be restricted to geomagnetic quiet days. Only the data from the 5 IQ (International Quiet) days of each month is used in the analysis. Even this may not grant immunity against intrusions of magnetic disturbance

effects considering the fact that we are close to the Solar Maximum and it is not always easy to find days entirely free of geomagnetic disturbances.

3.2.2 Identification of EEJ signature:

The main field of the internal origin dominates the data recorded by the Oersted. This has to be removed before any useful identification of the equatorial electrojet is feasible. The removal of the main field is achieved by subtracting out field derived from a reliable main field model. Here, we have used IGRF 2000, supplied by Oersted team [Olson et al., 2000], which uses 195 internal field coefficients (i.e. order is 13), one Dst-dependent internal and three Dst-dependent external coefficients for the removal of contribution due to ring current system. The basic input for the computation of the field is the satellite location and the Hourly Dst values that are readily available at the World Data Centers.

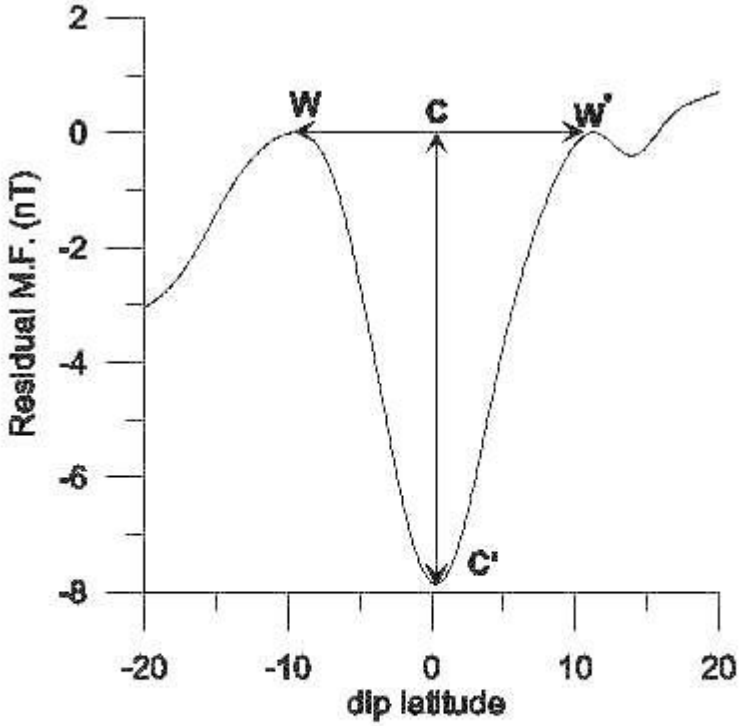

Fig. 3.1 : Typical signature of EEJ at satellite height for 135^0 E longitude pass on August 2, 1999.

After subtracting main magnetic field from the satellite data, we get the residual magnetic field ΔF, produced by external current sources like the electrojet, Sq and magnetospheric currents. This residual field, ΔF, is further smoothened out to remove spatial features with wavelengths less than 4^0 or so by subjecting it to low pass filtering before it is used to identify the EEJ. A typical EEJ signature in the satellite profile has been clearly described by Cain and Sweeney [1973]. The expected signature is shown in Figure 3.1. The signature is characterized by a minimum at the latitude of the EEJ axis accompanied by ' shoulders' of increased field on either side. Vertical distance between dip and shoulders (CC') in Figure 3.1, is a measure of the strength of EEJ (S) at the satellite location and the horizontal distance between two shoulders (WW') gives the width of EEJ at satellite height. This typical signature was successfully used for identifying the EEJ in the Pogo and Magsat satellite studies. We therefore, adapted it in the present analysis of the Oersted satellite data.

3.2.2.1 Algorithm:

A Fortran program was developed to automatically identify EEJ signatures from the selected satellite orbital data restricted to $\pm 20^0$ from the latitude of the dip equator and to process and store the transformed data useful for evaluation of the EEJ parameters. For 10 out of the 839 passes initially selected, available data did not cover this entire interval and these were therefore dropped from the analysis. Only passes, which showed a well-defined minimum within $\pm 5^0$ of the dip equator, were considered. 49 of the passes did not satisfy this condition. All the remaining passes had a well-defined minimum and at least one maximum (or shoulder). The Fortran program was designed to carry out the following operations:

1. If the pass had a well-defined minimum and two maxima, one on either side of the minimum, a linear trend was subtracted out to bring the two

maximum values to the same level. The justification for this is that the satellite height does not change enough within the $\pm 20^0$ of the dip equator to justify an asymmetry in the real electrojet signature. The values of resultant ΔF profile are stored for further analysis.

2. There are cases in which we get a maximum on one side of the minimum but on the other side instead of a peak we only get a sharp change in the gradient in the orbital profile. In this case, we first remove a linear trend from ΔF that brings the two edges of the EEJ viz. the peak on one side and the point where the change of gradient occurs, to the same level. In some of the cases a typical EEJ signal indicated in step 1 is obtained by the removal of this trend. The resultant profile is then saved for further analysis.
3. If that does not happen, it probably implies that the background due to the magnetospheric or Sq current systems is not fully removed. A cubic fit to our low latitude data segment outside the EEJ belt (defined by the two edges of the EEJ marked out in step 2) is removed. Step 2 is repeated. The iterations defined by steps 2 and 3 is repeated a maximum of 5 times.
4. There are cases when only one peak and a minimum are discernable. In this case an imaginary point symmetrically located with respect to the minimum is chosen as the possible position of the second peak on the other side of the minimum and step 3 is repeated. A maximum of 5 iterations is carried out.
5. In case of minimum without peak, the edges are considered to be at $\pm 12^0$ and steps 3 and 4 are repeated for maximum of 5 times.

784 equatorial passes were run through the above set of operations. Typical EEJ signatures were recovered from 513 of these passes while 267 continued to have a dip, one peak and a second peak that could only be inferred from a change of gradient. It should be mentioned in passing here that 45 of the satellite ΔF

profiles had distinct reversed EEJ or Counter-electrojet (CEJ) signature. Some of the CEJ events were simultaneously seen in the ground data as well, but the study related to CEJ will form a part of next chapter.

The entire ΔF profile between two edges of the EEJ and additional 40 points on either sides of the dip, consisting of around 300 to 350 data points, is used for obtaining the EEJ parameters corresponding to each of the passes. The 513 ideal EEJ signature passes as well as the 267 passes for which the signature was clear in one hemisphere and suggestive (but not so explicit) in the other hemisphere are used for the statistical study of estimates of the EEJ parameters.

3.3. EEJ parameters:

3.3.1 Empirical Model:

We shall take the point of view that the typical signature at satellite altitude above electrojet current system shown in figure 3.1 is associated with an eastward current flowing near dip equator and westward current on both flanks of the EEJ. We use the model for EEJ due to Onwumechili [1966a, b], which can reproduce the dip as well as the shoulders seen in the satellite. The X and Z components of the magnetic field from the continuous distribution of current density model

$$J = J_0 \frac{(a^2 + \alpha.x^2)}{(a^2 + x^2)^2} \frac{b^2}{(b^2 + z^2)^2}$$

is given by [Onwumechili and Ezema , 1992]

$$(sg \cdot z)P^4 X = \frac{1}{2} Ka\left[(v + \alpha v + 2\alpha a)(u + b)^2 + (v + \alpha v + 2a)(v + a)^2\right] \qquad (1)$$

$$-(sg.x)P^4 Z = \frac{1}{2} Ka(u + b)\left[(1 + \alpha)(u + b)^2 + (v + \alpha v + 3a - \alpha a)(v + a)\right] \qquad (2)$$

Where,

$$P^2 = (u + b)^2 + (v + a)^2$$

$$K = 0.2\pi J_0$$

$$u = |x| \quad and \quad v = |z|$$

$$sg \cdot x = sign\ of\ x = \frac{x}{u} \quad and$$

$$sg \cdot z = sign\ of\ z = \frac{z}{v}$$

Here the center of the current system has been taken as the origin, x is the latitudinal distance measured northward from the origin, y is eastward, and z is vertically downward distance from the current layer. *a* and *b* are the representative latitudinal and vertical scale lengths, respectively, α is dimensionless constant controlling latitudinal distribution of current, J_0 is the peak current intensity or the height-integrated current density at the center of the current system. If X and Z are in nT, J_0 is in Amperes/km.

3.3.2 New objective Technique for the Estimation of EEJ parameters:

The identification of the EEJ parameters is based on the above empirical model. Many of the earlier studies [e.g. Onwumechili and Agu, 1981b] had used the same model but they based their estimation of the EEJ parameters on the strength of EEJ, S, at axis and did not make use of the full EEJ signature. In order to derive the parameters K, *a* and α they assume that given the longitude and local time, these parameters do not vary from day to day. Using different sets of (S, *h*), where S is the EEJ strength at EEJ axis at altitude *h* of the satellite, they solved the above equations to get K, *a* and α. But we find that the shape of the signature (i.e. width and strength) changes from day to day even at a given longitude and local time.

Hence we have approached the problem in different way and computed the basic parameters K, *a* and α for each pass using the 300 to 350 data points defining the structure identified and stored by the process described in section 2. A Fortran program has been developed for the purpose. The height of the

electrojet is chosen as 106 km throughout. Contribution from sub-surface induced currents are neglected and the scalar field ΔF ($=\sqrt{X^2 + Z^2}$) is computed from X and Z in equations 1 and 2. The scheme involves the following steps:

1. For each EEJ pass, the center of the current system is chosen as the latitude of the minimum and a range of values are chosen for the parameters *a* and α. ΔF is computed along the satellite trajectory in the interval bounded by the two 'shoulders' defining the ends of the EEJ signature for the given pass. Only parameter sets that produce the 'shoulders' at the right locations are retained.
2. The parameter K is determined through a least square fit to ΔF along the satellite profile for the retained values of the parameters *a* and α. An additional parameter that can account for a constant baseline shift is also evaluated in the least square procedure to incorporate a possible offset in the satellite EEJ profile due to large-scale background currents not fully accounted for by the method.
3. Thus using these parameters viz., a, alpha, K and shift, a complete profile at satellite altitude is computed. The cross-correlation between the observed and computed profiles as well as the mean square differences between them are evaluated. The parameter set with lowest mean square difference and a cross-correlation greater than 0.7 is selected by the program as the best fit for the parameters of the EEJ for the given pass.

The flowchart of the automated program is given in Appendix 1. The methodology used has a distinct advantage that it is fully automated and objective subject, of course, to the basic assumptions that have gone into the algorithm. But it has to be tested out with an independent data to establish its authenticity and statistical reliability. This is described in the next section where the comparison of H (the horizontal component of the magnetic field)

of the observatory magnetic field data with the H variation on ground computed from the overhead satellite passes is described.

3.4 Comparison between satellite and ground observations:

3.4.1 Ground Magnetic field data:

To demonstrate the reliability of the model parameters deduced from the satellite data, it is essential to compare the actual ground observations and calculated values based on the satellite observations. As mentioned in the last section, the assumed height of the EEJ is 106 km. There were some severe restrictions imposed on such comparisons because the surface geomagnetic field values around the dip equator were only available from the Indian and American sectors.

We have used observatory data from Trivendrum (Dip Latitude -0.7^0, Geographic longitude 76.9^0), Alibag (Dip Latitude 9.8^0, Geographic Longitude 72.9^0) in the Indian sector. In the American sector we used Huancayo (Dip Latitude -1.4^0, Geographic Longitude 284.7^0) and Fuquene (Dip Latitude 16.2^0, Geographic Longitude 286.3^0). The comparison with ground data was made from pass to pass. It should be pointed out here that the identification of the EEJ on ground requires at least two stations, one close to the dip equator (the electrojet station) and the other a low latitude station (non-electrojet station) just outside the influence of the EEJ [Bhargava and Yacob, 1973]. A latitudinal chain of observatories, if available, will, however, provide better estimates of the EEJ [Fambitkoye and Mayaud, 1976].

The satellite does not always pass over the location of the chosen ground geomagnetic observatory. Comparisons were possible only when the satellite passed within longitude range of $\pm 5^0$ of the longitude of the stations or when there were at least two passes in a day within longitude range of $\pm 30^0$ of the

longitude of the chosen stations. In the first case the field on ground was calculated using the parameters determined for the given pass. In the second case the field computed at the two longitudes corresponding to the satellite passes were interpolated to obtain the field in the longitude zone of the given chosen stations. In doing so it has been tacitly assumed that the EEJ field has the same local time (LT) pattern at neighboring longitudes and two values though around 90 minutes apart can still be used for interpolating in longitude to get EEJ field at the given longitude and LT. Equations 1 can be used to obtain the EEJ contribution to H at any latitude. In all 39 passes were available for comparison of satellite and ground data in the Indian sector while only 30 data points were available for comparison of satellite data and ground data in the American sector.

For estimating the EEJ field in the Indian sector, hourly values of the geomagnetic field made available from the Trivandrum and Alibag observatories were used. Nighttime means were subtracted from the daytime hourly values and these were interpolated to determine the H at the local time of the crossing of the Oersted satellite. The interpolated value for Alibag was subtracted from that at Trivandrum to obtain the instantaneous value of $EEJH_{obs}$ at the time of satellite crossing. Similar data reduction techniques were utilized for Fuquene but in case of Huancayo, the daily traces had to down loaded from WDC, Kyoto site and re-digitized.

3.4.2 Comparative study:

For getting the estimate of the strength of the EEJ on ground from the parameters determined from the satellite, two methods can be used. The first is to estimate the peak EEJ strength on ground from the satellite parameters and this can be achieved by computing the H at the axis of the equatorial electrojet as deduced from the satellite data. The second is to compute the H at the electrojet and non-

electrojet station using the parameters deduced from the satellite data and then simulate the EEJH_{obs} as estimated from the ground by subtracting the H at the non-electrojet station from that of the electrojet station. These calculations are possible as the H at any latitude can be calculated once the parameters of the EEJ as deduced from the satellite data are accepted.

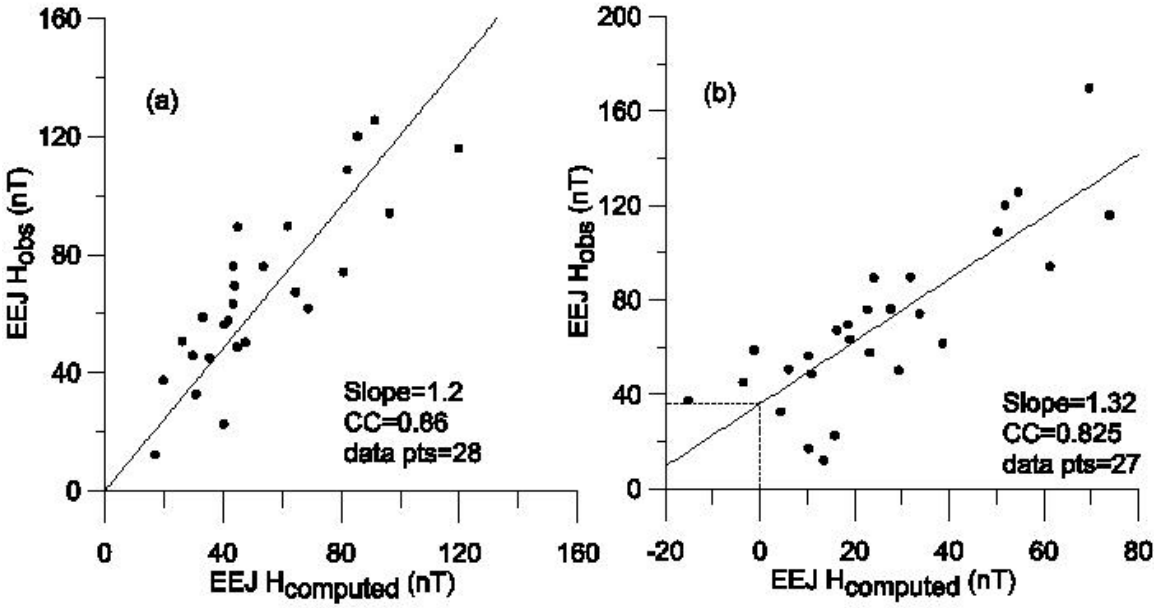

Figure 3.2 : Scatter plot of EEJ H_{obs} from American observatory data plotted against the EEJ $H_{computed}$ computed from satellite based EEJ parameters. In Figure 2a, EEJ $H_{computed}$ is computed at the axis of the EEJ while in Figure 2b EEJ $H_{computed}$ is estimated from the difference of the H computed at Huancayo and Fuquene.

Both the methods have been used here. Scatter plots are given in figures 3.2a and 3.2b for American sector and figures 3.3a and 3.3b for Indian sector. It is quite clear that the electrojet values determined from ground data correlate very well with the values computed from satellite observations. EEJ H_{obs} (electrojet H–nonelectrojet H) from ground observations and EEJ strengths on the ground at the EEJ axis, calculated from the satellite-based parameters, show a correlation of 0.86 in both the Indian and American sectors. This compares favorably with the results of Yacob [1977] who found correlation co-efficient of around 0.88 between

the surface EEJ H_{obs} in the Indian region, extrapolated to the satellite height using a parabolic current-band model of EEJ, and the EEJ strength as determined from satellite field. The correlations that we obtain are significant at 99.9% level for the given number of points. The corresponding scatter plots (see Figure 3.2a and 3.3a) also show that the scatter is symmetrically distributed about the mean regression line. It should be noted that the values computed at the electrojet axis are expected to be insensitive to the parameter α and to the position of the center of the electrojet. The excellent match confirms that the algorithm used has provided reliable estimates of *a* and K. We would like to emphasize that a better agreement cannot be expected considering the fact that there are differences in the longitude of the satellite pass and that of the ground stations and interpolation cannot be expected to exactly reproduce the actual variations at the station longitude.

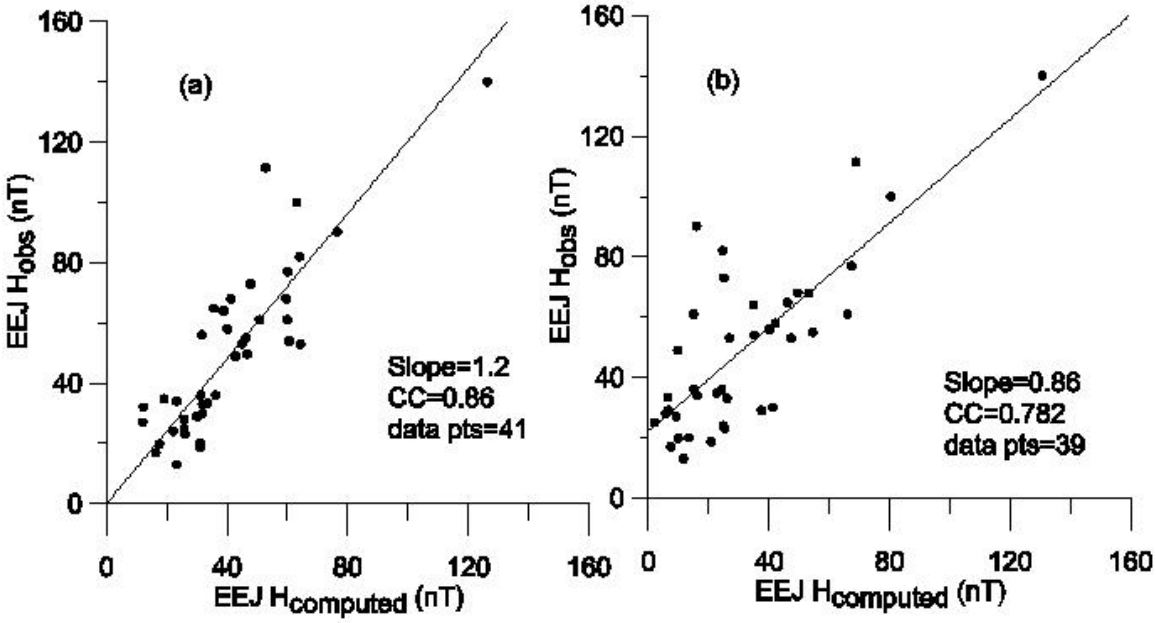

Figure 3.3 : Same as figure (3.2) but for Indian observatory data (Trivendrum- Allbag)

We next present the results obtained by computing from the satellite model parameters for each pass, the field at the ground station latitudes so that we actually simulate the procedure adopted for determining the EEJ H_{obs} from

ground measurements. Figure 3.2b & 3.3b show scatter plots between values so calculated at actual latitudes of the stations and the ground observations themselves. We do expect the correlations to be poorer than for the case of the EEJ axis since random errors in the estimated value of α and in position of the center of the EEJ are expected to increase the scatter. The correlations do decrease marginally but they are still significant at 99.9% level of confidence. We should also mention in passing that the H variations at the dip equator station (without subtracting field at Sq station) show very poor correlation with the EEJ $H_{computed}$ estimated from the satellite data. This is in conformity with the earlier findings that it is necessary to subtract out the background Sq for any meaningful comparison with the satellite estimates of the EEJ contribution, [cf. page 294 of Onwumechilli, 1997].

The scatter plots for both the Indian and American zones do show up an offset since the regression lines (especially in Figures 3.2b and 3.3b) do not pass through the origin. In American sector offset is around 40 nT, while in Indian region it is around 20 nT. This may be because of inadequate removal of the Sq variations, in the estimation of the $EEJH_{obs}$ from the ground observations. As expected this offset is greater in the American zone. The non-electrojet station should be ideally just outside the influence of the EEJ. At the latitude of Fuquene the Sq contribution will be much less than at the dip equator and the estimated $EEJH_{obs}$ for the Huancayo-Fuquene combination is likely to be more than its actual value. This is likely to be true to some extent for the Trivandrum-Alibag combination in the Indian zone but the degree to which $EEJH_{obs}$ is overestimated is likely to be much less.

Comparison of satellite and ground based data of the EEJ have been carried out earlier by Bhargava and Yacob [1973] in Indian region, Gouin [1973] in Central African region, Ebun Oni[1973] in the west African region and Osborne [1973] in

the Indian, Pacific and American regions using POGO data. They tried to compare POGO data at altitude 400 km with ground observations and get the relation X=kS, where X is the electrojet magnetic field recorded at the observatories on earth and S is the strength observed at 400 km by the satellite. The results obtained were not consistent with each other. They also argued that imperfect removal of the worldwide Sq is most likely to be the major cause of the scatter and not the crustal and upper mantle conductivity. The good correlation between EEJ at ionospheric heights and ground has been verified by Rastogi and Patil [1986] using the doppler shift of VHF echoes during quiet and disturbed days at Thumba.

Finally, we note that the excellent correlations between the ground and satellite estimation of the EEJ from two different longitude sectors fully authenticate the technique used for deducing the EEJ parameters from the satellite data. We do not claim a perfect estimation from pass to pass but it can be justifiably argued that the estimations should provide the base for the investigations of the statistical properties of the EEJ in different longitude regions around the globe.

3.5 Longitudinal Variation of the EEJ:

There are four main parameters of the EEJ whose longitudinal variations have been discussed in literature [cf. Onwumechilli, 1997]. These are the peak of the EEJ current given by J_o, the position of the electrojet axis x_0, the estimated width of the EEJ given by $W = \frac{2 \cdot a}{\sqrt{-\alpha}}$ and I_+, the total amount of positive eastward current flowing within the EEJ. If *a* is in km, I_+, the total positive current in amperes flowing between the two locations of zero intensity is given by

$$I_+ = aJ_o\left[(-\alpha)^{1/2} + (1+\alpha)\tan^{-1}\left(\frac{1}{-\alpha}\right)^{1/2}\right] \qquad (3)$$

In discussion, we also mention the width of EEJ at satellite and ground. The width of EEJ at satellite ($W_{satellite}$) is the direct observation of the distance between two peaks in the EEJ signature at satellite altitude and that on ground (W_{ground}) is the distance between two minima in the EEJ signature computed from the model parameters.

3.5.1 Interdependence of EEJ parameters :

It may be in place here, to look at the overall nature of the parameters derived form the satellite data. These are depicted in figure 3.4 a-e. Figure 3.4a shows how the parameter J_0, the peak current density is related to the H_{axis} computed for latitude of the electrojet axis on ground. A clear positive correlation and straight line fit is seen but there is a scatter which may be mainly attributed to variability in *a*. The scatter is not an indication of errors but only emphasizes the fact that the surface field is not entirely determined by the peak current density. This is more evident in Figure 3.4b where we have used I_+ instead of J_o. The reduction in scatter is obvious and shows that the total eastward current and not the peak current that is more relevant as far as ground magnetic effects are concerned.

Figure 3.4c shows how EEJ widths, on ground *Wground*, and that at the position of current system *W*, are related to each other. The plot shows linear dependence with slope just over unity (≈1.2). There is also a scatter which underlines the fact that two independent parameters *a* and α together determine *W* and therefore the relationship between the widths of EEJ at ground and 106 km is not simple and straight forward. The relationship between $W_{satellite}$ and W_{ground} is also examined, which is found to be linear but the width at the satellite height is about three times the width on ground.

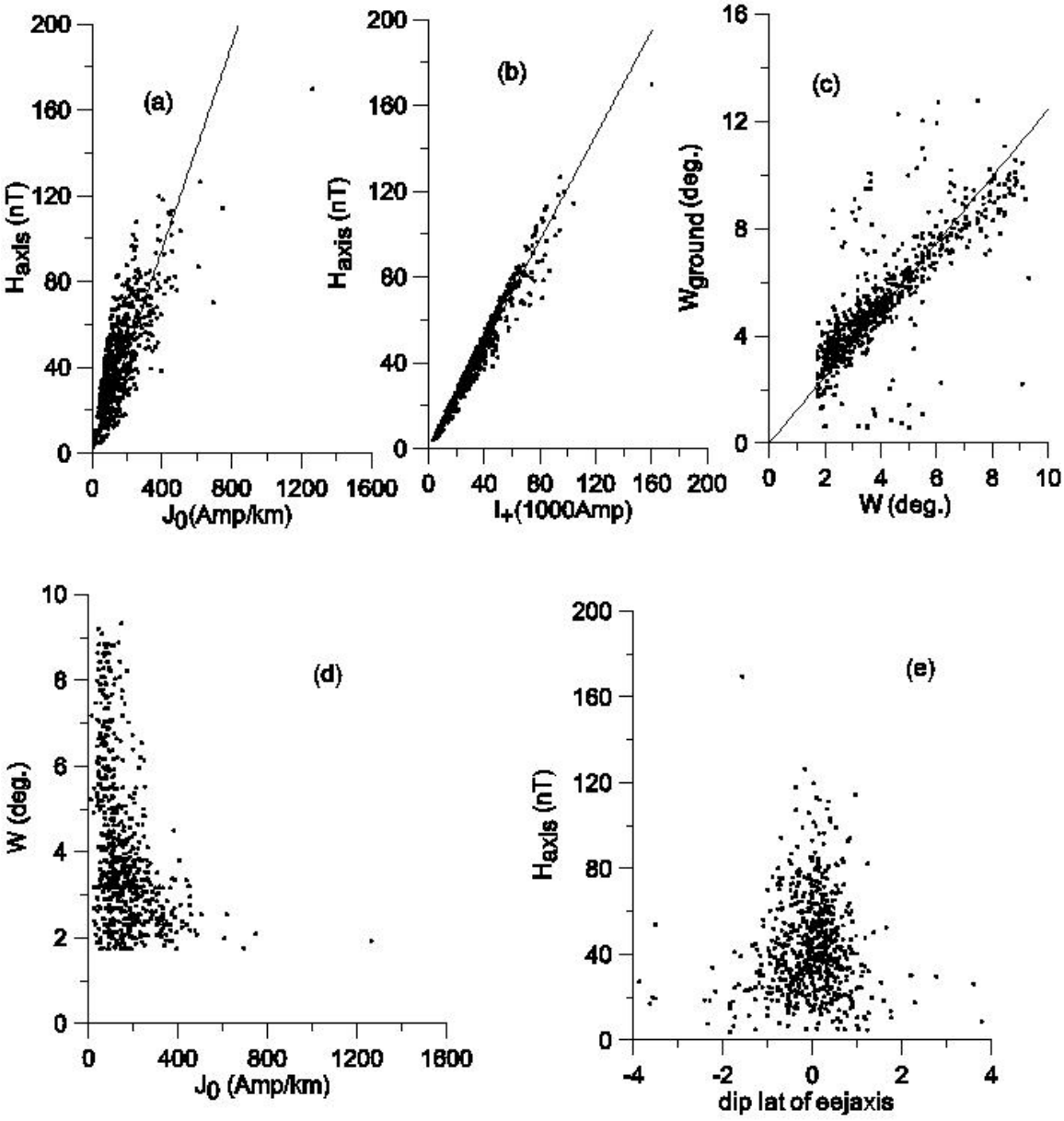

Figure 3.4 : Scatter plot for EEJ parameters determined from satellite data. See the text for definition of parameters.

Relationship between the peak current density and the width of the EEJ (W) at 106 km is plotted in figure 3.4d. This figure suggests larger the value of the peak current density, the smaller the scatter shown by the width of the electrojet on ground. For lower values of J_0, the width can range from 2^0 to 9^0, but for larger values of J_0, the width hovers around 2^0. This scatter may probably imply that when J_0 is small the signature of the EEJ at the satellite heights are smaller and

hence there is a greater chance of errors creeping in derivation of the structural parameters a and α which ultimately determine the width of the electrojet. The spread is, however, more towards larger widths and thus a significant part of the scatter may be genuine and could arise due to the fact that smaller peak currents may require larger width to reproduce a given signature at the satellite height. The standard deviations of the spread of the width scatter are reasonable and the parameter can thus supply reliable statistical data on the EEJ.

Finally Figure 3.4e shows how the position of EEJ axis with respect to the dip equator controls the EEJ H generated at the electrojet axis on ground. The diagram clearly demonstrates the fact that strength of EEJ is considerably reduced when its axis shifts away from the dip equator. The results can be expected on physical grounds. Furthermore, very large departures of the electrojet axis do not appear to be frequent and possibly constitute the population of out layers.

Finally Figures 3.4a-e, suggest that the parameters determined from the Oersted passes are suitable for a study of the statistical properties of the EEJ though it may not be the right choice for detailed analysis of individual case studies. In what follows, we concentrate on the statistically averaged values of the derived EEJ parameters and examine their dependence on the longitude, season and local time. In the process we shall determine whether these are consistent with the earlier studies based on POGO and Magsat.

3.5.2 Longitudinal variation of I_+, J_0, and width of EEJ:

Figure 3.5 shows longitudinal variation of average of total eastward current (I_+), peak eastward current intensity (J_0) and EEJ width on ground. Each point is the moving average of all the passes in a 30^0 bin centered at that longitude and the points are separated by 5^0. In this plot as well in all the plots that follow, the error bar corresponds to the estimated standard error of the mean. Total eastward

current (I_+) shows four peaks viz. at 0^0,120^0,200^0 and 270^0 E longitudes, while J_0 shows peak at 120^0 E and secondary peaks at 200^0 & 0^0 E longitude.

The total eastward current I_+ determined for the POGO satellite data by Onwumechili and Agu [1981a] showed well-defined peaks at 100^0 E, 190^0E and

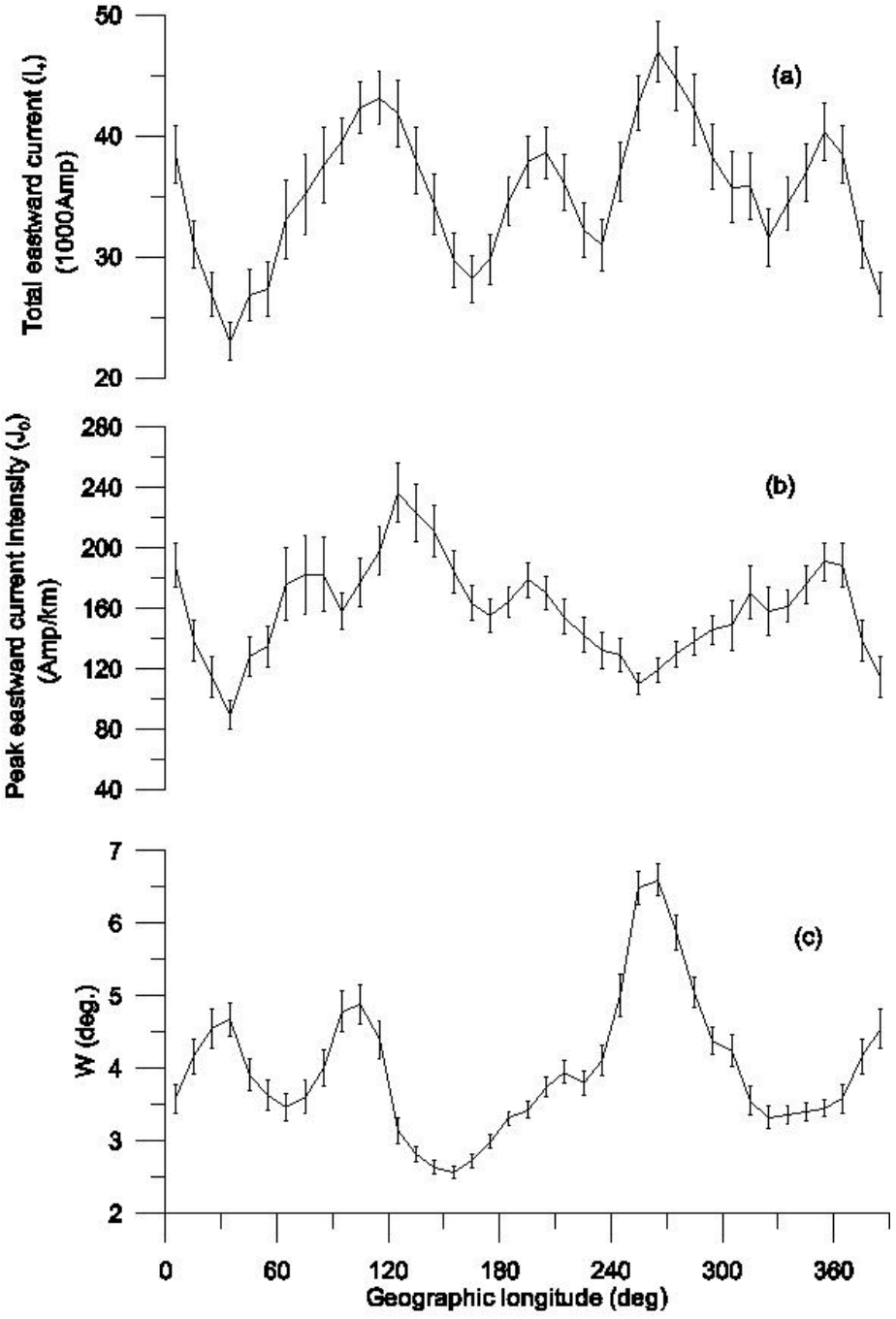

Figure 3.5 : Longitudinal structure of (a) I_+, (b)J_0 and (c) the electrojet width W plotted as a function of longitude. Error bars are estimated variance of the mean.

270^0E longitudes and a suggestion of a smaller peak around 360^0E longitude. This daytime average pattern for the September equinox is in broad agreement with the average pattern of the longitudinal profile of I_+ obtained by us.

Onwumechili and Agu [1981a] get three well-defined peaks for J_0 centered at 100^0, 190^0 and 270^0 E and a smaller peak around 350^0 E. We do not get the peak at 270^0 E. The magnitudes of the peaks are also less in our case. The dusk time horizontal currents deduced from Magsat analysis [Langel et al., 1993] revealed peaks at 280^0E and between 110–150^0 E, but showed no clear peak around 100^0 E. However, some of their figures depicting eastward electrojet signatures do show indications of peak at 360^0 E and around 180^0 E.

Figure (3.5c) shows that the EEJ width is largest in the American sector. It has two secondary peaks at 30^0 and 120^0 E longitudes. The peaks are well defined and statistically significant. The width varies from a 2.5^0 in the region 150^0E to as much as 6.5^0 in the American zone. Though the width of 4^0 obtained for the Indian zone is fairly consistent with the half-width of 2.9^0 reported by Oko et al. [1996] using observatory data, the variation of the EEJ width with longitude is much greater than that reported by Onwumechili and Agu [1981a]. They reported range of EEJ half widths varying from 220 to 280 km (which will correspond to a range in width of little more than a degree) and concluded that there are no systematic longitudinal variations of the EEJ width. This parameter was not evaluated in the Magsat analysis.

3.5.3 Diurnal variation of EEJ strength and EEJ axis:

The next parameter that we look for is position of the electrojet axis with respect to the dip equator. We have already noted from figure 3.4e that the EEJ strength decreases as its axis moves substantially away from the dip equator. This is further substantiated by the results presented in Figures 3.6a and 3.6b. In figure 3.6a, we have shown the variation of the mean field at the electrojet axis, as a

function of the local time of the pass. While in figure 3.6b, we depict the mean of the magnitude of the deviation of the position of the electrojet axis with respect to the dip equator. The mean is taken over data from all the longitude zones. The electrojet field on ground shows the expected temporal variation peaking around 11.30 hours and decreasing on either side. The position of the electrojet axis also shows a systematic temporal pattern being closest to the dip equator around the time the H on ground maximizes. This is consistent with the scatter plot depicted in figure 3.4e but more importantly it corroborates the findings of Fambitakoye and Mayaud [1976], who also found that the EEJ axis is located closest to the dip equator near local noon. This definitely adds credibility to the algorithms used here. There is a problem arising out of the fact that the LT variations are inter-woven with seasonal differences. The LT of the satellite crossing changes from month to month and the seasonal differences will also appear when we are trying to examine a LT feature. But, as we shall note later, there are reasons to believe that what we are looking at are actually LT differences here.

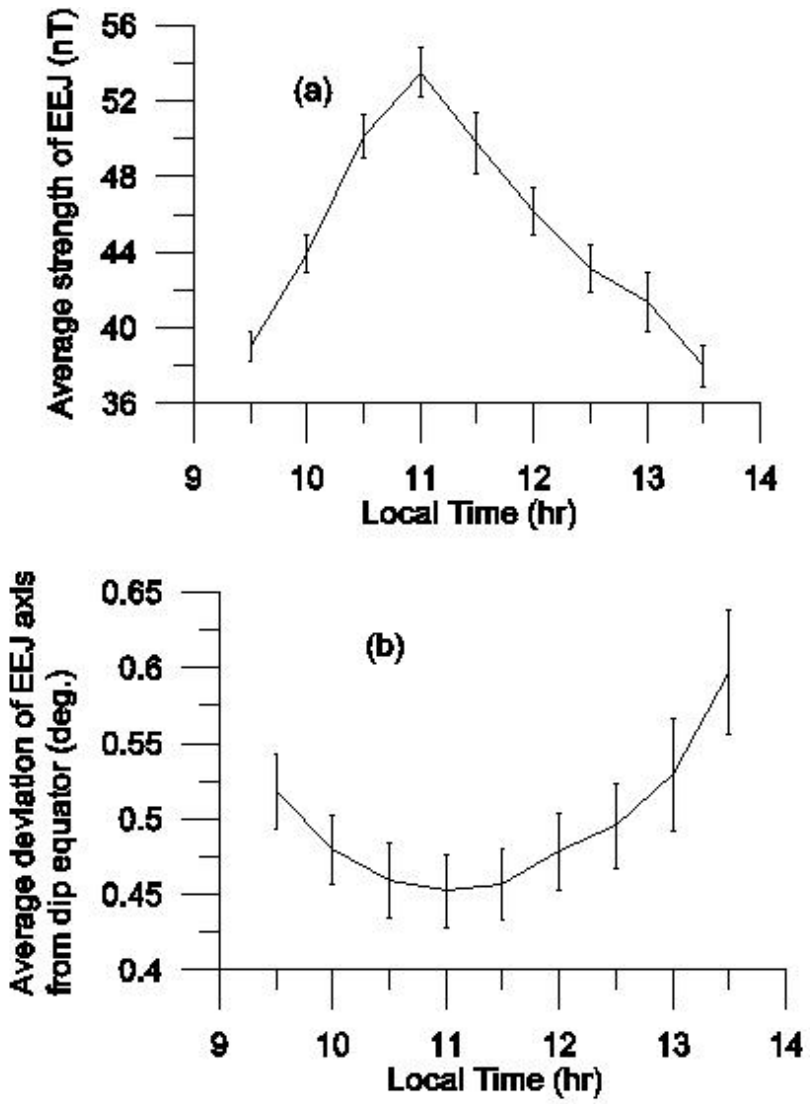

Figure 3.6 : (a) The mean EEJ strength and (b) the shift of the latitude of theaxis of the EEJ from the dip equator are plotted as a function of local time.

3.5.4 Zonal variation of EEJ axis:

We next look at the deviation of the EEJ axis from the dip equator as a function of longitude averaging over all LT (or months). The results of the analysis are presented in Figure 3.7a. One very significant feature that stands out is the tendency of the electrojet axis to shift away from the dip equator towards the geographic equator. Except for regions close to 150^0 E sector, this shift in the

average EEJ axis position towards the geographic equator is seen clearly everywhere. These results are consistent with those of Cain and Sweeney [1973] who were the first to report that the center of the EEJ deviates slightly from the dip towards the geographic equator. This feature is fairly persistent as seen from figures 3.7b and 3.7c, where we depicted the same parameters by month (Figure 3.7b) and by LT (Figure 3.7c).

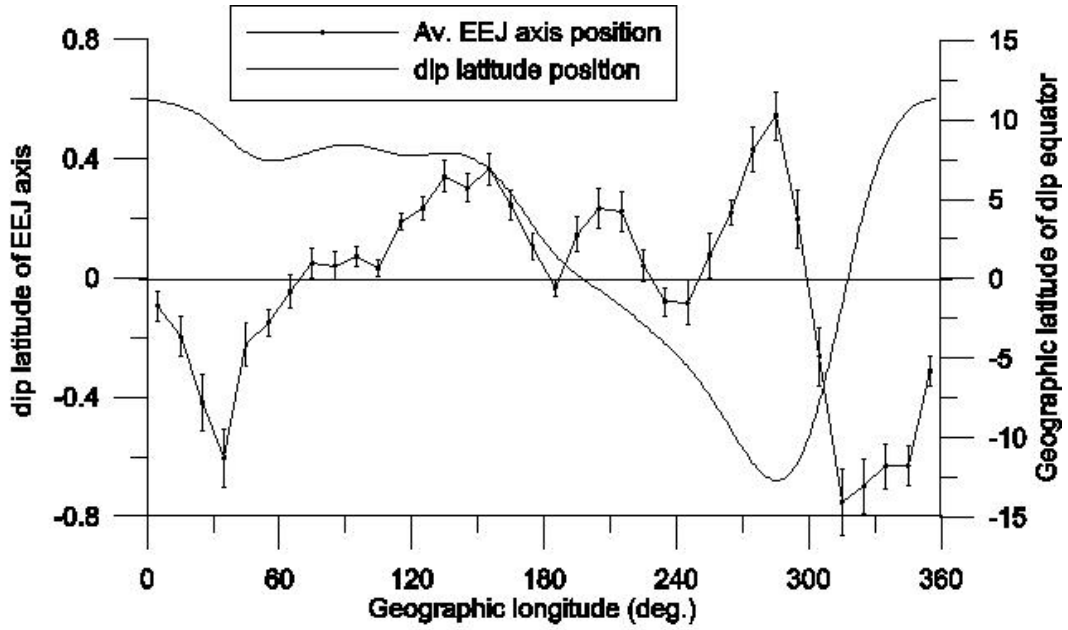

Figure 3.7a : The mean position of the electrojet axis w.r.t. the dip equator as a function of longitude with the corresponding variation of the latitude of the dip equator

In the longitude regions near 30^0 E, 285^0 E and 315^0 E, the deviation of EEJ axis from the dip equator is systematically larger ($>0.5^0$). Significantly, March and September month profiles do not show similar features, as one would expect if seasonal dependence dominate. These two equinoctial data sets represent different LT conditions and our results do suggest that LT variations are dominant. This adds credence to the argument, that the movement of EEJ axis position depicted in Figure 3.7c, represent genuine LT variations.

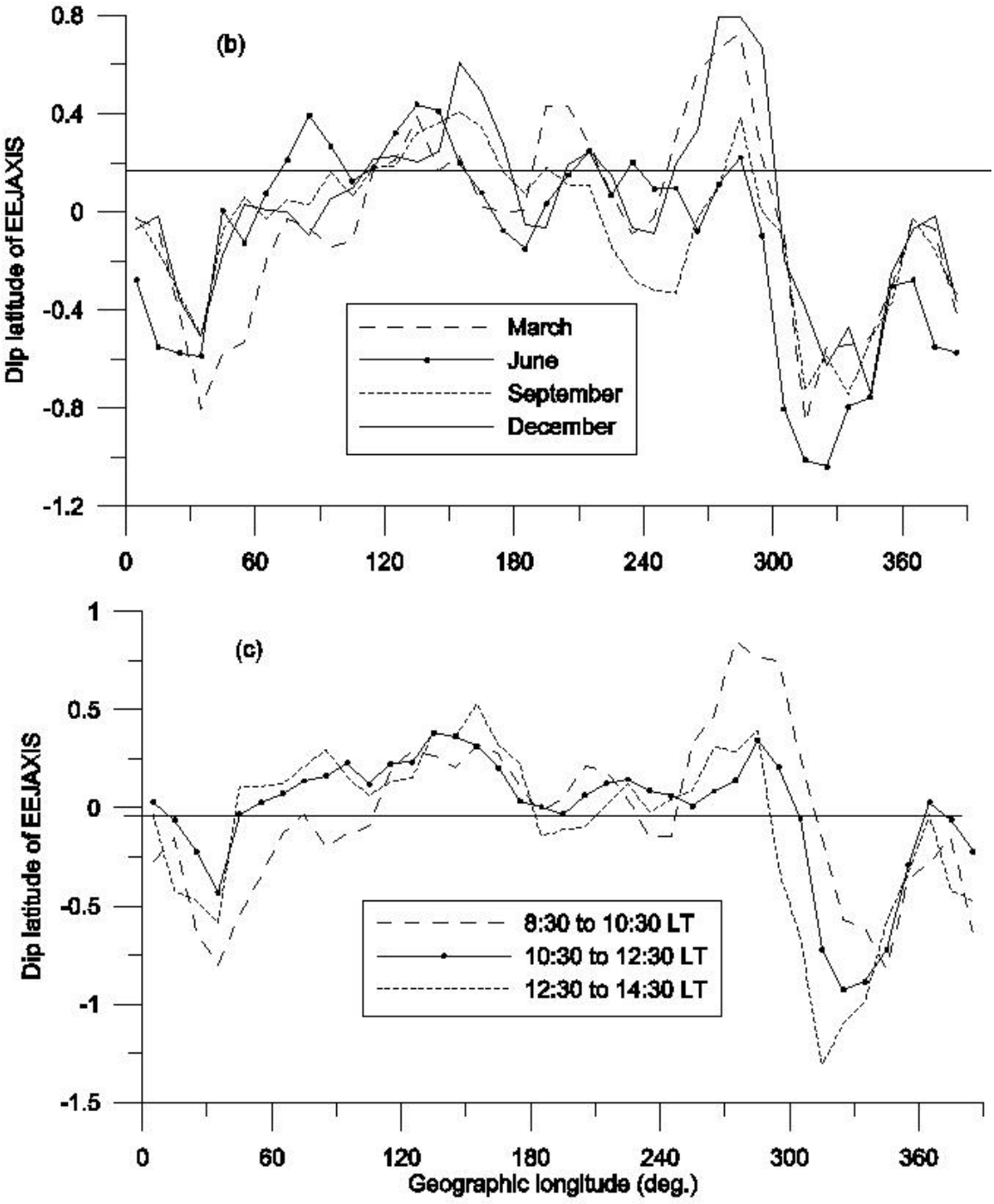

Figure 3.7: The position of the electrojet axis w.r.t. the dip equator for
(b) different months
(c) different local times

3.6 Longitudinal variation of EEJ strength computed on surface:

The EEJ phenomenon has been most extensively studied using ground magnetic data. In order to place our study in proper perspective, we present in this section, the ground magnetic manifestations of the longitudinal variation of EEJ strength and its day to day variability. We noted that the ground electrojet amplitude calculated at the axis of the EEJ shows the best correlation with the estimated surface electrojet H. This was true for both the Indian and American zones. We therefore use this parameter to study longitudinal characteristics of the EEJ as well as its day to day variability.

3.6.1 Average Variation:

In Figure 3.8, we present EEJ H on ground calculated at different longitudes. Each point plotted is the mean of all the passes in the 20^0 bin centered at that point and the points are separated by 5^0. The upper plot shows average amplitude of EEJ. These represent values computed at the latitude of EEJ axis. One can detect four clear peaks at 0^0, 110^0, 190^0 and 275^0E longitudes. The longitudinal structure of the EEJ H on ground resembles the total eastward currents depicted in Figure 3.5a, rather than the peak current as indicated by Figure 3.5b. It also suggests that the peak seen at 270^0 is associated with the increased width of the electrojet seen in the Figure 3.5c. The increased width is associated with larger *a* and it is not difficult to see from equations (1) and (2) that this will lead to larger magnetic field. A simple theoretical explanation based on increased ionospheric conductivity [Cain and Sweeney, 1973] cannot explain this multi-peak structure and this may have to be attributed to tidal variability.

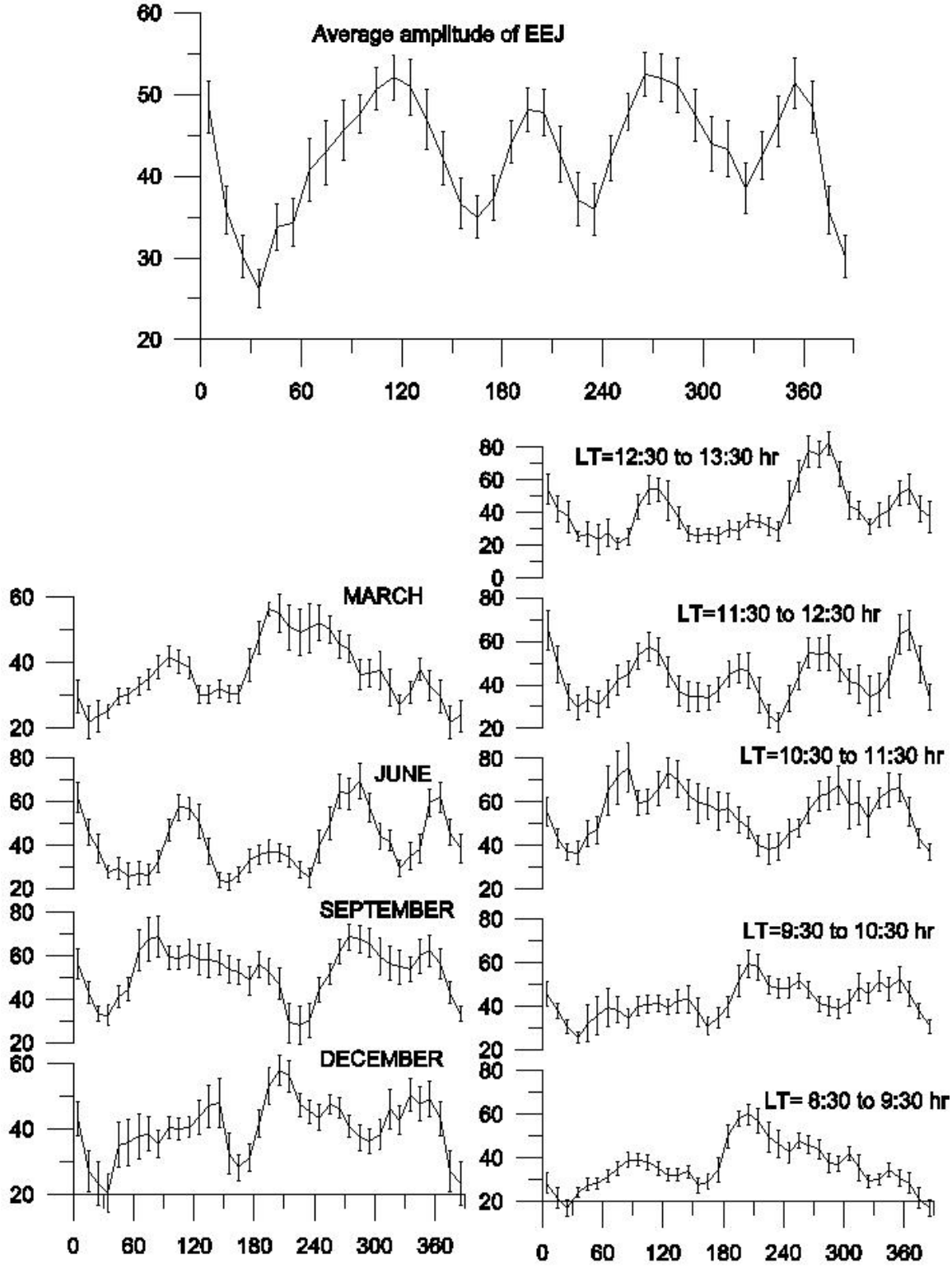

Figure 3.8 :The longitudinal variation of the EEJ strength (nT) on ground at the position of axis. The upper plot shows the average pattern, the lower left depicts the variations categorized in to different months while the lower right shows the variation categorized in terms of the local time of the satellite pass.

3.6.2 Seasonal and local time dependence:

In the lower part of the figure 3.8, we have the longitudinal structure categorized separately in terms of season and LT. Plots on the left-hand side show average amplitude of EEJ for different months, and the right hand side plots show that at different local times. The representing month is the central month of three months average; i.e. June indicates average of May, June and July data. Only in case of March, we have taken average of February and March to avoid the contamination arising from drastically different local times through the inclusion of April data. It should be emphasized again that the seasonal and LT dependencies are not independent as the LT of the pass changes from month to month. There is bound to be a degree of subjectivity in interpreting a particular signature as being due to seasonal changes or merely LT dependence.

The seasonal dependence brings out certain intriguing features. The peak around 180^0-200^0E is very distinct only from December to March. The peak around 120^0E is most clearly seen from March to June and the peak around 270^0E from June to September. The peak around 0^0E is persistent right through. Some of these could be genuinely seasonal and others mere artifact of the LT distribution with designated months.

The LT projection reveals a very interesting feature. Between 8:30 & 9:30 LT, the peak at 200^0 is largest. Then as LT increases, the strength at 200^0 decreases and the peaks at other longitudes start building up. At 11 hr LT, peak at 110^0 splits into two; one appears at 90^0 and the other at 125^0. It is worth examining the strength of peaks at different local times. The EEJ strength is always more for LT between 10:30 & 11:30 hr, with couple of exceptions. Plots suggests that the time of peak EEJ strength at 200^0 E is between 8:30 & 9:30 hr and not at around 11 hr. The dip equator at that longitude zone coincides with latitude of the geographic equator, hence one would expect the peak to lie at 11 hr. The other peaks in longitude show the expected peaking around local noon.

The amplitude of this peak at 180°-200°E at 0830 – 0930 hours LT is comparable with that of the other peaks at 11 hours. We examined the data at Jarvis Island (Dip latitude –0.12; Geographic longitude 199.97°E) and did not find any unusual LT traits that could justify such an early LT peak in EEJ. The electrojet peak was invariably around the expected local time. We are, thus, inclined to believe that we are looking at a seasonal effect and that the peak around 180-200°E would probably have been much larger if the satellite pass had been around noon in December to March sector.

The peak at 270°E is found to be largest between 12:30 to 13:30 hrs. However, corresponding seasonal variation indicates lower strength in this region. This may suggest that different modes are active at different longitudes and these alter the seasonal characteristics significantly.

3.7 Day to day variability in surface magnetic field:

What we have examined so far is the average pattern. Of much greater relevance is the variability from day to day. There is a longitudinal dependence of the EEJ because the Cowling conductivity that is responsible for the electrojet has a longitudinal dependence [Cain and Sweeny,1973; Jadhav et al., 2001]. The next question that one asks is whether the EEJ strength strictly follows the longitudinal structure defined by the conductivity every day. We have already seen from the average picture that the longitudinal structure of the EEJ is not determined entirely by conductivity. Since tides may be responsible for at least some of the peaks, we suspect that the day-to-day variability will have a clear longitudinal structure. Recent paper by Chandra et al [2000] clearly shows that the longitudinal variation of EEJ is not due to the variation of conductivity but is due to local electric field in the ionosphere.

James et al. [1996] studied the day-to-day variability using latitudinal array of stations in a narrow range of longitude and found that the correlation of ΔH at any station with equatorial station decreases as latitude of the station increases. Rangarajan [1992] using method of linear predictor filters have examined the relation between EEJ variations, at two ground stations separated in longitude. He was able to demonstrate that the EEJ H at Addis Ababa could be predicted fairly efficiently, given the time series of Trivandrum. The method is not easily applicable with satellite database of the type we have. Schlapp [1968] studied the variability of the EEJ from one day to another using coefficient of cross correlations between ground geomagnetic stations. He found that correlation drops to less than 0.5, if two stations are separated by 40^0 in longitude. We propose to use a similar cross correlation technique with the satellite data. The satellite data covers areas of the globe not accessible to surface measurements and can be expected to provide a more complete information.

The satellite can provide 14 to 15 crossings of the dip equator per day and may be expected to provide an excellent database for the correlation analysis. There are some problems that make the scenario slightly less attractive. Very rarely we have situation when the EEJ parameters can be derived from all the passes in the day. In practice a number of longitude sectors are missed out each day. This is not a very serious problem because the total number of useful passes is still adequate.

The longitude sectors have to be divided into a number of zones for the type of analysis undertaken. We use 20^0 bins and 18 of them cover the entire globe. The next problem arises because the pass need not pass through the center of the bin and passes that are close to the edges may not be representative of the bin. There may be sometimes two passes in a day in the same bin and sometimes the two passes in two neighboring bins may be closer to each other than to the centers they are supposed to represent. To minimize such distortions we divide the

globe into 18 equal bins in four ways starting with the first bin centered at 0^0, 5^0, 10^0 and 15^0 respectively. If ϕ_c represents the longitude of the center of any bin, then ϕ_c modulo 20 will be 0^0, 5^0, 10^0 and 15^0 respectively. The mean of these will represent bins centered at 7.5^0, 27.5^0, 47.5^0 and so on. If there are more than two passes on any day in any of the bin, their average EEJH will be taken as the value at the center of the bin.

Cross-correlation between any two bins is calculated from all the days, which had electrojet estimates in both the bins, irrespective of availability of data in any other bin. The number of points defining the correlation between any pair varies from pair to pair but is roughly around 30 or so. The same day's data cannot be used for all pairs for obvious reasons but this is not important as long as the number of points used for each pair is large enough for the sample to be considered representative of the population. We then take average of the four different estimates of the cross-correlation coefficients to enhance the reliability of the final estimate. The results of the analysis are presented in the correlation matrix presented in Table 3.2. All values are expressed in units of 0.01 and values significant at 99% are shown in bold. The diagonal elements, which should be one by definition, are replaced, in the table, by the variance for each bin.

The variance maximizes in the Indian and American sectors. There seems no obvious explanation for this. Also note that the correlation between the EEJ in the Indian and American sectors are significant. The correlation between the American and Indian zones was simultaneously computed using the ground data of Trivandrum and Alibag in the Indian sector and Huancayo and Fuquene in the American sector. The correlation of 0.53 from the satellite observations compares well with 0.45 obtained from ground data for the same days. The correlation patterns on the whole are not systematic with even the neighboring zones exhibiting poor correlation. This may be due to rather complex forcing

associated with the EEJ. We examine the correlation matrix in greater detail using powerful multivariate analysis technique.

Table 3.2: Correlation matrix in units of 0.01. Diagonal elements are the sample variance, and the correlations significant at 99% are shown in bold face.

					Zone number												
1	2	3	4	5	6	7	8	9	10	11	12	13	14	15	16	17	18
416	23	20	27	20	**42**	39	19	19	-16	-8	0	14	19	38	12	37	38
23	389	**55**	43	22	16	**44**	28	28	20	-5	-1	1	0	6	12	15	29
20	**55**	483	**45**	26	19	**44**	**55**	33	41	0	4	10	8	15	52	17	16
27	43	**45**	540	36	36	**48**	**52**	43	28	7	22	35	34	**53**	**63**	29	9
20	22	26	36	450	**45**	25	32	27	14	-5	-16	0	13	1	5	16	18
42	16	19	36	**45**	475	18	19	29	-13	-11	9	14	27	6	7	15	19
39	**44**	**44**	**48**	25	18	490	38	28	28	10	33	18	9	31	**57**	**50**	40
19	28	**55**	**52**	32	19	38	445	**53**	36	15	16	19	29	18	**47**	34	30
19	28	33	43	27	29	28	**53**	419	10	-5	0	-7	11	21	8	1	18
-16	20	41	28	14	-13	28	36	10	432	27	17	-3	-22	1	37	2	-17
-8	-5	0	7	-5	-11	10	15	-5	27	451	21	18	-2	9	16	5	-18
0	-1	4	22	-16	9	33	16	0	17	21	450	17	16	25	**54**	29	-26
14	1	10	35	0	14	18	19	-7	-3	18	17	414	**68**	**56**	53	40	34
19	0	8	34	13	27	9	29	11	-22	-2	16	**68**	502	**61**	**50**	35	36
38	6	15	**53**	1	6	31	18	21	1	9	25	**56**	**61**	479	49	27	23
12	12	**52**	**63**	5	7	**57**	**47**	8	37	16	**54**	53	**50**	49	466	38	23
37	15	17	29	16	15	**50**	34	1	2	5	29	40	35	27	38	454	**50**
38	29	16	9	18	19	40	30	18	-17	-18	-26	34	36	23	23	**50**	487

3.7.1 Principal Component Analysis:

The correlation matrix is a very important entity in the multivariate analysis technique. If the EEJ at different longitudes vary independently, the matrix will have 1 as the diagonal elements and 0 for all the non-diagonal ones. If the EEJ at different longitudes vary perfectly in unison, all the elements will be one. In the real world we expect a number of patterns of forcing which may work sometimes in unison and in opposition at other times, generating a complex correlation matrix of the type given in Table 3.2. The next question is whether the correlation matrix can itself be used to determine the natural modes of longitudinal structure of the EEJ. The Principal Component Analysis

[Gnanadesikan, 1977] does just that and we use this powerful technique to determine the natural patterns of longitudinal variations of the EEJ.

3.7.1.1 Basic Idea:

The basic idea of the principal component analysis is to describe the dispersion of an *n* component array by introducing a new set of coordinates so that the variance of the given points with respect to the derived coordinates are in decreasing order of magnitudes. In effect, instead of representing the data as values at 18 longitude points, we express it as coefficients of 18 orthogonal functions derived from the statistical property of the data itself. The variability of EEJ from day to day is represented by the corresponding variation of the coefficients of these functions. The major advantage of the technique is that the prescription of the choice of the function is such that the first few functions generally reproduce most of the variability in the data [Rajaram and Rajaram, 1983].

Let $H_{i,j}$ be the EEJH value at the longitude ϕ_j (j = 1,18) on day d_i (i =1, N). We express $H_{i,j}$ in the form

$$H_{i,j} = \sum_{k=1}^{18} D_k(d_i).\Phi_k(\phi_j)$$

Where functions Φ_k and D_k satisfy the following constraints

$$\sum_{j=1}^{18} \Phi_l(\phi_j).\Phi_k(\phi_j) = \delta_{lk}$$

and

$$\sum_{i=1}^{N} D_n(d_i).D_k(d_i) = \lambda_k \delta_{nk} .$$

The functions Φ and D are obtained by making a least square fit to the data itself. It turns out that functions Φ are the eigenvector of the matrix R_{jk} defined by

$$R_{jk} = \sum_{i=1}^{N} H_{i,j}.H_{i,k}$$

and

$$D_k(d_i) = \sum_{j=1}^{18} H_{i,j}.\Phi_k(\phi_j).$$

It is quite obvious that $\Phi_k(\phi_j)$ gives the longitudinal structure of the k^{th} component and $D_k(d_i)$ gives the contribution of that particular component on day d_i.

The procedure is to first obtain the matrix R_{ik} from the data and determine its eigenvalues and eigenfunctions. The eigenvalues and the eigenvectors are arranged in the descending order. The percentage of the variance accounted for by the component with eigenvalue λ_k is given by

$$P = \frac{\lambda_k}{\sum_{j=1}^{18} \lambda_j} \text{ x } 100.$$

Thus the first component explains largest percentage of the variance, the second the next and so on.

Since variability from day to day is with respect to the mean in any longitudinal bin, we can express $H_{i,j}$ as departures from the mean. We further normalize it with respect to the variance of the EEJH corresponding to that longitude bin. The matrix $R_{i,j}$ then becomes the correlation matrix. There are distinct advantages in adopting this scheme. We have already noted that EEJH is not obtained for all longitude bins on any given day. The EEJH forcing is known to be different on different days and it may be misleading to discuss the longitudinal structure of the variability from day to day by combining all the data together ignoring this factor. On the other hand the correlation between any two bins is a statistic, which is reliably determined, provided the number of common days for the two bins is large enough for the sample value to be treated as the population value.

Thus it is not necessary to restrict the analysis to days in which data is available in all the bins selected. Consequently bin sizes can be taken smaller to provide better resolution in longitude. A second advantage stems from the fact that the use of correlation rather than the covariance matrix is more appropriate for identification of coherent structures [Storch, 1999].

3.7.1.2 Application & Output of the analysis:

We use the correlation matrices determined earlier for the four sets of bin distributions, which are generated with slight offset with respect to each other. The eigenvalues and eigenvectors are determined and ordered in descending values of their eigenvalues for each of the matrices. Each normalized eigenvector has 18 elements, each of which represents the contribution made at the corresponding longitude bin. The 18^{th} and the first bins are obviously contiguous. We smoothen out these contributions by taking a five bin running mean and compare the four different estimates we have for the longitudinal structure of the contributions corresponding to each of the four sets. We find that the first component is almost same for all the four groups. The same is true for the other components except that the structure for the bins centered at 5^0 (modulo 20) is slightly different. The other 3 are very close to each other and the mean of 4 is also very close to them. This shows that the technique is fairly robust. Note that the overall sign of the eigenvector is irrelevant. The contribution of component is positive or negative depending upon the sign of D_k.

We depict in figure 3.9, the mean longitudinal structure of the first four components after multiplying contribution to each bin with the variance corresponding to that bin. This multiplication with the sample variance is necessary to make the comparison between the different longitude zones meaningful. The percentage of the variance accounted for each of the components is shown in figure 3.10. The results are quite dramatic and provide

considerable insight into the different types of forcing that contributes to the variability in the EEJ.

The first component, which accounts for nearly 30% of the day to day variability, is obviously global in character except that its contribution is reduced around 240^{0}E meridian. It may be readily interpreted as the electrojet variability due to global changes in solar ionizing radiation or tidal forcing.

The variability associated with other components appears to be generated by the longitudinal variations in separation between dip and geographic equators. The geographic equator orders the tidal forcing, while the dip equator dictates the symmetry of the conductivity of the ionosphere. To interpret these components, we have plotted the latitude of the dip equator along with each of the components.

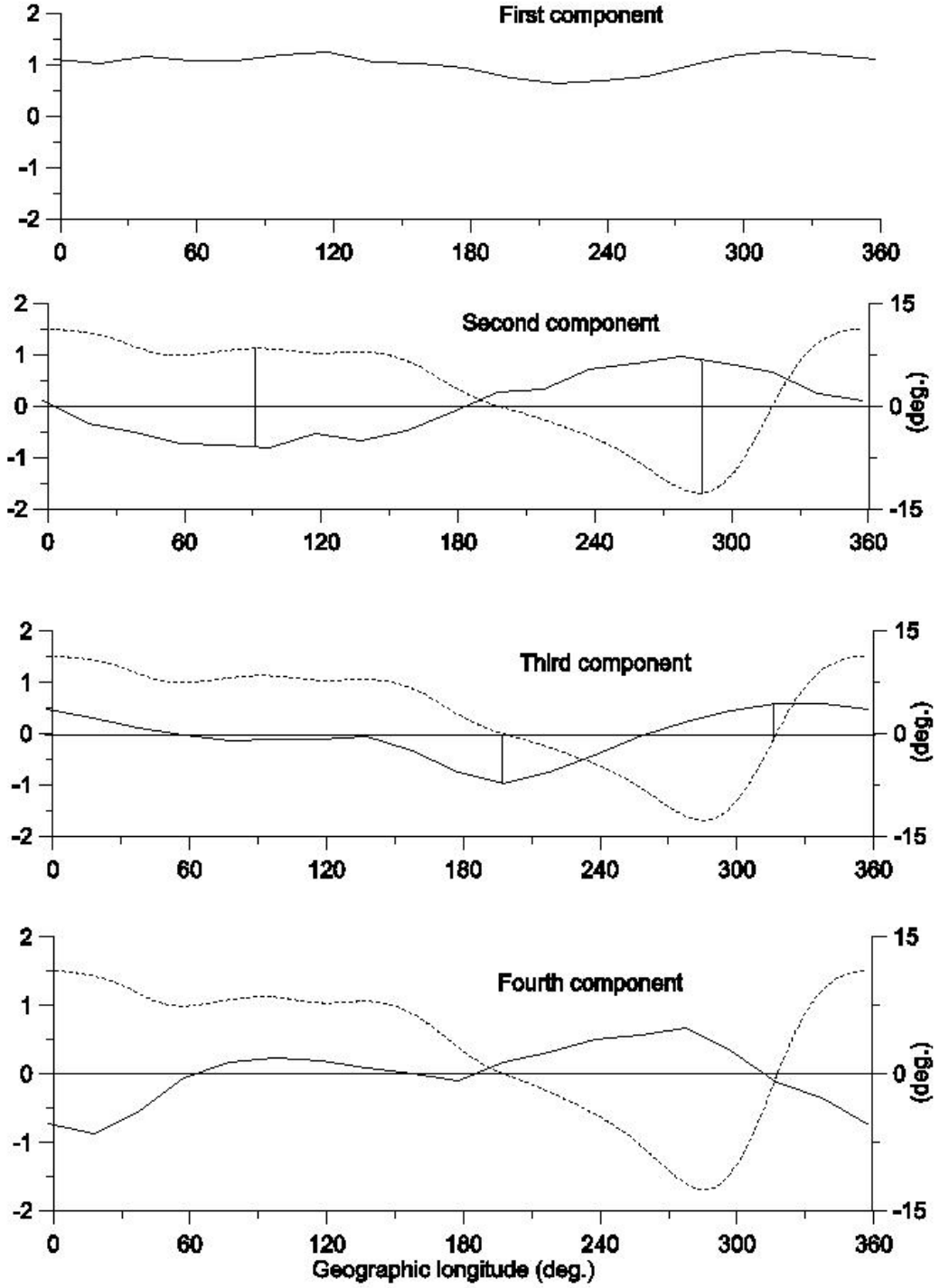

Figure 3.9 : The longitudinal structure of the first four components obtained from the Principal component analysis of the satellite data is presented. Except in first component, the profile of the latitude of the dip equator (dotted line) is also shown; the scale is shown on right hand side.

We can see that the 2nd component, which accounts for roughly 15% of the EEJ variability, follows the latitude of the dip equator as function of longitude except

a zone between 315^0E and 60^0E. It is exactly in this region that the component 4, which accounts for 10% of the variability, takes over and tracks the dip latitude profile. Note that the 4^{th} component contributes essentially in region east of 330^0E to the west of 30^0E where the impact of the 2^{nd} component is relatively modest. These components produce an equatorial electrojet contribution which is opposite in sign depending on whether the dip equator is in the northern or Southern hemisphere. These could also be a source of the seasonal variations of the EEJ.

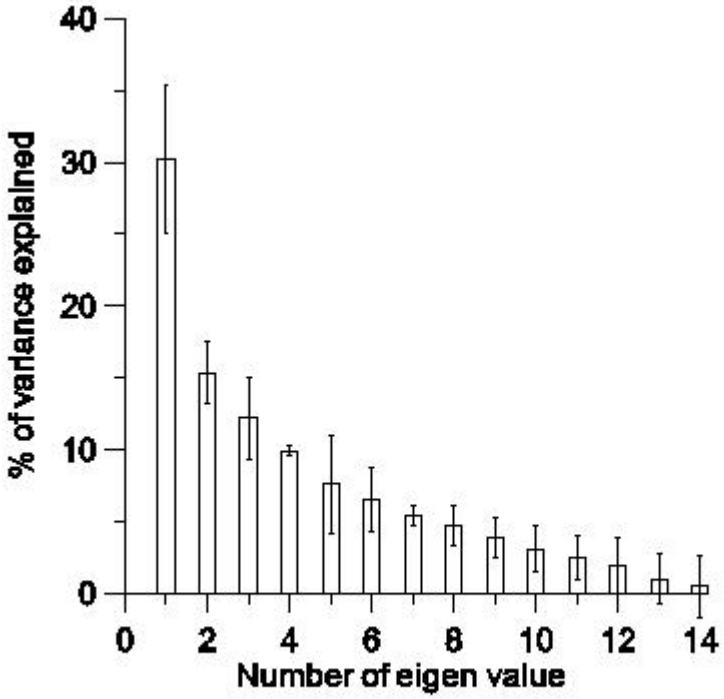

Figure 3.10 : Percentage of variance accounted for by the first for components

It is not really surprising that two components are required to account for the control of the latitude of the dip equator on the variability of the strength of the observed EEJ. The region in which fourth component dominates corresponds to the region where the location of the dip equator changes rapidly with longitude from around 13^0S to 12^0N. This rapid variation of the dip equator position is also accompanied by an anomalous orientation of the dip equator with respect to the geomagnetic field. The two are not perpendicular to each other as required by

the classical picture of the equatorial electrojet. In the zone just east of 300^0 E longitude, the deviation from the expected perpendicularity is around 12^0, which would mean that if the electrojet flows along the dip equator its contribution to the eastward declination component is almost 20% of the H variations [Jadhav et. al., 2001]. We would expect that the response of the EEJ to changes in tidal forcing should be different in such a zone and it is therefore not surprising that an additional component manifests itself in this region.

Finally component 3, which contributes around 12.5% to the EEJ variability, is most conspicuous in the regions where the dip equator crosses the geographic equator. It is probably responsible for the apparently anomalous peak at 200^0E region discussed earlier. The singular behavior of the EEJ is not obvious in the 330^0E region probably because it is masked by the contribution from fourth component.

It should be pointed out that the first four components together account for a little over two-third of the variability of the EEJ. The other components that are responsible for the remaining contribution to the variability in EEJ could be because of various other processes including the presence of non-migrating tides. The errors inherent in the determination of the EEJ parameters could also be responsible for the apparent variability not explained for by the first four components.

We have concentrated on the longitudinal structure of EEJ component. No attempt has been made to determine $D_k(d_i)$, the contribution of the k^{th} component of day d_i, which requires EEJ contribution on a given day from all 18 longitudinal bins.

3.8 Results and Discussion:

We have shown that the magnetic field observations obtained from the Oersted satellite can form an excellent data base for studying not only the longitudinal structure of the equatorial electrojet but also the sources responsible for its variations from day to day. We have devised an objective method for identifying the signature of the equatorial electrojet and determining the parameters that define its basic structure and found that it works out very well in describing the surface manifestations of the EEJ as seen in the observatory data.

For the estimation of the EEJ parameters we have assumed that the electrojet current flows at a height of 106 km in the ionosphere and neglected the subsurface induced currents for computing the field at the satellite height. There is some justification in making such an assumption. Number of rocket measurements in the equatorial region has confirmed that the peak electrojet current flows at 106-km altitude [Maynard and Cahill 1965, Sampath and Sastry 1979]. Fambitkoye and Mayaud [1976] found no measurable induction of the electrojet field in Central Africa while Ducruix et al. [1977] have shown theoretically that electrojet induced field is negligible at least along the noon meridian. Yacob [1977] examined internal induction by the EEJ in India with ground and POGO satellite geomagnetic observations and found that the internal field contribution is small. This could be regarded as some justification for neglecting geomagnetic induction. Furthermore, sub-surface conductivity is also a variable quantity and making even intelligent guesses of its underlying longitudinal structure would lead to a bias in the estimated induced currents.

We have also assumed, that the electrojet signature, at satellite height, is generated by the currents described by the empirical model of Onwumechilli [1967]. The model incorporates an eastward electric current at the dip equator and a westward current at the low latitude flanks. There have been suggestions [Stening, 1995] that shoulders can be due to the satellite passing through a field

aligned currents which it encounters on each side of the dip equator but this has not been substantiated through actual calculations. Signatures similar to the satellite observations have been reported using ground based array data [Hesse, 1982; Hutton, 1967a,b; Forbush and Casaverde, 1961; Oldenburg, 1976; Fambitakoye and Mayaud, 1976] and reproduced using an eastward current at the dip equator flanked on either side by westward currents possibly associated with EEJ return currents. The model of Onwumechilli [1967] works on a similar philosophy and has been successfully used earlier to determine EEJ parameters from satellite magnetic field data.

In the ultimate analysis, the justification of the technique is in the stable and consistent results established on the basis of the model used. The consistency in the correlation of the ground observations and the corresponding field computed from the deduced satellite parameters, for both the Indian and American sectors, is very encouraging. It should however be cautioned that no claim is made that the identification of the parameters is accurate on a pass to pass basis. There is, however, compelling evidence to show that the deduced parameters can reproduce statistically consistent characteristics of the EEJ.

There is also considerable degree of consistency in reproducing many of the features obtained earlier [cf. Onwumechilli, 1997] using satellite magnetic measurements. We obtain a similar multi-peak longitudinal structure for the EEJ and the locations of these peaks are also similar. The consistency of the results obtained from two independent satellite measurements suggests that these structures are real. We believe that the longitudinal structure of the EEJ cannot be explained on the basis of the conductivity distribution in the equatorial ionosphere and asymmetrical tidal forcing has to be necessarily invoked. The distribution of the EEJ currents in longitude is season and LT dependent and the two controlling factors cannot be separated given the limited amount of data

available and the season dependent LT of the satellite passes. Some of the quantitative differences from earlier findings may be attributed to this.

We do find a clear indication that the axis of the EEJ tends to move away from the dip equator towards the geographic equator as suggested by Onwumechili [1985]. This tendency gets slightly blurred close to the regions where the latitude of the dip equator changes rapidly with longitude. More remarkably the position of the EEJ axis deduced from satellite exhibits a local time dependence similar to what has been observed on ground [Fambitkoye and Mayaud, 1976] being closest to the dip equator around noon. There is also a clear indication that the EEJ strength weakens as the axis moves away from the dip equator. These features appear in the global average and unfortunately there is not enough data to make a statistically reliable study of the longitudinal structure of this phenomenon.

The width of the electrojet varies considerably with longitude and is as high as 6.5^0 in the American zone compared to around 2.5^0 in the 120-180^0 belt. This variation is statistically significant and is consistently seen in many individual passes [Jadhav et. al., 2001], which is presented in chapter 2 and it is surprising that it is not present in the POGO data [Onwumechili, 1985]. In fact the peak in the EEJ signature around 270^0E is connected more with an enhancement of the width of the EEJ, as J_0 does not exhibit any peak in this region. The American sector is unique in the sense that the latitude of the dip equator changes rapidly across this region and the angle between the line of zero dip and the horizontal component of the ambient magnetic field also deviates from the perpendicularity. The rapid fluctuation of the width of the EEJ with longitude in the region between 240^0 E and 360^0 E may be connected with this anomaly.

By far the most far-reaching results obtained through the analysis presented here are the conclusions based on the analysis of the variability of the EEJ strength on

ground on day-to-day basis. The variations estimated in two different longitude bins on the same day form the basis of the correlation of changes detected in the two bins from one day to another. The correlation matrices generated give the numbers consistent with the values detected from the ground data in the Indian and American sectors but suggest that the correlations may be very small even between neighboring zones in many longitude sectors. However, when the correlation matrices are subjected to the principal component analysis a very clear picture emerges. The results of the analysis appear to be fairly robust and reveal many interesting features hitherto unnoticed.

The first component, which accounts for 30% of the variability, provides the global response of the EEJ to changes from one day to another. The second and fourth components, which account for 15% and 10% of the variance respectively, are driven by forcing that depends on whether the location of the EEJ in that sector is in the northern or southern hemisphere. Models, which assume that the dip equator coincides with the geographic equator, cannot predict such a forcing. Both the components may be contributing to the seasonal variation of EEJ. The fourth component dominates where the contribution of the second is modest. We tend to believe that the forcing responsible for the generation of the 4^{th} component is associated with the peculiar nature of geomagnetic field geometry in the region from 300^0E to 60^0 E. Finally the 3^{rd} component accounts for 12.5% of the variation and contributes in regions where the dip and geographic equators are close to each other. Thus the analysis brings out three types of basic forcing; a mode that is same throughout the globe, a mode that exhibits hemispherical asymmetry associated with the location of the dip equator and a mode that is prominent in regions where the dip and geographic equators coincide. Together these account for two-third of the over all variability of the EEJ. The remaining components may be associated with more complex processes associated with non-migratory tides or mere noise associated with the errors connected with the identification of the EEJ parameters. The technique appears to be very promising

and could find more critical application as more of the data from the Oersted satellite gets analyzed.

We have shown that an analysis of just one-year of the Oersted total field data restricted to geomagnetically quiet days can generate considerable amount of valuable information on the EEJ. The study has underlined the importance of using satellite data and using powerful multivariate analysis techniques for optimum utility. The inadequacies of the existing models of the EEJ appear to be palpable. The Oersted is continuously providing data and promises to provide the source for a more complete statistics. Statistics can also be improved by not restricting the analysis to IQ days, though this may in turn increase the errors in estimation of the EEJ parameters. The vector data may also provide vital information especially with regard to the importance of meridional currents.

Chapter 4
Study of reverse EEJ signature observed at Oersted

4.1 Introduction:

The reverse equatorial electrojet, better known as equatorial counter electrojet (CEJ) is an enigmatic phenomenon, yet to be understood in terms of physical processes. First detected as a reversal of the H field near local noon at Addis Ababa by Gouin [1964], it is later known to occur rather frequently in the early morning or late afternoon hours [Gouin and Mayuad, 1967]. Rastogi [1974] showed that difference in H component between electrojet and non-electrojet station was a better indicator of reversal. Its occurrence is influenced by lunar phase [Sastry and Jayaken, 1972] and level of solar activity [Rastogi, 1974]. But these influences do not reflect the day-to-day occurrence of the CEJ and represent only broad statistical features.

Earlier, CEJ using ground magnetic field data has been studied by many workers [Rastogi 1974a,b, Mayaud 1977, Bhargava and Sastry 1979, Stening 1992, Doumouya et. al. 1998]. But very few attempts have been made to study CEJ using satellite data. Cohen and Achache [1990] used measurements of the X and Z components from Magsat data to show that ionospheric currents were systematically observed to flow eastward at dusk but westward at dawn, suggesting that CEJ effect was most of the time, measured at dawn (80% of the days). Langel et al. [1993] pointed out the fact that the EEJ description obtained from Magsat data is biased by the necessary use of a main field model and concluded that the CEJ effect was not really observed in the Magsat dawn data. After inspecting POGO data, Cain and Sweney [1973] reported three days indicating reverse EEJ signature. Onwumechili [1985] argued that the reverse signature could result from the satellite flying immediately below a current layer

additional to the well-known electrojet at 107-km altitude, while Kane [1973] showed this may be case of CEJ. In the present chapter, we have tried to analyze the reverse signature of EEJ observed in the Oersted satellite data.

To study the longitudinal variation of CEJ, ground database has several limitations. Due to mountains and oceans, it is not possible to have close longitudinal observations of equatorial electrojet, which has really restricted our understanding of CEJ. Further, the improper selection of Sq station may not result in CEJ occurrence. Hence study of CEJ using satellite data can provide deeper insight into zonal variation of CEJ. In the present chapter, an attempt in this regard has been made for the first time.

It is desirable that the CEJ should be understood in terms of tidal forcing and thus requires an understanding of its longitudinal structure. Very little work has been carried out in this direction, though it has been found [Rastogi, 1973] that some of the CEJ have longitudinal width of few hours only. The Oersted satellite with its extensive longitudinal coverage offers an excellent opportunity of examining this aspect. There is of course a restriction imposed by the fact that during the period examined the local time passes were restricted from morning to noon hours and did not encompass the afternoon CEJ.

4.2 Data Selection and Treatment:

We have analyzed scalar magnetic field (F) from Oersted satellite for first five quiet days of each month for the period of April' 1999 to March' 2000. Table 4.1 shows selected quiet days, corresponding local times and Ap indices. For the proper identification of the CEJ, it is necessary to select quiet days and remove the variations due to the main field. Here, we have used the main field model [Olson et al. 2000] derived from the Oersted data, which has degree and order up to 13 and also incorporates correction for second order Dst variations. This model has a

RMS misfit of approximately 2 nT for the total field intensity and 4 nT for each component.

A Fortran program, which has been discussed in more detail in the previous chapter gives residual magnetic field (△F) for each pass in the latitude range of 20^0N to 20^0S. Since eastward localized current produces southward magnetic field above the current system, the EEJ signature has V-shaped N-S profile and CEJ has ∧-shaped profile. So, when ∧-shape is observed in residual magnetic field at satellite height, we consider that as CEJ signature. A typical CEJ signature at satellite is shown in figure 4.1.

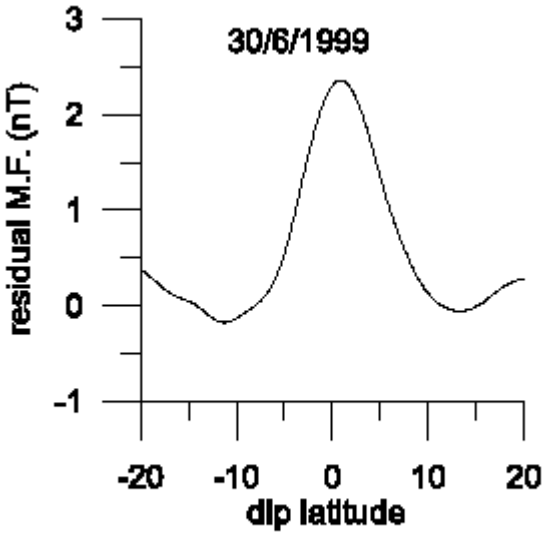

Fig. 4.1 A typical Reverse EEJ signature of residual M.F. seen at Oersted height.

As discussed in the introduction, earlier attempts to study the reverse signature observed at satellite were not so productive. Hence first we have to examine the genuineness of the signature. We have therefore compared the reverse EEJ signature at satellite with ground data. This is discussed in the next section.

Table 4.1

DATE	LT (hr)	Ap
13 April'99	13.7	3
15 April'99	13.67	4
22 April'99	13.57	4
23 April'99	13.55	5
24 April'99	13.54	6
25 April'99	13.52	4
11 May'99	13.28	2
16 May'99	13.20	3
17 May'99	13.19	2
22 May'99	13.11	3
31 May'99	12.98	2
14 June'99	12.77	2
21 June'99	12.66	2
22 June'99	12.65	2
30 June'99	12.53	3
4 July'99	12.47	2
5 July'99	12.45	2
16 July'99	12.29	4
17 July'99	12.27	3
18 July1999	12.26	4
19 July'99	12.23	4
2 August'99	12.03	6
3 August'99	12.01	4
10 August'99	11.91	5
14 August'99	11.85	4
5 September'99	11.52	6
6 September'99	11.50	5
8 September'99	11.47	8
24 September'99	11.23	5
25 September'99	11.22	4
6 October' 99	11.05	6
7 October' 99	11.04	5
9 October' 99	11.00	6
18 October' 99	10.87	6
19 October' 99	10.86	6
20 October' 99	10.84	3
30 October' 99	10.69	6
4 November' 99	10.62	5
15 November' 99	10.45	5
26 November' 99	10.28	4
27 November' 99	10.26	2
14 December' 99	10.01	3
21 December' 99	9.90	2
22 December' 99	9.89	1
23 December' 99	9.88	2
26 December' 99	9.83	2
8 January' 00	9.63	5
9 January' 00	9.62	3
17 January' 00	9.49	3
18 January' 00	9.48	3
21 January' 00	9.43	2
4 February' 00	9.22	5
17 February' 00	9.02	6
18 February' 00	9.01	1
19 February' 00	9.00	3
20 February' 00	8.99	5
4 March' 00	8.78	3
15 March' 00	8.62	2
16 March' 00	8.60	2
26 March' 00	8.45	3
27 March' 00	8.43	4

4.3 Detailed analysis of CEJ observed in satellite data:

Scatter plots between ground and satellite EEJ strength data shown in the previous chapter, show very good correlation between the two, which has encouraged us to believe in the data and our method of analysis. In this section, we point out some occasions on which we could support reverse EEJ signature observed at satellite height by the ground CEJ observations. Here we have used provisional data from Trivendrum (Dip Latitude -0.7^0, Geographic longitude 76.9^0) as equatorial ground station and Alibag (Dip Latitude 9.8^0, Geographic Longitude 72.9^0) as Sq ground station.

Figure 4.2 shows event on 22nd May' 99. Figures on left hand side, show satellite observations at different universal times (UT), while figure on right hand side shows ground observation of EEJ in the Indian zone (75^0E longitude) on the same day. The solid line shows the curve for hourly averaged values of EEJ, while dotted curve is the running average. Bottom X-axis shows local time (LT), while upper axis shows UT in hours. UT and longitude of the satellite pass is the time and longitude at dip equator crossing. Ground observation shows afternoon (around UT=7 hr to 12 hr) CEJ effect on 22nd May' 99. Satellite passes at UT= 7.86 hr and 9.5 hr show CEJ signature, while pass at 4.5 UT (at this UT ground data does not show CEJ) shows EEJ signature. We expect the satellite pass at 11.2 hr UT to show CEJ signature, but it does not. Local time for that pass is 13.1 hr and that for ground is 16.2 hr. Longitude of middle satellite pass is 79^0, which is close to Trivendrum. Thus for the same longitude and time we have satellite and ground observations, which give consistent results.

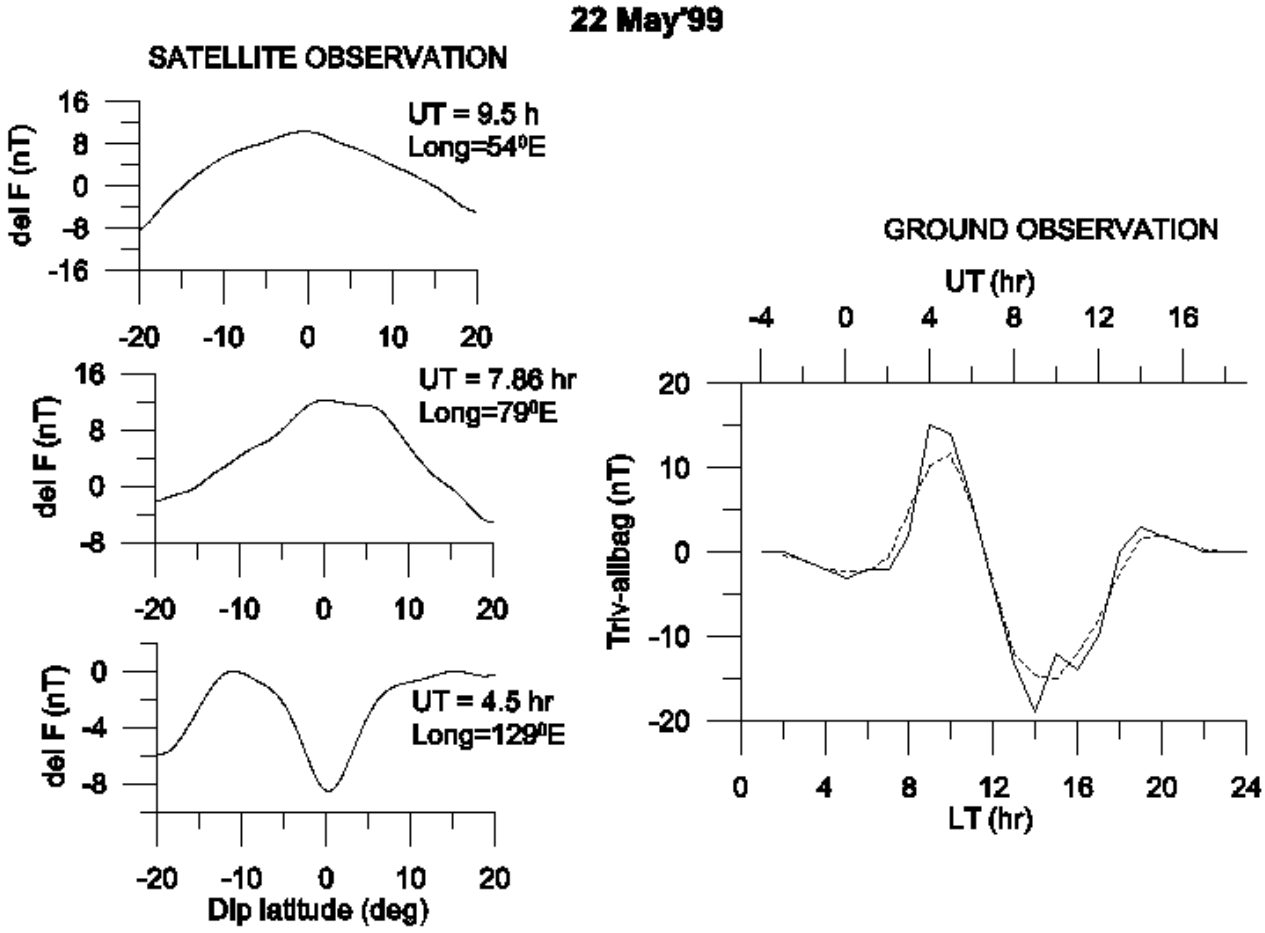

Figure 4.2 : Event on 22 May'99.
Figures on left hand side show residual M.F. Vs dip latitude for satellite passes at different UT's and longitudes.
Figure on right hand side shows hourly averaged value of EEJ strength (Trivendrum-Alibag) from ground observations. Dotted curve shows running average. Bottom axis is local time, while upper axis shows UT.

Figure 4.3 shows event on 14th December'99. In ground data, CEJ is seen between 0 to 5 UT. Satellite pass at 4.7 UT shows CEJ signature but pass at 6.7 UT, which is out of the range of CEJ, has EEJ characteristic. Pass at 3 UT is expected to have CEJ signature, but satellite pass does not show. Local time for this pass is 10 hr and on ground LT is 8 hr.

Thus, whenever, the satellite is in the longitude belt of the ground station observing the CEJ, the satellite also sees the CEJ. However, the satellite does not see the CEJ if its longitude is even 30^0 away.

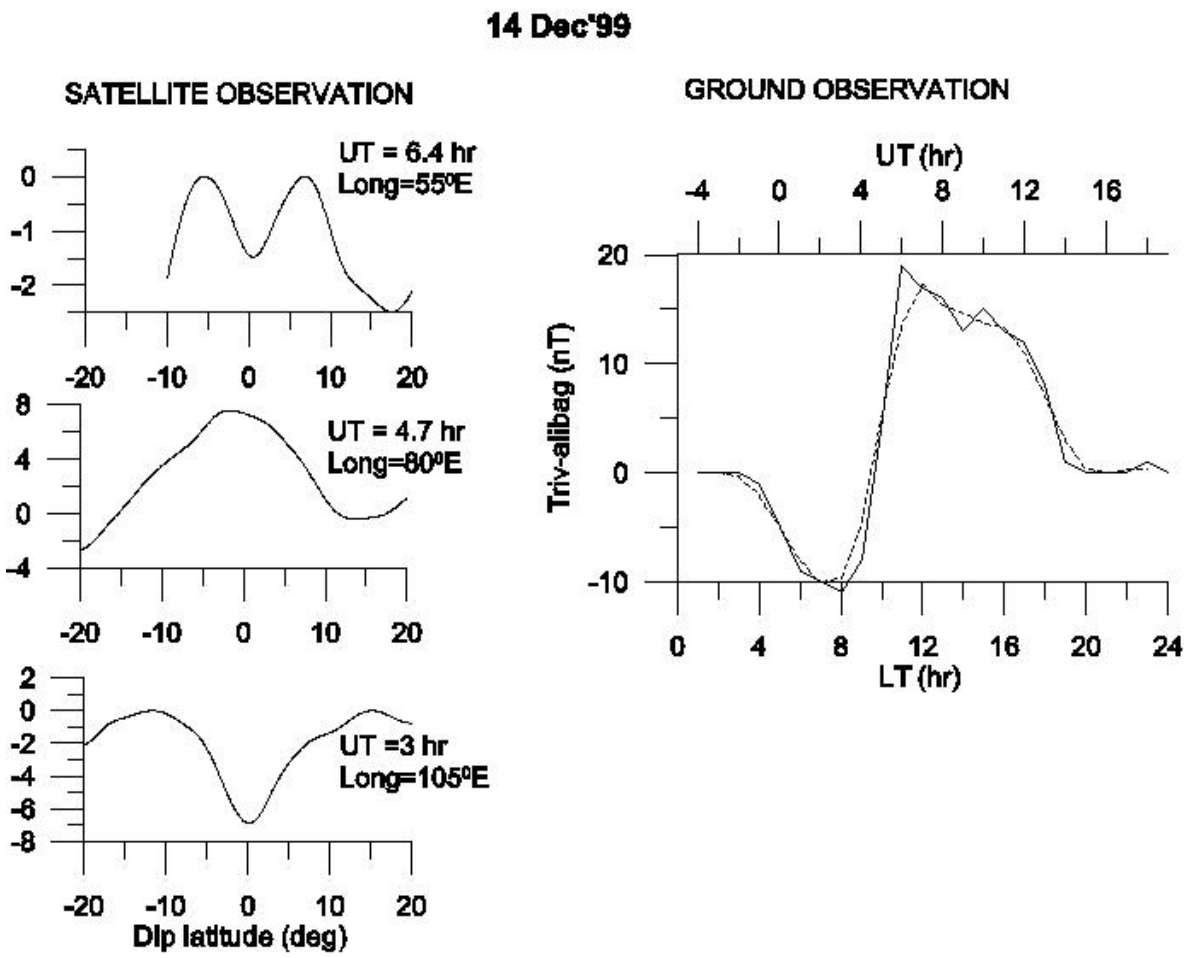

Figure 4.3 : Event on 14 December'99.
Same as Figure (4.2)

Figure 4.4 shows event on 22nd June' 99. Ground data shows clear CEJ signature in the morning (UT= 1 to 3 hr) and afternoon (UT= 10 to 11 hr) hours. Satellite pass at 2 UT shows CEJ, while at 5.5 UT when ground station observes EEJ pattern, shows EEJ signature. But satellite pass at 10.5 UT does not reproduce the CEJ. The LT for this pass is 12.65 hr and that on ground is 15.5 hr. This indicates that the CEJ is confined to less than 3 hours width in longitude. Here, it should be noted that even though the longitudes of satellite pass and ground station do not match, both are showing CEJ effect.

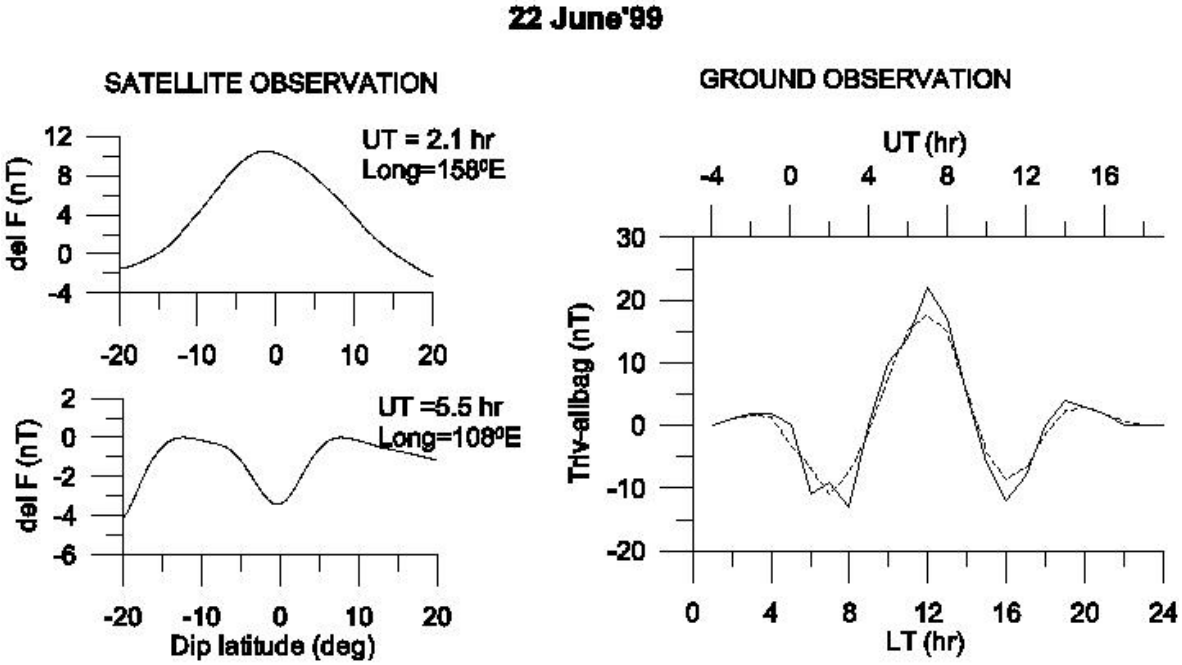

Figure 4.4 : Event on 22 June'99.
Same as figure (4.2)

Other events, on which reverse EEJ signature seen at the satellite is supported by the CEJ of small duration (≥1 hr) observed in the Indian ground station data even though the satellite longitude is far moved from the station longitude. This has been summarized in Table 4.2. The Table includes date, UT of the event, LT, longitude and type of the satellite observation. In the table LT and type of ground observation are also shown. The CEJ events seen by the satellite, which has UT greater than 13 hr, i.e. night hours (≥ 18 hr) at Indian station are not included in the Table. Type ' CEJ' in the ground observation indicates the depression of $\triangle H$ below night level. ' $CEJ_{pre\ hr}$' indicates the presence of CEJ at previous hour. Since we are using hourly averaged values of ground EEJ data, it is possible that the instantaneous negative $\triangle H$ values are averaged out at that hour. '$\triangle H_{norm}$' indicates normal diurnal pattern of EEJ and the ' Depression in H' indicates the presence of some depression on the normal diurnal pattern that does not go below night level. Due to the crude definition of nighttime level and improper removal of Sq, it is not always possible to achieve ideal reproduction of CEJ. Hence we can regard the

depression in H as a tentative indication of westward current, which is not sufficiently strong for the field to go below the nighttime level.

On 21st Jan' 00 between 8 and 13 UT, ground data show some depression in H and satellite passes at 7.4 and 12.3 UT show CEJ. We do not know whether it is an indication of westward current. Thus, except event number 2, we find almost all CEJ events in satellite observations are supported by the ground data. It has been noticed that the CEJ seen by the ground data is not always supported by the satellite data. On 10th August'99, ground data has CEJ at 4 to 6 UT, while satellite pass at that time shows EEJ signature but with a small amplitude.

Table : 4.2

Sr. No.	DATE	UT	SATELLITE			GROUND	
			LT	LONG	TYPE	LT	TYPE
1	13 April' 99	0.53	13.7	172	CEJ	5.53	CEJ
2	15 April' 99	11	13.7	42	CEJ	16	ΔHnorm
3	23 April' 99	2.2	13.55	170	CEJ	7.2	$CEJ_{pre\ hr}$
4	25 April' 99	2.55	13.5	165	CEJ	7.55	$CEJ_{pre\ hr}$
5	22 May' 99	7.86	13.1	79	CEJ	12.86	CEJ
6		9.5	13.1	54	CEJ	14.5	CEJ
7	14 June' 99	9.15	12.76	54	CEJ	14.15	Depression in H
8	22 June' 99	2.12	12.65	158	CEJ	7.12	CEJ
9	14 Dec' 99	4.7	10	80	CEJ	9.7	CEJ
10	21 Jan' 00	0.72	9.4	131	CEJ	5.72	Depression in H
11		7.4	9.4	31	CEJ	12.4	Depression in H
12		12.3	9.4	316	CEJ	17.3	Depression in H
13	17 Feb' 00	12.4	9	308	CEJ	17.4	Depression in H
14	18 Feb' 00	11.8	9	318	CEJ	16.8	Depression in H
15	20 Feb' 00	0.45	9	128	CEJ	5.45	Depression in H

4.4 Statistical Analysis:

As mentioned earlier, for a given day, satellite can have maximum 15 daytime passes at different longitudes, but not all of them provide EEJ signature. In effect, we always have less than 15 passes. Observation shows that on a given day, more than one pass can have CEJ signature. So in the present study, frequency of occurrence of CEJ corresponds to the ratio of total number of passes having CEJ signature to the total number of passes when data were available. We find around 5% of passes show CEJ signature. It should be noted that our statistics does not cover the post noon sector.

4.4.1 Seasonal and Local Time variation of CEJ occurrence Frequency:

Statistical analysis shows that the frequency of occurrence of CEJ varies with seasons. Unfortunately, we do not have observations at constant local time for all 12 months. So, on seasonal variation, local time variation is also sitting. Figure 4.5 shows frequency of CEJ occurrence observed in each month. We see that in the month of January it shows maximum and secondary peak lies in June, July and August. If we plot frequency of CEJ occurrences verses local time (see figure 4.6), it should reflect the information of figure 4.5. We see that afternoon peak (12-13 hr) is larger than morning (9-10 hr) peak. This is because December, January and February months have 9-10 hr local time, whose total CEJ occurrence frequency is less than the months of local time 12- 13 hr. From this, it is certainly clear that even though Jan, Dec and Feb have same local time, Jan peak is distinct. Similarly, for early morning and late afternoon hours we expect the frequency to be large, but we still get 12-13 hr peak which corresponds to June solstice months. This only indicates that the June peak is large and genuine.

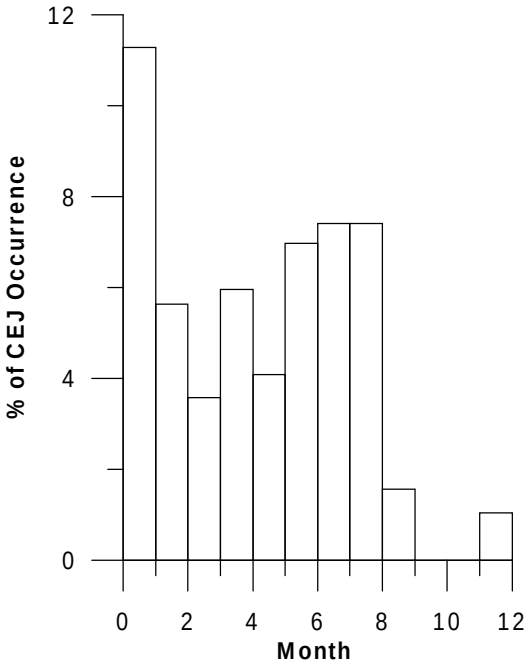

Figure 4.5: Percentage of CEJ Occurrence Vs Month

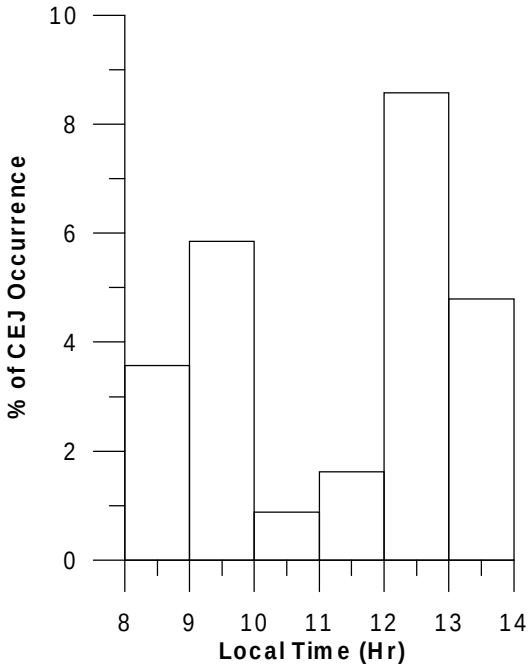

Figure 4.6: Percentage of CEJ Occurrence Vs Local Time

4.4.2 Zonal variation of CEJ occurrence Frequency:

Using satellite data, it is possible to examine the zonal variation of CEJ, which otherwise is very difficult. We observe that in the 300^0 to 330^0E longitude zone the frequency of CEJ occurrence is the maximum (figure 4.7). In the same figure, we have also plotted angle between horizontal magnetic field and dip vector. We see that the magnetic field makes larger angle with horizontal direction in 300^0 to 330^0E longitude zone. Secondary peak lies in the 120^0 to 180^0E longitude zone.

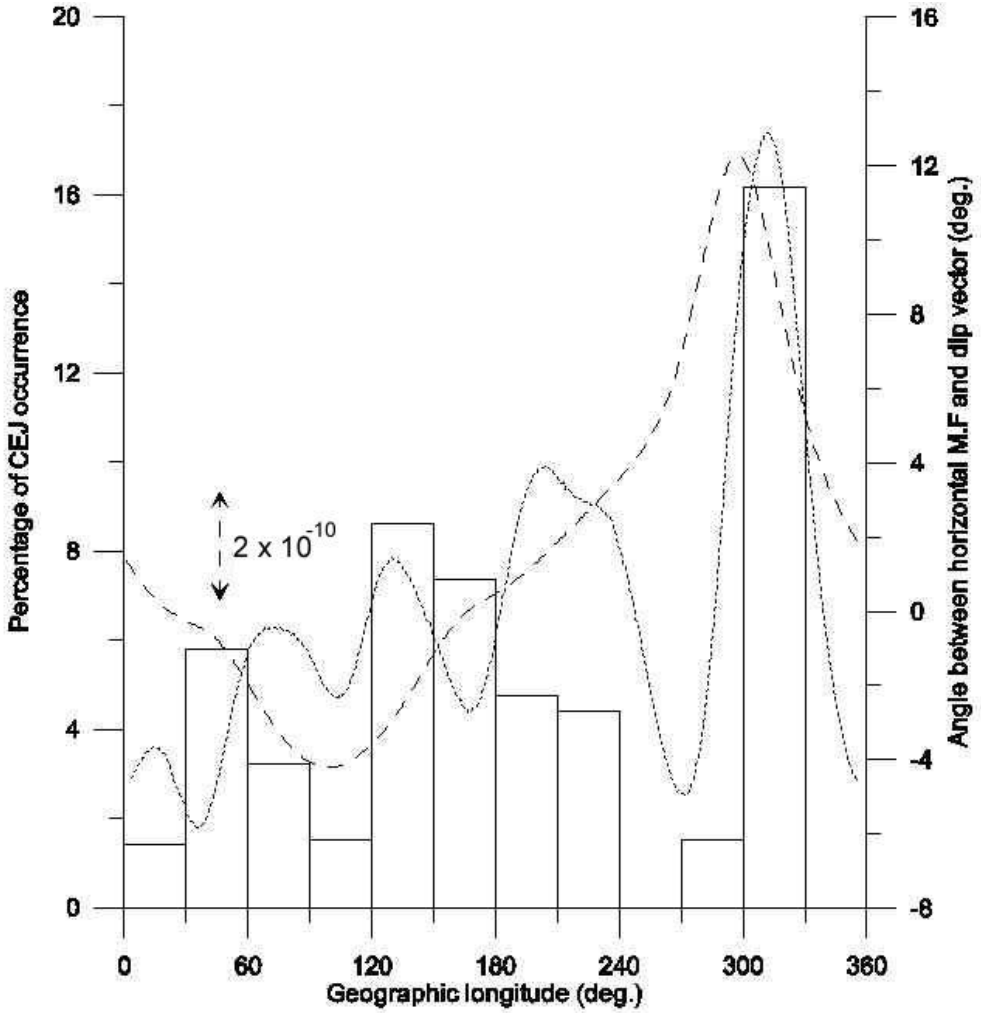

Figure 4.7 : Bar chart shows percentage of CEJ occurence Vs longitude.
Dotted curve shows angle between Horizontal M.F. & Dip vector.
Dashed curve shows B^{-2} i.e. Cowling conductivity curve.
Scale is shown by arrow.

Comparison of this with zonal variation of EEJ strength (figure 4.8) indicates that in the zones where the EEJ strength is large, the frequency of CEJ occurrence is small. This is in agreement with the extensive study of ground data done by Rastogi [1974b].

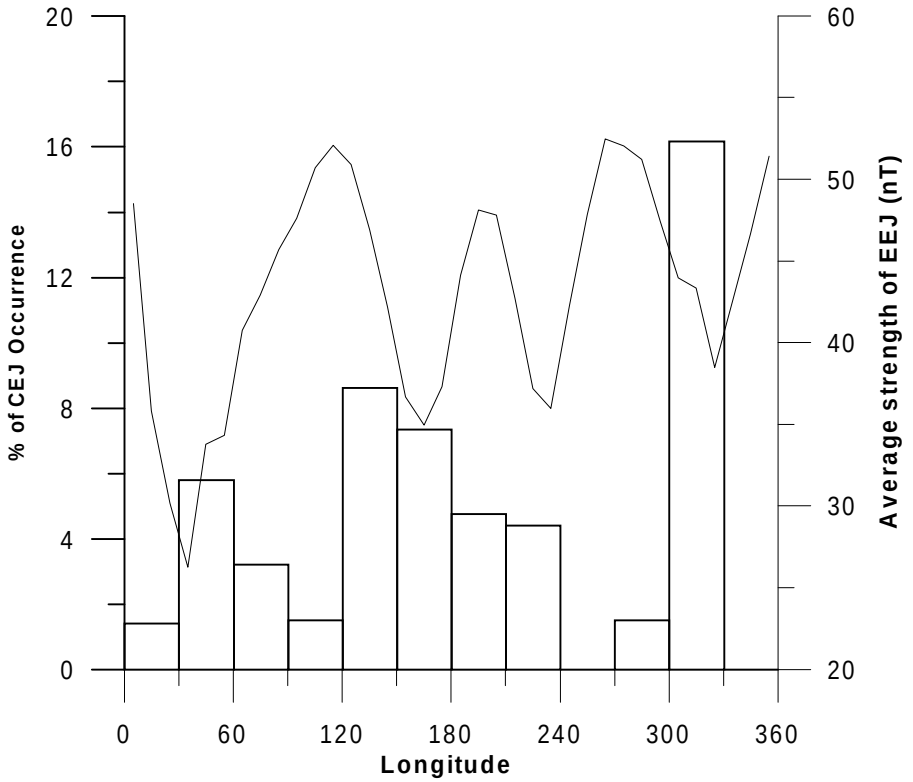

Figure 4.8: Zonal comparison between CEJ Occurrence frequency (bar chart) and EEJ strength (line curve).

4.4.3 Variation of CEJ axis:

CEJ axis or the centre of the CEJ is defined as the dip latitude position characterized by the maximum in the residual field signature seen at satellite altitude. Figure 4.9a shows histogram of dip latitude of CEJ axis, which indicates that the percentage of CEJ occurrence is less when the centre of CEJ is near the dip equator at 106 km. It may suggest that the centre of the westward current system happens to be away from the dip equator at 106-km altitude. Figure 4.9b shows dip latitude of CEJ axis verses longitude, where continuous line curve shows running average. It is almost divided into two hemispheres, one is below 180^0E and other is after 180^0E longitude. In the American sector, it is more north of the dip equator and in the Indian region it is more south of the dip equator. The comparison of this with geographic position of the dip equator shows that when the dip equator is

south of the geographic equator, the CEJ axis is shifted to the north of the dip equator and vice versa.

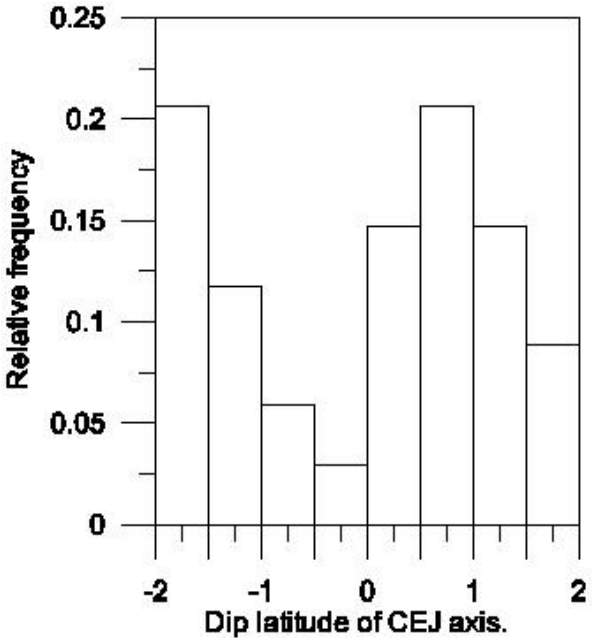

Figure 4.9a : Histogram of CEJ axis position.

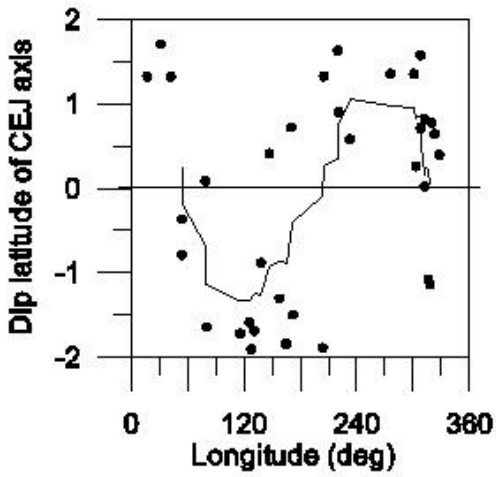

Figure4.9b : Plot of CEJ axis position Vs Longitude.

4.5 Implications for Numerical Modelling:

Our analysis of EEJ structure using Oersted satellite has brought out few important features there are relevant from the point of view of numerical modelling.

(1) Longitudinal Width:

There have been suggestions [Rastogi, 1974a,b] based on ground data that CEJ have probably small longitudinal extent of two hours or less. This has however been referred [Mayaud, 1977] with the counter argument that the limited longitudinal coverage may be responsible for arriving at such conclusions and CEJ as a rule may be 5-8 hours in longitudinal extent. Our satellite-based analysis indicates that the CEJ is never seen beyond two successive passes. The natural conclusion is that at least the pre-noon CEJ has almost always a narrow longitudinal extent consistent with the findings of Rastogi [1974a,b].

(2) The centre of CEJ appears to be shifted away from the dip equator towards the geographic equator in both the hemispheres. There are very few CEJ events centred at the dip equator.
(3) CEJ has a tendency to occur more often in the regions where the EEJ is relatively weak. This is also consistent with the findings of Rastogi[1974a,b].
(4) There is significantly greater probability of CEJ occurrence in the 300^0–330^0E longitude sector, where the direction of the $\overline{\nabla} I$ at the dip equator deviates significantly from the direction of magnetic north.

The first of these strongly suggests the role of non-migrating tides, as the CEJ signature does not appear to move with the sun as expected for the migrating tides. Therefore, any CEJ model should take recourse to non-migrating effects and meteorological and storm time dynamo effects assume greatest importance.
The second and third points suggest the importance of incorporating the geomagnetic field orientation with respect to the geographic axis. Hence the numerical models should not ignore the relative orientation of geographic and geomagnetic coordinate system.
The last point is of very significant importance. We look at it within the simplest of models that consider the variation of inclination with latitude [Untiedt, 1967].

The electric current can be written explicitly in terms of the electric fields parallel and perpendicular to the ambient magnetic field and anisotropic conductivities in the form [Untiedt, 1967],

$$\overline{J} = \sigma_0 \overline{E}_{\parallel} + \sigma_1 \overline{E}_{\perp} + \sigma_2 \frac{\overline{B} \times \overline{E}_{\perp}}{B} \qquad (4.1)$$

where $\overline{E}_{\parallel}$ and $\overline{E}_{\perp}$ are components of the electric field vector parallel and perpendicular to the ambient magnetic field $\overline{B}$ and $\sigma_0, \sigma_1, \sigma_2$ are the parallel, Pedersen and Hall conductivities respectively. The conductivity tensor and the form of the equations are discussed in detail in subsequent chapters.

X direction is chosen along the magnetic field $\overline{B}$ (northward), Y eastward, and Z downward. Untiedt [1967] expressed equation (4.1) in the form of components as

$$J_X = (\sigma_0 C^2 + \sigma_1 S^2) E_X + \sigma_2 S E_Y - (\sigma_0 - \sigma_1) C S E_Z \quad (4.2)$$

$$J_Y = -\sigma_2 S E_X + \sigma_1 E_Y - \sigma_2 C E_Z \quad (4.3)$$

$$J_Z = -(\sigma_0 - \sigma_1) C S E_X + \sigma_2 C E_Y + (\sigma_0 S^2 + \sigma_1 C^2) E_Z \quad (4.4)$$

where *C* and *S* are defined in terms of the inclination '*I*' as,

$C = \cos I$

$S = \sin I$

Sine, we are interested in a narrow belt around $I = 0$,

$\Rightarrow \quad C \sim 1.0, \qquad S \sim I$

Thus current equations can be re-expressed as

$$J_X = \sigma_0 E_X + \sigma_2 I E_Y - (\sigma_0 - \sigma_1) I E_Z \quad (4.5)$$

$$J_Y = -\sigma_2 I E_X + \sigma_1 E_Y - \sigma_2 E_Z \quad (4.6)$$

$$J_Z = -(\sigma_0 - \sigma_1) I E_X + \sigma_2 E_Y + \sigma_1 E_Z \quad (4.7)$$

Using the above equations, the electric field components can be expressed as

$$E_X = \rho_0 J_X + (\rho_1 - \rho_0) I J_Z - \frac{\sigma_2}{\sigma_1} I E_Y \quad (4.8)$$

$$E_Z = (\rho_1 - \rho_0) I J_X + \rho_1 J_Z - \frac{\sigma_2}{\sigma_1} E_Y \quad (4.9)$$

where $\rho_1 = \frac{1}{\sigma_1}$ and $\rho_0 = \frac{1}{\sigma_0}$

Substitution of equation (4.8) and (4.9) into (4.6) gives,

$$J_y = \left(\sigma_1 + \frac{\sigma_2^2}{\sigma_1}\right) E_Y - I \frac{\sigma_2}{\sigma_1} J_X - \frac{\sigma_2}{\sigma_1} J_Z \quad (4.10)$$

At the dip equator, $I = 0$,

$$\therefore \qquad J_y = \left(\sigma_1 + \frac{\sigma_2^2}{\sigma_1}\right) E_Y - \frac{\sigma_2}{\sigma_1} J_Z \quad (4.11)$$

We note that even if J_X is not zero at the dip equator, it does not affect the current at dip, because $I = 0$.

However, we have the requirement that $\nabla \cdot \bar{J} = 0$

Untiedt' s formalism defines a current function ψ such that

$$J_Z = \frac{\partial \psi}{\partial Z} \quad \text{and} \quad J_Y = -\frac{\partial \psi}{\partial Y}$$

This defines a closed solenoidal current loop and requires that

$$\frac{\partial J_Y}{\partial Y} = 0$$

We can assume inclination as $I = \alpha[X - X_d(Y)]$,

where $X_d(Y)$ denotes the *X*-coordinate of the dip equator. It is generally assumed that X_d is independent of Y. That is tantamount to assuming that the gradient of *I* is along the ambient magnetic field. If it is not so then we note that the line along which the dip is zero (which is the region of largest Cowling conductivity) is not perpendicular to the magnetic field direction.

For simplicity, we can take $X_d = \beta y$, where we measure a distance from a point where the dip equator coincides with $X = 0$. If we assume J_X and J_Z do not vary significantly with Y then, $\frac{\partial J_Y}{\partial Y} = 0$ will yield

$$\sigma_3 \frac{\partial E_Y}{\partial Y} = -\alpha\beta \frac{\sigma_2}{\sigma_1} J_X$$

$$\frac{\partial E_Y}{\partial Y} = -\left(\frac{\alpha\beta\sigma_2}{\sigma_3\sigma_1} \right) J_X \tag{4.12}$$

$$E_Y \approx E_Y(0) - Y\left(\frac{\alpha\beta\sigma_2}{\sigma_3\sigma_1} \right) J_X \tag{4.13}$$

This implies that the parallel current, J_X will change J_Y through E_Y.

Note that we expect the EEJ current flow along the dip equator and since this line is not perpendicular to the magnetic field, it will generate a field aligned current (J_X) which will produce a gradient in J_Y along Y.

In principle this can lead to reversal but more comprehensive analysis needs to be carried out.

4.6 Summery and Discussions:

In the present chapter, we have studied reverse EEJ signature seen in the Oersted satellite data for the epoch April'1999 to March'2000. We have shown that the reverse EEJ signature at satellite indicates the counter electrojet. This has been achieved by examining the data simultaneously at satellite and ground. Events shown in figure 4.2, 4.3 and 4.4 show good agreement between satellite and ground observations. CEJ events seen by satellite, taking place after 13 UT, are not observed in the Indian station ground data, due to nighttime. For the events between 0 to 13 UT, we get a good correlation between satellite and ground observations.

We find that whenever, the satellite is in the longitude belt of the ground station observing the CEJ, the satellite also sees the CEJ. However, the satellite does not see the CEJ if satellite and ground differ in longitude by 30^0 or more. It is seen that the CEJ is never seen beyond two successive passes. This suggests that the longitudinal width is not more than 3 hours, at least for the pre-noon CEJ. This result of narrow longitudinal extent is consistent with the findings of Rastogi [1974a]. This gives different insight into the longitudinal variation of the CEJ occurrence on a given day.

Statistical study of the centre of the westward current system shows that it is not exactly at the dip equator but slightly off the dip equator. This can give rise the current flow across the dip equator, which also had been seen by the earlier ground observations [Fambitakoye 1990]. The longitudinal variation of the centre of the CEJ current system depicts that, the centre lies south of the dip equator for Indian sector and north of the dip equator of American sector. This shows that the

centre of CEJ appears to be shifted away from the dip equator towards the geographic equator in both the hemispheres.

It is also seen that there is significantly greater probability of CEJ occurrence in the 300^0–330^0E longitude sector, where the departure of magnetic field from the horizontal plane at dip equator is maximum.

All these aspects of the investigation indicate need to be incorporated in the numerical model of CEJ. For migrating tide, we expect the CEJ signature to follow the sun, but in our analysis CEJ does not appear to move with the sun, this indicates the importance of the role of non-migrating tides. Therefore, any CEJ model should take recourse to include the non-migrating effects. The asymmetry of geomagnetic equator with respect to geographic equator also needs to be included in the model. The most important feature that comes out from the analysis is the necessity to model the anomaly seen in the 300^0–330^0E longitude zone. Here, we have put forward the layout of the model, which could account for the anomaly associated with the large deviation of dip equator vector from the magnetic north direction. Further detailed analysis is required in this regard, in order to improve the future modelling and understanding of the counter electrojet phenomenon.

Rastogi [1974b] studied CEJ at all available observatories and highlighted few characteristics of it. It states that the percentage of occurrence of CEJ is the maximum in the morning (7 hr) and afternoon (14 hr) hours and during minimum solar activity. In our analysis, even though the seasonal variation is sitting on the local time variation, figure (4.6) is quite consistent with his findings. Bhargava and Sastri [1979] found that for the afternoon CEJ, primary peak of occurrence lies around June and secondary peak lies in January. For the present data set, even though local time variation is sitting on seasonal variation of CEJ occurrence frequency, we get peaks in the month of January and June. January peak is larger

than that of June that could be due to the difference in local times in two months. For early morning and late afternoon times we expect the frequency to be maximum, but our results show it peaks at 9-10 LT and 12-13 LT hours, which are in January and June month respectively. Thus our results are consistent with the June and January peak observed in the earlier investigations.

During particular epoch, the largest occurrence was observed at a station experiencing the weakest normal EEJ current e.g. Indian sector. These features were later confirmed by Marriott et al. [1979]. Figure (4.8) is in agreement with these results.

The geomagnetic activity has been found to respond to the changes in the interplanetary plasma parameters such as the speed of the plasma, magnetic field embedded in it, proton density etc. Among them, the interplanetary magnetic field (IMF) is most effective in controlling the seasonal as well as diurnal variation of the magnetic disturbance. Many workers have tried to get correlation between changes in equatorial electric fields and IMF. Fejer et al. [1979] found that east-west component of the IMF appears to be unimportant, but the north-south component has some effect; rapid reversals from south to north are sometimes correlated with reversals of the equatorial east-west electric field during both daytime and nighttime. Kane [1978] compared CEJ events (both morning and afternoon) with IMF data. His results show that around 33% events are correlated with the reversal of B_Z , but in other cases he did not find any such relation.

On the same line of thought, we tried to make a comparative study of B_Z component of IMF field and CEJ as observed by Oersted, but unfortunately it was not possible due to non availability of B_Z data at most of the times of studied events. For few cases when data were available, we found 50% events are associated with reversal of B_Z . We tried to see its correlation with solar wind

speed and ion density. But did not find any sensible dependence. We also tried to see the dependence of CEJ on IMF polarity. For the available polarity data, we find CEJ is associated with away polarity. Fambitakoye et al. [1990] have studied the global pattern of the magnetic effects of the disturbed ionospheric dynamo resulting from the storm and showed that the pattern corresponds to CEJ effect at the equatorial latitudes at ground stations and strong meridian current flow across the equator. Blanc and Richmond [1980] provided evidence for disturbed ionospheric dynamo process through numerical simulation. However, this numerical simulation assumed the complete closing of the currents through EEJ apriori located between 10^0N and 10^0S in latitude, and therefore it could not account for the current flow across the dip equator. Thus for the better understanding of CEJ mechanism, further extensive study of reverse signature at satellite and ground data from all available zones is required.

Thus our study strongly emphasizes the importance of satellite data in studying the longitudinal variation of the CEJ.

Chapter 5
Study of short period fluctuations

The ionosphere, in general and the equatorial electrojet in particular are known to respond to short period fluctuations and produces significant changes in their amplitudes. Equatorial enhancement of short period variations should be an important part of any effort to model the EEJ. From the observational viewpoint, extensive work has been carried out on amplitude modulation, but very little on phase changes introduced in these fluctuations. Analysis presented in this chapter attempts to look into this aspect.

This chapter deals with the ionospheric modulation of compressible hydromagnetic waves, in the frequency range of 10-80 mHz (Pc3-4), which has been examined using the scalar magnetic field data obtained from the Oersted satellite and ground magnetic data from the Japanese sector. It also studies the pulsation of frequency range 1-4 mHz (Pc5-6) using equatorial chain of magnetic observatories in the West African region.

5.1 Ionospheric modulation of compressible hydomagnetic waves (10-80 mHz):

5.1.1 Introduction

Geomagnetic pulsations, in the period range of 1 to 1000 mHz are manifestations of hydromagnetic waves generated through a combination of mechanical and electromagnetic forces. They originate mainly in the magnetosphere but are observed both on the surface of the earth and at satellite altitudes at various radial distances. Recently, there has been an increased interest in the study of compressional waves in the 10 to 100 mHz frequency range making up the Pc3-4 and Pi2 pulsation [Kim and Takahashi, 1999; Kim et al., 1998]. These investigations have utilized satellite and ground data to identify cavity wave oscillations from the amplitude and phase relations between the satellite and surface measurements. An uncertainty in estimating the extent of modifications introduced by the ionosphere can come in the way of an unambiguous identification. We therefore examine, in the present study, the amplitude and phase

changes introduced by the ionosphere on compressional hydromagnetic waves passing through it. A combination of ground based geomagnetic data from the low latitude Japanese sector and the data from the Oersted satellite has been utilized in the analysis.

Since Oersted is a polar orbiting satellite, it spans all latitudes, which allows us to study the latitudinal variation associated with the hydromagnetic wave. An orbital period of approximately 100 minutes implies that temporal variations with periods well in excess of one minute or so cannot be unambiguously identified because the spatial variations associated with quiet day ionospheric currents, including the equatorial electrojet, can masquerade as temporal variations in the satellite data. The study has, therefore, been restricted to frequencies in excess of 10 mHz.

Ground based support is provided by the data from the Japanese stations of Kanoya (KAN; Co-ordinates: Geographic 31^0 25' N, 130^0 52' E; Geomagnetic 21.4^0N, 200.3^0E), Kakioka (KAK; Co-ordinates: Geographic 36^0 13' N, 140^0 11' E; Geomagnetic 26.9^0N, 208.3^0E) and Memambetsu (MEM; Co-ordinates: Geographic $43^0$54' N, $144^0$11' E; Geomagnetic 34.9^0N, 210.8^0E). Kanoya being closest to the equator is probably best suited to the study of compressible modes. The component field data from these stations have sampling rates of 1 second and a resolution of 0.01 nT. The scalar magnetic field values used in the analysis are calculated from vector data provided by the fluxgate magnetometers at the geomagnetic observatories.

The present study examines specific periods that are characterized by the presence of oscillations (within the frequencies of interest) both in satellite and in ground data. Both day and nighttime events have been examined. The daytime events scan pre-noon and noon sectors.

5.1.2 Data Selection and Treatment:

The analysis is restricted to satellite passes in the geographic longitude zone between 125^0 E and 155^0 E to minimize any complexities that may arise in the data interpretation

because of large differences between satellite and ground station longitudes. This often decides the range of geomagnetic latitudes for which the data is acceptable for a given orbit.

The background field has first to be subtracted form the observed field values at each satellite point. The special reference field model, IGRF(10c/99), based on the Oersted data [Olson and Sabaka, 1999] is used here. The model includes internal main field coefficients to the order 13, secular changes to the order 8 and corrections for external fields derived from Dst values. It has been accepted as the IGRF (International Geomagnetic Reference Field) model for epoch 2000. The RMS error of the departures from the observed quiet time fields at satellite orbits is around 3 nT for latitudes within 50^{o} of the geomagnetic equator. The total field is computed from the model using hourly Dst values for external field corrections and subtracted from the satellite scalar magnetic field (F) to get the residual scalar magnetic field ($\bullet$F) data that forms the basic time series in our analysis.

Plots of the satellite field (with IGRF model field subtracted out) and the corresponding ground station values were generated. The plots showed fairly clear signature of oscillations in both the satellite and ground data for all the events considered. A typical plot of the unfiltered satellite residual field and Kanoya magnetic field variations for the pass on November 11, 1999 pass (a) are presented in figure 5.1 with the current geomagnetic latitude of the satellite shown on the top axis. The plots show clear oscillations in both the fields that are closely related. This establishes the quality and suitability of the data for the present analysis.

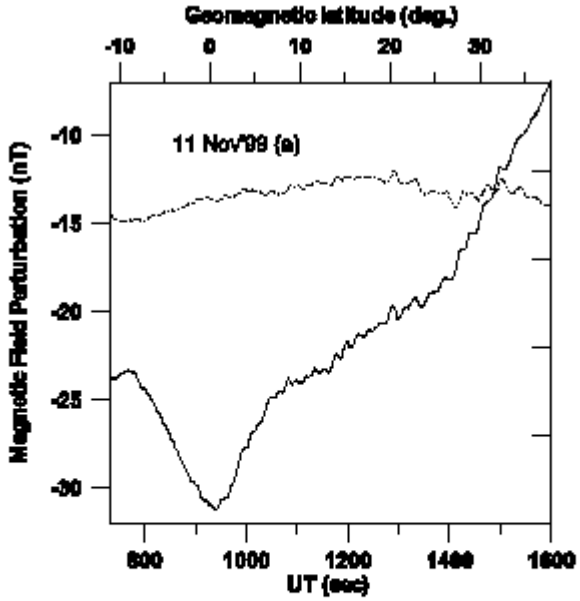

Figure 5.1: Plot of the unfiltered satellite scalar field (△F) variations (full lines) for a single pass. The corresponding field variations at Kanoya (baseline arbitrary) multiplied by a factor of 1.5 are also shown (dashed lines).

A total of around 60 days of satellite scalar data were similarly examined out of which around 25% of passes exhibited oscillations in the selected longitude zone. The set selected for the present study includes two nighttime passes and six daytime passes. The details for each of the selected passes (date, universal time (UT), local time (LT), geomagnetic latitude and geographic longitude) are given in Table 5.1.

In the next step, to remove long period trends and high frequency noise, the time series of the satellite and the three ground stations was passed through a band pass filter that allowed only 10 to 100 mHz oscillations. The filtered time series for the satellite and three ground stations consisting of 1024 points for each pass are used for further analysis.

Table : 5.1

Date	UT Range (Hr : Min)	Local Time Range (Hr : Min)	Geomagnetic Latitude Range (Deg)	Geographic Longitude Range (Deg)
14 March' 99	16:13 – 16:30	26:25 – 25:53	+24.47 to -39.18	153 - 141
5 April' 99(a)	16:33 – 16:50	26:05 – 25:34	+23.18 to -39.60	143 - 131
3 April' 99	03:45 – 04:02	14:03 – 13:33	-31.96 to +26.14	155 - 143
5 April' 99(b)	04:05 – 04:22	14:01 – 13:31	-32.49 to +26.03	149 - 137
1 May' 99	03:23 – 03:40	13:41 – 13:10	-37.35 to +23.04	155 - 142
2 Nov' 99	01:08 – 01:26	10:52 – 10:22	-35.27 to +22.54	146 - 134
11 Nov' 99 (a)	00:12 – 00:29	10:32 – 09:52	-10.97 to +46.86	155 - 141
11 Nov' 99 (b)	01:43 – 02:00	10:50 – 10:20	-46.14 to +12.23	137 - 125

5.1.3 Coherence and Cross Phase

In order to establish the coherence of the oscillations at the satellite and ground stations, the resultant data is subjected to an analysis similar to the one adopted by Kim and Takahashi [1999]. This involves obtaining the power spectral density for the satellite and the three ground stations and also the cross-spectral analysis of the data [Robinson,1983] to obtain the coherence and the phase relations between the satellite and each of the ground station time series. Identical analysis was performed for each of the passes listed in Table 5.1 using time series of 1024 points for each of the series. Frequency peaks that could be clearly identified and showed significant coherence between satellite and ground data are listed for all the events in Table 5.2. Barring a few exceptions coherence is greater than 0.9 for all the peaks.

Table : 5.2

DATE	PEAK FREQ. (mHz)	BAND WIDTH (mHz)
14 March' 99	26.3	25.3-27.0
	17.5	16.7-17.5
5 April' 99	29.0	28.2-30.3
	24.4	22.2-25.6
3 April' 99	48.8	45.4-50.0
5 April' 99	27.0	25.6-28.6
1 May' 99	43.5	40.0-50.0
	37.0	36.4-40.0
	32.3	31.2-33.3
	25.0	24.4-26.3
2 Nov' 99	40.0	38.5-41.7
11 Nov' 99 (a)	66.7	58.8-71.4
	52.6	50.0-58.8
	44.4	41.7-47.6
	32.8	31.2-33.3
	28.6	25.6-29.8
	23.2	22.7-24.4
11 Nov' 99 (b)	51.3	50.0-55.5
	26.3	25.3-27.0
	13.7	12.8-14.3

We display in figure 5.2 results for one nighttime event and two daytime events representing different local time conditions. The left panel corresponds to nighttime, the middle panel represents the afternoon (LT 13-14 Hrs.) conditions while the right panel corresponds to forenoon (LT 10-11 Hrs.). The ionospheric conductivity, which depends on the solar zenith angle, is much greater in the afternoon sector. The upper panel of figure 5.2 depicts the power spectral density (PSD) at the satellite height and the corresponding PSD at the three ground stations. Comparison of the spectra reveals that a number of peaks are common. The relationship between the spectra is brought out by the coherence between the signals at the satellite and the three ground stations at various frequencies depicted in the middle panel. The coherence at the well-defined common peaks is better than 0.9.

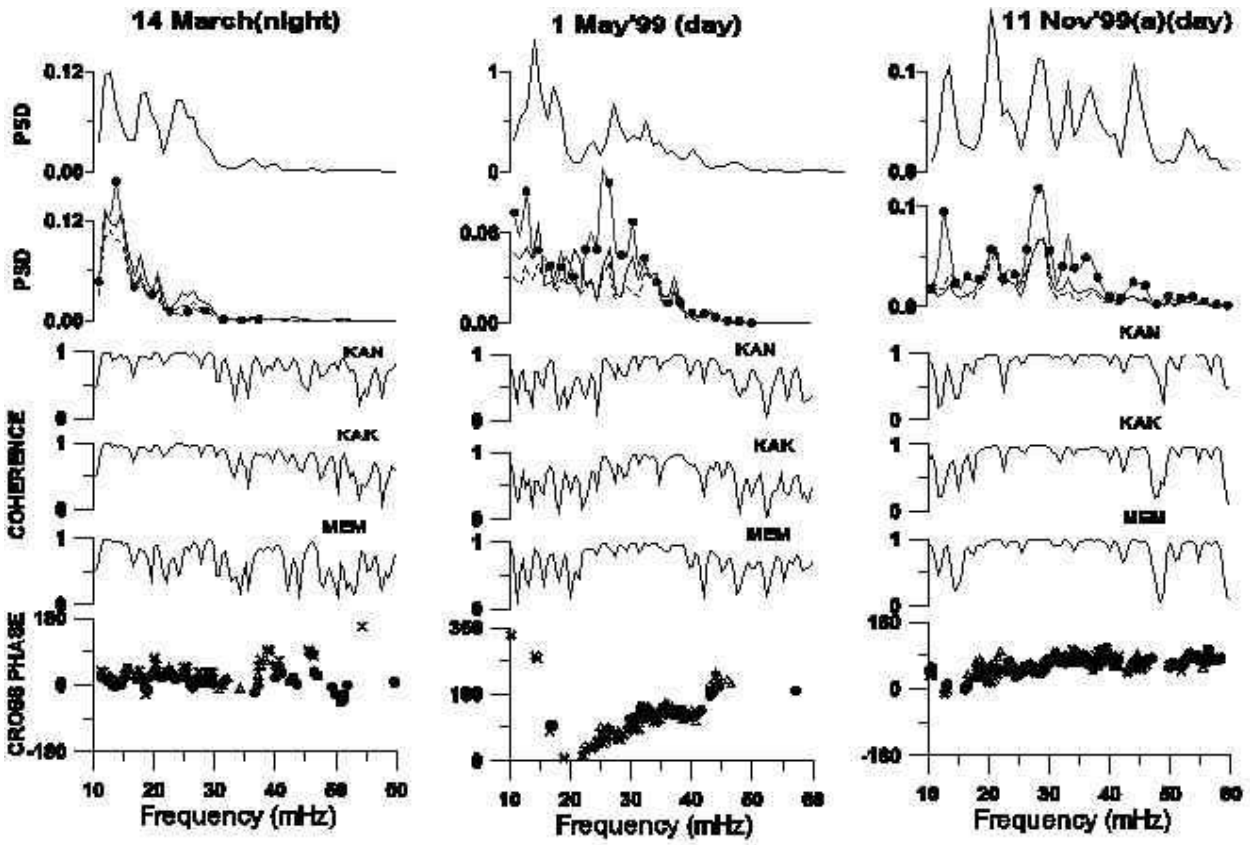

Figure 5.2 : Spectral power density (PSD) for satellite, Kanoya (—), Kakioka (- -), Memambetsu (–▲–) and coherence with satellite oscillations for each of the ground stations. Cross phase for Kanoya (●), Kakioka (△) and Memambetsu (×) are depicted when coherence with satellite oscillations is greater than 0.85. These are for night, afternoon and forenoon passes.

The lower panel shows the cross-phase or the phase difference between the satellite and ground signals at the three stations. The phases are represented by discrete symbols characteristic for each station when coherence exceeds 0.8 for that particular frequency. The cross-phase information is very revealing. It clearly shows that the satellite and ground oscillations are in phase during the night conditions. The results are very consistent for Kanoya (•) and Kakioka (Δ) while Memambetsu (x) shows considerable scatter at high frequencies in the region where there are no significant peaks in the satellite or ground spectra. The phase lag is close to zero even in the daytime at very

low frequencies but the phase lag increases with frequency. The rise is much steeper in the afternoon than in the forenoon hours. The phase lag thus increases with frequency as well as the conductivity of the ionospheric medium it is passing through. This feature is consistently brought out by the cross-phases at all the three ground stations.

5.1.4 Time and Latitudinal Structure:

The analysis carried out establishes the cross-phases in an elegant way but it does not provide any information on the time and latitudinal structure of the pulses associated with the peaks determined by the spectral analysis. This is achieved through band pass filtering.

We use the 1024 point time series generated for each the passes and pass it through a band pass filter centered at the each of the peaks listed in Table 5.2. The width of the band pass used for the filtering process is also listed against each frequency peak in the table.

Figure 5.3 gives the resultant time variations at satellite and at Kanoya for two nighttime and two daytime events. The figures show that hydromagnetic oscillations occur in bursts, which occur almost simultaneously at ground and satellite heights. In the nighttime events the pulses at the satellite and ground have about the same amplitude but during the day the amplitude of the pulses at the satellite heights are significantly larger especially at the lower latitudes.

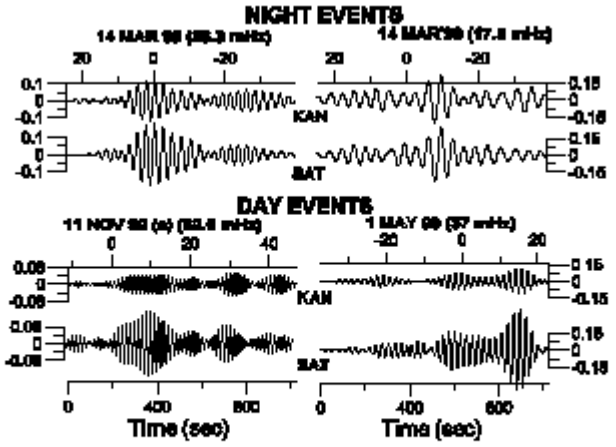

Figure 5.3. Examples of filtered time series for specific passes. These are for night and daytime passes.

While it appears quite obvious from the figure that the same source of oscillations are seen at the two heights, it is possible to get a quantitative confirmation by taking the correlation between the satellite and ground time series at various time lags. There are standard test for testing the significance for the level of correlation obtained [Fisher, 1970] and it is always better than 99.9% in all the cases. In fact in the majority of cases the correlation is in the region of 0.8 to 0.9 and with over 1000 points used, the level of confidence is quite close to certainty.

The time lag required for the maximum cross correlation gives another estimate of the phase delay because it indicates how much the filtered ground data has to be shifted backward in time to get the best correlation with the corresponding satellite data. In figure 5.4, we show the comparison between the phase delay obtained from the cross correlation analysis with the corresponding phases obtained from the coherence analysis described in section 5.1.3. The figure includes the phases computed for all the stations at all the peaks listed in Table 5.2. The plot shows that the phase delay obtained by the two methods are always very close. This increases our confidence in our result.

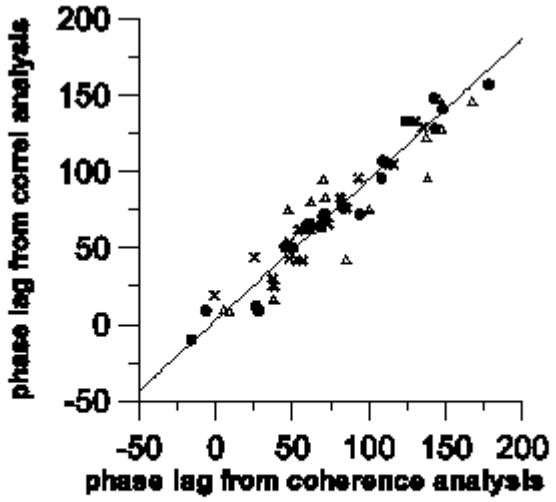

Figure 5. 4. Comparison of phase lags from coherence and correlation of filtered time series for all peaks inTable 5.2 . Symbols have the same meaning as in figure 5.2.

We show, in figure 5.5, the phase delays at Kanoya as a function of frequency, for all passes analyzed. The plot reaffirms the conclusions obtained from just one nighttime and two daytime passes depicted in figure 5.2. The nighttime (Δ) ionosphere does not introduce any phase delay while during the day (•,), a phase delay is produced by the ionosphere. This phase delay increases with frequency and also with the conductivity of the ionosphere.

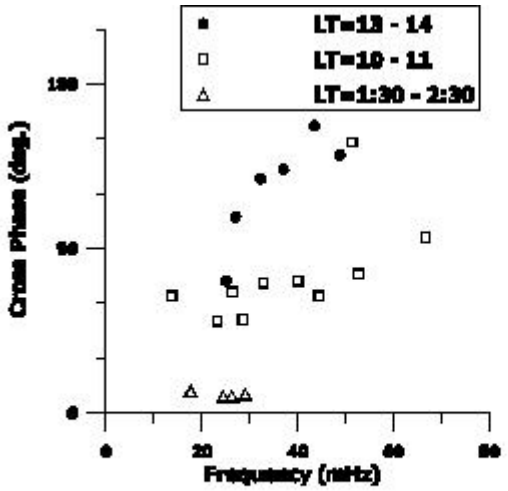

Figure 5.5 : Phase lags as a function of frequency of the oscillations for all the peaks in Table 5.2.

We noted from figure 5.3 that the amplitude of the pulses at the satellite is larger than the corresponding amplitudes on ground during the day lit hours. In order to determine whether it is universally true, we plot in figure 5.6 a histogram depicting the percentage of daytime events (each event corresponds to a single filtered time series) showing enhanced amplitudes in each of latitude bins marked out in the figure. For the purpose of the present classification, if the satellite amplitude is more than 1.5 times the observed value on ground, we consider it as a case of enhancement. The ground station exhibiting the best correlation with the satellite for the event is taken as the reference.

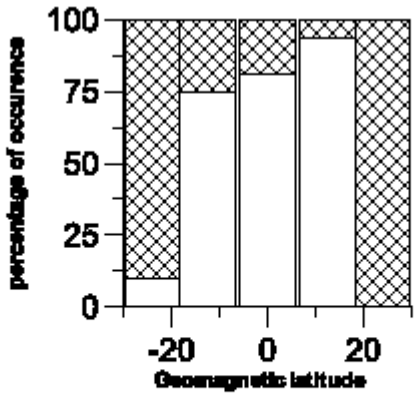

Figure 5.6. Histogram depicting Percentage of events showing amplitude enhancement (>1.5) in each latitude bin (hatched is no enhancement).

It is quite clear from the histogram in figure 5.6 that the satellite amplitude is enhanced within $\pm 20^{o}$ of the dip equator while outside this region the satellite and ground amplitudes are nearly same. The ground station is fixed and the observed amplitude cannot in any way depend on the position of the satellite. This enhancement could be a result of partial screening of the wave due to the enhanced conductivity associated with the equatorial electrojet region. Screening generates a weak image current that reduces the field below the ionosphere but in the process enhances the field above.

Unfortunately no suitable ground station was available in the electrojet region to verify this.

5.2 Study of Pc5-6 oscillation during IEEY:

5.2.1 Data and Method of Analysis:

Comparison of satellite and ground data showed that dayside ionosphere introduces phase shifts in the in coming wave. We expect that the EEJ region should experience a longer phase shifts; a conjecture that could not be verified as we did not have any ground data in the equatorial region.

We try to examine this possibility using a ground array across the EEJ. However, we could acquire data at one-minute sampling interval and therefore, the study looks at a different frequency regime.

During International Equatorial Electrojet Year (IEEY) 1993, 10 geomagnetic observatories, covering dip latitudes from 6^0 N to 6^0 S were set up in the West African region, which are listed in Table 5.3.

Table : 5.3

Sr. No.	Station	Station Code	Latitude (^{0}N)	Dip-latitude (^{0}N)	Longitude (^{0}W)
1	Tombouctou	TOM	16.733	5.513	3.0
2	Mopti	MOP	14.508	3.288	4.087
3	San	SAN	13.237	2.017	4.879
4	Koutiala	KOU	12.356	1.136	5.448
5	**Sikasso**	**SIK**	**11.344**	**0.124**	**5.706**
6	Nielle	NIE	10.203	-1.017	5.636
7	Korhogo	KOR	9.336	-1.884	5.427
8	Katiola	KAT	8.183	-3.037	5.044
9	Tiebissou	TIE	7.218	-4.003	5.241
10	Lamto	LAM	6.233	-4.988	5.017

It is seen from the table that all the observatories are sitting in a very narrow belt of longitude of width 2-3^0. Hence this set can be considered as the ideal for the study of latitudinal propagation of oscillations. Sikasso (SIK) is very close to dip equator (~0.12^0 dip) and can be considered as the dip equatorial station in the present study. We

examine the amplitude enhancement and phase shifts introduced by the highly conducting region responsible for the EEJ.

Table : 5.4

Date	Ap
5th April'93	87
9th May'93	48
4th June'93	54

Enhancement or the cross phases at off-equatorial stations are computed with respect to SIK. We have performed the analysis for the most disturbed days of the month. Here, we shall be presenting results for three days, which are listed in Table 5.4, along with the corresponding Ap indices. The analysis has been performed for H as well as D component. The one-minute of data interval puts a restriction on the frequency range to be studied. The raw data plots for H and D components on 5th April'1993 is shown in figure 5.7. It is seen that the day is highly disturbed and normal diurnal pattern vanishes. The figure shows clearly that the signature of the pulsations is present at all stations.

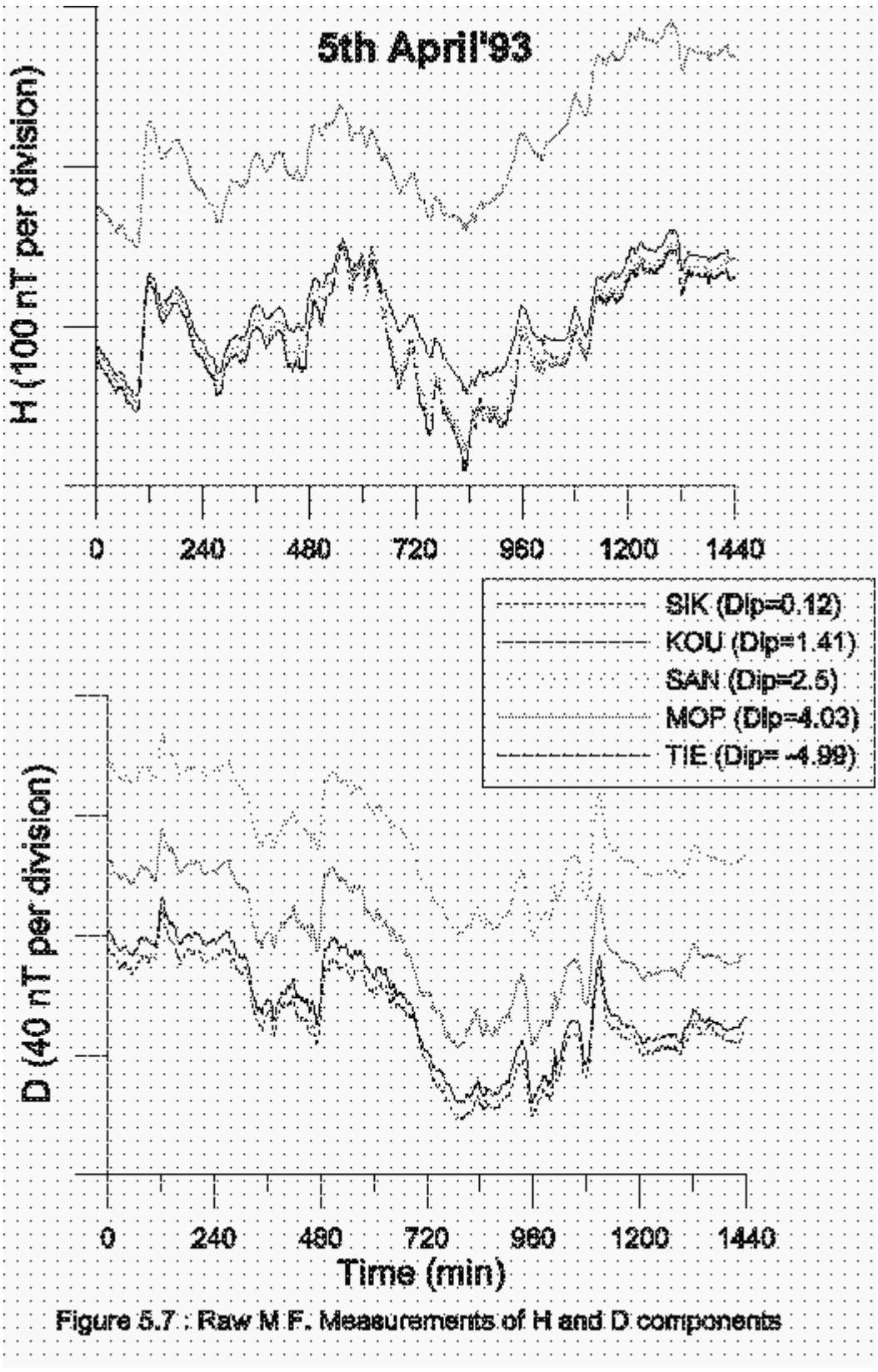

Figure 5.7 : Raw M.F. Measurements of H and D components

In order to study the local time dependence, we have divided each day into two-two hours intervals. Each two-hour data has been passed through band pass filter for 0.4 to 4 mHz oscillations. The power spectrum of H component on 5th April'93 is depicted in figure 5.8. The curve shown by dotted lines represents equatorial station (SIK). It is clearly seen from these plots that during daytime the power at SIK is largest, indicating the ionospheric enhancement at the dip equator. Similar plot for D component is shown in figure 5.9, which does not clearly indicate the daytime equatorial enhancement.

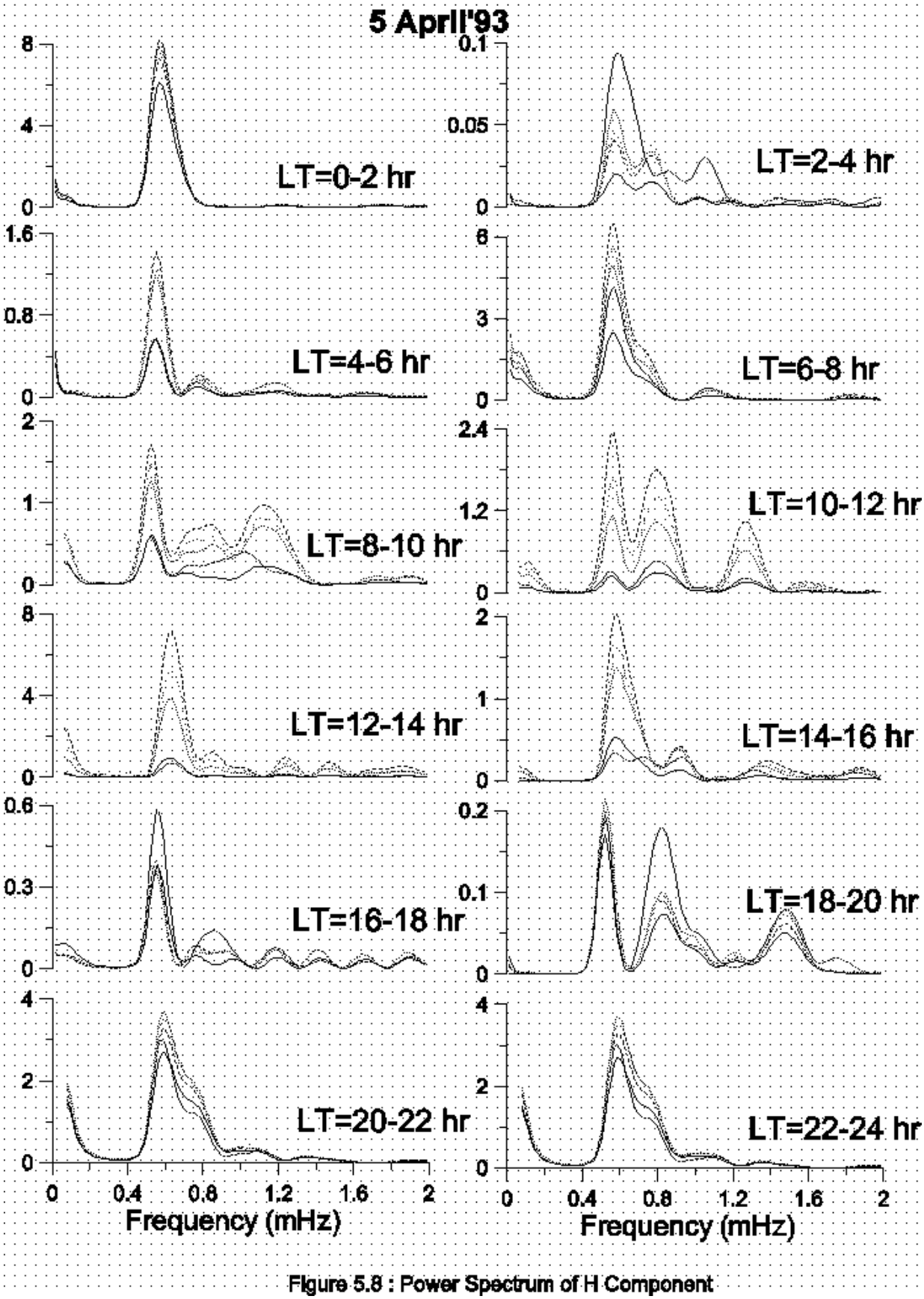

Figure 5.8 : Power Spectrum of H Component

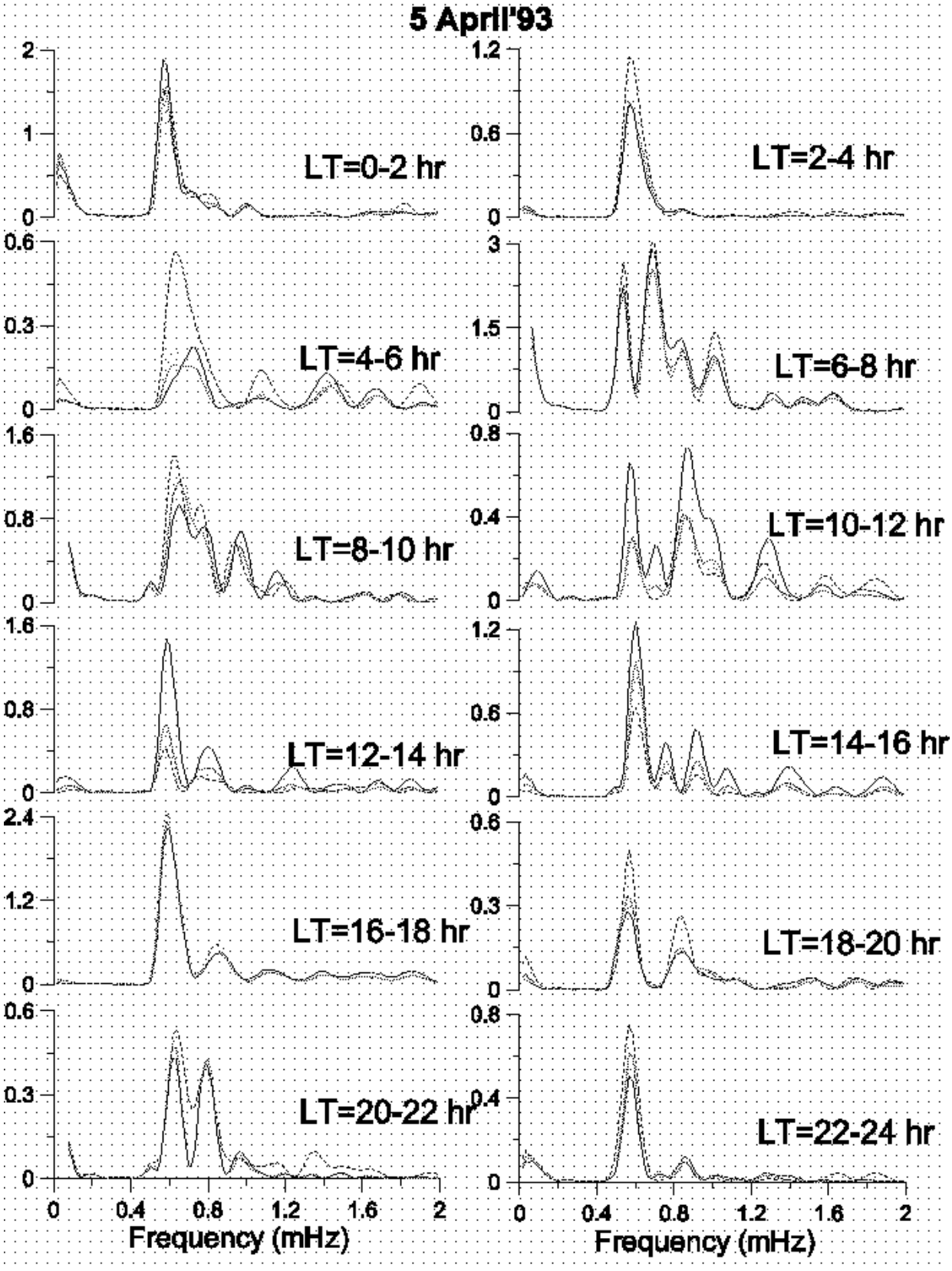

Figure 5.9 : Power Spectrum of D Component

5.2.2 Local time dependence of average enhancement:

The next task is to quantify the enhancement. Traditionally we define enhancement as the ratio of power at equatorial station to off-equatorial station. Average of this enhancement, putting all the frequencies together at different local times for different days yield the pattern shown in figure 5.10. Left-hand side plots are for H component while D component is shown on right hand side. It is seen that H component does show daytime enhancement but it does not peak at local noon, whereas D component does not follow any particular pattern. Here we have performed coherence analysis and only those frequencies are considered for averaging, at which coherence between equatorial and off-equatorial station is greater than 0.8. There is an alternative to define enhancement as the difference between powers at equatorial and off-equatorial stations. Since the pulsation amplitude does not show any dependence on the time of occurrence, this definition of enhancement should be valid. The picture obtained after defining this new enhancement is depicted in figure 5.11. This clearly brings the diurnal pattern of the equatorial enhancement for H component, which peaks at local noon. D component shows daytime decrease at the equator, except on 9th May'93, the station very close to dip equator (NIE=1.2^{0}S) does not show the decrease. The error bars indicate that the estimates are quiet stable, except for D component on 9th May'93, where the strength was very small. The larger power at the off-equatorial station may suggest the strengthening of D component at the fringes of the electrojet.

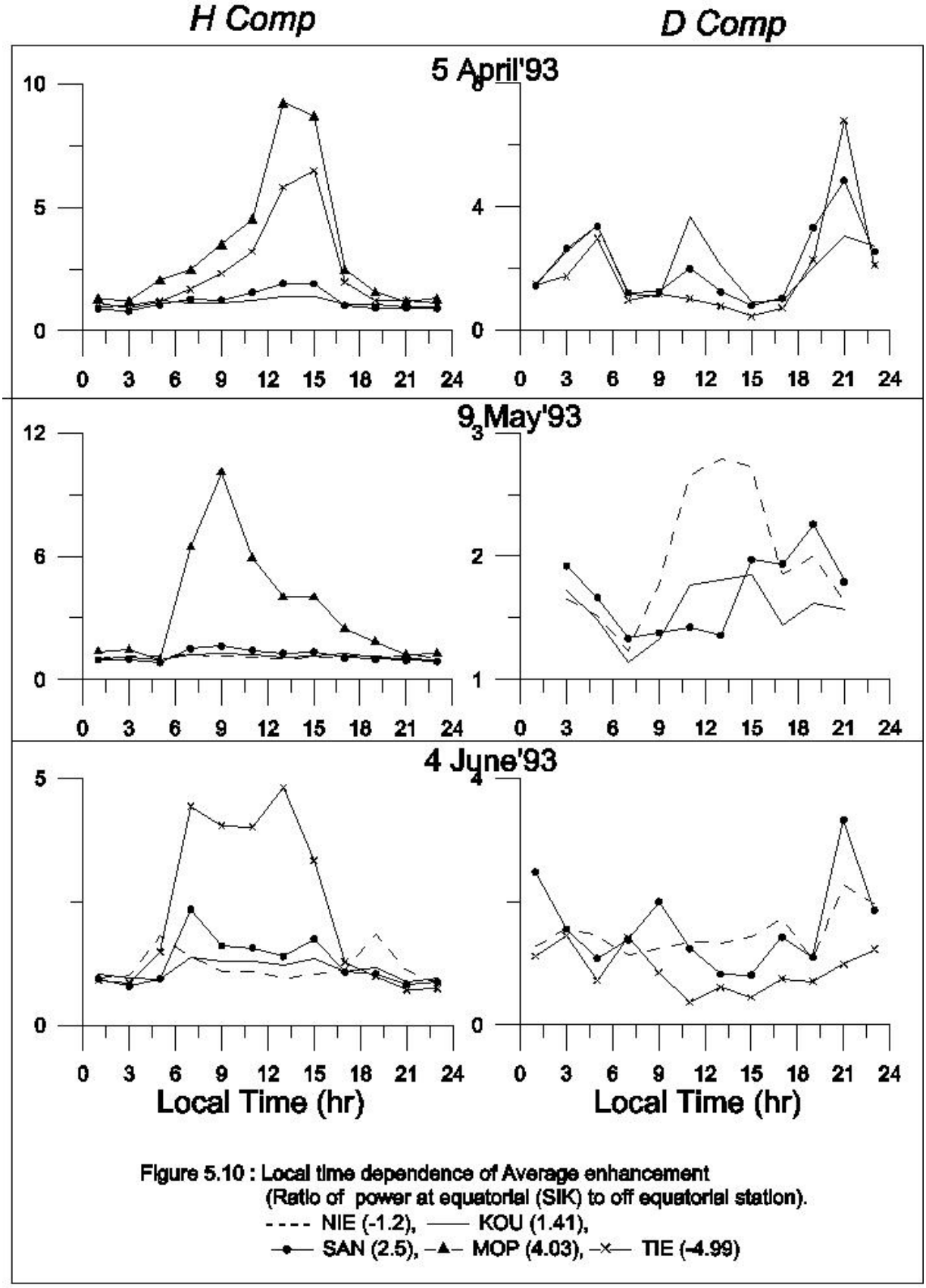

Figure 5.10 : Local time dependence of Average enhancement
(Ratio of power at equatorial (SIK) to off equatorial station).
---- NIE (-1.2), —— KOU (1.41),
—●— SAN (2.5), —▲— MOP (4.03), —×— TIE (-4.99)

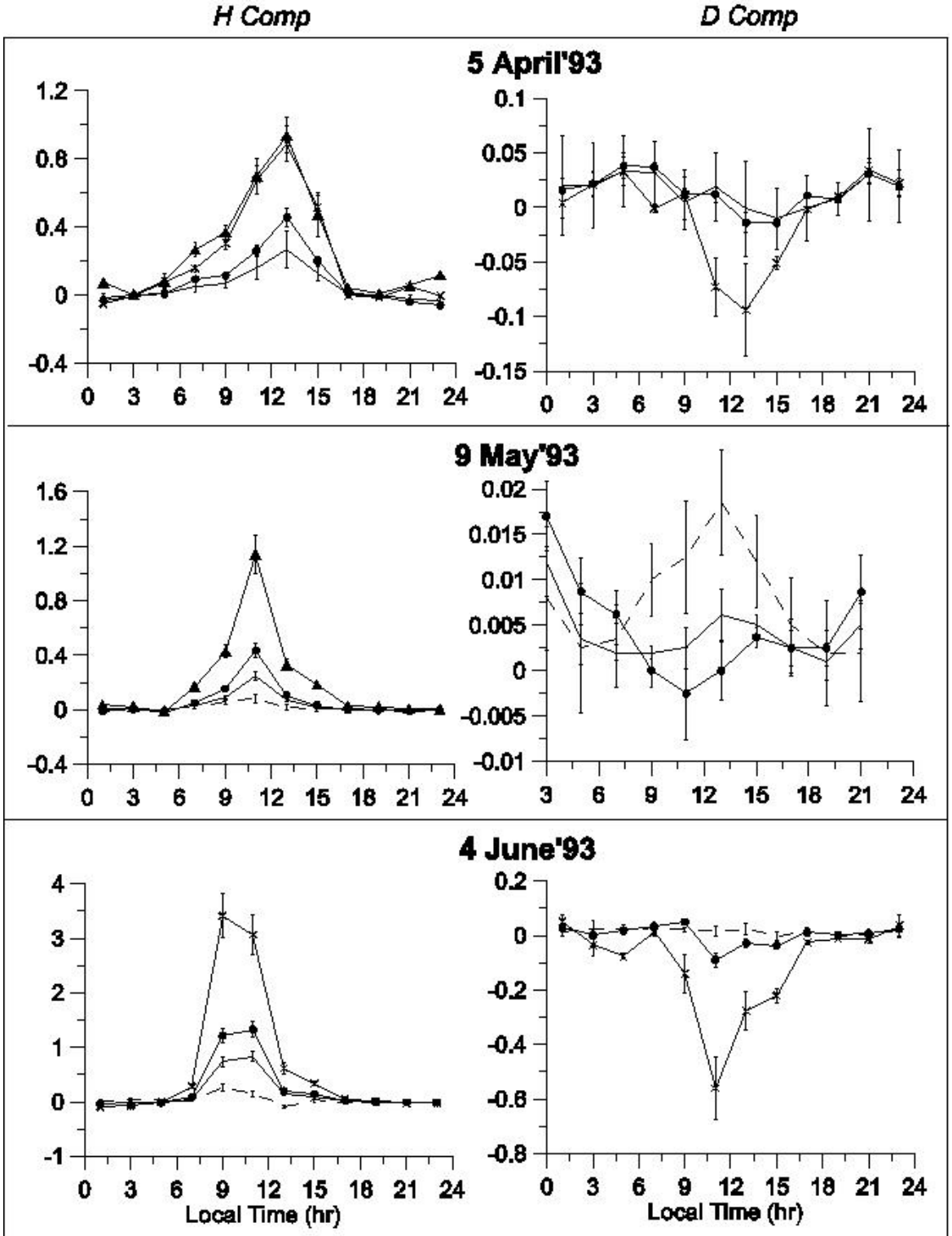

Figure 5.11 : Local time dependence of Average enhancement (Difference between the power at equatorial (SIK) and off equatorial stations).
---- NIE (-1.2), —— KOU (1.41),
–•— SAN (2.5), –▲– MOP (4.03), –×— TIE (-4.99)

5.2.3 Frequency dependence of Enhancement at different LTs and stations:

In order to investigate the frequency dependence of enhancement, we have plotted the ratio of power at SIK to MOP (dip=4.03^{0}N) as a function of frequency at different local times (see figure 5.12). The scatter plot clearly shows the daytime enhancement, which we have already seen, in the previous section. It is observed that the enhancement is larger at lower frequencies. While this dependence is not so obvious for nighttime when the enhancement is almost null.

The scatter plot of enhancement for different stations is plotted in figure 5.13. Here we have put all the local times together. The stations are arranged downward with increasing dip latitude. Left-hand side panel is for H component while right hand side panel for D component. The scatter in H component systematically increases with the latitude, suggesting the equatorial dependence, whereas D component scatter does not systematically follow the latitudes.

5.2.2 Latitudinal Structure of the Enhancement:

To examine this aspect of pulsation, we have taken enhancement with respect to the station that is located at the fringe of the EEJ. Hence, for 5th April'93, we have computed enhancement with respect to TIE (dip=5^{0}S). The results are depicted in figure (5.14), where different plots are for different frequency zones (grouped as 0.4-1 mHz, 1-2 mHz, 2-3 mHz, and 3-4 mHz) and local times. The latitudinal structure clearly shows the daytime equatorial effect. Though the enhancement is more for lower frequencies, which is seen from the scatter plot in figure (5.12), the individual case may show different behaviour. But generally, it follows the trend, with few exceptions.

A suggestion was made by Mason [1963], that the width of enhancement is frequency dependent and higher frequencies see a narrower EEJ. In order to study the frequency dependence of latitudinal width of the enhancement, we carried out this exercise. We fitted quadratic into the points in figure (5.14) and tried to examine, how the width of enhancement changes with frequencies. We found that inspite of large variability, the

general trend shows that the width increases with frequency, which is contradictory to the findings of Jain and Srinivasacharya [1975].

5.2.3 Local time and Frequency Dependence of Cross Phase:

In section 5.1 we have seen that the cross phases between satellite and ground stations have local time dependence and increases with frequency. Next, we want to examine the behaviour in the lower frequency range. Here the cross phases are between equatorial ground station and off equatorial ground stations; only those values are considered whose coherence coefficient is greater than 0.8. Hence the phases are for the latitudinal propagation, while in earlier case, they were for vertical propagation introduced due to ionosphere. Unfortunately, no equatorial station was working during that time, hence we do not really know whether the phases are due to vertical propagation or latitudinal propagation.

Figure (5.15) plots cross phases between SIK and SAN (dip = 2.5^0N) verses local times at different frequencies. The solid line curve indicates the average. It is seen that the phase differences between electrojet station and off equatorial station are more during daytime for all frequencies and we also observe that phases increase with frequency. This is quite consistent with Oersted results drawn above.

Further we take the average of phase differences at all frequencies and plot it verses local time for different stations (see figure 5.16). The figure shows that the average values are large at daytime and the phases increase with the latitude of the off-equatorial station. The error bars in the figure indicate the standard error mean.

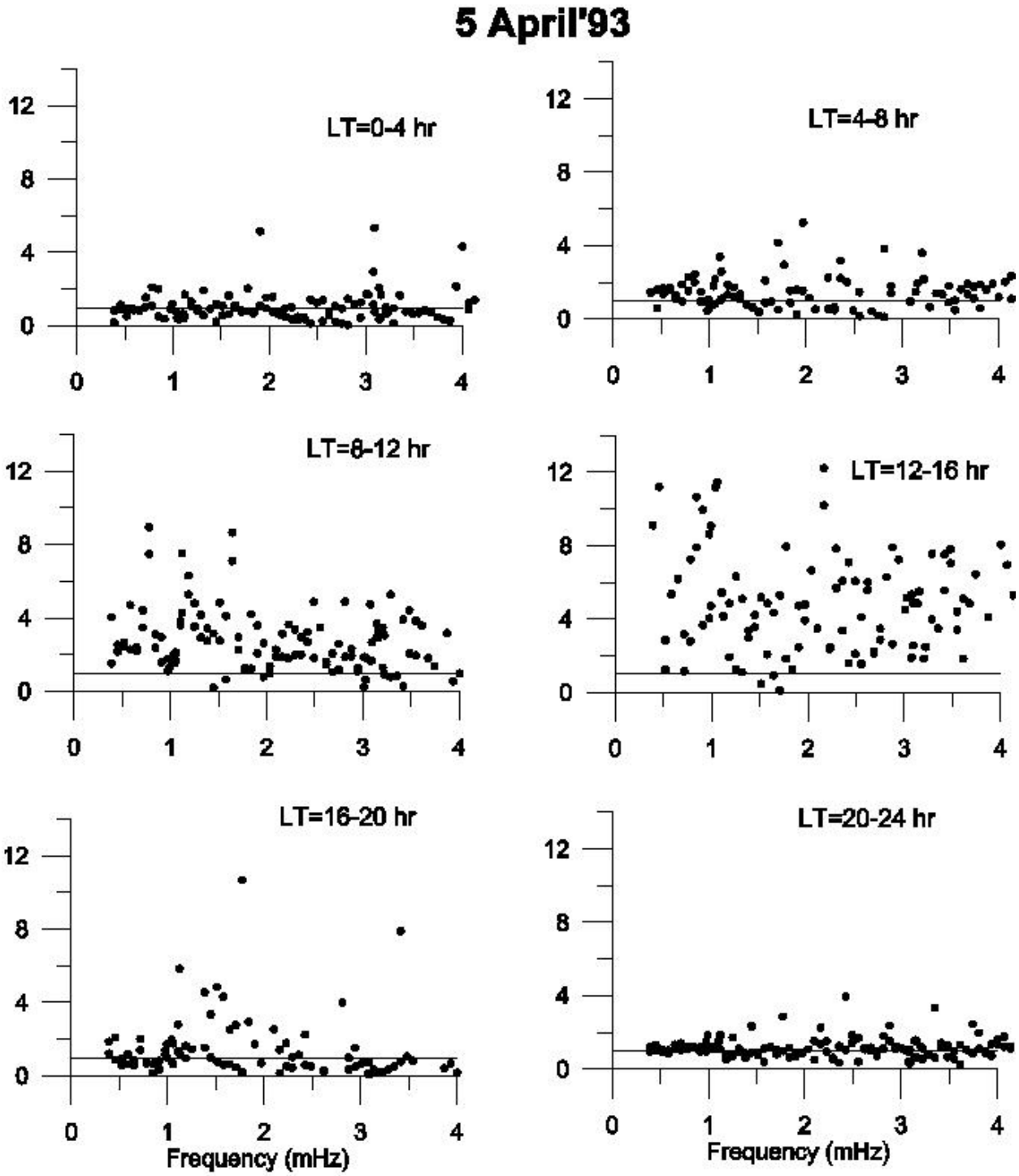

Figure 5.12 : Ratio of power in H comp at SIK to MOP

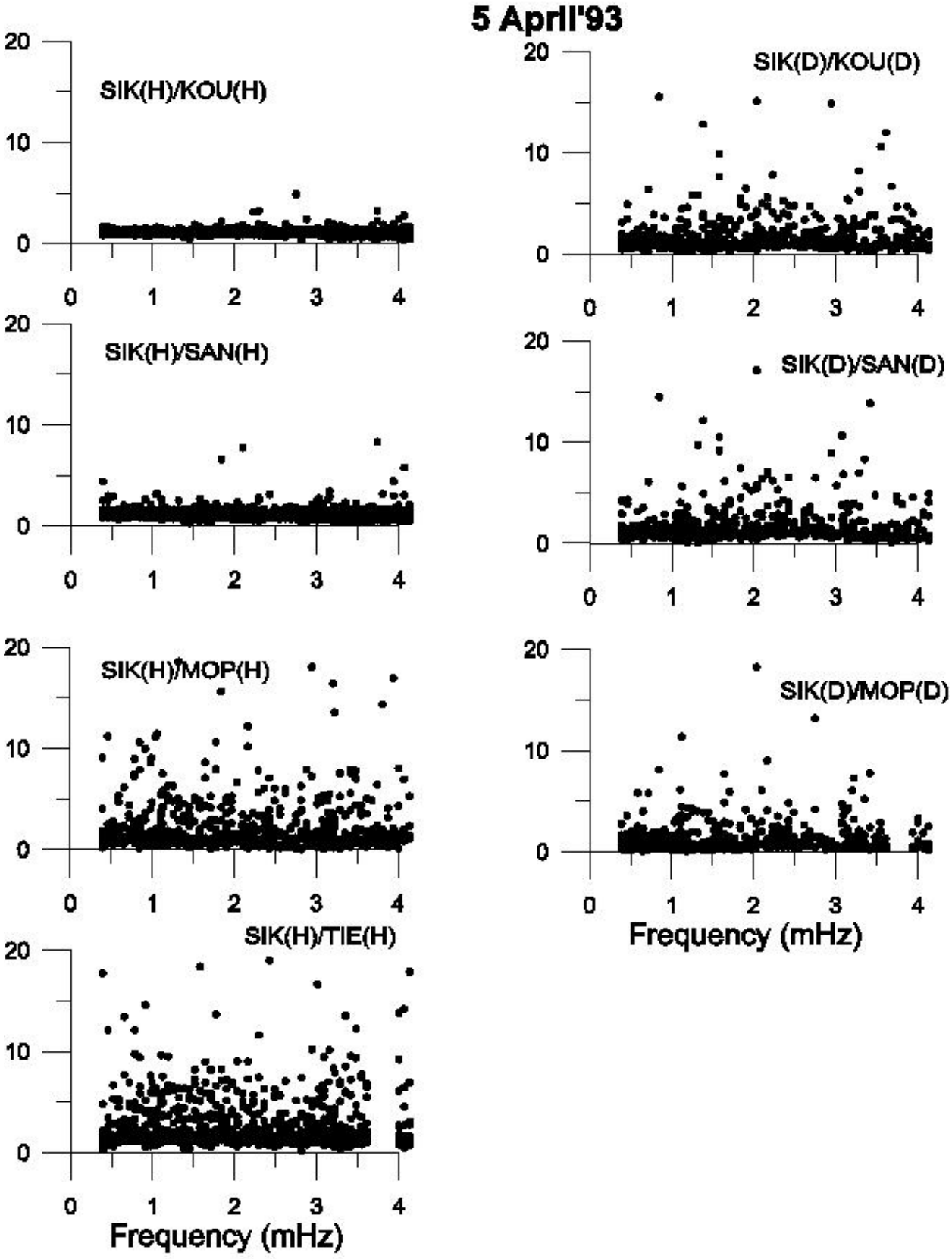

Figure 5.13 : Scatter Plot of Enhancement at Different stations.

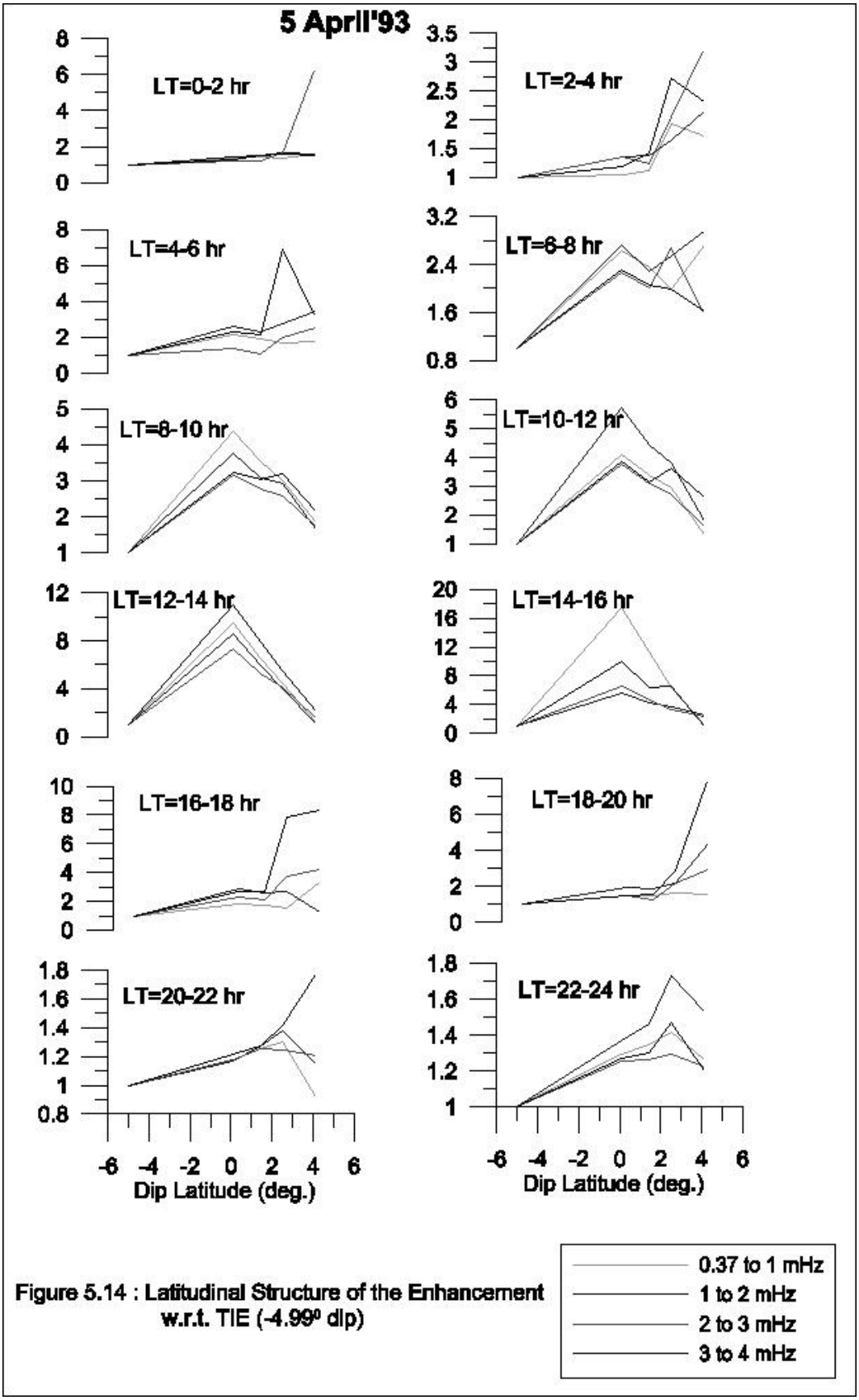

Figure 5.14 : Latitudinal Structure of the Enhancement w.r.t. TIE (-4.99° dip)

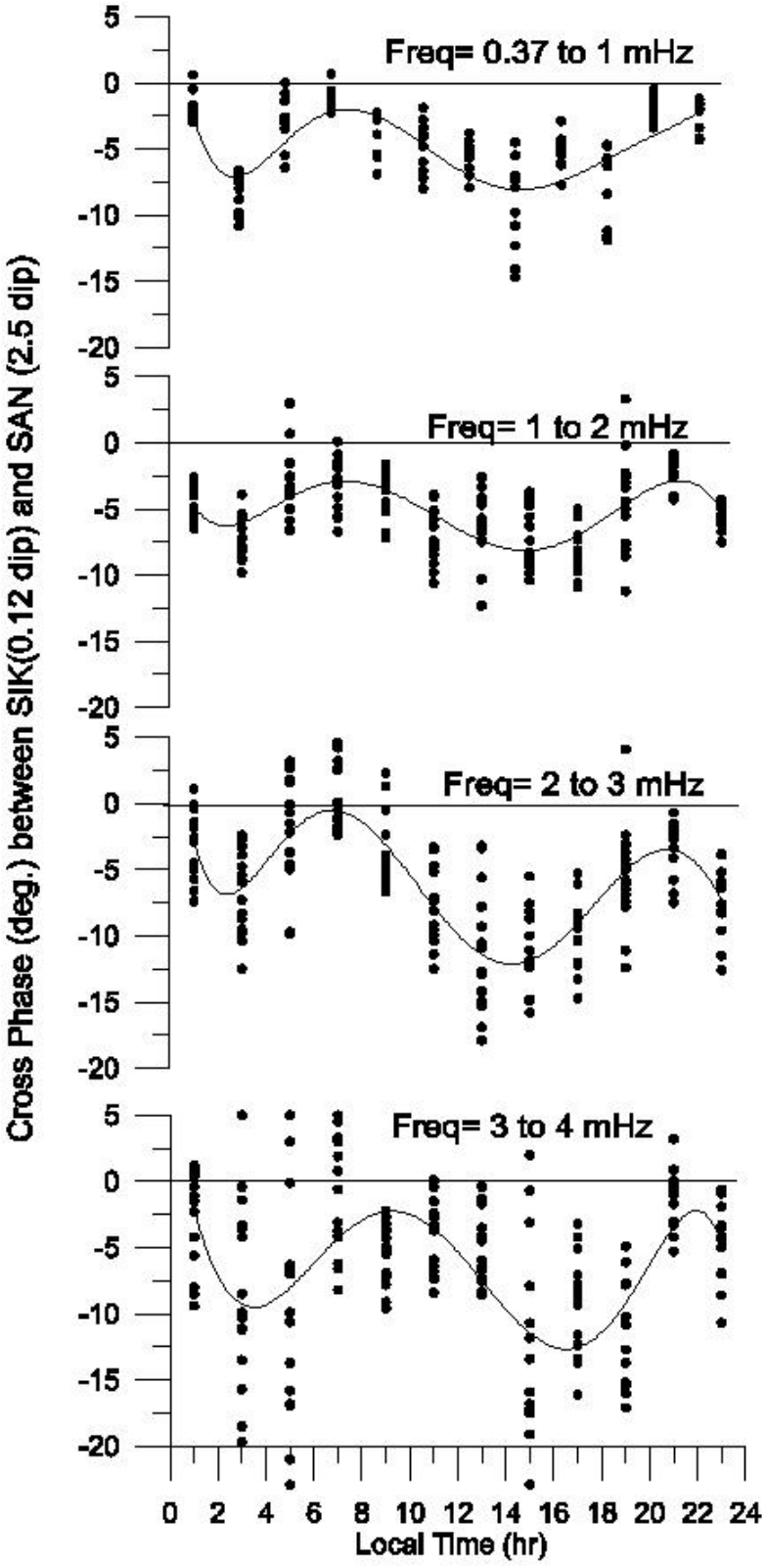

Figure 5.15 : Local time and frequency dependence of cross phases

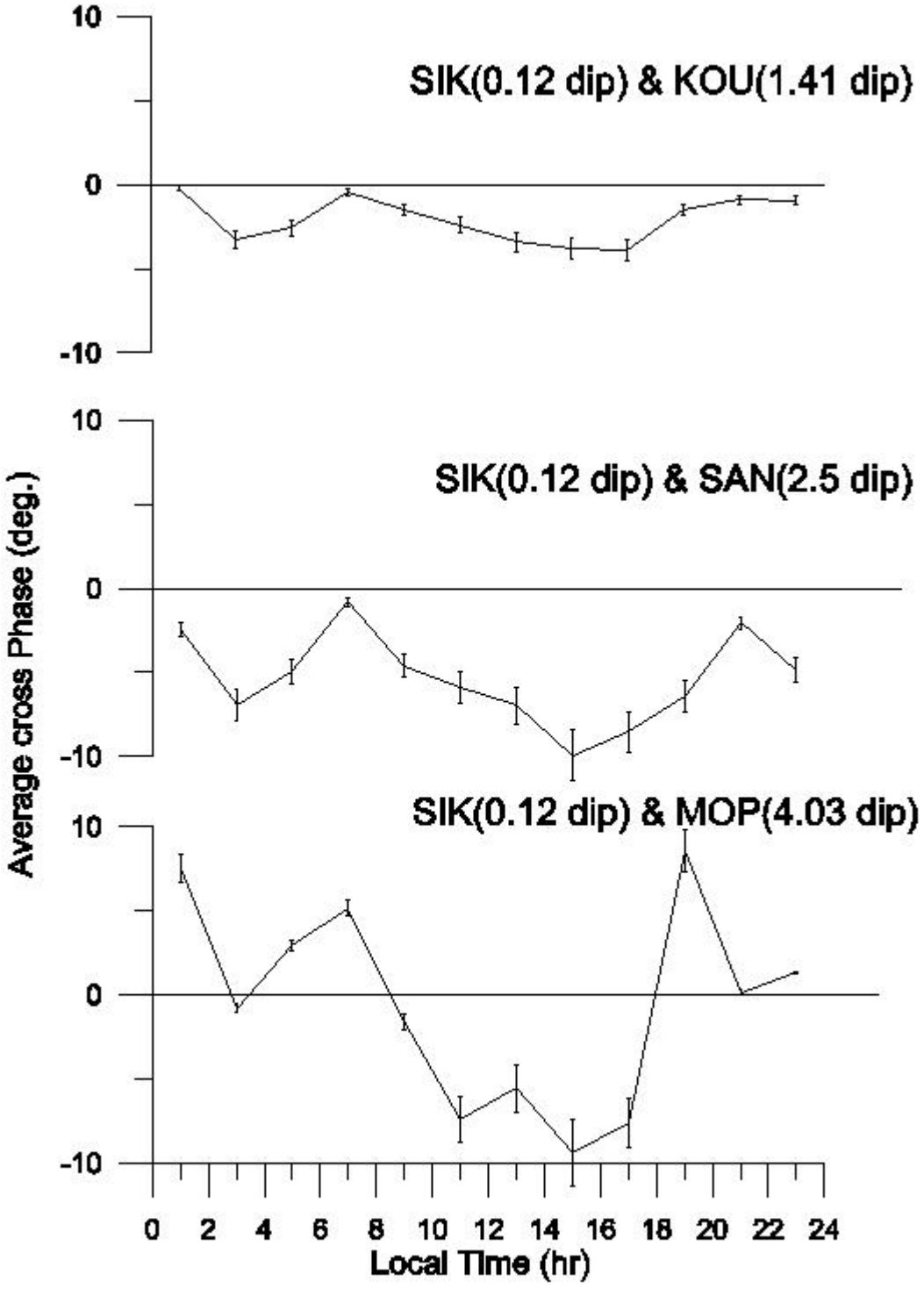

Figure 5.16 : Average Cross phase in H component at different stations

5.3 Implications for numerical Modelling:

The main results contained in this chapter should have implications in terms of modelling of ionospheric current system.

(1) We have seen that the daytime ionosphere introduces a shift in phase of the hydromagnetic wave impinging on it. The phase shift is greater for higher frequencies and higher conductivity of the ionosphere.

(2) Secondly there are significant phase differences in the oscillations recorded at the centre of the electrojet and below the fringes of the electrojet.

(3) The equatorial enhancement is in general higher for lower frequencies as compared to the higher frequencies.

We should note that the oscillations recorded at a station at low or equatorial latitude would have reached either directly across the geomagnetic field lines or alternately oscillations could have reached the auroral zone first and then got transmitted to equatorial region through the earth-ionosphere wave guide [Kikuchi and Araki, 1979a,b].

The fact that Pc5-6 oscillations observed in the African sector have phase at the equator lagging that of the off-equatorial station, may suggest that we are looking at a wave travelling from pole to the equator. There are two problems associated with such an interpretation:

(1) The wave transmitted in the earth-ionosphere cavity is instantaneous [Kikuchi and Araki, 1979b] and can not account for the phase lag over a short latitudinal span defined by the electrojet.

(2) One-dimensional propagation within the ionosphere will take too long time to reach equatorial latitudes [Kikuchi and Araki, 1979a] and will not be consistent with the observations.

Furthermore, the model of Kikuchi and Araki [1979b] can not explain why the phase lag is enhanced during the day lit hours. It more likely that the wave lag is introduced with

the equatorial E-region and we have examined the propagation of the hydromagnetic wave through the ionosphere.

Effect of the ionosphere on the hydromagnetic waves has been most extensively studied in the high latitudes where the magnetic field is normal to the ionosphere. Inspite of the fact that such a geometry is not valid in the low latitudes, results of Nishida [1978] have been used by Kim and Takahashi [1999] to discuss the phase shifts introduced by the low latitude ionosphere. The phase shifts predicted by the model turn out to be very small. Hence so far no adequate model is available for the modulation of hydromagnetic waves in the equatorial region. Recently, Fedorov et al [1999] put forward a model for the ionospheric propagation of hydrodynamic disturbances in the equatorial electrojet region, which is discussed in chapter 8.

5.4 Summary and Discussion:

In section 5.1, we have presented few results of the study of compressible hydromagnetic waves using the Oersted magnetic field data analyzed in conjunction with the ground magnetic data available with a sampling rate of 1 second. We find a high degree of coherence between the satellite and fixed ground oscillation despite the fact that the satellite covered a significant latitudinal distance. Even the time structures show a high degree of correlation over the large orbital distance. This suggests that the incident hydromagnetic waves are phase coherent over a large range of latitudes. We have been able to demonstrate that the wave undergoes significant phase delay as it passes through the dayside ionosphere. The phase delay increases with increase in frequency of the oscillation as well as the electrical conductivity of the ionosphere. The frequency dependence is consistent with the results of Kim et al. [1998] (cf. Figure 9 in their paper).

Fairly realistic theoretical models are available for computing shielding and phase delays introduced by the high latitude ionosphere {Nishida,1978; Hughes and Southwood, 1976] where the ambient magnetic field is nearly perpendicular to the

ionospheric boundary over a range of latitude. These models are not applicable in our case. In the latitudes of our interest the ambient field is almost horizontal at the equator and its inclination varies with latitude and is almost 45^{o} near the latitude of the Japanese stations. Kim and Takahashi [1999] computed the phase delay based on the model of Nishida [1978] and found that the phase shifts predicted are too small. Our values are in fair agreement with the observed phase delays of Kim and Takahashi [1999] around 50^{0} to 60^{0} at the period of 20 mHz. These are much larger than the 7^{o} to 25^{o} suggested by the model calculations. A full fledged non-local model which takes into account the varying inclination and conductivity with latitude may be required to provide the right answers.

The analysis based on West African data of sampling interval of one minute reveals many important aspects of magnetic pulsations of range 1-4 mHz. The average equatorial enhancement in horizontal component is found to be highest at local noon. The diurnal variation of the enhancement is more clearly seen in the difference rather than in the ratio. The average ratio of equatorial station to off equatorial station situated at 5^{0}S is around 9 during daytime. Latitudinal structure of oscillations also nicely follows the electrojet structure. The electrojet effect in D component is seen through increased strength at the fringes of the electrojet. The daytime equatorial enhancement in H component and off-equatorial enhancement in D component have also been observed by Pathan et al. [1999] and Jain and Srinivasacharya [1975] for Indian stations. We observe that the enhancement is frequency dependent and it is larger for lower frequencies. Mason [1963] suggested that the width of enhancement is frequency dependent and increases with decreasing frequency. This found some support in the findings of Jain and Srinivasacharya [1975]. Phase shifts between equatorial and off-equatorial stations are found to vary with latitude, local time and frequency. The average phase difference between the dip station and the station at dip latitude of 2.5^{0}N is about 12^{0} for the pulsations in the frequency range between 3 and 4 mHz. It is found that the phase differences increase with frequency and maximize near local noon.

The equatorial ionosphere is characterized by a large latitudinally localized zonal conductivity (σ_{yy}). Ionospheric conductivity depends on local time, and the equatorial large σ_{yy} appears only during the daytime. It is expected that this high conductive ionosphere affects the incident electromagnetic signal. Because the phase lags of equatorial pulsations appear during the daytime, the phase lags must be related to the high ionospheric conductivity. Thus ionospheric conductivity at the dip equatorial position plays crucial role in the equatorial enhancement of the pulsations and also in the phase differences introduced. Shinohara et al. [1998] also identified the phase lags of Pc4-5 pulsations across the dip equator during the daytime for Brazilian station array and found that the pulsations show larger phase lags for higher frequencies. These results are quite consistent with our findings.

Our analysis shows that the daytime ionosphere effects are important and need to be modelled, if the observed ground magnetic signature have to be interpreted in terms of magnetospheric generation and propagation. The most significant finding relates to the introduction of phase shifts by the ionosphere over a broad range of frequencies.

Chapter 6
Atmospheric Tides

6.1 Introduction:

By atmospheric tides we generally mean those planetary scale oscillations whose periods are integral fractions of a solar or lunar day. The detection and study of tidal oscillations is usually based on a long series of recordings of pressure in particular, but also of wind and temperature, made at different observatories widely distributed over the globe; some investigators have also used radio, rockets and satellites measurements.

Observational and theoretical studies over the last two decades have yielded significant progress in the understanding of the subject. In contrast to sea tides, which have been known and described for over two thousand years; atmospheric tides were not observed, until the invention of the barometer by Torricelli in 1643. The barometer shows daily changes of mass distribution of the atmosphere. Newton already recognized that there ought to be a tidal response in the atmosphere similar to that in sea, but he concluded that it would be too weak to be observed. After collecting and harmonically analyzing data from thirty stations for diurnal, semidiurnal, and terdiurnal components, Kelvin [1882] put forward the resonance theory, which was, however not corroborated by rocket measurements. The increased data availability by the mid-1960s, emerged in better understanding of tides. Classical theory based on Laplace's equation, has proved adequate for the description of the observed solar semidiurnal [Butler & Small 1963] and the diurnal surface pressure and stratospheric wind oscillations [Lindzen 1967b]. Thus "classical tidal theory" [Chapman and Lindzen, 1970] explains many of the qualitative features of the observed diurnal and semidiurnal tides analytically.

6.2 Observations:

Before proceeding to the mathematical theory of atmospheric tides, it is appropriate for us to present a description of the phenomena.

The sea tides are measured by means of tide gauges, which record the height of the water surface. Obviously the air tides cannot be measured in this way, as the atmosphere has no such boundary surface. The alternative is to use barometer at the bottom of the atmosphere. In the tropics, the barometer does show a marked variation of period of half a solar day. For many years, almost all data analyses for atmospheric tides were based on surface pressure data. Therein, it was found that the amplitude of semidiurnal component decreases with latitude, resulting in peak at the equator. Although tidal oscillations in surface pressure are generally small, the huge amount of data makes it an effective tool of study.

In the upper atmosphere, where thermotidal oscillations are the major components, ground data can not throw much light on the understanding of the tidal behavior. Radiosonde data for stations between 30°N and 76°N [Johnson 1955, Harris 1959, Finger and Teweles 1962,1966] have described solar diurnal and semidiurnal contributions to temperature and horizontal wind fields between the ground and 30km. Wallace and Hartranft [1969] found that at mid and tropical latitudes, diurnal wind oscillations are significantly associated with local topographic features at the earth's surface. However, at higher altitudes (above 25 km) and at arctic latitudes the diurnal oscillations are global following the sun. In 1960s, the Meteorological rocket network, produced a substantial body of data on winds between 40 and 60 km. These measurements have shown the existence of a strong diurnal wind oscillation with amplitude of about 8 m/s at 50 km. In the altitude range 80-100 km an important source of wind information comes from the ionized trails left by the numerous meteors disintegrating there. These trails are carried by the neutral wind and may be tracked from the ground by the observation of reflected radio signals. This radio meteor data suggest that the diurnal oscillation may be bigger than the semidiurnal oscillations.

Later in 1980s, a variety of radar types were used for the study of mesosphere and lower thermosphere, including EISCAT (European Incoherent Scatter), Meteor wind (MWR), Medium Frequency (MFR), and partial reflection radars. Data have been gathered for the campaigns of STEP (Solar Terrestrial Energy Programme) and its parts e.g. MLTCS (Mesosphere Lower Thermosphere Coupling Study). In the case of the MFRs data sets are often continuous due to design improvements in the systems.

The major impact upon the observational knowledge of the thermal tides has due to UARS satellite-system HRDI (High Resolution Doppler Imager) and WINDII (Wind Imaging Interferometer) [Burrage et al., 1996a,b]. These have confirmed the general global and seasonal tidal structures found by ground based radars (MFR and MWR), but have added useful details due to their true global coverage ($0\text{-}70^0$) and height coverage which extends into the thermosphere [McLandress et al., 1996a,b]. CRISTA 1 (Cryogenic Infrared Spectrometers and Telescopes for the Atmosphere) mission that was performed during 1994 has also proved useful in the study of tides [Ward et al. 1999].

6.3 Classical theory of Atmospheric Tides:

The earth's atmosphere responds to gravitational and thermal forces in a manner analogous to forced mechanical vibrations. As it is possible to analyze the forcing term into harmonic components, the steady-state responses of the atmosphere to these forces constitute atmospheric tides.

The theory of atmospheric tides has two main parts:

(a) The investigation of the sources of periodic excitation.

(b) The calculation of the atmospheric response to the excitation.

The former could include a consideration of atmospheric composition, chemistry, solar spectrum and molecular absorption etc., which will be discussed in next

section. In this section, we discuss the later which, deals in principle, all the problems involved in the general circulation of the entire atmosphere. The section begins with the description of equations for the atmospheric response to arbitrary excitations invoking numerous assumptions and approximations. It also gives attention to the method of solution for the equations obtained.

6.3.1 The calculation of the atmospheric response to the excitation:

6.3.1.1 Assumptions:

1) The motion of the atmosphere may be descried by classical fluid equation (Navier-Stokes equation), for a compressible gas.
2) Atmosphere is in thermodynamic equilibrium & obeys the perfect gas law,

$$P = \rho RT \tag{6.1}$$

Changes of R with height are ignored.

3) The atmosphere is in a state of hydrostatic balance ,

$$\frac{1}{\rho}\frac{\partial P}{\partial z} = -g \tag{6.2}$$

4) Thickness of the atmosphere is small compared to the radius of the earth.
5) Earth is regarded as perfectly hard solid sphere of radius '*a* ' with perfectly smooth surface.
6) All dissipative forces are ignored.
7) Fluctuations associated with tidal oscillations are perturbations in the ambient atmosphere & the entire problem is tackled through linearization

$$\rho = \rho_0 + \delta\rho \tag{6.3}$$

Where,

$\rho_0 \equiv \rho_0(z)$ = Ambient state

$\delta\rho \equiv \delta\rho\,(z,\theta,\varphi)$ = perturbation

8) Vertical velocity (w) is small compared to horizontal velocities, but dw/dz can not be ignored.

9) Background winds are neglected. They are very important in order to obtain fully realistic soution for the tides. In the presence of background winds, the tidal equations are no longer separable and different modes predicted by the classical theory get coupled.

6.3.1.2 Equations:

We now investigate the equations based on the above approximations. Before all, let us introduce the variables used in the equations.

Let

θ = Colatitude

φ = East longitude

t = Time

u = Southward velocity

v = Eastward velocity

w = Upward velocity

δP = Pressure perturbation

$\delta \rho$ = Density perturbation

δT = Temperature perturbation

J = Thermotidal heating per unit mass per unit time.

Ω = Gravitational tidal potential

ω = Earth's rotation rate

$$\gamma = \frac{C_p}{C_v} = 1.4$$

$$\kappa = \frac{\gamma - 1}{\gamma} = \frac{2}{7}$$

From equations (6.1) and (6.2), we obtain

$$p_0 = p_0(0)\, e^{-x} \qquad (6.4)$$

$$\rho_0 = \frac{p_0}{gH} \qquad (6.5)$$

where, $H = \frac{RT_0}{g}$ (6.6)

$$x = \int_0^z \frac{dz}{H} \quad (6.7)$$

and T_0 = basic temperature distribution.

Equation of momentum gives linearized equations for northerly & westerly momentum respectively as follows:

$$\begin{aligned} \frac{\partial u}{\partial t} - 2\omega\, v\cos\theta &= -\frac{1}{a}\frac{\partial}{\partial\theta}\left(\frac{\delta P}{\rho_0} + \Omega\right) \\ \frac{\partial v}{\partial t} + 2\omega\, u\cos\theta &= -\frac{1}{a\sin\theta}\frac{\partial}{\partial\varphi}\left(\frac{\delta P}{\rho_0} + \Omega\right) \end{aligned} \quad (6.8)$$

The Coriolis term in these equations describe the advection of the earth's momentum due to its rotation.

Hydrostatic pressure relation gives rise to

$$\frac{\partial}{\partial z}\delta P = -g\delta\rho - \rho_0\frac{\partial\Omega}{\partial z} \quad (6.9)$$

Equation of continuity gives,

$$\frac{d\rho}{dt} = \frac{\partial}{\partial t}(\delta\rho) + w\frac{\partial}{\partial z}\rho_0 = -\rho_0\chi \quad (6.10)$$

where

$$\chi = \nabla\cdot v = \frac{1}{a\sin\theta}\frac{\partial}{\partial\theta}(u\sin\theta) + \frac{1}{a\sin\theta}\frac{\partial V}{\partial\varphi} + \frac{\partial w}{\partial z}$$

Thermodynamic energy equation, where heating is produced by both external sources (J) and adiabatic compression can be written as

$$\frac{R}{\gamma-1}\frac{dT}{dt} = \frac{R}{\gamma-1}\left(\frac{\partial\delta T}{\partial t} + w\frac{dT_0}{dz}\right) = \frac{gH}{\rho_0}\frac{d\rho}{dt} + J \quad (6.11)$$

Perfect gas law $P = \rho RT$, after linearizing yields

$$\frac{\delta P}{P_0} = \frac{\delta T}{T_0} + \frac{\delta\rho}{\rho_0} \quad (6.12)$$

Using (6.12) to eliminate δT from (6.11), we obtain

$$\frac{dP}{dt} = \gamma gH \frac{d\rho}{dt} + (\gamma - 1)\rho_0 J \tag{6.13}$$

Let,

$$G = -\frac{1}{\gamma P_0}\frac{dP}{dt} \tag{6.14}$$

In tidal theory we generally concern with fields periodic in time & longitude.

$$\therefore \quad field = f_e^{\sigma,s}(\theta, z)\, e^{i(\sigma t + s\phi)} \tag{6.15}$$

where,

$2\pi/\sigma$ = solar or lunar day or its suitable fraction.

$s = 0, \pm 1, \pm 2, \pm 3, ...$

Let $f = \sigma/2\omega$

=>

$$\sigma = \frac{2\pi}{fraction(s/l\ day)}$$
$$f = \frac{2\pi/fraction(s/l\ day)}{2\left(2\pi/(s/l\ day)\right)} = \frac{1}{2(fraction(s/l\ day))} \tag{6.16}$$

For diurnal wave, $f = 0.5$

For semidiurnal wave, $f = 1$

For two-day wave, $f = 0.25$ & so on.

Equation (6.8) to (6.12) after modification reduces to

$$H\frac{\partial^2 G^{\sigma,s}}{\partial z^2} + \left(\frac{dH}{dz} - 1\right)\frac{\partial G^{\sigma,s}}{\partial z} = \frac{g}{4a^2\omega^2} F\left(\left(\frac{dH}{dz} + \kappa\right)G^{\sigma,s} - \frac{\kappa J^{\sigma,s}}{\gamma gH}\right) \tag{6.17}$$

where,

$$F = \frac{d}{d\mu}\left(\frac{1-\mu^2}{f^2-\mu^2}\frac{d}{d\mu}\right) - \frac{1}{f^2-\mu^2}\left(\frac{s}{f}\frac{f^2+\mu^2}{f^2-\mu^2} + \frac{s^2}{1-\mu^2}\right) \tag{6.18}$$

and $\mu = cos\theta$

Equation (6.17) can be solved by the method of separation of variables.

Assume that $G^{\sigma,s}$ may be written as,

$$G^{\sigma,s} = \sum_n L_n^{\sigma,s}(Z)\,\Theta_n^{\sigma,s}(\theta) \tag{6.19}$$

and

$$J^{\sigma,s} = \sum_n J_n^{\sigma,s}(Z)\,\Theta_n^{\sigma,s}(\theta) \tag{6.20}$$

where, the set $\{\Theta_n^{\sigma,s}(\theta)\}$ for all n is complete for $0 \le \theta \le \pi$.

Substitute (6.19), (6.20) in (6.17), we get

$$\therefore\ F\left(\Theta_n^{\sigma,s}\right) = -\frac{4a^2\omega^2}{gh_n^{\sigma,s}}\,\Theta_n^{\sigma,s} \tag{6.21}$$

and

$$H\frac{d^2L_n^{\sigma,s}}{dz^2} + \left(\frac{dH}{dz} - 1\right)\frac{dL_n^{\sigma,s}}{dz} + \frac{1}{h_n^{\sigma,s}}\left(\frac{dH}{dz} + \kappa\right)L_n^{\sigma,s} = \frac{\kappa}{\gamma\, gHh_n^{\sigma,s}}\,J_n^{\sigma,s} \tag{6.22}$$

where,

$h_n^{\sigma,s}$ = Constant of separation

= Equivalent depth

The boundary conditions on $\{\Theta_n\}$ are that they be bounded at the poles (i.e. at $\theta = 0, \pi$). With these conditions equation (6.21) defines an eigenvalue problem where $\{h_n\}$ is the set of eigenvalues.

$\{h_n\}$ is often called the set of *equivalent depths* and the eigenfunctions $\{\Theta_n\}$ are often called *Hough functions.*

Equation (6.22) is called as 'Vertical structure equation'

Equation (6.21) is called as 'Laplace's Tidal equation'

6.3.1.3 Methods of solution for Laplace's Tidal equation:

We have equation (6.21)

$$\frac{d}{d\mu}\left(\frac{1-\mu^2}{f^2-\mu^2}\frac{d\Theta_n}{d\mu}\right)-\frac{1}{f^2-\mu^2}\left[\frac{s}{f}\frac{f^2+\mu^2}{f^2-\mu^2}+\frac{s^2}{1-\mu^2}\right]\Theta_n+\frac{4a^2\omega^2}{gh_n}\Theta_n=0 \qquad (6.23)$$

This equation has been studied for well over a century, and Hough's work in this regard is useful. In this section, we simply outline a formal solution procedure. Equation (6.23) in general, does not have obvious solution, so expansion procedure is necessary. Only at $s = 0, f = 1$ [Solberg, 1936] and for non-rotating earth [Sibert 1961] and for $h = \infty$, (Haurwitz [1940] & Neamtarr [1946]) the above equation has obvious solutions.

It turns out that equation (6.21) has regular solutions for the whole domain $0 \le \theta \le \pi$. Thus, we might, seek power series solutions of (6.21). Unfortunately, the substitution of such a series into (6.21) leads to an infinite set of fifth order recursion relations, that is, each relation involves five of the power series coefficients. However, as Hough [1898] noted, the use of an expansion in associated Legendre Polynomials leads to a much more tractable set of third-order recursion relations.

Let

$$\Theta_n^{\sigma,s}=\sum_{m=s}^{\infty}C_{n,m}^{\sigma,s}\,P_m^s(\mu) \qquad (6.24)$$

Substituting (6.24) into (6.21) and after modification we get,

$$K_m^s D_{n,m-1}-M_{n,m}^{\sigma,s}C_{n,m}+L_m^s D_{n,m+1}=0 \qquad (6.25)$$

$$K_m^s C_{n,m-1}-N_m^{\sigma,s}D_{n,m}+L_m^s C_{n,m+1}=0 \qquad (6.26)$$

Where,

$$
\begin{aligned}
K_m^s &= \frac{(m+1)^2(m-s)}{(2m-1)m^2} \\
L_m^s &= \frac{m+s+1}{(2m+3)} \\
N_m^{\sigma,s} &= \frac{m+1}{m} - \frac{s}{fm^2} \\
M_{n,m}^{\sigma,s} &= f^2\left(\frac{m+1}{m} - \frac{s}{fm^2}\right) - (m+1)^2 \frac{h_n g}{4a^2\omega^2}
\end{aligned}
\tag{6.27}
$$

and auxiliary constants $D_{n,m}{}'$ s are defined as

$$
\frac{2(m+1)^2(m-s)}{m^2(2m-1)} C_{n,m-1} + \frac{(m+s+1)}{2m+3} C_{n,m+1} = 2\left(\frac{m+1}{m} - \frac{s}{fm^2}\right) D_{n,m}
$$

By analogy with the case of N homogeneous equations in N unknowns, where self-consistency requires that the determinant of the coefficient equals zero.

$$
\begin{vmatrix}
-M_{n,m}^{\sigma,s} & L_s^s & 0 & 0 & \cdot & \cdot & \cdot & \cdot \\
K_{s+1}^s & -N_{s+1}^{\sigma,s} & L_{s+1}^s & 0 & \cdot & \cdot & \cdot & \cdot \\
0 & K_{s+2} & -M_{n,s+2}^{\sigma,s} & L_{s+2}^s & 0 & \cdot & \cdot & \\
0 & 0 & \cdot & \cdot & \cdot & \cdot & \cdot & \cdot
\end{vmatrix} = 0 \tag{6.28}
$$

which yields the eigenvalues for symmetric eigenfunctions.

$$
\begin{vmatrix}
-N_s^{\sigma,s} & L_s^s & 0 & 0 & \cdot & \cdot & \cdot & \cdot \\
K_{s+1}^s & -M_{n,s+1}^{\sigma,s} & L_{s+1}^s & 0 & \cdot & \cdot & \cdot & \cdot \\
0 & K_{s+2} & -N_{s+2}^{\sigma,s} & L_{s+2}^s & 0 & \cdot & \cdot & \\
0 & 0 & \cdot & \cdot & \cdot & \cdot & \cdot & \cdot
\end{vmatrix} = 0 \tag{6.29}
$$

which yields the eigenvalues for antisymmetric eigenfunctions.

Equations (6.28) & (6.29) are polynomials in h_n, hence solution of these determinants, gives values of h_n. Infinite order of the determinant results in the infinite number of h_n values (roots). Therefore, in practice, we have to truncate it

at some stage. Let for order L, the solution of $D_L(h) = 0$, be $h_1, h_2, \ldots h_L$. If for order $(L + 1)$, the set of solutions does not alter much then we can truncate at L.

In the set of solutions $\{h_n\}$, n corresponds to different modes.

In wind (1, 1) first 1 gives value of s, and second 1 corresponds to mode.

For $s = 1$, symmetric modes are (1, 1), (1, 3), (1, 5), … for positive h_n

and (1, -2), (1, -4),… for negative h_n

Antisymmetric modes are (1, 2), (1, 4),…. for positive h_n

and (1, -1), (1, -3),…. for negative h_n

So after determining $\{h_n\}$ our next task is to find out Hough coefficient $\{C_{n,m}\}$. Standard texts [Chapman and Lindzen 1970] do not make any mention of the intricacies involved in the determination of the eigen values and a straight forward application of the recursion relation leads to singularities. Recourse was, therefore, taken to the original publications of Hough [1897 & 1898]. Latitude dependence of symmetric and antisymmetric Hough functions for the migrating diurnal and semidiurnal modes are shown in figure (6.1) and (6.2).

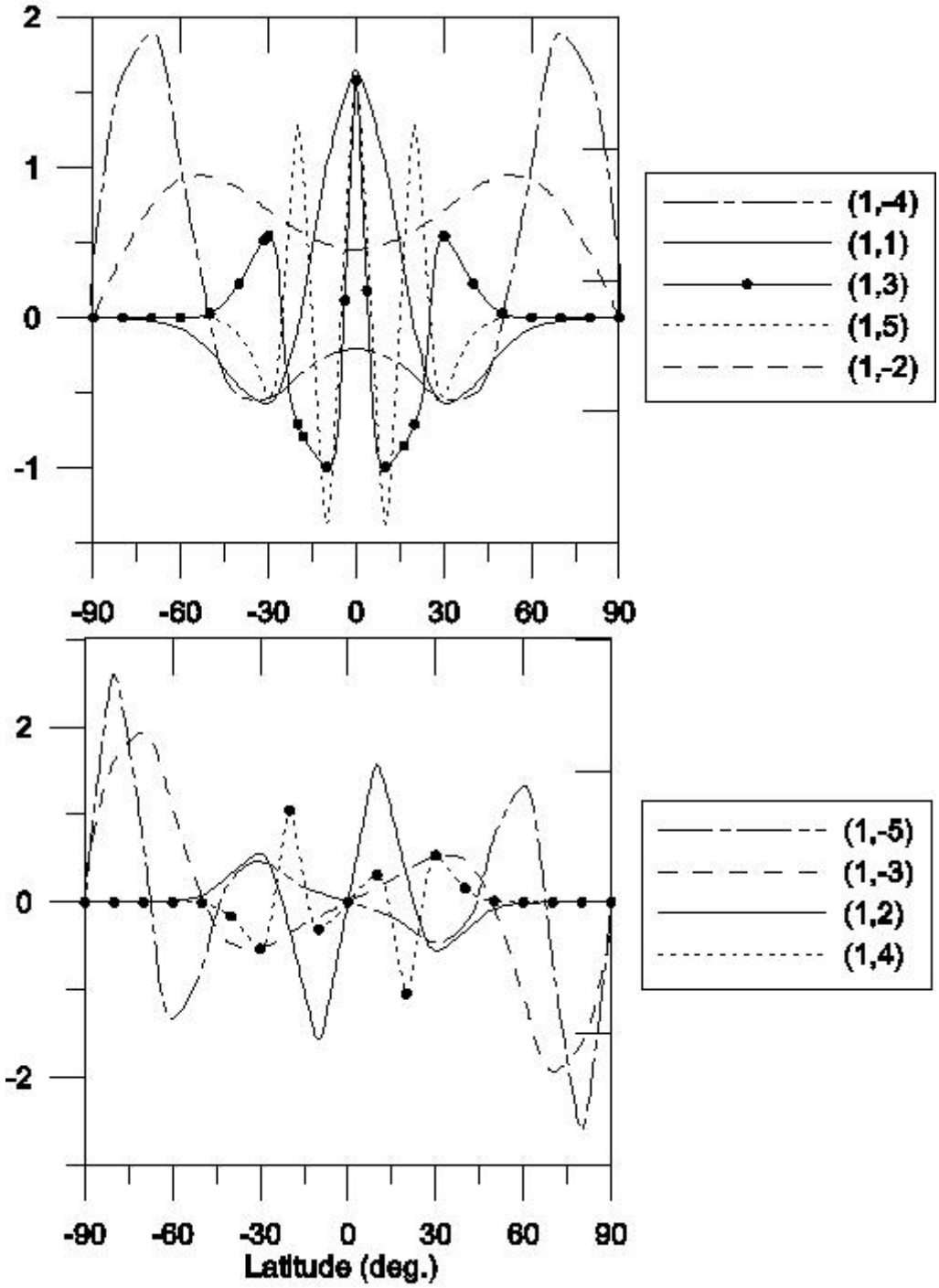

Figure 6.1 : Symmetric (top) and antisymmetric (bottom) Hough functions for migrating solar diurnal thermal tide.

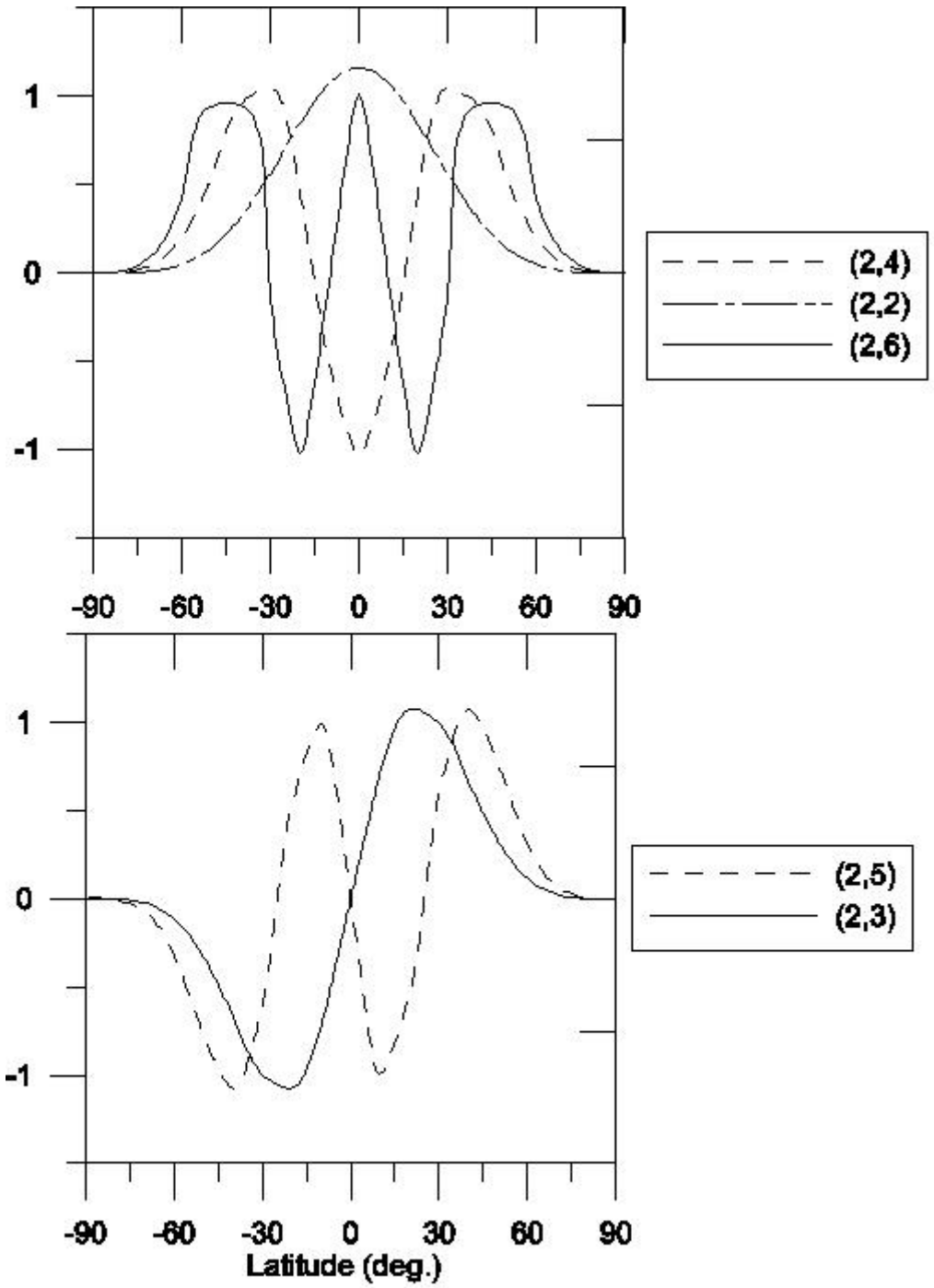

Figure 6.2 : Symmetric (top) and antisymmetric (bottom) Hough functions for migrating solar semidiurnal thermal tide.

After getting Hough' s coefficients, we have to normalize it.

In equation (6.24), if normalized associated Legendre polynomials are used so that for s>0,

$$P_{m,s}(\mu) = \sqrt{\frac{2m+1}{2}\frac{(m-s)!}{(m+s)!}}\, P_m^s(\mu)$$

Therefore equation (6.24) can be rewritten as

$$\Theta_n^{\sigma,s} = \sum_{m=s}^{\infty} \hat{C}_{n,m}^{\sigma,s}\, P_{m,s}(\mu)$$

where

$$\hat{C}_{n,m}^{\sigma,s} = C_{n,m}^{\sigma,s}\sqrt{\frac{2(m+s)!}{(2m+1)(m-s)!}} \tag{6.30}$$

Let $$(F_n)^2 = \sum_{m=s}^{\infty}\left(\hat{C}_{n,m}^{\sigma,s}\right)^2 \tag{6.31}$$

If we choose to normalize then we define,

$$\left(\overline{C}_{n,m}^{\sigma,s}\right)normalised = \frac{\hat{C}_{n,m}^{\sigma,s}}{F_n} \tag{6.32}$$

Thus,

$$\therefore \Theta_n^{\sigma,s} = \sum \overline{C}_{n,m}^{\sigma,s} P_{m,s}(\mu) \tag{6.33}$$

satisfies,

$$\begin{aligned} &\int_{-1}^{1} (\Theta(\mu))^2\, d\mu \;\; = 1 \\ &\int_{-1}^{1} \Theta_m(\mu)\,\Theta_n(\mu)\, d\mu = 0 \qquad where \;\; m \neq n \end{aligned} \tag{6.34}$$

6.3.1.4 Solution to Vertical structure equation:

Finite Difference method:

Let us reduce equation (6.22) to canonial form by the change of variables given by (6.4) or (6.7).

Let,

$$L_n = e^{x/2} Y_n \qquad and \qquad x = -\log\left(\frac{P_0}{P_0(0)}\right) \tag{6.35}$$

Therefore equation (6.22) becomes

$$\frac{d^2Y_n}{dx^2} - \frac{1}{4}\left(1 - \frac{4}{h_n}\left(\kappa H + \frac{dH}{dx}\right)\right)Y_n = \frac{\kappa J_n}{\gamma g h_n} e^{-x/2} \qquad (6.36)$$

It is seen that the above equation is a well-behaved, non-singular differential equation for the reasonable choices of H. However, except for particularly simple choices of H, there are no simple closed form solutions. This is due to the H dependence on temperature, which varies irregularly with altitude. When H is a constant (isothermal atmosphere) or when $\kappa H + dH/dx$ is a constant, (6.36) has homogeneous solutions, which are either exponential or sinusoidal. When dH/dz is constant, it may be shown that (6.36) has homogeneous solutions in the form of Bessel Functions. Treatments of tidal problems along the above lines have been given by Siebert [1961], Butler and Small [1963], Lindzen [1967a] and others. Here, we approach the solution numerically using finite difference method, which provides flexibility in the choice of H and J.

Boundary conditions for finite difference method:

Given our assumption of a smooth spherical earth, the lower boundary condition is simply $w=0$ at $x=z=0$.

For the upper boundary condition one generally requires that the kinetic energy density should remain bounded as $z \to \infty$. This in turn requires that $y_n(x)$ remains bounded as $x \to \infty$. Consider an atmosphere with an isothermal top where H is a constant and $J_n=0$. Hence (6.36) becomes

$$\frac{d^2y_n}{dx^2} - \frac{1}{4}\left[1 - \frac{4\kappa H}{h_n}\right]y_n = 0 \qquad (6.37)$$

For $h_n < 4\kappa H$ the solution of (6.37) is

$$y = Ae^{i\lambda x} + Be^{-i\lambda x} \qquad (6.38)$$

Where,

$$\lambda = \sqrt{\frac{\kappa H}{h_n} - \frac{1}{4}} \tag{6.39}$$

The term $e^{i\lambda x}$ is associated with upward propagation of energy and $e^{-i\lambda x}$ with downward propagation. Thus if there is no energy sources at $x = \infty$, then $B = 0$. It is generally referred to as the radiation condition.

Thus, for one particular mode *n*, we obtain *y* as a function of height.

Next we can calculate *u, v, w* using following formulae,

$$u = \sum_n u_n(x) U_n(\theta) \tag{6.40}$$

$$v = \sum_n v_n(x) V_n(\theta) \tag{6.41}$$

$$w = \sum_n w_n(x) \Theta_n(\theta) \tag{6.42}$$

where,

$$U_n = \frac{1}{f^2 - \cos^2\theta}\left(\frac{d}{d\theta} + \frac{s\cot\theta}{f}\right)\Theta_n$$

$$V_n = \frac{1}{f^2 - \cos^2\theta}\left(\frac{\cos\theta}{f}\frac{d}{d\theta} + \frac{s}{\sin\theta}\right)\Theta_n$$

$$u_n = \frac{\gamma g h_n e^{x/2}}{4a\omega^2}\left(\frac{dy_n}{dx} - \frac{1}{2}y_n\right) \tag{6.43}$$

$$v_n = \frac{i\gamma g h_n e^{x/2}}{4a\omega^2}\left(\frac{dy_n}{dx} - \frac{1}{2}y_n\right)$$

$$w_n = -\frac{i\sigma}{g}\Omega_n + \gamma h_n e^{x/2}\left[\frac{dy_n}{dx} + \left(\frac{H}{h_n} - \frac{1}{2}\right)y_n\right]$$

6.4 Sources of Excitation:

As discussed earlier, the sources of tidal excitation can be of two types viz. gravitational and thermal. Thermal tides are strongest and are of major concern, in the present study. Whereas gravitational source, which will be primarily due to moon and secondarily due to sun, has been ignored. Only a very small fraction of solar radiation is absorbed by the earth' s atmosphere above 100-km altitude,

hence the thermal tides are mostly excited in the middle and lower atmosphere. It has been established that O_3 and H_2O absorption in earth' s radiation budget is significant [Reddy 1988].

If infinitesimal amount of heat δQ is added per unit mass of air in infinitesimal time δt then,

$$\delta Q = J\delta t \tag{6.44}$$

where $J = J(z,\theta,\phi,t)$ is the heating rate.

Since no explicit function is known for *J*, it may be expanded as a series,

$$J = \sum_n J_n(z,\theta)e^{i(\sigma t+s\phi)} \tag{6.45}$$

Chapman and Lindzen [1970] assumed that the variables of $J_n(z,\theta)$ are separable. They considered only symmetric modes, neglecting seasonal variations and assumed that latitudinal and vertical profiles of both diurnal and semidiurnal heating rates are identical. While, Forbes and Garrett [1978], Groves [1982a,b] took seasonal variation into account. Chapman and Lindzen [1970] considered the calculation done by Manabe and Moller [1961] for water vapour heating, where bands involved are primarily the near infrared. They considered the computations done by Leovy [1964] for O_3 absorption, which essentially takes place in the Hartley and Huggins bands in the ultraviolet (2000-3700 A) and the Chappuis band in the visible region (4400-7600 A).

Forbes and Garrett [1978] used the U.S. Standard Atmosphere [1976] midlatitude ozone model for the heating calculations. Due to the flat distribution of ozone with respect to zenith angle above 35 km, latitude variations in ozone are neglected. They adopted the parameterizations given by Schoeberl and Strobel [1978] for heating by O_3 absorption, which represent improvements of the original parameterizations of ozone heating introduced by Lindzen and Will [1973]. For water vapour absorption, they used customary method as given in Siebert [1961].

In order to get more realistic estimates of thermal sources, one can consider heating due to O_3, O_2 & H_2O, which is described below and has been used in the present thesis.

6.4.1 Heating rates due to 'PHODIS':

PHODIS is a software package developed by Arve Kylling [1995] for Linux system, to calculate photodissociation rates for O_2, O_3, NO_2, CO_2…etc and also computes the heating rate due to O_3 & O_2 scattering in the wavelength region 116nm to 850nm. It provides six different model atmospheres for different latitude sectors and seasons. Here we have used the one for tropical region (15^0N). It includes pressure (mv), temperature (K), density of air, O_3, O_2, H_2O, CO_2, NO_2 (cm^{-3}) for altitudes varying from 100km to 0km. Temperature, pressure & ozone profiles are needed to calculate the optical properties i.e. optical depth, phase function and single scattering albedo (which is the ratio of optical depth of scattering to total optical depth) of the atmosphere. The package also facilitates the consideration of water cloud, cirrus cloud, background aerosols, and different albedos into the computation of heating rates. The absorption and scattering cross sections (cm^2) are taken from Molina and Molina [1986]. We modified the 'PHODIS' package to obtain the heating rates at all times of a day, at heights 0 km to 100 km, for any day of the year. Supplementary calculations of solar zenith angle at a given location and time are also made.

Figure (6.3) shows typical output from PHODIS on 21 March, at the geographic equator during noontime.

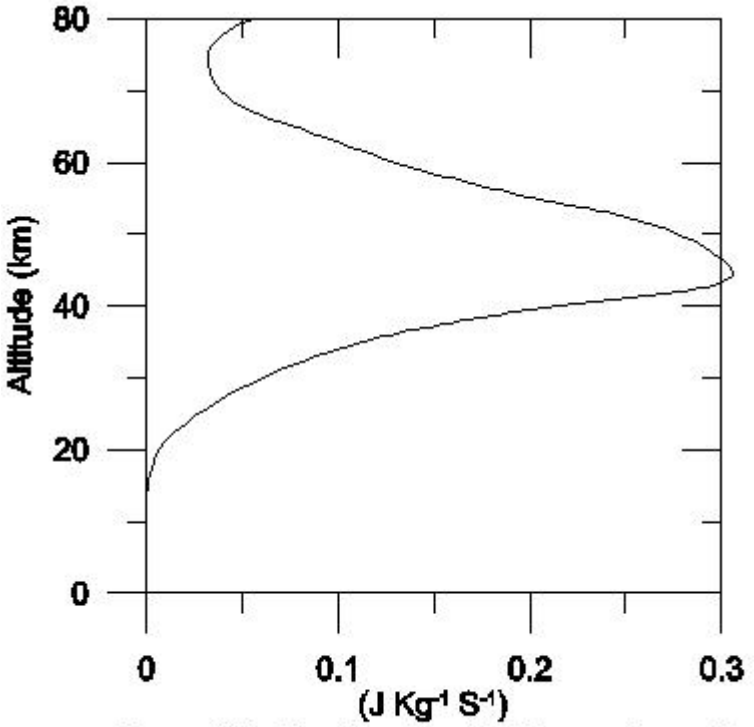

Figure 6.3: Phodis output during equinox at geographic equator at noon time.

6.4.2 H_2O heating computations:

6.4.2.1

The radiative heating rate by individual molecule is traditionally calculated by the rate of temperature change per unit time defined by

$$\frac{\partial T}{\partial t} = \frac{Q}{\rho C_p} = -\frac{1}{\rho C_p}\frac{\partial S}{\partial s} \qquad (6.46)$$

Where,

Q = Radiative heating (absorbed energy) per unit volume per unit time

ρ = Air density

C_p = specific heat at constant pressure.

S = Radiative Flux of the absorbed energy and is expressed as

$$S(u) = \sum_{\lambda} I_{\infty}(\lambda) \cdot A(\lambda, u) \qquad (6.47)$$

Where,

I_{∞} = Incident solar energy flux at the top of the atmosphere.

u = amount of absorber in the slant column of unit area is given by

$$u = \int_s^\infty n\, ds = \int_z^\infty n \sec\chi\, dz \qquad (6.48)$$

χ = solar zenith angle

n = number density

A = absorptivity which is the ratio of absorbed to incident radiation and is a function of u and wavelength λ.

Howard et al. [1956a,b] have summarized their experimental results for the integrated absorption function for each absorption band of H_2O into the following formulae,

$$A = \int_{\Delta\lambda} A_\lambda d\lambda = C u^d (P+e)^k , \qquad (6.49)$$

for weaker absorption (smaller u, u<10) and

$$A = \int_{\Delta\lambda} A_\lambda d\lambda = C + D\log u + K\log(P+e) , \qquad (6.50)$$

for stronger absorption (larger u, u ≥ 10)

Howard et al. [1956] gave the parameters *c, d, k, C, D, K* for different wavelength bands of the formulae (6.49) & (6.50) for calculating the absorption by H_2O.

Mass density (ρ) of H_2O can be converted into number density n as follows,

$$n = \frac{\rho \times 18}{6.023\times 10^{23}} \qquad (6.51)$$

Next $$u = n \times \mu \qquad (6.52)$$

where $$\mu = \frac{35}{\left(1224\cos^2\chi + 1\right)} \qquad (6.53)$$

Then, read values of *c, d, k, C, D, K* and substitute in the equations (6.49) & (6.50) to get A and then add up A's due to all the bands to get total absorbed energy. After this, in 1982, Groves gave another method to find out heating due to H_2O.

6.4.2.2 Groves Method:

In terms of hemispherically averaged downward and upward energy fluxes $F^{\downarrow}$, $F^{\uparrow}$ of solar radiation incident on a horizontal surface at height z, the heating rate per unit mass of atmosphere is

$$J_a = \frac{1}{\rho}\frac{d}{dz}\left(F^{\downarrow} - F^{\uparrow}\right) \tag{6.54}$$

Where, ρ = Air density

With clear skies the absorption of A of the downward flux is defined by

$$F^{\downarrow} = \cos\chi \; S_0(1 - A) \tag{6.55}$$

Where,

S_o = Solar flux out side of the atmosphere

χ = Solar zenith angle

For water vapour, various empirical formulae have been devised which relate A to STP path length of water vapour y. With y in cm units, Lacis & Hanjen [1974] give,

$$A(y) = \frac{2.9y}{\left[(1+141.5y)^{0.635} + 5.925y\right]} \tag{6.56}$$

For $10^{-2} \le y \le 10\,\text{cm}$ (6.56) lies within the 1% of the absorption curve of Yamamoto [1962] which in turn was derived from the low-resolution spectral measurements by Howard et al. [1956] of the major water vapour bands.

To get y, let us use, $$\mu = \frac{35}{\left(1224\cos^2\chi + 1\right)^{0.5}} \tag{6.57}$$

$\Rightarrow y = n\mu$

n = column number density of H_2O

Substitute this y in equation (6.56) to get $A(y)$ and calculate $F^{\downarrow}$ using (6.55). Let $F^{\uparrow} = 0$. Thus equation (6.54) gives heating rate due to H_2O.

In our model calculations we have used Groves method for H_2O heating.

Figure (6.4) shows heating rates due to Groves method. It shows that the major H_2O heating takes place in troposphere, but besides that secondary peak occurs near 50km altitude.

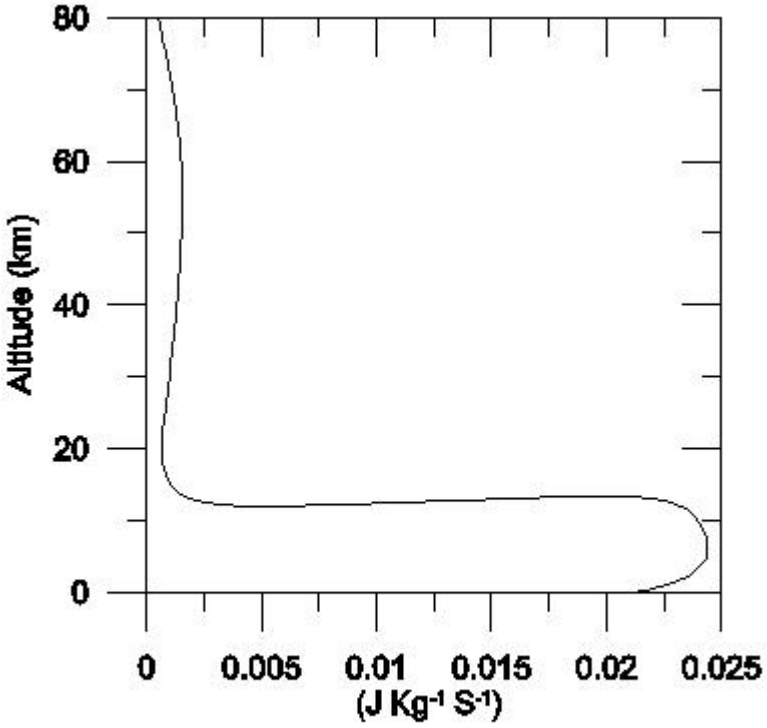

Figure 6.4: H_2O heating using Groves method during equinox at geographic equator at noon

6.5 Determination of $J^s_{m,n}$:

Equation (6.45) can be expressed in terms of Hough functions as follows

$$J = \sum_{s,m}\sum_{n} J^s_{m,n}\Theta^s_{m,n}(\mu)\, e^{i(s\phi+mt)} \qquad (6.58)$$

This yields $J^s_{m,n}$ as

$$J^s_{m,n} = e^{i(phase)}\int_0^{\pi} J_a(\theta)\,\Theta^s_{m,n}(\theta)\sin\theta\; d\theta \qquad (6.59)$$

To determine $J^s_{m,n}(z)$, one can obtain the heating rates as a function of local time, latitude and height. Then at a number of altitudes and latitudes the heating rate

is expanded in a series of Fourier harmonics of periods 24, 12 and 8hr. At each height, the latitude distribution of each Fourier coefficient is decomposed into Hough modes. Thus for each Hough mode the heating rate becomes available as a function of latitude and height.

Vertical structures of the O_3, O_2 and H_2O heating rates for semidiurnal and diurnal modes on 21st March are shown in Figures (6.5) and (6.6). It is seen from the figures that the major heating for both H_2O and (O_3+ O_2) is associated with the (2,2) and (1,-2) modes. In contrast to Chapman and Lindzen [1970], the vertical heating structure varies between different Hough modes of the same period. Groves [1982a] evaluated the diurnal and semidiurnal components of heating rate by ozone absorption in the presence of a lower reflecting layer. He used ozone density model based on observational data for January, April, July and October months at heights 0 to 80km and latitudes 0^0 to 90^0. His values were considerably lower than Chapman and Lindzen [1970] computations, whereas Forbes and Garrett [1978] calculations show higher values. The computations done here for ozone heating are more consistent with Chapman and Lindzen [1970] than Forbes and Garrett [1978]. The ratios of diurnal peak heating amplitudes (1,-2):(1,1):(1,3) for O_3 & O_2 heating in mesosphere are 1:0.26:0.07 and for H_2O heating are 1:0.27:0.07. In the case of semidiurnal tidal motions, the ratios of (2,2):(2,4):(2,6) for O_3 & O_2 heating are 1:0.39:0.22 and for H_2O heating are 1:0.36:0.21.

The shape of present water vapour heating profile is same as that computed by Forbes and Garrett [1978], but different than Chapman and Lindzen [1970]. The difference is due to the new absorption term introduced by Yamamoto [1962]. It is noticed from the plots that additional peak emerges in the lower thermosphere for O_3+O_2 heating. This is believed to be entirely due to O_2 scattering in the region 119-210 nm, evaluated by PHODIS.

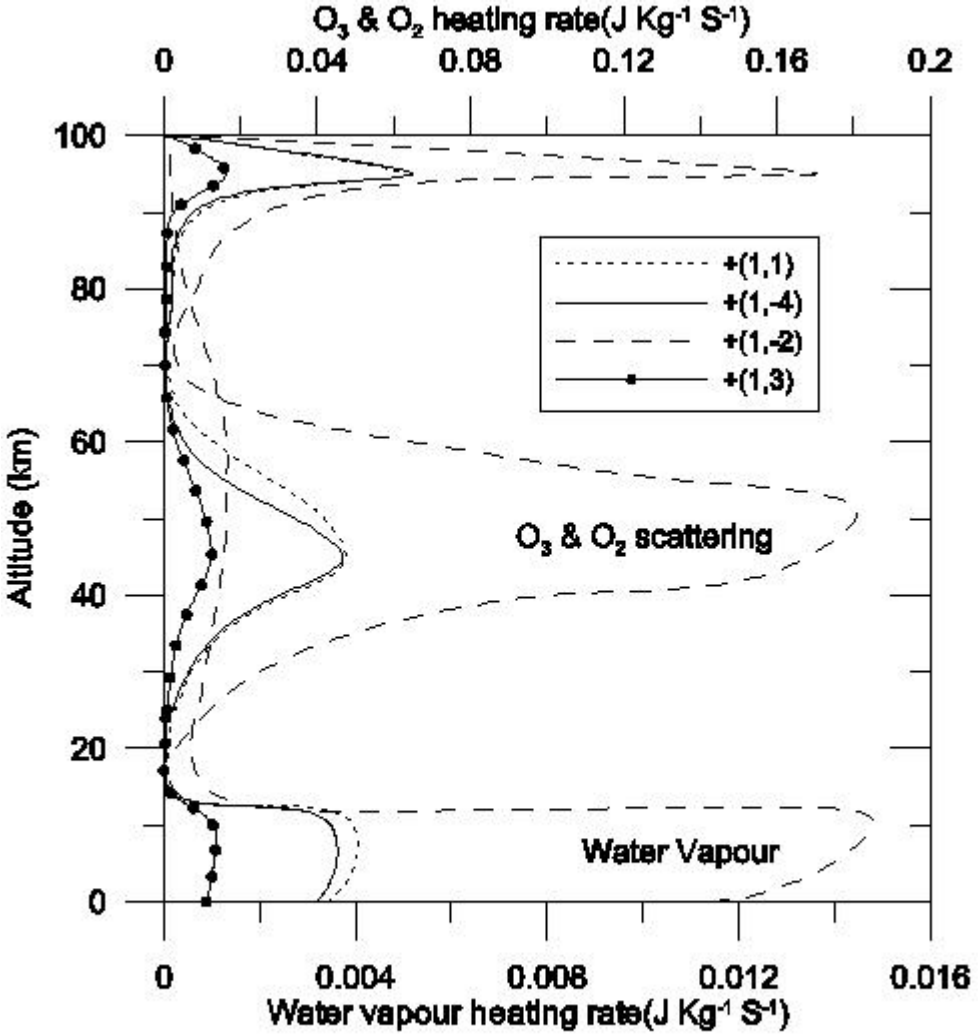

Figure 6.5: Diurnal heating rates during equinox, due to H_2O absorption and O_3 & O_2 scattering, decomposed into Hough modes.

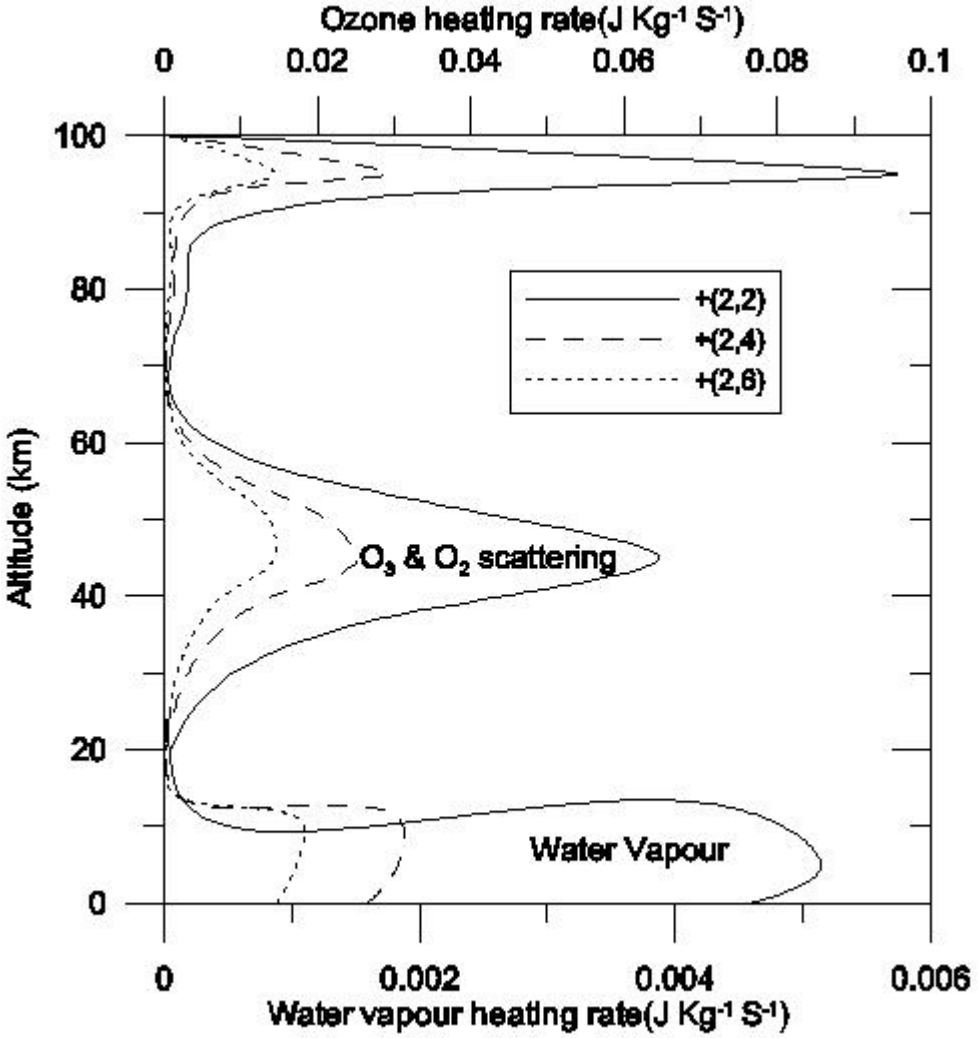

Figure 6.6: Same as figure (6.5), but for Semidiurnal component

6.6 Model Results:

Using equations (6.40), (6.41) and (6.42), the northerly (u), westerly (v) and upward (w) velocities have been computed for diurnal and semidiurnal components. We have seen in the previous section that (1,-2) and (2,2) are the most dominant modes. For diurnal calculations we have considered (1,-2), (1,1), (1,3) and (1,5) modes and the amplitude of total northerly velocity is depicted in figure (6.7). Figure (6.8) & (6.9) shows amplitude and hour of maximum for semidiurnal component of northerly velocity respectively. Semidiurnal computations include (2,2), (2,4), (2,6) modes. The basic temperature profiles

used are the equatorial standard and isothermal at 260K. It is found that the diurnal thermotidal oscillations are not much sensitive to the temperature structure, while semidiurnal oscillations in the ionosphere are.

Figures clearly depict the exponential growth of amplitude at low latitudes for diurnal tides, while semidiurnal tides exhibit the similar behaviour at all latitudes. It has been observed from the figures that in the lower thermosphere solar semidiurnal winds are as large as the diurnal winds, except that they tend to be greater at middle to higher latitudes whereas the diurnal winds are largest at low latitudes. The results obtained here are comparable with those by Chapman and Lindzen [1970] for diurnal and semidiurnal components.

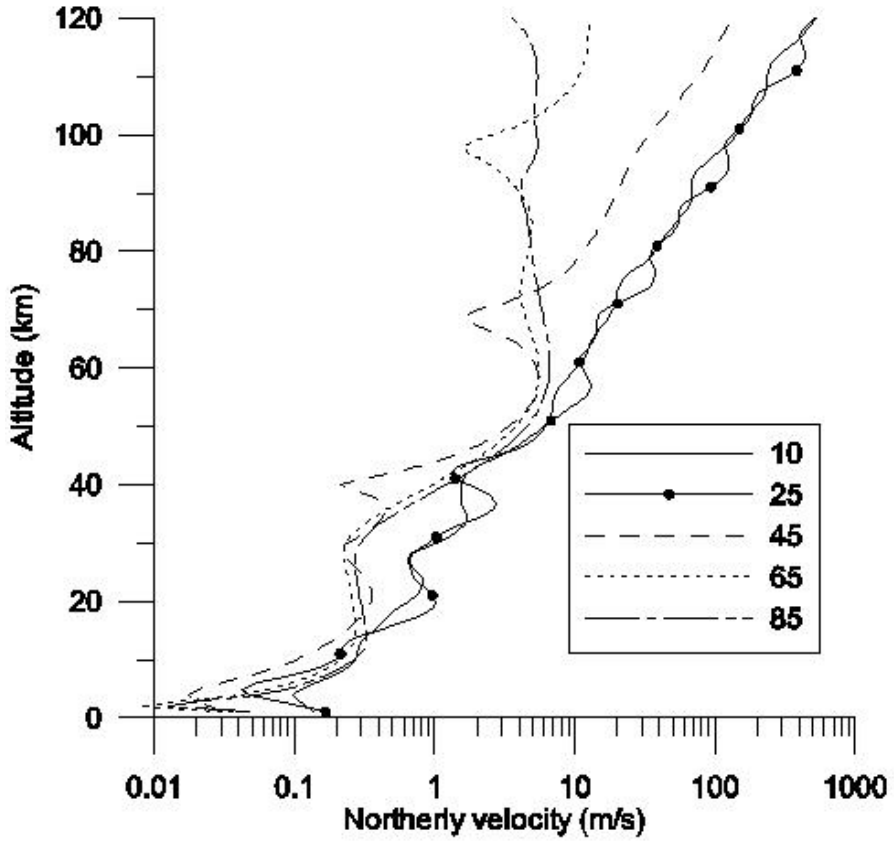

Figure 6.7: Amplitude of the solar diurnal component of u at various latitudes, Isothermal $T_0(z)$ assumed.

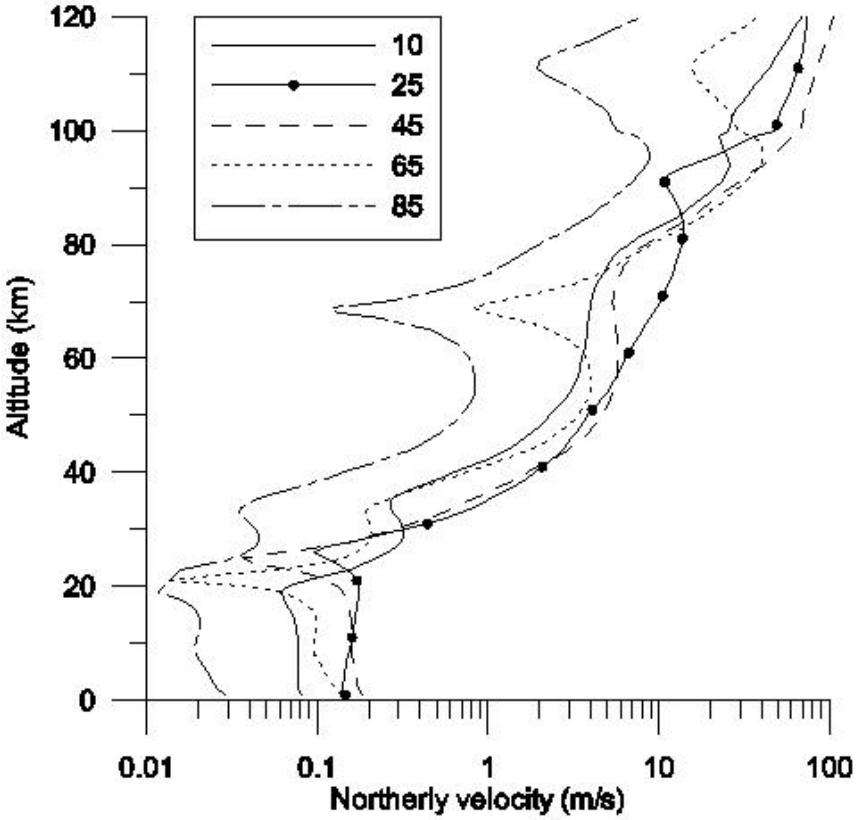

Figure 6.8: Amplitude of the solar semidiurnal component of u at various latitudes Equatorial $T_0(z)$ assumed.

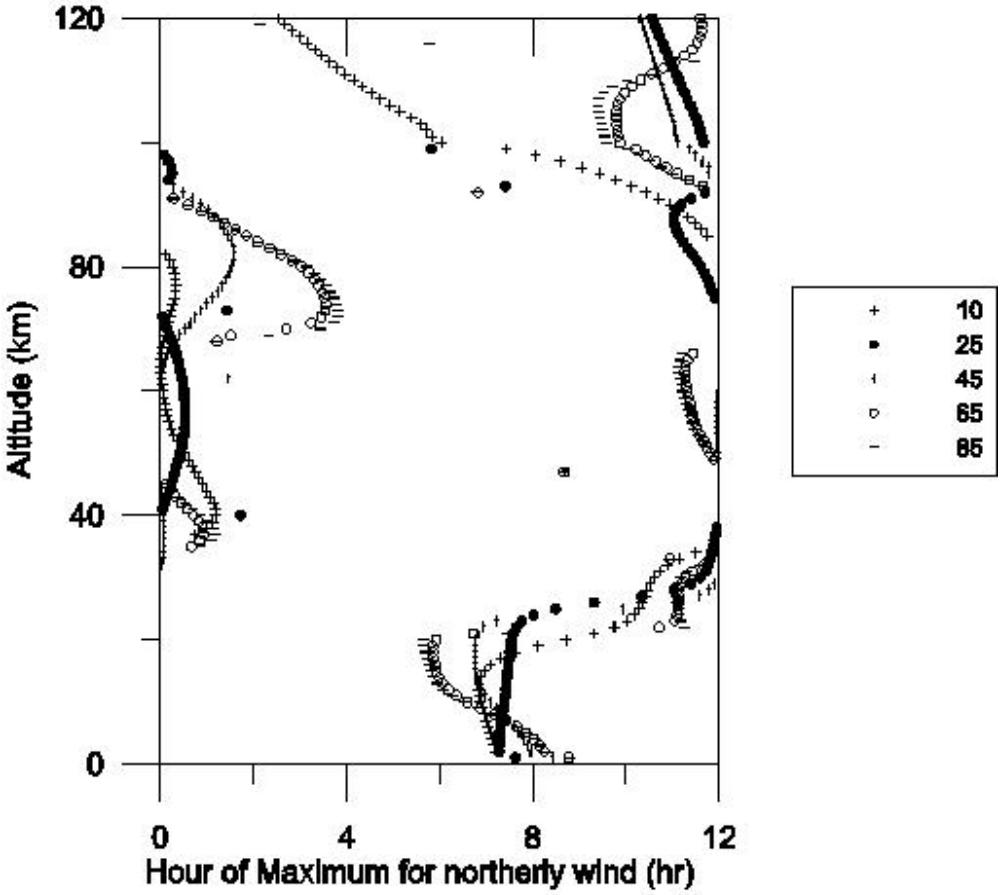

Figure 6.9: Phase (hour of maximum) of the solar semi-diurnal component of u at various latitudes; Equatorial $T_0(z)$ assumed.

Thus in this chapter, a three dimensional model of the thermospheric tidal structure for equinox conditions is constructed, where input heating rates are more reliable, but it has ignored all dissipative type mechanisms.

6.7 Global Scale Wind Model:

The Global-Scale Wave Model (GSWM) solves the linearized and extended Navier-Stokes equations for steady-state global temperature and wind perturbations. The GSWM Fortran code currently runs on NCAR' s Cray J90 computer.

Standard GSWM tidal results account for realistic tidal forcing due to ozone (absorption of solar UV radiation) and water vapor (absorption of solar IR radiation). Above 12km the standard model run uses background winds determined from measurements made by the HRDI instrument on UARS. The data are 6-year monthly and zonally averaged values that are smoothed and interpolated. Below 12km the winds are from the semiempirical model of Groves/MSIS. The GSWM background temperature and density are taken from the MSISE90 model using a 10.7-cm solar flux value of 120 and an Ap of 4. Background ozone concentrations can also be modified for numerical experiments. The standard configuration uses 6-year monthly and zonally averaged measurements from the HALOE instrument on the UARS satellite below 50 km and UARS MLS measurements above 50 km.

Upward propagating tidal amplitudes increase with altitude as the density of the atmosphere decreases, however wave dissipation effects become important in the middle and upper atmosphere. GSWM accounts for a number of tidal dissipation effects. Tidal damping may come from many strong and weak mechanisms. Other short-term or small-scale waves that originate according to terrain, called gravity waves, tend to disrupt tidal components by causing turbulence and accelerating the air along with the global-scale tide. Between 80-100km, at the mesopause, gravity waves become large enough to interfere with diurnal tides by "dragging" the background atmosphere to the phase speed of the tide, and by causing eddy currents that disrupt energy propagation.

Above about 90-100km in the lower thermosphere, the decreasing density of the air causes wave motion to be dominated by molecular diffusion rather than fluid flow, decreasing the efficiency of energy transfer, and further dampening the tides. Above the thermosphere, tides are dissipated by the radiation of energy into space (Newtonian cooling) and drag caused by the tides' acceleration of charged particles in the ionosphere.

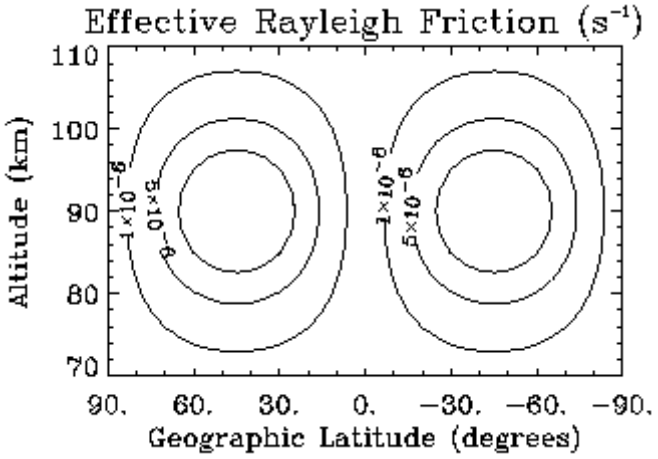

Figure 6.10: Rayleigh friction coefficient

The GSWM uses an effective Rayleigh friction coefficient (after Miyahara and Forbes, 1991] in calculations of the diurnal tide to parameterize gravity wave drag effects. The above figure (6.10) shows the GSWM coefficients for solstice conditions. The equivalent equinoctal coefficients are an order of magnitude smaller.

The turbulence generated by breaking or dissipating gravity waves generates diffusion effects, which are felt by all tidal fields. GSWM calculates the divergence of heat and momentum flux due to eddy diffusion directly using coefficients after Garcia and Solomon [1985]. Illustrations of GSWM January and April eddy diffusion coefficients indicate the magnitude of the altitudinal, latitudinal, and seasonal variations associated with this dissipative effect.

Thus, the model also accounts for the effects of empirical background climatologies of zonal mean temperature, neutral density, zonal wind and ozone concentration, as well as wave dissipation.

A typical amplitude counter plot from GSWM for diurnal tides on a grid of altitude verses latitude is shown in figure (6.11) below. These results match well with our model calculations below 120-km altitude. But above 120-km, the

GSWM values are less in magnitude due to the dissipative forces taken into account.

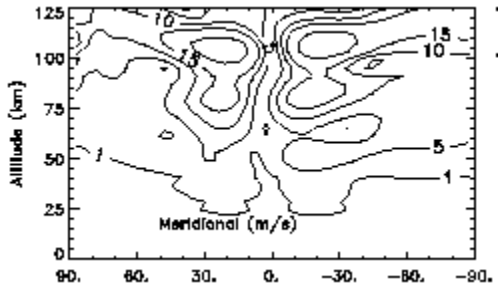

Figure 6.11: Output from GSWM

6.8 Summery:

Though GSWM is the most rigorous and widely accepted model used for tidal studies, it has many limitations as regards the motivation of the present studies.. GSWM provides values only during four months viz. January (solstice), April (equinox), July (solstice) and October (equinox). Secondly, it considers only symmetric modes, while observations show that the antisymmetric components are also important in the tidal study. GSWM does not make a mention of the modes used for the computation of diurnal and semidiurnal motions. It also does not account for the non-migrating tides, which are vital as reflected in our observational studies (refer to chapter 3 and 4).

Our model calculations use more recent ways of computing the heating source and more suited to study the tidal motions in the equatorial region. The present model takes into account any number of modes viz. (1,-2),(1,1),(2,2) ..etc. as far as the limitations of our approach are concern, it does not account for the dissipative forces that can be caused by turbulence, molecular diffusion of heat and momentum, infrared cooling and ion drag etc. It also does not incorporate the tidal interactions of gravity waves in the mesosphere. Inspite of the drawbacks, our model is more suited to examine the tidal effect on EEJ.

The computation of heating rates in this chapter is essentially for the middle atmosphere i.e. below 100km altitude. In the thermosphere (> 80 km), the sources of tidal excitations are (1) In situ absorption of EUV (20-100 nm), UV (120-175 nm) and Schumann-Runge radiation (175-200 nm) in the range of 90-200 km altitude. (2) In situ momentum coupling arising from the interaction of diurnal winds and diurnally varying ion drag in the F region. (3) The energy and momentum of propagating tides arriving in the thermosphere from the lower atmosphere where they are originally excited. Since PHODIS, calculates the heating rates for the wavelength region 116-850 nm, the (1) has been partially taken into account. Hence heating rates show additional peak in the thermosphere. This makes the velocities to increase, but since dissipative forces are not taken into account the magnitudes remain large, which is inconsistent with the observations. The above sources of excitation in the thermosphere has been analyzed by Forbes [1982a,b].

Comparison of migrating tidal model with the measurements gives some unsolved features. Part of the discrepancy may be due to the contribution to the total tide of the non-migrating component. Non-migrating tidal components are also harmonics of a solar day, but unlike migrating tides, they do not have a zonal wavenumber equal to their frequency. This means that they may be stationary, or propagate either eastward or westward. CRISTA 1 mission [Ward et al. 1999] and radar observations at Tirunelvelli have found that the actual observed amplitudes are less than GSWM predictions. This could be attributed to the different background temperature profiles or the presence of non-migrating tides.

Garrete and Forbes [1978] solved the tidal equations for a spherical, rotating, viscous atmosphere with anisotropic ion drag. They used this model for the predictions regarding the variation of the thermospheric structures with height, latitude, local time, and solar cycle and found many features of thermospheric

structure which could not be recovered from any available combination of incoherent scatter and/or satellite measurements.

Thus, it should be clear from the chapter that the tidal theory results do not yet give good match with observations. This needs further refinement of inclusion of non-migrating tides, dissipative forces and more realistic background temperature profile.

The program and the method of solution adopted here, is such that it can perform tidal computations for any mode, e.g. two-wave, planetary scale waves etc., provided the corresponding heating terms are available. Hence, we can examine how the electrojet model responds to different tidal modes. It is this very point where our model scores over GSWM. Even though the GSWM is made more general by relaxing the assumptions in the classical theory, it does not stand with actual observations. The main aim of this chapter is to provide the tidal model, which is flexible for different parameters involved such as temperature, pressure, different tidal modes etc. so that day to day variability of the tidal components can be studied. This will further go as input for electrojet modelling computations. Since GSWM lacks the possibility of computations on day to day basis, it does not fulfill our requirement. Hence we recommend our model computations for the calculation of Equatorial Electrojet modelling.

Chapter 7
Ionospheric Conductivity

In the first chapter, we have introduced the term ionospheric conductivity. In order to estimate the ionospheric currents, which is the principal interest of the present thesis, the knowledge of conductivity is essential. Hence in the present chapter, we have carried comprehensive study of ionospheric conductivity.

7.1 Theoretical consideration:

Earth' s geomagnetic field plays a very important role in determining the conductivity of the ionosphere. In order to understand this let us consider the motion of ions and electrons in the presence of a magnetic field $\vec{B}$, an electric field $\vec{E}$ and net collision frequency υ with the background neutrals. The equation of motion for a particle of mass M, velocity $\vec{V}$ and charge q in the rest frame of the neutral medium can be expressed as:

$$\frac{d}{dt}\vec{V} = \frac{q}{M}(\vec{E} + \vec{V} \times \vec{B}) - \upsilon \vec{V} \qquad (7.1)$$

In the absence of collision, the particle will gyrate with a cyclotron frequency $\omega = \frac{qB}{M}$ around the magnetic field. If the magnetic field is measured in nT, the electron cyclotron frequency is given by $\omega_e \approx 176B\,(nT)$ and the ion cyclotron frequency by $\omega_i = 0.097\frac{B}{A}(nT)$, where A is the ionic mass in atomic mass units. In the ionosphere, the electron cyclotron frequency is more than 10^4 times the typical ion cyclotron frequency. The electrons gyrate in anti-clockwise direction while the ions in the clockwise direction.

The ion and electron velocities are measured with respect to the background neutrals. The last term in equation (7.1) tries to bring down the velocity of particles to neutral velocity (zero by choice of the frame of reference). If the first term on the right hand side were not there, the velocity of the particle would exponentially go down to zero as $V_o e^{-\upsilon t}$, where V_0 is the velocity of the particle at time zero.

In the absence of electric fields, the charged particles move with a constant velocity $V_{//}$ along the magnetic field. The effect of electric field depends on whether the electric field is parallel or perpendicular to the field. In the presence of an electric field parallel to the magnetic field, denoted by $E_{//}$, the parallel velocity, $V_{//}$, will increase indefinitely within non-relativistic limit unless collisions are there. If the collisions are there, then the final velocity is given by

$$V_{II} = \frac{qE_{II}}{M\upsilon} \qquad (7.2)$$

In most of the ionosphere '$M\upsilon$' is so small (at least for the electrons), that $E_{//} \approx 0$ to have reasonable values of $V_{//}$. In other words electrons will short out any electric field parallel to the magnetic field. The magnetic field line is, therefore, nearly an equipotential and the ionospheric conductivity parallel to the magnetic field is very large. We note straightaway that the ionospheric conductivity is highly anisotropic.

In order to estimate the conductivity from the motions of electrons and ions due to the component of the electric field perpendicular to the magnetic field (denoted by $E_{\perp}$), we have to appreciate the fact that the motion can be resolved into two components with widely differing time scales. The cyclotron motions are rapid while the drifts of our interest are essentially due to quasi-static electric fields. The velocity $\vec{V}$ can be expressed as

$$\vec{V} = \vec{V}_D + \vec{v}$$

Where $\vec{v}$ represents the fast varying cyclotron motion and $\vec{V}_D$ the slowly varying drift whose time variations are of lower order. The cyclotron motions take care of the time variation while the drift term can be obtained by putting the right hand side to zero. In the absence of collisions ($\upsilon = 0$), a vector cross product with the magnetic field vector $\vec{B}$ yields

$$\vec{V}_D = \frac{\vec{E}_\perp \times \vec{B}}{B^2} \; . \qquad (7.3)$$

$\vec{V}_D$ cancels out the electric field effect in the first term on right hand side of momentum equation and we have only an additional gyration motion of the particles. Note $\vec{V}_D$ is independent of charge and mass and thus both electrons and ions will move with same velocity and therefore there will be no net currents due to this drift. Thus in the absence of collisions, the electric field cannot sustain any currents.

In the presence of collisions, a slightly different approach is followed. It is obvious from equation (7.1), that the right hand side will vanish only if $\vec{V}_D$ has a component along $\vec{E}$ as well as a component along $\vec{E} \times \hat{b}$, where $\hat{b}$ is a unit vector along $\vec{B}$. $\vec{V}_D$ can be expressed as $\vec{V}_D = \alpha \, \vec{E}_\perp + \beta \, \vec{E}_\perp \times \hat{b}$ and α, β can be evaluated by substituting it back in equation (7.1). Using the fact that $\left(\vec{E}_\perp \times \hat{b}\right) \times \hat{b} = -\vec{E}_\perp$, the drift can be expressed as

$$\vec{V}_D = \frac{1}{B} \frac{\omega^2}{\omega^2 + \upsilon^2} \vec{E}_\perp \times \hat{b} + \frac{1}{B} \frac{\omega \upsilon}{\omega^2 + \upsilon^2} \vec{E}_\perp \qquad (7.4)$$

The first term in the drift has the same sign for both the ions and electrons but will contribute to the currents in the ionosphere when there is a relative difference between the collision frequencies of the species. The second term, which becomes significant if υ is larger, has opposite sign for electrons and ions because of the sign of ω and is also responsible for existence of currents in the

ionosphere. Because of collisions, the magnitude of drifts for ions and electrons are also different. As $\nu \to 0$, drifts tend to the same value and the electric field does not produce any currents as noted from equation (7.3). Finally, the first term of equation (7.4) contributes to Hall current while the second term produces the Pedersen current.

The current $\vec{J}$ is defined as the sum of total electron and ion currents and is given by

$$\vec{J} = n_i e\vec{V}_{Di} - n_e e\vec{V}_{De} = ne\left(\vec{V}_{Di} - \vec{V}_{De}\right)$$

where n_e and n_i are electron and ion densities and $\vec{V}_{De}$ and $\vec{V}_{Di}$ are electron and ion drift velocities respectively. In practice there may be more than one species, which can be easily accommodated through a summation. The electron and ion number densities can be taken equal *(= n)* in the ionosphere as charge neutrality is satisfied to a very high degree of accuracy. In the above expression, $e = 1.6022 \cdot 10^{-19}$ C is the magnitude of the charge of an electron.

Using equation (7.4), $\vec{J}$ can be expressed as

$$\vec{J} = \sigma_0 \vec{E}_{\parallel} + \sigma_1 \vec{E}_{\perp} + \sigma_2 \hat{b} \times \vec{E}_{\perp} \qquad (7.5)$$

Where σ_0, σ_1 and σ_2 are parallel, Pedersen and Hall conductivities respectively.

$$\sigma_0 = ne^2\left(\frac{1}{M_i \nu_i} + \frac{1}{M_e \nu_e}\right) \qquad (7.6a)$$

$$\sigma_1 = \frac{ne}{B}\left(\frac{\frac{\nu_i}{\omega_i}}{1+\frac{\nu_i^2}{\omega_i^2}} + \frac{\frac{\nu_e}{\omega_e}}{1+\frac{\nu_e^2}{\omega_e^2}}\right) \qquad (7.6b)$$

$$\sigma_2 = \frac{ne}{B}\left(\frac{1}{1+\frac{\nu_e^2}{\omega_e^2}} - \frac{1}{1+\frac{\nu_i^2}{\omega_i^2}}\right) \qquad (7.6c)$$

Note that the Hall current is mainly associated with the electrons while Pedersen currents are carried by the ions. The subscripts *e* and *i* signify the values of the parameters for the electrons and ions respectively.

Similarly, longitudinal, Pedersen and Hall mobilities of species '*s*', of mass M_s and density n_s are defined as

$$\mu_{0s} = \frac{e\, n_s}{M_s \upsilon_s}$$

$$\mu_{1s} = \frac{e\, n_s \upsilon_s}{M_s\left(\omega_s^2 + \upsilon_s^2\right)} \qquad \text{and}$$

$$\mu_{2s} = \frac{e\, n_s \omega_s}{M_s\left(\omega_s^2 + \upsilon_s^2\right)}$$

7.2 Standard Conductivity Profiles:

Expression derived for parallel, Pedersen and Hall conductivity, viz. (7.6a), (7.6b) and (7.6c) can be rewritten as

$$\sigma_0 = e^2\left(\frac{n_e}{m_e \nu_e} + \frac{n_-}{m_- \nu_-} + \frac{n_+}{m_+ \nu_+}\right) = \frac{1}{B}\sum_r \frac{e_r n_r \omega_r}{\nu_r} \qquad (7.7)$$

$$\sigma_1 = \frac{1}{B}\sum_r \frac{e_r n_r \nu_r \omega_r}{\nu_r^2 + \omega_r^2} \qquad (7.8)$$

$$\sigma_2 = -\frac{1}{B}\sum_r \frac{e_r n_r \omega_r^2}{\nu_r^2 + \omega_r^2} \qquad (7.9)$$

where, the summation is taken over *r* = e(electrons), - (negative ions), + (positive ions).

Thus, in construction of conductivity model, knowledge of the charge particle composition as well as the effective collision frequencies for momentum transfer between the ions, neutrals, and electrons is required. Chapman [1956] formulated the conductivities for the appropriate ionospheric conditions. Richmond [1972] gave a sophisticated conductivity model using Chapman's formalism. In his model he solved for the photochemistry of the E region, taking into account all the processes of photoionization, recombination, etc., and making some empirical rate coefficient adjustments to fit observed data. This has been discussed further in more detail.

7.2.1 Richmond's Conductivity model:

In this model, the densities of electrons and ions are computed by balancing photoionization rates with chemical loss rates in an infinite plane atmosphere.

The XUV spectrum is divided into 48 bands. The flux Φ_n for the n^{th} band is dependent on the solar 10.7 cm radiation index, $F_{10.7}$ according to

$$\phi_n = \phi_n^0 \left(\frac{F'_{10.7}}{F^0_{10.7,n}} \right) P_n \qquad (7.10)$$

where

$$F'_{10.7} = F_{10.7} - 0.0573\left(F_{10.7} - 143\right) - 0.001273\left(F_{10.7} - 143\right)^2 \qquad (7.11)$$

and ϕ_n^0 is the flux at the solar activity level represented by $F^0_{10.7,n}$, based on data of Swider [1969] and Hinteregger [1970]; and P_n is a power derived from data of Swider [1969] and Hall and Hinteregger [1970]. Equation (7.11) is empirically determined to yield the following relation between the maximum E-region electron density at the subsolar point and the true $F_{10.7}$ index as

$$N_m(E) = 10971 \times 10^5 \left(\frac{F_{10.7}}{143} \right)^{0.422} cm^{-3}$$

7.2.1.1 Photoionization rates:

The absorption cross sections, $A_{j,i}$, ionization coefficients, $\eta_{j,i}$, and fractions of N_2 & O_2 which are dissociatively ionized, $\xi_{1,i}$ and $\xi_{2,i}$ are based mainly on Richmond [1970]. The photo-production rates of N_2^+, O_2^+, O^+, and N^+ are

$$\begin{aligned}
Q_1 &= n_1 \sum_{i=1}^{48} \phi_i e^{-\mu_i} \left[1-\xi_{1,i}\right] \eta_{1,i} A_{1,i} \\
Q_2 &= n_2 \sum_{i=1}^{48} \phi_i e^{-\mu_i} \left[1-\xi_{2,i}\right] \eta_{2,i} A_{2,i} \\
Q_3 &= n_2 \sum_{i=1}^{48} \phi_i e^{-\mu_i} \xi_{2,i}\ \eta_{2,i} A_{2,i} + n_3 \sum_{i=1}^{48} \phi_i e^{-\mu_i}\ \eta_{3,i} A_{3,i} \\
Q_4 &= n_1 \sum_{i=1}^{48} \phi_i e^{-\mu_i} \xi_{1,i}\, \eta_{1,i} A_{1,i}
\end{aligned} \tag{7.12}$$

where

$$\mu_i = \frac{1}{\cos\chi} \sum_{j=1}^{3} A_{j,i} \int_h^{\infty} n_j(h')dh' \tag{7.13}$$

χ is a solar zenith angle. n_1, n_2, n_3 are the neutral densities of N_2, O_2 and O respectively.

7.2.1.2 Neutral Number densities and Temperatures:

For the heights above 120 km, the neutral densities n_1, n_2, n_3 are given by Jacchia [1971], it also gives neutral temperature T_n . Thus for heights above 120 km,

$$T_e = T_n + \left[T_e(150) - T_n\right] \cdot \left(\frac{F'_{10.7}}{150} \right) \tag{7.14}$$

where

$$T_e(150) = T_n + (h-120) \cdot (7^0\ per\ km) \tag{7.15}$$

h is altitude in km. This formula is designed to give a reasonable solar cycle variation of N_m(F1).

The height integrated number density of the i^{th} neutral species from altitude h to the top of the atmosphere is,

$$\int_h^\infty n_i(h')dh' = \frac{kT_n(h)}{m_i g} n_i(h) \qquad (7.16)$$

for an atmosphere in diffusive hydrostatic equilibrium, where k is the Boltzmann constant, n_i and m_i are the number density and molecular mass of the i^{th} species, and g is the acceleration due to gravity.

For the heights below 120 km, neutral densities are taken from Keneshea et al. [1972], it also provides height integrated number densities. Below 120 km, hydrostatic equilibrium does not apply to the individual species, but it does apply to the gas as a whole. Then the neutral and electron temperatures are found from

$$T_n(h) = \frac{g\sum_i m_i \int_h^\infty n_i(h')dh'}{k\sum_i n_i(h)} \qquad (7.17)$$

and

$$T_e(h) = T_n(h)$$

7.2.1.3 Electron and Ion densities:

Ions N_2^+, O_2^+, O^+, and N^+ are lost mainly through the following reactions:

(1) $N^+ + O_2 \xrightarrow{k1} O_2^+ + N$

(2) $N^+ + O_2 \xrightarrow{k2} NO^+ + O$

(3) $N_2^+ + O_2 \xrightarrow{k3} O_2^+ + N_2$

(4) $N_2^+ + O \xrightarrow{k4} NO^+ + N$

(5) $O^+ + O_2 \xrightarrow{k5} O_2^+ + O$

(6) $O^+ + N_2 \xrightarrow{k6} NO^+ + N$

(7) $O_2^+ + e^- \xrightarrow{k7} O + O$

(8) $NO^+ + e^- \xrightarrow{k8} N + O$

(9) $O_2^+ + NO \xrightarrow{k9} NO^+ + O_2$

(10) $O_2^+ + N \xrightarrow{k10} NO^+ + O$

Reaction rates *k1,……,k6* are taken from Richmond [1970].

Upon balancing production and loss rates for NO^+, O_2^+, and O^+, we get their respective densities as

$$D_1 = \frac{Q'_{NO^+}}{k8 \cdot D_4}$$

$$D_2 = \frac{Q'_{O_2^+}}{k7 \cdot D_4} \qquad (7.18)$$

$$D_3 = \frac{Q_3}{k5 n_2 + k6 n_1}$$

where, Q'_{NO+} and Q'_{O2+} are the net production rates of NO^+ and O_2^+, which are derived by taking into account the charge-transfer reactions, and D_4 is electron density.

Charge neutrality requires that

$$D_4 = D_1 + D_2 + D_3$$

so that D_4 is found to be

$$D_4 = \frac{D_3}{2} + \left[\left(\frac{D_3}{2} \right)^2 + \frac{Q'_{O_2^+}}{k7} + \frac{Q'_{NO^+}}{k8} \right]^{1/2} \qquad (7.19)$$

The recombination rates k7 and k8 are empirically chosen to provide approximate observed E and F1 peak electron densities.

7.2.1.4 Collision to Gyrofrequency ratios:

The following formulas are derived from the ion mobility data of Mason [1970] for NO^+, O_2^+, and O^+ ions respectively

$$\frac{\upsilon_1}{\omega_1} = \left\{ (1.07 n_1 + 1.06 n_2) \left(\frac{T_N}{500^0 K} \right)^{-0.16} + 0.60 \left(\frac{T_N}{500^0 K} \right)^{-0.19} n_3 \right\} \frac{10^{-12}\ gauss\ cm^3}{B}$$

$$\frac{\upsilon_2}{\omega_2} = \left\{ 1.08 \left(\frac{T_N}{500^0 K} \right)^{-0.17} n_1 + 2.02 \left(\frac{T_N}{500^0 K} \right)^{0.37} n_2 + 0.61 \left(\frac{T_N}{500^0 K} \right)^{-0.19} n_3 \right\} \frac{10^{-12}\ gauss\ cm^3}{B}$$

and

$$\frac{\upsilon_3}{\omega_3} = \left\{ 0.89 \left(\frac{T_N}{500^0\, K} \right)^{-0.20} n_1 + 1.16 \left(\frac{T_N}{500^0\, K} \right)^{0.05} n_2 + 0.89 \left(\frac{T_N}{500^0\, K} \right)^{0.36} n_3 \right\} \frac{10^{-12}\, gauss\, cm^3}{B}$$

The experimental data of Pack and Phelps [1961,1966] for e^--N_2 and e^--O_2 collisions and theoretical estimates of Henry and McElroy [1968] and Itikawa [1971] for the momentum transfer cross section of e^-- O collisions yield

$$\left| \frac{\upsilon_4}{\omega_4} \right| = -\frac{\upsilon_4}{\omega_4} = \left\{ 2.59 \left(\frac{T_e}{300^0\, K} \right)^{0.90} n_1 + 2.44 \left(\frac{T_e}{300^0\, K} \right)^{0.55} n_2 + 0.83 \left(\frac{T_e}{300^0\, K} \right)^{0.83} n_3 \right\} \frac{10^{-16}\, gauss\, cm^3}{B}$$

This model neglects the electron-ion collisions. The estimated collision frequencies have accuracies of 25% or better for the interactions relevant to the earth's E-region. The above theoretically derived estimates [Mason 1970] for the collision frequencies, are based upon the interactive forces of ion-neutral collisions. In cases where, drift tube measurements of ion mobilities are available, Mason's estimates agree well with the experimental values. However, most of these experiments are valid for temperatures less than 300^0 K, where ion-neutral interactions are dominated by induced dipole forces. The collision frequencies are relatively easy to compute if the ion charge and neutral particle polarizability are known. Above 300^0 K, the short-range quantum mechanical repulsion and resonant charge exchange become dominant, and these effects are more difficult to estimate. In above estimates of collision frequencies, which decrease with temperature, are derived for short-range quantum mechanical repulsion; those that increase with temperature indicate resonant charge exchange as the dominant interactive mechanism. The errors in the relative number densities of N_2, O_2, and O have only minor effects on the conductivity distribution.

7.2.1.5 Conductivity Profile:

Thus parallel, Pedersen and Hall conductivities are computed between 80 km to 200 km using

$$\sigma_0 = \sum_{j=1}^{4} \frac{D_j q_j}{B} \cdot \frac{\omega_j}{\upsilon_j} \tag{7.20}$$

$$\sigma_1 = \sum_{j=1}^{4} \frac{D_j q_j}{B} \cdot \frac{\upsilon_j / \omega_j}{1 + \left(\upsilon_j / \omega_j\right)^2} \tag{7.21}$$

and

$$\sigma_2 = -\sum_{j=1}^{4} \frac{D_j q_j}{B} \cdot \frac{1}{1 + \left(\upsilon_j / \omega_j\right)^2} \tag{7.22}$$

where, q_j is the charge of the j^{th} charged species. Above 200 km, Pedersen and Hall conductivities are calculated by extrapolation, which are assumed to be approximately

$$\sigma_1(h) = \sigma_1(200\,km) e^{-0.02(h-200)} \tag{7.23}$$

and

$$\sigma_2(h) = \sigma_2(200\,km) e^{-0.04(h-200)} \tag{7.24}$$

where h is in kms.

Typical plots of electron density and conductivities based on this Richmond's model are shown in Figure (7.1), whereas ratios of collision to gyro-frequencies, are shown in Figure (7.2).

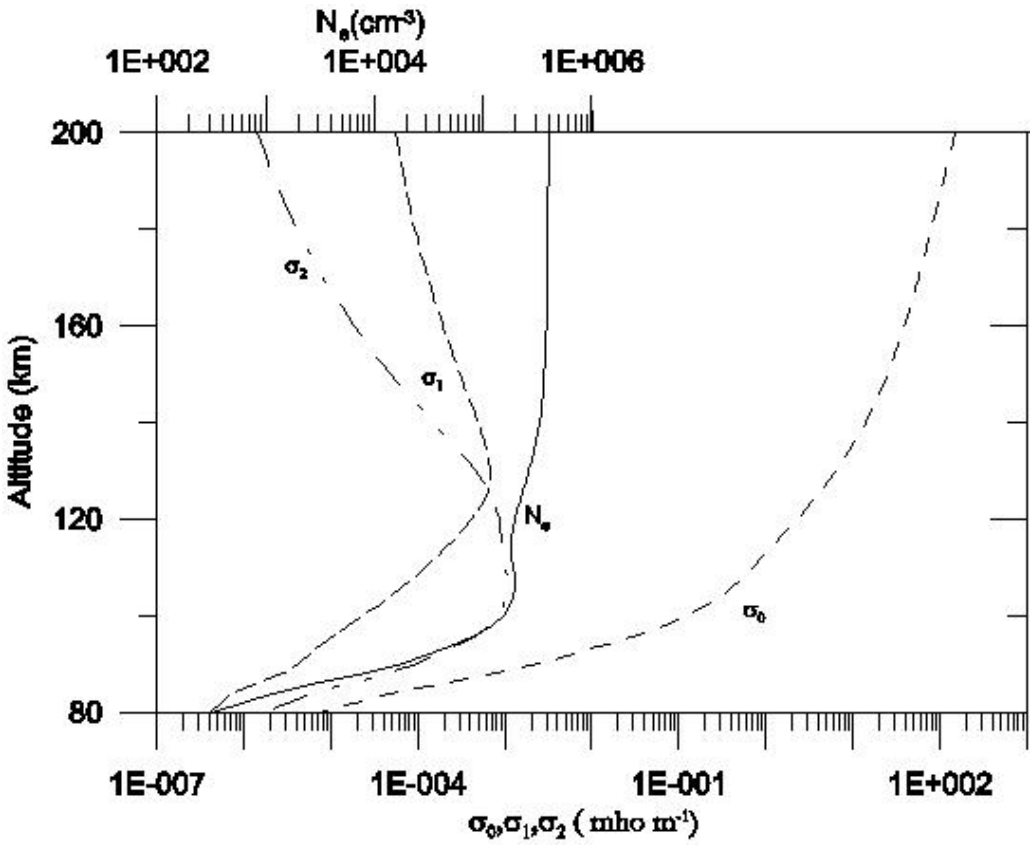

Figure 7.1 : Electron densities and conductivities at χ=0, after Richmond's model

It is seen from figure (7.2) that, ratios (υ/ω) for NO^+, $O2^+$ and O^+ ions are almost identical; while that for electrons has magnitude of order 4 less.

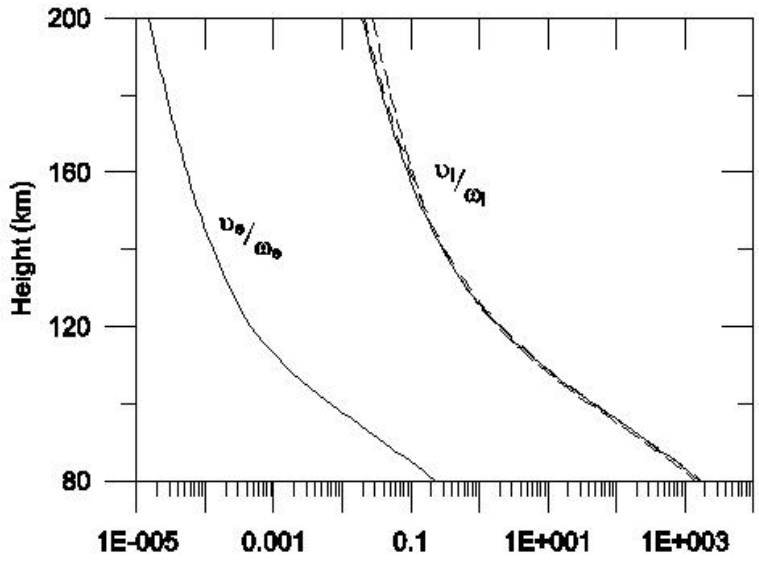

Figure 7.2: Ratio of collision to gyrofrequencies for electrons (υ_e/ω_e) and for NO^+, O_2^+, and O^+ ions (υ_i/ω_i)

7.2.2 Forbes Model:

Forbes and Lindzen [1976] recalibrated the Richmond's model to fit a different set of observed electron concentrations [Rush and Miller,1973].

Although electron-ion collisions are negligible in the lower E region, υ_{ei} becomes comparable with υ_{en} above about 140 km. Forbes uses Nicolet's [1953] expression for the electron-ion collision frequency

$$\upsilon_{ei} = \left[34 + 4.18 \log_{10}\left(\frac{T^3}{[e]} \right) \right] [e] 10^{-6} T^{-3/2} \quad mks \;\; units \qquad (7.25)$$

Here the Debye radius determines the cross section for momentum transfer due to the long-range Coulomb nature of the interactions. The experimental work of Anderson and Goldstein [1955] supports equation (7.25).

Figure (7.3) shows the comparison between conductivity profile due to Forbes' model and Richmond's model. From 120 km onwards, the ratio of collision to gyrofrequency for electrons differ, and at 200 km it is almost twice, hence parallel

conductivity from Forbes model becomes half of the Richmond's estimates at 200 km. Pedersen and Hall conductivities retain their magnitudes.

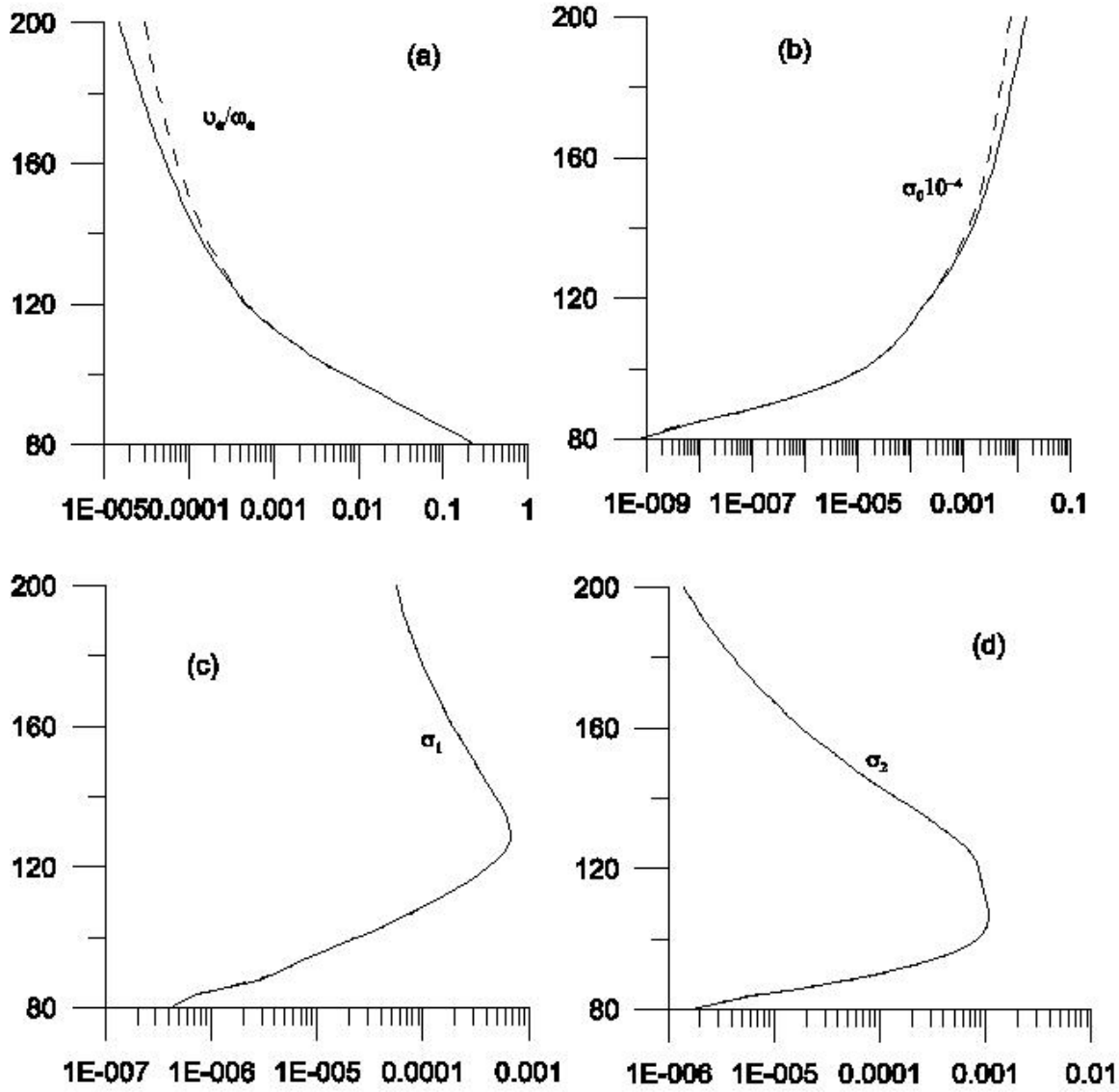

Figure 7.3: Comparison between Richmond (solid line) and Forbes (dashed line) conductivity profile

7.3.1 Modified Oxygen ion-Oxygen atom collision frequency:

The collisional processes connect the absorption of incident radiation by some atmospheric constituents to increased temperatures in Earth's atmosphere. Consequently, the degree to which a model calculation of atmospheric heating can replicate observed atmospheric behaviour is affected by the values of collision frequencies included in the calculation. In the case of oxygen atoms and oxygen ions (O^+), collisions between those species determine the transfer of solar radiant energy to the ionosphere and thermosphere. During an O^+-O collision, strong resonance charge exchange interaction causes an electron to be transferred from an oxygen atom to an atomic oxygen ion. In this process, a high-energy ion, produced by photoionization due to solar radiation, is converted into a high-energy oxygen atom, heating the thermosphere. Considering the dominance of oxygen atoms and ions in the thermosphere and ionosphere, and large resonance charge exchange cross section, this mechanism of charge transfer becomes the main mechanism for heating of the thermosphere.

Owing to uncertainties in measurements and theory, a discrepancy between the theoretical and empirical values of collision frequency has persisted for the last ten years. Some consistency has recently been obtained theoretically by noticing that three independent calculations, using different methods, give results within a few percent of each other. These calculations are due to Stubbe [1968], Stallcop et al. [1991], and Pesnell et al. [1993]. The latest expression for the collision frequency is given by Pesnell et al. [1993], and is given by

$$\upsilon_3 = 3.0\times10^{-17} T_r^{1/2}(1-0.135\log T_3)^2[O] \quad s^{-1} \qquad (7.26)$$

where $T_r = \dfrac{(T_i + T_n)}{2}$, with T_i and T_n are the ion and neutral temperatures,

$T_3 = T_r/10^3$ and [O] the oxygen atom density in m^{-3} units.

The theoretical collision frequency is given by Dalgarno[1964], which can be approximated by the following formula given by Salah [1993]

$$\upsilon_3 = 2.35\times10^{-17} T_r^{1/2}[O] \quad s^{-1} \qquad (7.27)$$

This equation is based on a curve fitting of the numerical values of the collision frequency given by Dalgarno [1964], with margin errors of 5% for T_r between 500 and 2000^0K. Omidvar et al. [1998] defined a factor F, often called the Burnside factor, as the ratio of the empirical to the theoretical collision frequencies whose deviation from unity is a measure of inconsistency between theory and observation. They used extensive observational data sets of incoherent scatter radar and Fabry-Perot interferometer measurements taken at the Millstone Hill Observatory and three methods of analysis. These are the methods of linear-least-squares, a method due to Hines et al. [1997], and a third method based on lognormal distribution of the data. While the linear-least-squares and lognormal distribution methods are based on Gaussian and lognormal distributions respectively, no distribution assumption is made in the Hines et al. [1997] method, and this makes the method more general. The linear-least-squares and the Hines et al. [1997] methods give consistent estimates for F, differing in values from each other by only a few units in their third decimal places. This leads Omidvar et al. [1998] to conclude that the Pesnell et al. [1993] formula is more realistic to calculate collision frequency, within an uncertainty of 8%.

7.3.2 Calculation of conductivity using Pesnell et al. [1993] formula:

As we have seen in chapter 1 -section , that below 200 km altitude, the ion and neutral temperatures are almost identical, in above formula we can replace T_r by T_n. The comparison between Forbes model and our (new) prescription with Pesnell et al. [1993] formula for O-O^+ collision frequency is depicted in figure (7.4a). At lower heights (<100km), where O^+ ion density is negligible, the modified collision frequency due to Pesnell et al. [1993], and Nicolet collision frequency model do not differ. Since O^+ ion density increases monotonically beyond 120 km, it can be seen from figure (7.5b) that the difference starts building up. At 200 km, it is less than one order of magnitude. Parallel conductivity is almost unaffected between 80 km to 200 km altitude ranges.

Pedersen and Hall conductivities differ above 150 km where O^+ density is significant, and at 200 km it reduces to half the value in Forbes model.

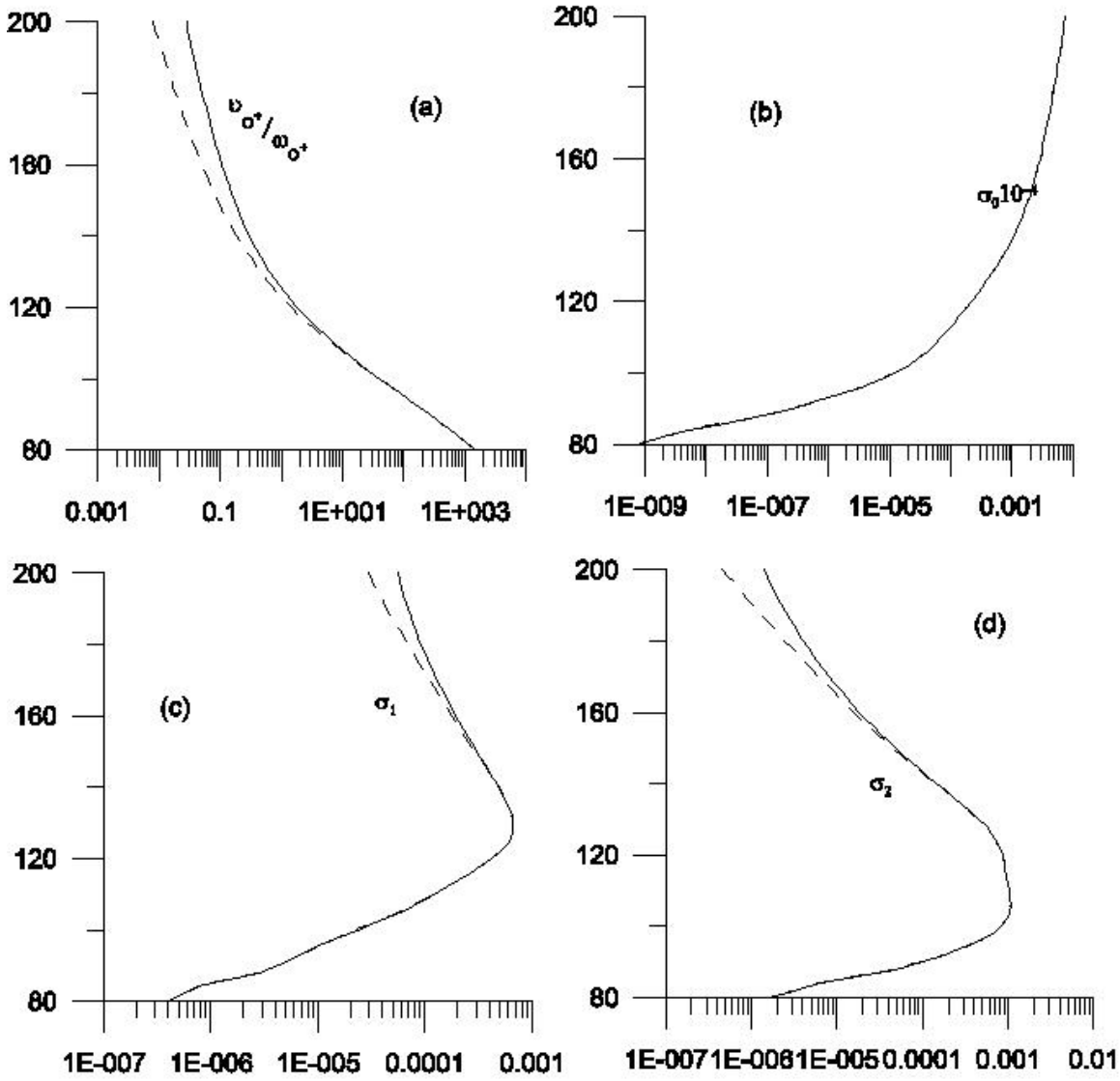

Figure 7.4: Comparison between Forbes model(solid line) and new O+ collision freq (dashed line) conductivity profile

7.4 Availability of realistic data base:

Thus, in above conductivity models, the neutral densities that are input parameters, are taken from some standard atmospheric models and charge particle densities are calculated by balancing the photochemical equations. If by some means, we could able to estimate these parameters on a given day, time, and location, the conductivity calculations will be more realistic. Fortunately, atmospheric and ionospheric models provide us the above parameters, which are based on number of satellite and rocket measurements.

In support of the space physics community, NSSDC has accepted as one of its responsibilities the archiving and distribution of model parameters. Most importantly, NSSDC' s model archive includes international standard models: the COSPAR International Reference Atmosphere (CIRA) of the Committee on Space Research (COSPAR), and the International Reference Ionosphere (IRI). These models are implimented and regularly improved by special working groups set up by the responsible scientific unions. NSSDC' s international arm, the World Data Centre-A for Rockets & Satellites, is one of the centers that receive the newest editions of these international standard models for distribution to interested users.

7.4.1 Atmospheric models:

Below 50 km the atmosphere can be assumed to be homogeneously mixed and can be treated as a perfect gas. Above 80 km the hydrostatic equilibrium gradually breaks down as diffusion and vertical transport become important. The major species in the upper atmosphere are N_2, O, O_2, H, He. The first global models of the upper atmosphere were developed by L. G. Jacchia in the early sixties based on theoretical considerations and satellite drag data. Since the launch of Sputnik 1 in 1957, orbit decay of artificial satellites has been used to derive atmospheric data.

Several national and international organizations have established committees for the development of atmospheric reference models, e.g., the International Civil Aviation Organization (ICAO), the Committee on Space Research (COSPAR), and the Committee on Extension to the standard atmosphere (COESA). Probably the most widely used and well-established model is the COSPAR International Reference Atmosphere (CIRA), an effort that started in 1961 with the publication of CIRA-61. CIRA-72, the third generation of this model, CIRA-86, includes Jacchia' s 1971 model.

With the launch of the OGO 6 satellite in 1969, in situ measurements of atmospheric parameters by mass spectrometer became available. At about the same time, ground-based incoherent scatter radars started to monitor the thermospheric temperature. A. E. Hedin and his co-workers combined data from these two data sources to establish the Mass Spectrometer Incoherent Scatter (MSIS) models: MSIS-77, -83, -86. The CIRA and MSIS groups joined forces in 1986 and MSIS-86 became the upper part of CIRA-86.

7.4.1.1 MSIS model 1986:

The Mass-Spectrometer-Incoherent-Scatter (MSIS) model describes the neutral temperature and densities in the upper atmosphere (above about 100 km). MSIS-86 constitutes the upper part of the COSPAR International Reference Atmosphere (CIRA) 1986. The MSIS model is based on the extensive data compilation and analysis work of A. E. Hedin and his colleagues. Data sources include measurements from several rockets, satellites (OGO 6, San Marco 3, AEROS-A, AE-C, AE-D, AE-E, ESRO 4, and DE 2), and incoherent scatter radars (Millstone Hill, St. Santin, Arecibo, Jicamarca, and Malvern). The model expects as input year, day of year, Universal Time, altitude, geodetic latitude and longitude, local apparent solar time, solar F10.7 flux (for previous day and three-month average), and magnetic Ap index (daily or Ap history for the last 59 hours). For these conditions the following output parameters are calculated:

number density of *He, O, N_2, O_2, Ar, H*, and *N*, total mass density, neutral temperature, and exospheric temperature. Hedin and Thuillier [1988] compared all three MSIS models with each other and with the Jacchia 1970 and 1977 models.

7.4.1.2 MSISE 1990:

The MSISE model describes the neutral temperature and densities in Earth' s atmosphere from ground to thermospheric heights. Below 72.5 km the model is primarily based on the MAP Handbook [Labitzke et al., 1985] tabulation of zonal average temperature and pressure by Barnett and Corney, which was also used for the CIRA-86. Below 20 km these data were supplemented with averages from the National Meteorological Center (NMC). In addition, Pitot tube, falling sphere, and grenade sounder rocket measurements from 1947 to 1972 were taken into consideration. Above 72.5 km MSISE-90 is essentially a revised MSIS-86 model taking into account data derived from space shuttle flights and newer incoherent scatter results. The MSIS-86 model has been recommended for thermospheric calculations (above 120 km). MSISE is also not the model of preference for specialized tropospheric work. It is rather for studies that reach across several atmospheric boundaries, hence more proper choice in the calculation of conductivity profile from 80 km to 200 km. Output parameters of the model are neutral densities and temperature from ground to thermosphere.

7.4.1.3 CIRA model:

The COSPAR International Reference Atmosphere (CIRA) provides empirical models of atmospheric temperature and densities. Above 120 km, in the thermosphere, CIRA-86 is identical with the MSIS-86 model. In addition to the empirical model, CIRA-86 includes the theoretical thermosphere model of D. Rees and his colleagues at University College, London. Results from 50 global simulations with this model have been stored in computer-readable form and

can be reconstructed on VAX or PC computers. The output parameters are neutral temperature and densities in the thermosphere.

7.4.2 Ionospheric models:

Knowledge of the ionospheric electron density is essential for a wide range of applications, e.g., radio and telecommunications, satellite tracking, and Earth observation from space. Considerable efforts have, therefore, been concentrated on modeling this ionospheric parameter. Several ionospheric models are readily available such as, the phenomenological Chiu model, the Bent model that has been used extensively for satellite tracking, the semi-empirical SLIM model based on theoretically obtained grid values, and the recent FAIM model that uses the Chiu formalism together with the SLIM results. The International Reference ionosphere (IRI) is probably the most mature of these models, having undergone more than two decades of scrutiny and improvement.

The ionospheric electron density profile exhibits several peaks with the F2-peak being the largest and most important. Using spherical harmonics world maps have been developed for the F2-peak critical frequency foF2; the F2-peak electron density is linearly related to foF2 squared. Similar maps have been established for the propagation factor M(3000)F2, which is related to the height of the F2-peak. This listing includes the widely used set of coefficients recommended by the International Radio Consultative Committee (CCIR), the newly proposed set of the International Union of Radio Science (URSI), and the mission-specific maps obtained by the Japanese Ionospheric Sounding Satellite-b (ISS-b) during 1978-1979. MINIMUF and IONCAP are software packages designed specifically for radio propagation purposes. They are available from NOAA' s World Data Center A for Solar-Terrestrial Physics in Boulder, Colorado.

Fewer mostly mission-specific models have been developed for the electron temperature, ion composition (relative ion densities in percent) and the ion drift,

the latter being closely related to the forcing electric field. The International Reference Ionosphere, the most complete representation of the ionosphere, includes models of the ion temperature, electron temperature, ion composition, and ion drift.

At present, almost all, empirical models of ionospheric parameters are limited to non-auroral, magnetically quiet conditions. Major efforts are underway to extend ionospheric predictability beyond these limitations. A promising venue seems to be the inclusion of real-time data from the newly developed automatically recording and scaling ionosondes. These and other measurement techniques are discussed in a report published by NSSDC: *D. Bilitza*, The Worldwide Ionospheric Data Base, NSSDC 89-03, Greenbelt, Maryland, 1989.

7.4.2.1 IRI model:

The International Reference Ionosphere (IRI) is an international project sponsored by the Committee on Space Research (COSPAR) and the International Union of Radio Science (URSI). These organizations formed a Working Group in the late sixties to produce an empirical standard model of the ionosphere, based on all available data sources. Several steadily improved editions of the model have been released. For given location, time and date, IRI describes the electron density, electron temperature, ion temperature, and ion composition in the altitude range from about 50 km to about 2000 km; and also the electron content. It provides monthly averages in the non-auroral ionosphere for magnetically quiet conditions. The major data sources are the worldwide network of ionosondes, the powerful incoherent scatter radars (Jicamarca, Arecibo, Millstone Hill, Malvern, St. Santin), the ISIS and Alouette topside sounders, and in situ instruments on several satellites and rockets. IRI is updated yearly during special IRI Workshops (e.g., during COSPAR general assembly). Several extensions are planned, including models for the ion drift, description of the auroral and polar ionosphere, and consideration of magnetic storm effects.

A typical output of IRI model on 21st March' 2000 at 12 hr local time and at dip equator along 75^0E longitude is sketched in Figure (7.5). The sunspot number is taken as 120. Figure (7.5a) compares the electron densities from IRI and Richmond' s models. It can be seen from this comparison that the E region electron density peak in IRI is not as sharp as that in Richmond' s model, when densities are plotted in logarithmic scale. Above 120-km altitude, IRI values are almost half of Richmond's values. Figure (7.5b) draws the number densities of N_2^+, O^+, O_2^+ and electron in linear scale.

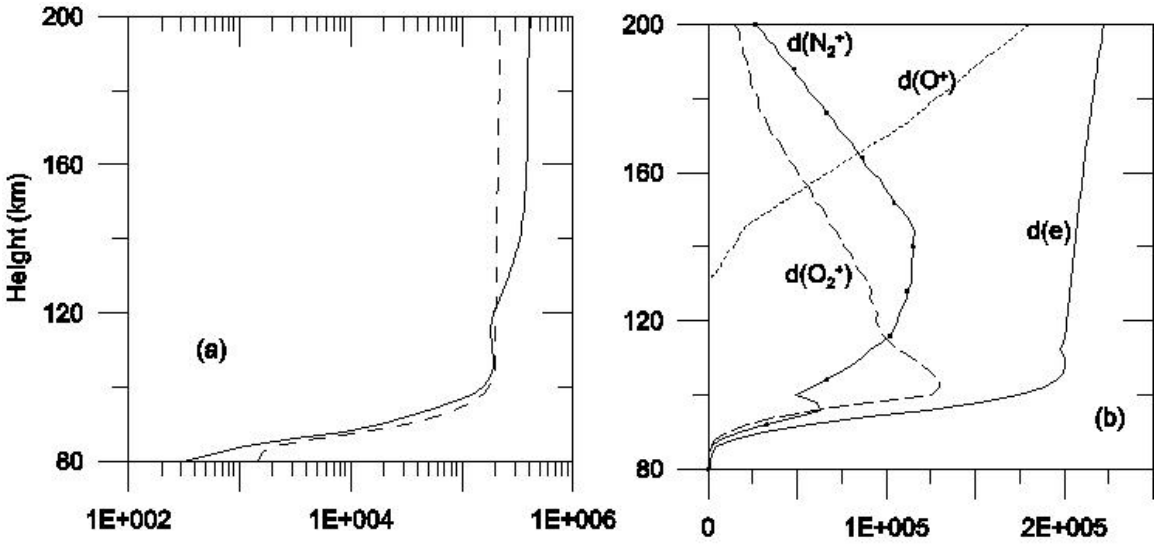

Figure 7.5: (a) Comparison of electron density between Richmond's model (solid) and IRI model (dashed) (b) Number densities of different species

7.5 Conductivity calculations based on real data:

Computation of conductivity based on real data set can be achieved using two different prescriptions; one is same as old i.e. Forbes' s prescription and second using modified O^+ collision frequency by Pesnell et al. [1993]. In the succeeding subsections, these two cases have been discussed.

7.5.1 Earlier Formalism (Forbes' s) + IRI + MSISE:

Here we have used Forbes theoretical backup, and IRI and MSISE models are for 21st March' 2000, at dip equator along 75^{0}E longitude and at local time equal to 12 hr. The sunspot number is 120, and solar zenith angle at that location is 8^0. The ratio of collision to gyrofrequency for electrons and other ions have been estimated in Figure (7.6a), which shows that the structure and relative magnitudes of these ratios are same as the earlier calculations based on standard model. Figure (7.6b-d) plots the variation of Parallel, Pedersen and Hall conductivities as a function of height, and compares this with Forbes model. In spite of all the complexities involved in using the real database, the overall structure of all conductivities remains the same. In order to get smooth picture, we have taken 11 point mean where the data interval is 1 km. The small undulations are quite expected due to high solar activity. The Hall conductivity maximizes at 90-120 km altitude. Here the ion-neutral collision frequency is greater than the ion gyrofrequency but the electron collision frequency is much less than the electron gyrofrequency, hence contribution from electrons is dominant in Hall conductivity. In this case the electrons can have E x B drift but the ions cannot.

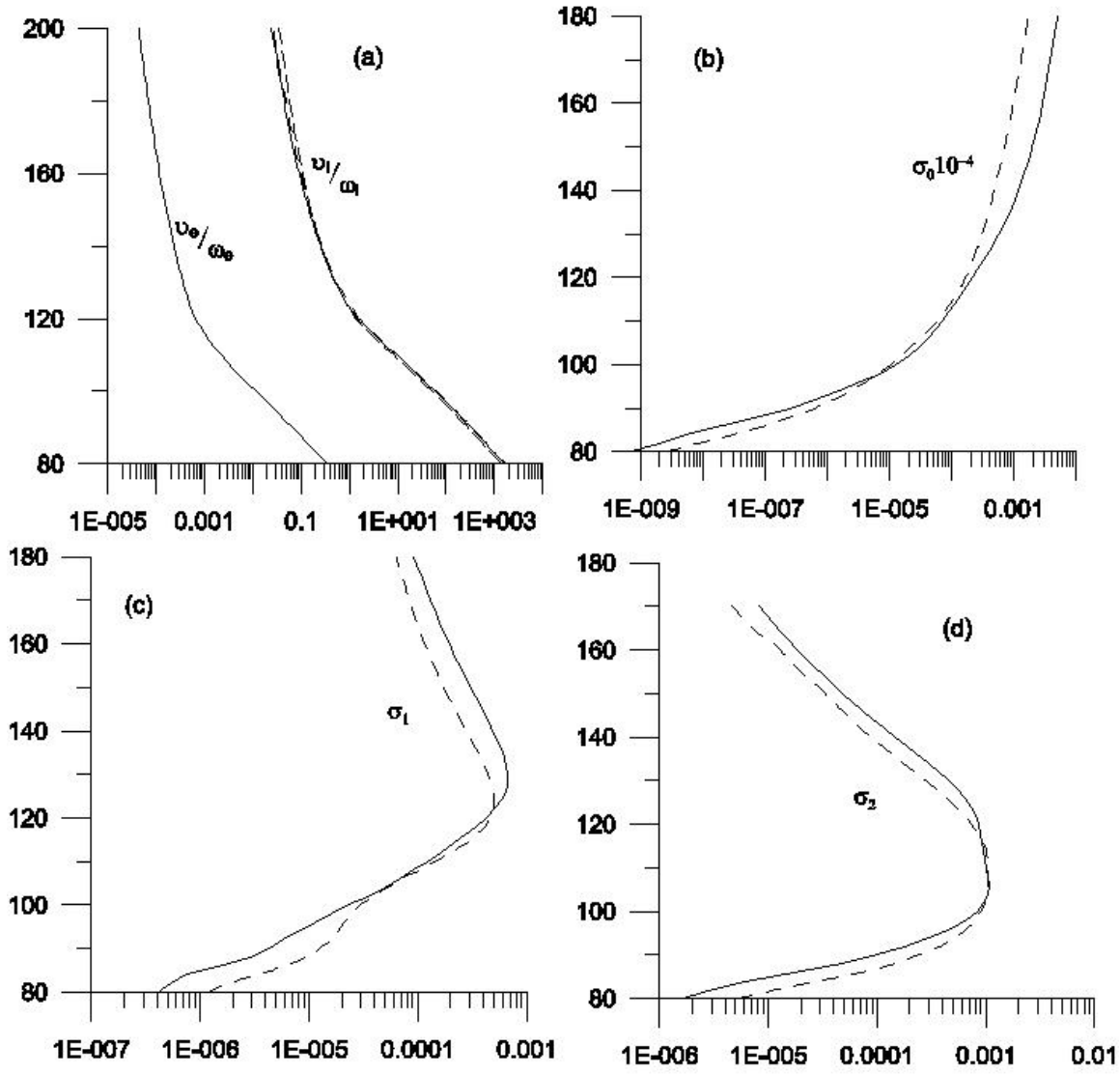

Figure 7.6 :Comparison between Forbes model (solid line) and a model based on IRI & MSISE (dashed line) conductivity profile. Computations are at dip equator of 75°E longitude, 12 LT & equinoxial conditions.

7.5.2 Pesnell's O^+ collision frequency model + IRI + MSISE:

The discussion made so far claims that this combination should produce more precise estimates of the conductivity. In this section, let us compare the computations based on earlier formalism with modified formalism using real database. Figure (7.7) shows that the difference between the ratio of collision to gyrofrequency for O^+ for old and new formalism is same for real data base and standard database. At lower heights (<100 km) all the methods show similar

values, due to the negligible density of O^+ ion. Parallel conductivity is unaffected, while other two, show difference above 160 km.

Careful investigation of all these cases substantiates that the formalism and the input data set affect the conductivity calculations considerably.

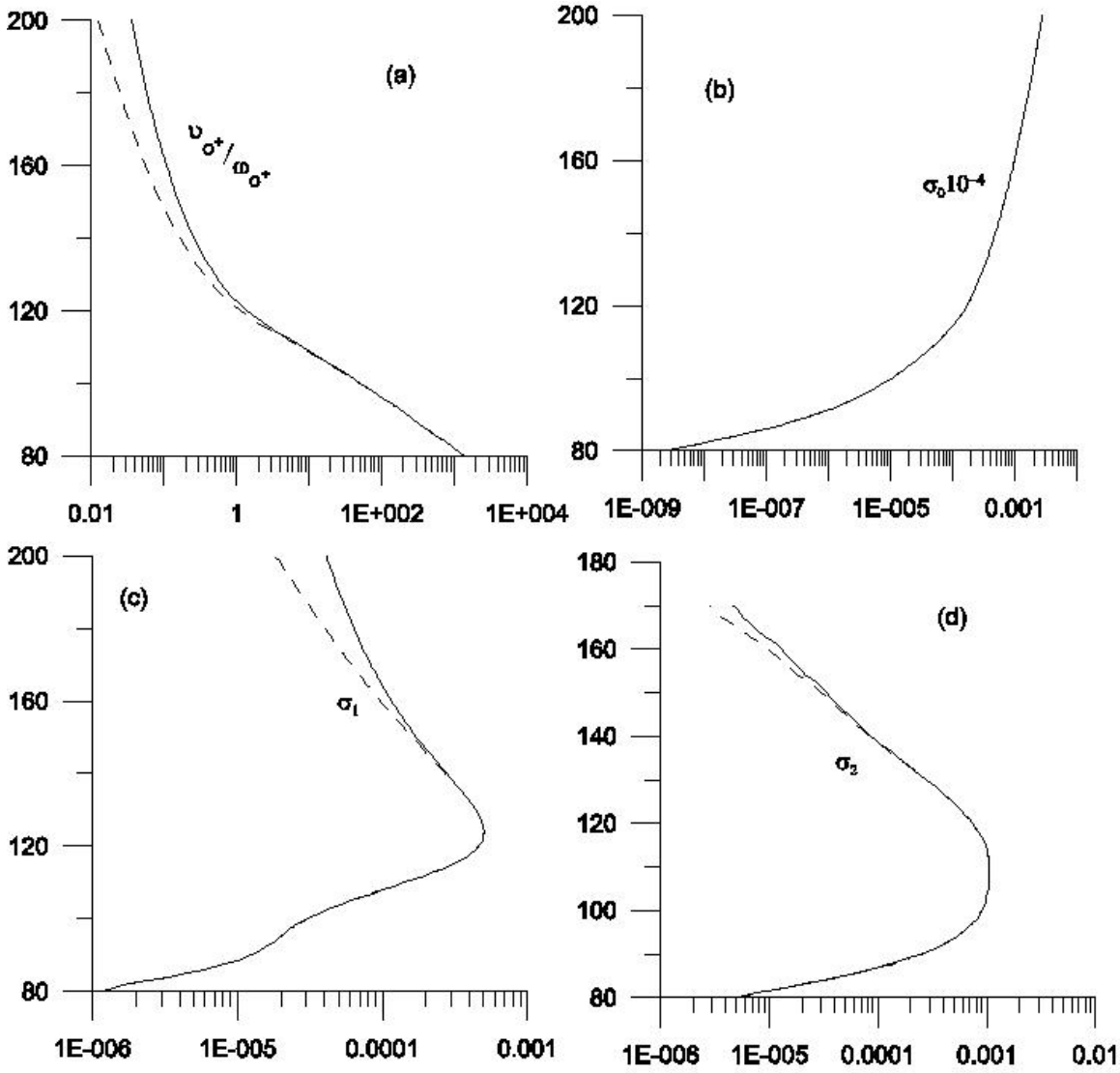

Figure 7.7: Comparison between Forbes (solid line) and New model (dashed line) based on real data

7.6 Conductivity profile computed by WDC-Kyoto:

http://swdcdb.kugi.kyoto-u.ac.jp/wdc also provides ionospheric conductivity model based on IRI and CIRA models. The collision frequency computations are based on Banks and Kockarts[1973], which are same as that of Forbes. Hence these computations are substantially same as our section (7.5.1) calculations.

7.7 Physical mechanism responsible for the observed Conductivity profile:

We have seen in the first section that in a collisionless magnetoplasma, electrons and ions execute oppositely directed circular motions in a plane normal to the magnetic field at angular frequencies ω_e and ω_i. Application of an electric field normal to $\vec{B}$ results in $\vec{E} \times \frac{\vec{B}}{B^2}$ motion, which is independent of the charge and mass of the particle and is thus, referred to as a plasma drift. An electric field parallel to $\vec{B}$ produces helical motions in different directions for oppositely charged particles and corresponds to a current along $\vec{B}$. The gyrofrequencies define a natural time scale for the motion of charged particles in the presence of a magnetic field. In partially ionized plasma, such as the earth's lower ionosphere, the competing effects of ion-neutral or electron-neutral collisions must be taken into account.

Let us define Z_e as the height at which $\omega_e = \upsilon_{en}$ (above 70 km during midday) and Z_i as the height at which $\omega_i = \upsilon_{in}$ (about 130 km during midday). Consider now the response to an electric field normal to $\vec{B}$ for following three cases:

Case (1) $Z<Z_e$

Below Z_e, $\omega_i < \upsilon_{in}$ and $\omega_e < \upsilon_{en}$, so that the particle motions essentially ignore the existence of the magnetic field. Current flow in the same direction as the electric field (Pedersen current) but is negligibly small in magnitude because of the low levels of ionization, which exist at these heights.

Case (2) $Z>Z_i$

This is the F region, where $\omega_i > \upsilon_{in}$ and $\omega_e > \upsilon_{en}$. Particle motions are controlled mainly by the magnetic field, and collisional effects of the neutral gas are relatively unimportant. An electric field normal to $\vec{B}$ produces a plasma drift approximately equal to $\vec{E} \times \frac{\vec{B}}{B^2}$; current flow is negligible.

Case (3) $Z_e<Z<Z_i$

In the region where $\omega_e > \upsilon_{en}$ and $\omega_i < \upsilon_{in}$, only electrons move at the drift velocity $\vec{E} \times \frac{\vec{B}}{B^2}$ (Hall current), whereas the ions are constrained by collisions with the neutral gas.

In all three regions an electric field parallel to $\vec{B}$ drives a current along $\vec{B}$. The magnitude of parallel conductivity is about 4 order greater than other two; this leads to treat magnetic field lines as equipotential lines for all practical purposes.

7.8 Computation and comparison of Cowling conductivity:

At the dip equator where the magnetic dip angle *I = 0*, the effective conductivity turns out to $\sigma_3 = \sigma_1 + \frac{\sigma_2^2}{\sigma_1}$, which is also known as Cowling conductivity. In the study of equatorial dynamics, this conductivity plays important role. To assess the factor, by which Cowling conductivity is boosted over Pedersen conductivity, we present figure (7.8a) due to Maeda and Kato [1966]. It shows that at local noon, maximum σ_2/σ_1 is about 16 at a little above 100 km altitude in midlatitudes. From Figure (7.8b), we find that at an altitude of 100 km near local noon, the maximum σ_2/σ_1 for the dip equatorial zone is about 43 and σ_3/σ_1 is about 100. At local midnight in the midlatitudes σ_2/σ_1 peaks at an altitude of about 90 km where σ_2/σ_1 is about 1.7.

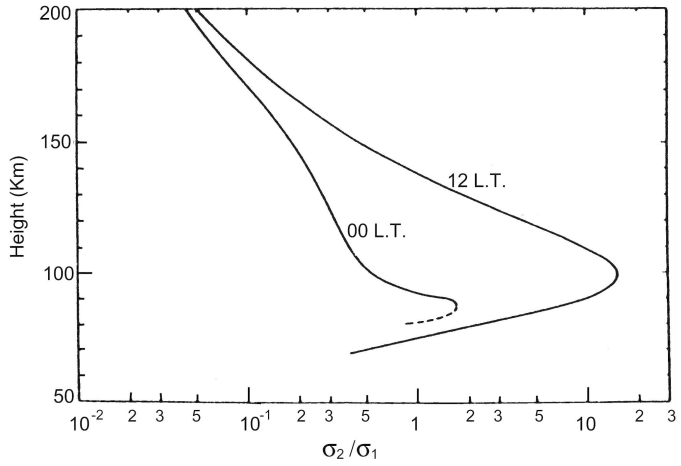

Figure 7.8a : Height distribution of σ_2/σ_1 in midlatitudes. (after Maeda and Kato [1966])

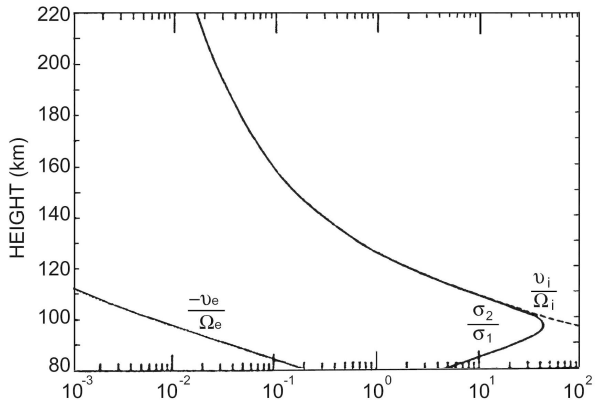

Figure 7.8b : Ratio of Collision to Gyrofrequency for electrons, Positive ions and (σ_2/σ_1) in the dip equatorial zone for $B = 29.3\mu T$. (after Richmond [1973a]).

The Cowling conductivity computed using different models is shown in Figure (7.9). The structure shows all the models agree well at around 100 km, where the peak Cowling current flows. At higher altitudes, the estimates from different models vary considerably.

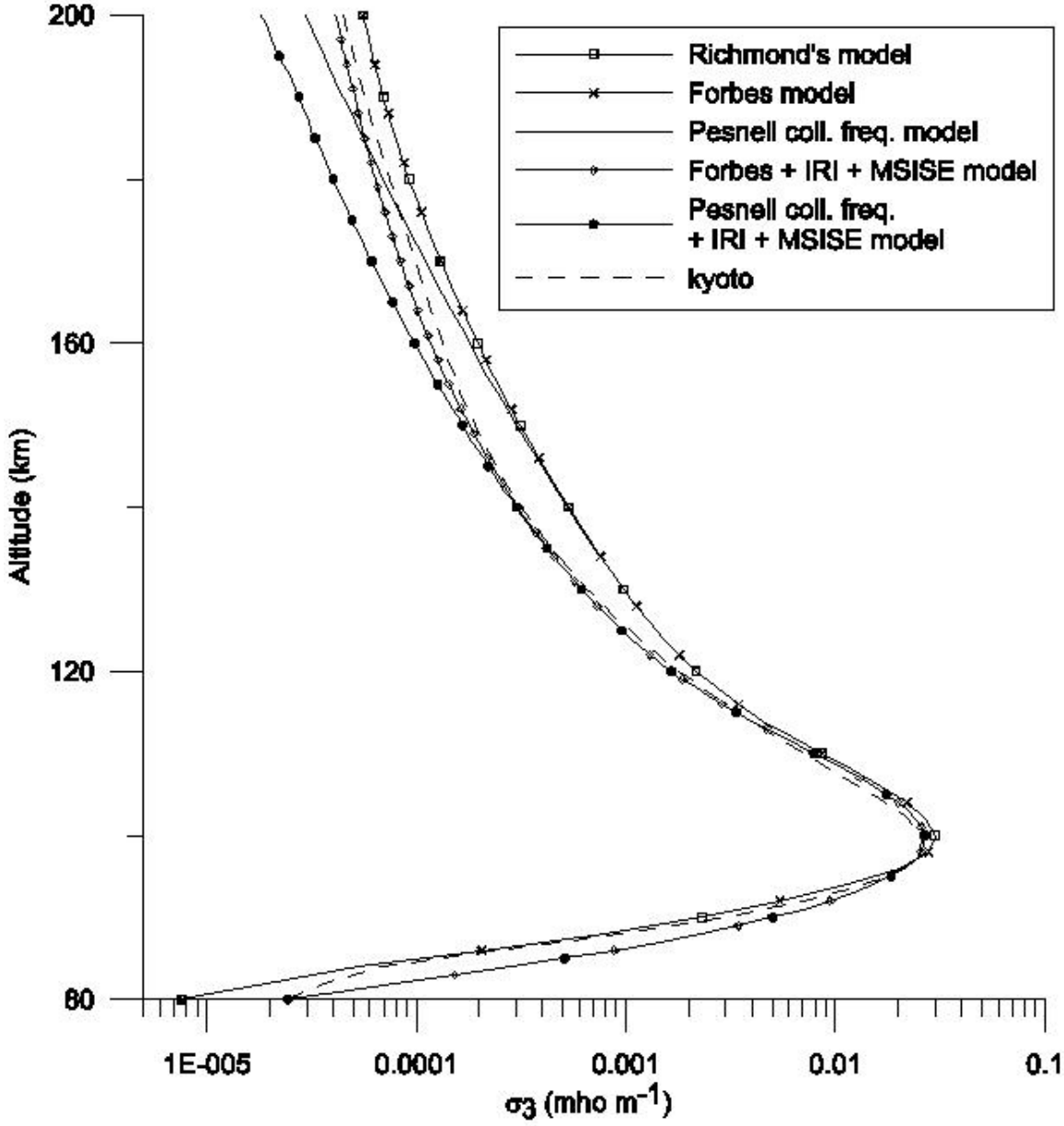

Figure 7.9: Comparison of Cowling conductivity for all models.

7.9 Variation of conductivity as a function of other parameters:

So far we have seen the variation of parallel, Pedersen, and Hall conductivity as a function of altitude. The Hall and Pedersen conductivities also vary as a function

of latitude and longitude. Essentially this dependence comes through the ionization density. The neutral densities can be considered as a function of altitude alone. So the conductivity variation with other parameters is same as the variation of electron number density.

7.9.1 Latitudinal variation:

Below 120 km, the electron number density mainly has solar zenith angle dependence and it varies as $\cos^{1/2}(\chi)$. The behaviour of F_2 region is very complicated and depends on geomagnetic latitude. The vertical distribution of the electron density in F_2 region can not be described in terms of the balance between ionization and recombination but rather as the effect of diffusion. As a result of which, above 120 km, some strange latitudinal structure emerges. The typical output of electron densities from IRI model at different heights is shown in Figure (7.10). Since Pedersen, Hall and Cowling conductivities drops considerably at higher altitudes, the basic behaviour of the profile remains unchanged.

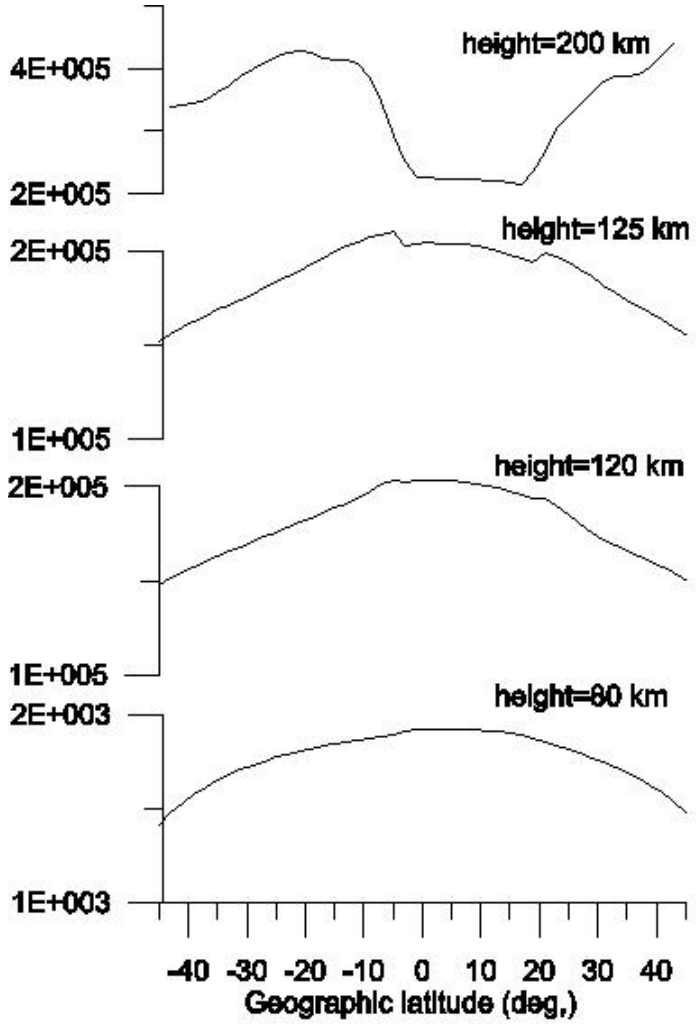

Figure 7.10: Variation of electron number density as a function of latitude at different altitudes

7.9.2 Longitudinal Variation:

The atmospheric and ionospheric models used are independent of longitude, hence there is no longitudinal change observed in the conductivity profile. The longitudinal variation can emerge through the local time differences.

7.9.3 Local time Variation:

At noontime the solar zenith angle is minimum, which results in higher conductivity. Below 120 km, the electron density has $\cos^{1/2}(\chi)$ dependence, but at

higher altitudes the relation violets due to anomalous F region. A typical variation of conductivity profile at different local times is shown in Figure (7.11). At noontime, the magnitude is about 1 order higher than that at 6 LT, whereas nighttime it reduces by a factor of 10^3.

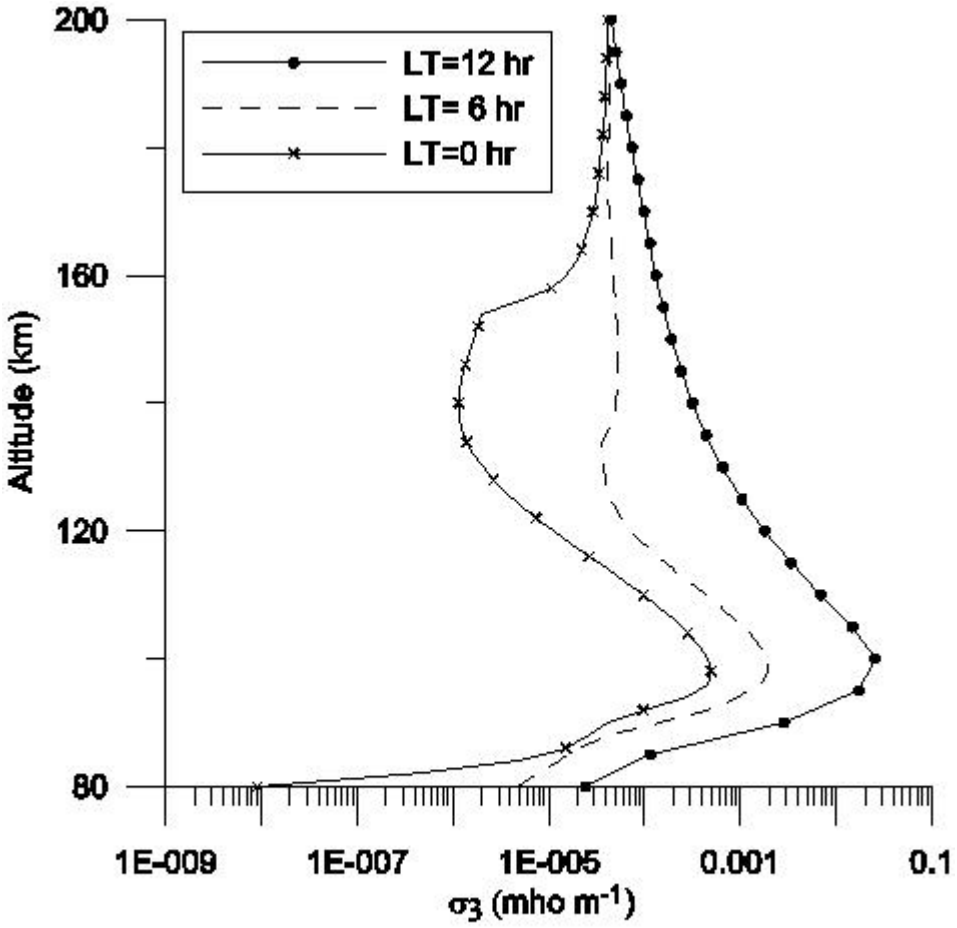

Figure 7.12: Variation of Cowling conductivity at different local times

7.10 Conclusion:

Ionospheric conductivity plays major role in the ionospheric current system. Detailed study of ionospheric conductivity carried out in this chapter explores different aspects of the conductivity. Present chapter discusses the earlier standard models of conductivity such as Richmond's and Forbes models. It also

introduces a new model based on Pesnell et al [1993] formula for O^+-O collision frequency. All these computations are performed for more realistic estimates of ionospheric parameters. The comparative study reveals that the formalism and the input data set have significant influence on the height profile of conductivity. For the theoretical computations of the low latitude current systems, different conductivity models are useful in order to study their conductivity dependence. We believe that our model along with the realistic input data sets will improve the estimates of ionospheric currents in future model calculations. The study of dependence of conductivity on different parameters such as latitude, longitude, and local time, certainly gives better insight into the global structure of the conductivity.

Chapter 8
Basic Framework for Modeling of Ionospheric Currents

8.1 Introduction:

Results presented in chapters 2, 3 and 4 have established that there is considerable longitudinal variation not only in the electrojet strength and width but also in the day to day variability. These differences cannot be accounted by the variations in the Hall or Cowling conductivities due to the changes in the magnetic field strength in the different longitudinal sectors. This is one aspect that current EEJ models have not addressed partly because of lack of sufficient evidence. Though longitudinal variability in the electrojet strength and day to day variability have been reported from ground measurements, a global picture can be provided only by a global satellite coverage presented in the earlier chapters of this thesis. We address this problem in this chapter. We realize that to start from its basics and develop a full scale working model will be beyond its scope of a single thesis. What we try to put together in this chapter is the simplest internally consistent model that can be used to understand the observations of the day to day variability in the global patterns of the EEJ.

The underlying physics necessary to explain the equatorial electrojet phenomenon is that the enhancement at the dip equator is merely associated with the special field line geometry of the geomagnetic field around the dip equator. Both the Sq and EEJ variations are driven by the atmospheric tides (primarily associated with differential solar heating and having a smaller contribution from lunar gravitational forcing) and their variability from day to day should be linked with the tidal variability.

Atmospheric tides propagating upwards through the middle atmosphere are a major source generating electric fields and currents in the low and mid-latitude

ionosphere. Atmospheric solar tides are global-scale waves with periods that are harmonics of a 24-hour day, which have been studied in detail in chapter 6. Migrating tidal components propagate westward with the apparent motion of the sun, so their zonal wave numbers are identical to their frequency. These components are thermally driven by the periodic absorption of solar radiation throughout the atmosphere, primarily the absorption of Ultra-violet radiation by stratospheric ozone and of Infrared by water vapor in the troposphere. The computations and programs developed in chapter 6, provide the basic input for the driving tides. The ionospheric conductivity required to sustain the currents is obtained from the algorithms described in chapter 7.

To understand how the atmospheric tides generate electric fields and currents, we first note that any neutral motion (with a velocity $\overline{V}$) will result in the change in the electric field. In section 7.7, we have seen that in the altitude range of 80-160 km, where $\upsilon_{en} < \omega_e$ and $\upsilon_{in} > \omega_i$, the ionosphere is most favorable to sustain steady state currents. Through the persistent numerous collisions of the ions with neutral particles, the wind drags the ions along while the electrons are left behind gyrating round $\overline{B}$. Consequently, this initial current flow accumulates positive charges (ions) up front and negative charges (electrons) behind. The flow therefore polarizes the charges and the current is not divergent free. The current has to be rendered divergence free by the build up of an electrostatic electric field E that is traditionally regarded as derivable from an electrostatic potential Φ, thus

$$\overline{E} = -\overline{\nabla}\Phi \qquad (8.1)$$

The total electric field $\overline{E'}$ is obtained from

$$\overline{E'} = \overline{E} + \overline{V} \times \overline{B} \qquad (8.2)$$

The corresponding current is then given by

$$\overline{J} = \tilde{\sigma} \cdot \left(\overline{E} + \overline{V} \times \overline{B}\right) \qquad (8.3)$$

Where $\tilde{\sigma}$ is the conductivity tensor.

It is important to note that $\overline{\nabla} \cdot \bar{J}$ has to vanish in order to ensure that charges do not buildup. Since $\overline{V}$ is dynamically introduced and is not constrained by any such requirement from electrodynamics, a constraint is automatically introduced on $\overline{E}$.

Thus,

$$\overline{\nabla} \cdot \left[\tilde{\sigma} \cdot \left(-\overline{\nabla}\Phi + \overline{V} \times \overline{B}\right)\right] = 0 \qquad (8.4)$$

Equation (8.4) has to be solved with appropriate boundary conditions to determine Φ and the electric field thus obtained has to be substituted in equation (8.3) to get the currents. The boundary conditions are generally imposed on the currents instead of the potential. For example as the lower atmosphere below say 80 km is highly resistive, one can impose the condition that current normal to the lower boundary has to vanish. A high latitude boundary condition is also imposed as the high latitude field lines extend to tens of earth radii and it is assumed that ionospheric currents are restricted to a definite volume specified by an outer spatial boundary or equivalently by a high latitude boundary. The exact application of the boundary condition is also dictated by considerations of numerical stability of the solutions.

Equation (8.4) can in principle be solved for any field configuration but in practice many simplifying assumptions are made to make the problem tractable and interpretation of the results meaningful. One assumes that the ambient magnetic field can be represented by a dipole and geomagnetic co-ordinates are adapted for the calculations. It is also usually assumed that the distinction, between geographic and geomagnetic co-ordinate systems, is unimportant and the tilt of the dipole to the geographic axis is ignored. Our results presented in chapters 3 and 4, indicate that this may not be an acceptable simplification.

Further simplifications naturally present themselves because the quasi-static nature of the variations ensures that explicit time derivative of the magnetic and electric fields can be ignored. It follows then from the Maxwell equations that the curl of the electric field has to be zero. Since the variations of the fields in the vertical direction are much more rapid than in the east-west direction, the zonal components of the electric field cannot vary significantly with height. This makes the concept of height-integrated conductivity meaningful at least in regions where the build up of a vertical electric field can be ignored. Earlier models of the ionospheric current systems assumed that the currents flow in a thin spherical shell represented by the dynamo region and ignored any vertical (radial) currents flowing out of the shell. Since the horizontal electric fields that drive the currents do not vary with height and the ground measurements only see the effect of height integrated currents, dynamo models were considerably simplified by replacing σ_1 and σ_2 by their corresponding height integrated values Σ_1 and Σ_2 respectively. Height integrated version of equation (8.4) is used with the additional condition that the vertical current $J_Z = 0$. The models were able to reproduce the observed variation of the Sq current system but the equatorial electrojet could not be fitted into this simple height integrated picture.

Baker and Martyn [1953] computed the effective conductivity in the ionosphere. Consider ionosphere as a plane sheet and X-axis along magnetic south and Y-axis along east in this plane, Z-axis points upwards. Let *I* be the inclination i.e. the angle made by the magnetic field $\overline{B}$ to the plane. Let $\hat{i}, \hat{j}, \hat{k}$ be unit vectors in the directions of X,Y and Z axes respectively.

$\therefore \quad \overline{E} = E_x\hat{i} + E_y\hat{j} + E_z\hat{k}$

Let $\hat{b}_{\parallel}$ and $\hat{b}_{\perp}$ be the unit vectors parallel and perpendicular to the magnetic field respectively.

Therefore we can write,

$$\overline{B} = B\hat{b}_{\parallel} = -B\cos I\ \hat{i} - B\sin I\ \hat{k}$$

$$\therefore\quad \hat{b}_{\parallel} = -\cos I\ \hat{i} - \sin I\ \hat{k} \quad \text{and} \qquad \hat{b}_{\perp} = \sin I\ \hat{i} - \cos I\ \hat{k}$$

We know that the Hall current is proportional to the vector $\hat{b}_{\parallel} \times \overline{E}$, hence

$$\overline{J} = \sigma_0 \overline{E}_{\parallel} + \sigma_1 \overline{E}_{\perp} + \sigma_2 \left(\hat{b}_{\parallel} \times \overline{E}\right) \tag{8.5}$$

where,

$$\overline{E}_{\parallel} = \left(\overline{E} \cdot \hat{b}_{\parallel}\right)\hat{b}_{\parallel} = \left(E_x \cos^2 I + E_z \cos I \sin I\right)\hat{i} + \left(E_x \cos I \sin I + E_z \sin^2 I\right)\hat{k}$$

$$\overline{E}_{\perp} = \left(\overline{E} \cdot \hat{b}_{\perp}\right)\hat{b}_{\perp} + E_y\ \hat{j} = \left(E_x \sin^2 I - E_z \cos I \sin I\right)\hat{i} + E_y \hat{j} + \left(-E_x \cos I \sin I + E_z \cos^2 I\right)\hat{k}$$

and

$$\hat{b}_{\parallel} \times \overline{E} = E_y \sin I\ \hat{i} + \left(-E_x \sin I + E_z \cos I\right)\hat{j} - E_y \cos I\ \hat{k}$$

Therefore,

$$\begin{aligned}\overline{J} = {} & \left[\left(\sigma_0 \cos^2 I + \sigma_1 \sin^2 I\right)E_x + \sigma_2 E_y \sin I + \left(\sigma_0 - \sigma_1\right)E_z \cos I \sin I\right]\hat{i} \\ & + \left[\sigma_1 E_y - \sigma_2\left(E_x \sin I - E_z \cos I\right)\right]\hat{j} \\ & + \left[\left(\sigma_0 - \sigma_1\right)E_x \cos I \sin I - \sigma_2 E_y \cos I + \left(\sigma_0 \sin^2 I + \sigma_1 \cos^2 I\right)E_z\right]\hat{k}\end{aligned} \tag{8.6}$$

Zero vertical current gives rise to

$$E_z = \frac{\left[\sigma_2 E_y \cos I - \left(\sigma_0 - \sigma_1\right)E_x \cos I \sin I\right]}{\left(\sigma_0 \sin^2 I + \sigma_1 \cos^2 I\right)}$$

Thus we get

$$J_x = \sigma_{xx} E_x + \sigma_{yy} E_y \tag{8.7}$$

$$J_y = -\sigma_{xy} E_x + \sigma_{yy} E_y \tag{8.8}$$

where

$$\sigma_{xx} = \frac{\sigma_0 \sigma_1}{\left(\sigma_0 \sin^2 I + \sigma_1 \cos^2 I\right)} \tag{8.9}$$

$$\sigma_{xy} = \frac{\sigma_0 \sigma_2 \sin I}{\left(\sigma_0 \sin^2 I + \sigma_1 \cos^2 I\right)} \tag{8.10}$$

$$\sigma_{yy} = \frac{\left[\sigma_0 \sigma_1 \sin^2 I + \left(\sigma_1^2 + \sigma_2^2\right)\cos^2 I\right]}{\left(\sigma_0 \sin^2 I + \sigma_1 \cos^2 I\right)} \tag{8.11}$$

At the dip equator,

$$\sigma_{xx} = \sigma_0, \qquad \sigma_{xy} = 0, \qquad \sigma_{yy} = \sigma_1 + \frac{\sigma_2^2}{\sigma_1}$$

Thus the effective conductivity becomes $\sigma_1 + \sigma_2^2/\sigma_1$, which is known as Cowling conductivity. Since $\sigma_2 > \sigma_1$, the Cowling conductivity is much larger than the Hall and Pederson conductivity in the medium. This enhancement of the current around the dip equator explains the existence of the equatorial electrojet. Hence this model essentially explained the existence of the EEJ. At slightly higher latitudes, the vertical field will have a significant component along the geomagnetic field lines. The charges will then leak along the highly conducting geomagnetic field lines neutralizing the polarization field.

Maeda [1955,1957] and Kato [1956,1957] showed that the diurnal wind field was necessary to reproduce the daily magnetic variations on the ground. Further Kato [1966a,b] estimated that the diurnal winds of sufficient magnitude could indeed be generated in the lower thermosphere.

Untiedt [1967] was first to recognize that vertical current was not completely inhibited at the equator. Using a two dimensional meridional model (briefly discussed in chapter 4) of the electrojet which neglects the effects of local winds and local time variations, Untiedt found that permitting vertical current flow results in a doubling of the equatorial northward magnetic variation over the thin shell value. Since, this model actually solves the partial differential equation, it was mathematically more complicated than the earlier models. Further this model was refined by Sugiura and Poros [1969] and applied to different longitude sectors.

Richmond [1973] examined the physical features of EEJ in detail with the aid of a numerical model, which includes neutral air winds and two-stream instability. Since the electrojet usually extends much further in the east-west direction than

in vertical or north-south directions, Richmond assumed that the longitudinal gradients are negligible. He also assumed that the electrojet is symmetric about the magnetic equator and the electron density is unaffected by electric fields. This gives closed mathematical solution for the electric fields and currents. He found that the electric field and currents at a given point are strongly dependent on conditions along the entire magnetic field line, but are relatively independent of conditions along neighbouring field lines. The height-varying east-west winds affect currents a few degrees off the dip equator more strongly than at dip equator. Finally the north-south winds cause currents to flow across the equator, but are relatively uninfluential on the eastward electrojet currents.

Stening [1968] set up an equivalent circuit for the calculation of the current flows in the ionosphere given the conductivity and wind velocity distributions with the inclusion of the Hall effect. Using equivalent electric circuit method, Reddy and Devasia [1978] studied the generation of electric fields and currents by local winds in the equatorial electrojet.

Forbes and Lindzen [1976] solved 3 dimensional equation for EEJ, with boundary conditions as at the equator meridional current equal to zero and at latitude of 7^0, vertical current becomes zero, i.e. 3D model reduces to thin shell dynamo model. They assumed a simple dipole magnetic field, and hence the north-south symmetry of the electrojet. Diurnal (1,-2), (1,1) and semidiurnal (2,2), (2,4) neutral wind components have been used in their model. This model showed that the inclusion of vertical currents near the magnetic equator nearly doubles the magnetic variation obtained from the thin-shell dynamo model, relaxing the need for E-region diurnal wind speeds as large as those required by previous workers. Ananda Rao and Ragava Rao [1979] introduced sizable vertical winds with a 6 hour periodicity within this model framework and were able to generate a reversal of the electrojet currents.

The models discussed above look at the Sq and EEJ as separate entities connected the earth through boundary condition or through transported electric fields. Takeda and Maeda [1980, 1981] was the first to look at Sq and EEJ as a unified approach that could take into account the Sq as well as the EEJ current systems. They computed 3D current structure in the ionosphere (90-400 km) for (1,-2) mode of tidal wind as well as for (2,2) and (2,4) modes. Takeda [1982] calculated 3D ionospheric currents and field aligned currents generated by asymmetrical ionospheric dynamo self-consistently. Thus their method does not impose artificial boundary conditions unlike earlier models. This model, therefore took the first step in providing a basic self-consistent 3D model of the ionospheric dynamo numerically solvable as a boundary value problem.

Singh and Cole [1987] have developed a method using the dipole field geometry for numerically solving a suitably formulated ionospheric-wind dynamo equation for the electrostatic potential and field, with boundary value approach. They further derived the prescription for generating 3D electric current density in a magnetic meridional plane in the equatorial and low-latitude ionosphere. The model is very elegant and adopts a unified approach that can provide both the Sq and electrojet field in an internally consistent way. There is also an additional advantage that it is computationally more efficient than the models of Takaeda and Maeda as it involves a solution of an ordinary differential equation instead of a two dimensional partial differential equation.

8.2 Basic requirements for numerical model for EEJ:

The Sq and EEJ variations can be used as a diagnostic tool for monitoring atmospheric motions provided the clear correlations are established between the two. The introduction of a variety of radars for monitor mesospheric tides should give an additional impetus for the development of models of the Sq. and EEJ. Some attempts have been made to deduce the source of the day to variability in Sq and electrojet to the change to the variability of amplitude and phase of winds

[Marriot et al.,1979;, Hanuise et al., 1983] but these are based on simplified symmetric models of the ionspheric dynamo which cannot take into the longitudinal dependence of the phenomenon.

Ideally we would like to have a model that can account for the correlation of the Sq and electrojet strength on a day to day basis and the role of neutral winds in the generation of such correlation. We would like it account for the special phenomenon of CEJ which involves the reversal of the ionospheric currents within the electrojet region without a corresponding change outside the electrojet belt.

It should be emphasized that the interest in the EEJ should not be confined to the currents and magnetic fields only. The entire dynamics of the low latitude ionosphere is controlled by the electric fields generated by the dynamo action. The selected modeling procedures should be able to generate the electrical structure in the low latitude ionosphere.

As a result of above discussion, for an acceptable model of ionospheric current system, one would seek a three dimensional model which take realistic inputs of atmospheric tides and conductivity and is able to examine and produce globally self-consistent Sq and EEJ electric fields and currents. The model should account for the ground, satellite and rocket observations.

To include all desirable features into a single model is a daunting task. For example relatively higher percentage of occurrence of CEJ in the longitude range of 300- 330^0 E could be attributed to the fact that in that region, the dip equator is not perpendicular to the direction of the magnetic field. This is an entirely new factor which account for some of the special features of electrojet in the American zone but it is not easy to include such complex features in a global model. The CEJ was also confined to a very narrow longitudinal belt and the phenomenon

could be related to non-migratory tides driven either the lower atmospheric meteorology or disturbance dynamo effects propagated from higher latitudes. Again no clear-cut forcing algorithms are available for inclusion in a global model. Furthermore, inclusion of localized features into a global model can generate numerical instabilities.

Finally, the persistent feature of the longitudinal dependence of the EEJ on the dip latitude position with respect to the geographic equator has to be necessarily taken into account. The model should have the flexibility for future up gradation and for variation of the input parameters to enable its use, as a diagnostic tool for neutral wind motions, in future.

8.3 Scope of present model:

The model formulated here does not attempt to examine to incorporate all the features of the geomagnetic field geometry but takes into account the effect of the location of the dip equator with the geographic equator by solving the dynamo equation in a dipole geomagnetic field geometry. While the dip equator defined by a dipole field does differ from the actual dip equator, we believe that the simplified geometry should provide sufficient insight into mechanism operating.

The methodology developed by Singh and Cole [1987] appears most elegant and promising. The procedure has, however, not been used so far to obtain a working model of the ionospheric current system. We pick up the thread from where they left it and try to put a model that can be used to reproduce the observations in a quantitative way. The method is also computationally more efficient than the scheme of Takeda and Maeda [1980, 1981], which requires the solution of 2-dimensional partial differential equation. We are also able to bring out, in a more transparent manner, how the different harmonics in tides and conductivity combine to generate the harmonic structure in the current system.

The present model carries out the computations using dipole magnetic field and assumes that the field lines are equipotential. The neutral wind and conductivity computations are performed for latest data sets. The tidal wind components that are essentially calculated in geographic coordinate system are transformed to geomagnetic coordinate system. We have confined ourselves to migratory tides, though the approach adopted in chapter 6 can be augmented to include non-migratory contributions. We also work within the boundaries of classical tidal theory for the sake of technical simplicity. Thus background winds and ion drag terms are not included. Though the effect of neutral winds on the electrodynamics can be included, their contribution through modification of tidal structure cannot be incorporated.

The choice of the conductivity model is very important [Richmond, 1979] and we have made some improvements in the existing conductivity models as described in chapter 7. Some basic uncertainties in the values of collision frequencies still remain.

8.4 Development of Model for EEJ:

8.4.1. Definition of coordinate system:

We work with the dipole co-ordinate system. The parameters defining the dipole co-ordinates are

$$p = L = \frac{R}{R_E}, \qquad r = \phi, \qquad and \qquad q = \frac{\cos\theta}{R^2} = \frac{\sin\lambda}{R^2}$$

where, R = Radial distance of the point from the centre of the dipole magnet.

R_E = Radius of the earth

θ = Colatitude

λ = Geomagnetic Latitude

ϕ = Geographic Longitude

Scale factors h_p, h_q, h_r defining the spatial metric are given as

$$h_p = \frac{R_E \cos^2 \lambda}{\sqrt{1+3\sin^2 \lambda}}$$

$$h_q = \frac{R_E p^3 \cos^6 \lambda}{\sqrt{1+3\sin^2 \lambda}}$$

$$h_r = R_E p \cos^3 \lambda$$

The basic unit vectors defining the axis of the co-ordinate system are:

$\hat{q}$ -along the dipole field (pointing towards south)

$\hat{r}$ -pointing east, parallel to geomagnetic latitude contours and

$\hat{p}$ -normal to both the above axes that is positive upward

Note in this chapter the co-ordinate 'r' refers to the longitude in the geomagnetic co-ordinates and should not be confused with the radial parameter 'r' used in some of the earlier chapters.

8.4.2. Basic Principles used for setting up Model Equations:

The expression that provides the basic link between ionospheric conductivities and currents can be written using equation (8.3) as

$$\bar{J} = \sigma_0 \bar{E}_{\parallel} + \sigma_1 \left(\bar{E}_{\perp} + \bar{V} \times \bar{B}\right) + \sigma_2 \left(\bar{B} \times \frac{\left(\bar{E}_{\perp} + \bar{V} \times \bar{B}\right)}{B} \right) \qquad (8.12)$$

where $\bar{E}_{\perp} = E_p \hat{p} + E_r \hat{r}$

$$\bar{J} = J_p \hat{p} + J_r \hat{r} + J_{\parallel} \hat{q}$$

Therefore different components of current can be written as

$$J_p = \left(\sigma_1 E_p - \sigma_2 E_r\right) + \left(\sigma_1 V_r + \sigma_2 V_p\right) B \qquad (8.13)$$

$$J_r = \left(\sigma_1 E_r - \sigma_2 E_p\right) + \left(-\sigma_1 V_p + \sigma_2 V_r\right) B \qquad (8.14)$$

The first term on RHS of above two equations provides the contribution of electrostatic field while the second term is the wind driven dynamo component.

Let $J_{wp} = \left(\sigma_1 V_r + \sigma_2 V_p\right) B$ *and* $J_{wr} = \left(-\sigma_1 V_p + \sigma_2 V_r\right) B$

$$J_p = \left(\sigma_1 E_p - \sigma_2 E_r\right) + J_{wp} \qquad (8.15)$$

$$J_r = \left(\sigma_1 E_r - \sigma_2 E_p\right) + J_{wr} \tag{8.16}$$

In order to get V_p and V_r, we have to convert the tidal velocities computed in spherical geographic co-ordinates to spherical geomagnetic co-ordinates and then take a scalar product with the relevant unit vectors.

Defining an electrostatic potential Φ such that

$$E_p = -\frac{1}{h_p}\frac{\partial \Phi}{\partial p}$$

$$E_r = -\frac{1}{h_r}\frac{\partial \Phi}{\partial r}$$

Therefore equation (8.15) and (8.16) can be rewritten as

$$J_p = -\left(\frac{\sigma_1}{h_p}\frac{\partial \Phi}{\partial p} - \frac{\sigma_2}{h_r}\frac{\partial \Phi}{\partial r}\right) + J_{wp} \tag{8.17}$$

$$J_r = -\left(\frac{\sigma_1}{h_r}\frac{\partial \Phi}{\partial r} - \frac{\sigma_2}{h_p}\frac{\partial \Phi}{\partial p}\right) + J_{wr} \tag{8.18}$$

8.4.3 Application of $\overline{\nabla} \cdot \bar{J} = 0$:

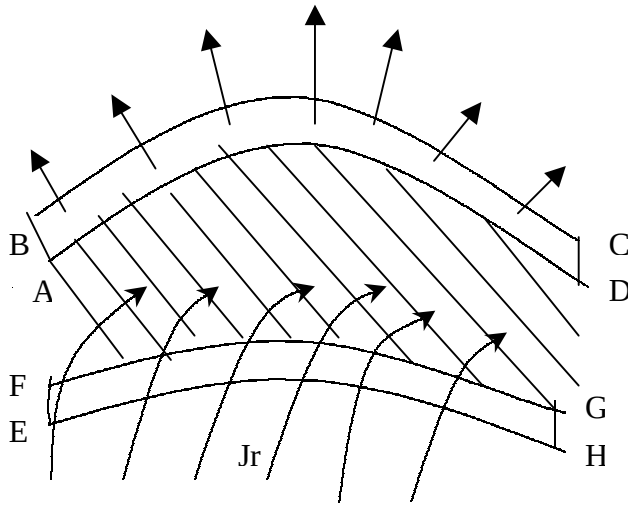

Figure 8.1

Consider geometry depicted in above figure 8.1. There are two surfaces situated at longitudes $r = r_0$ and $r = r_0 + \Delta r$, which are not seen in the figure. There are two more surfaces viz. (ABCD) and (EFGH) defined at different radial distances with longitudinal width of Δr and latitudinal extent from $-q$ to $+q$, where field line intersects the base of the ionosphere. Let (ABCD) be characterized by $p = p_n$ while q varies from $-q_n$ to $+q_n$. Whereas surface (EFGH) is defined by $p = p_0$ and q varies from $-q_0$ to $+q_0$.

Consider the volume enclosed between (ABCD) and (EFGH) and two surfaces at $r = r_0$ and $r = r_0 + \Delta r$.

Since the region below the base of the ionosphere is regarded as a perfect insulator, no current flows into the base of the ionosphere. Hence,

$$J_p = 0 \qquad \text{for } p = p_0$$

and $J_q = 0$ at the end points of the field lines.

Since $J_q = 0$ at the ends of the volume, it does not contribute to the net current flowing out of the upper surface $p = p_n$ has to be compensated by the divergence

of the current J_r flowing in and out of the volume through surfaces located at longitudes $r = r_0$ and $r = r_0 + \Delta r$.

The net current flowing out of the volume for every value of *p*, should be zero,

$$\int_{-q(p)}^{q(p)} J_p h_q h_r dq + \int_{p_0}^{p} dp \int_{-q(p)}^{q(p)} dq \frac{\partial}{\partial r}\left(h_p h_q J_r\right) = 0 \tag{8.19}$$

Consider first term,

$$\begin{aligned}\int_{-q(p)}^{q(p)} J_p h_q h_r dq &= \int_{-q(p)}^{q(p)} \left[-\frac{\sigma_1}{h_p}\frac{\partial \Phi}{\partial p} + \frac{\sigma_2}{h_r}\frac{\partial \Phi}{\partial r} + J_{wp} \right] h_q h_r dq \\ &= -A\frac{\partial \Phi}{\partial p} + B\frac{\partial \Phi}{\partial r} + \rho_{wp}\end{aligned} \tag{8.20}$$

where,

$$A = \int_{-q(p)}^{q(p)} \frac{h_q h_r}{h_p}\sigma_1 dq \tag{8.21}$$

$$B = \int_{-q(p)}^{q(p)} h_q \sigma_2 dq \tag{8.22}$$

$$\rho_{\omega p} = \int_{-q(p)}^{q(p)} h_q h_r J_{\omega p} \sigma_2 dq \tag{8.23}$$

Second term can be written as,

$$\int_{p_0}^{p} dp \int_{-q(p)}^{q(p)} dq h_p h_q \frac{\partial J_r}{\partial r} = -\int dp \left[C\frac{\partial \Phi}{\partial r} + D\frac{\partial^2 \Phi}{\partial r^2} + E\frac{\partial \Phi}{\partial p} + B\frac{\partial^2 \Phi}{\partial r \partial p} - \rho'_{wr} \right]$$

where,

$$C = \int_{-q(p)}^{q(p)} h_p h_q \left[\frac{\partial}{\partial r}\left(\frac{\sigma_p}{h_r} \right) \right] dq \quad = \int_{-q(p)}^{q(p)} \frac{h_p h_q}{h_r}\frac{\partial}{\partial r}(\sigma_p) dq \tag{8.24}$$

$$D = \int_{-q(p)}^{q(p)} \frac{h_p h_q}{h_r}\sigma_p dq \tag{8.25}$$

$$E = \int_{-q(p)}^{q(p)} h_q \frac{\partial}{\partial r}(\sigma_H) dq \tag{8.26}$$

$$\rho'_{\omega r} = \frac{\partial}{\partial r}\int_{-q(p)}^{q(p)} J_{\omega r} h_p h_q dq \tag{8.27}$$

Hence equation (8.19) gives dynamo equations as

$$A\frac{\partial \Phi}{\partial p} = B\frac{\partial \Phi}{\partial r} + \rho_{\omega p} - I \qquad (8.28)$$

and $$\frac{\partial I}{\partial p} = C\frac{\partial \Phi}{\partial r} + D\frac{\partial^2 \Phi}{\partial r^2} + E\frac{\partial \Phi}{\partial p} + B\frac{\partial^2 \Phi}{\partial p \partial r} - \rho'_{\omega r} \qquad (8.29)$$

where I is the field line integrated meridional current flowing into the volume of the slice of width dr between the surfaces ABCD and EFGH in figure 8.1 and defined as

$$I = \int_{p_0}^{p} dp\left[C\frac{\partial \Phi}{\partial r} + D\frac{\partial^2 \Phi}{\partial r^2} + E\frac{\partial \Phi}{\partial p} + B\frac{\partial^2 \Phi}{\partial p \partial r} - \rho'_{wr} \right] \qquad (8.30)$$

8.4.4 Framework for solutions:

The two first order differential equations (8.28) and (8.29) have to be solved using the appropriate boundary conditions. Both the boundary conditions are applied on I, where I represents the total meridional current, flowing into the volume of the slice dr bounded by the two surfaces ABCD and EFGH in Figure 8.1. The surface EFGH is taken at the lower boundary of the ionosphere, which is sufficiently low into the neutral atmosphere so that no currents flow through it. We take it at 80 km. here. The surface ABCD is defined by the parameter p.

The condition $I = 0$ is naturally satisfied at the lower boundary as both the current and the area of the bounding surface vanish.

Since we believe that the Sq currents become sufficiently weak at high latitudes, we infer that at sufficiently large p, no meridional currents will flow into the slice volume and I will vanish again. In getting at the solution we use the shooting method. We start with $I = 0$ and an initial guess for Φ at the upper boundary purely from stability considerations (Singh and Cole, 1987). Mersons algorithm, which is Runge-Kutta method of order 4 is used to extend the solution at the lower boundary. The initial guess is then refined till I, is zero at the lower boundary also.

The upper boundary is chosen as some arbitrary $p = p_{upper}$. The choice of the upper boundary is achieved through trial and error in such a way that increasing it does not alter the solution within.

Once and I and Φ are determined as a function if p and r, the electric fields E_p and E_r can be evaluated taking the respective spatial derivatives. The current components J_p and J_r are then determined from equations (8.17) and (8.18). All components of transverse currents and electric fields can thus be evaluated at any point within the ionosphere.

To get the parallel current J_q, we have to solve the equation

$$\frac{\partial}{\partial q}(h_r h_p J_q) + \frac{\partial}{\partial p}(h_q h_r J_p) + \frac{\partial}{\partial r}(h_p h_q J_r) = 0 .$$

The flow of the program requires the prescription of the solar zenith angle (or the date and UT) for generating the right inputs of the conductivity through the IRI model for charge densities, and MSISE model for neutral densities. This is also required for the calculation of heating rates from the Phodis model. Given these the parameters A, B, C, E and the parameters ρ_{wp}, $\rho'_{w[}$and ρ'_{wr} can be evaluated for the purpose of solving the differential equation. We present the parameters in Figure 8.2 as a function of height of the field line at the equator. These parameters have been evaluated under equinoxial noontime conditions for sunspot number 120. For the tides diurnal modes (1,1), (1,-2) and (1,-4) and semi-diurnal modes (2,2), (2,4) and (2,6) have been used.

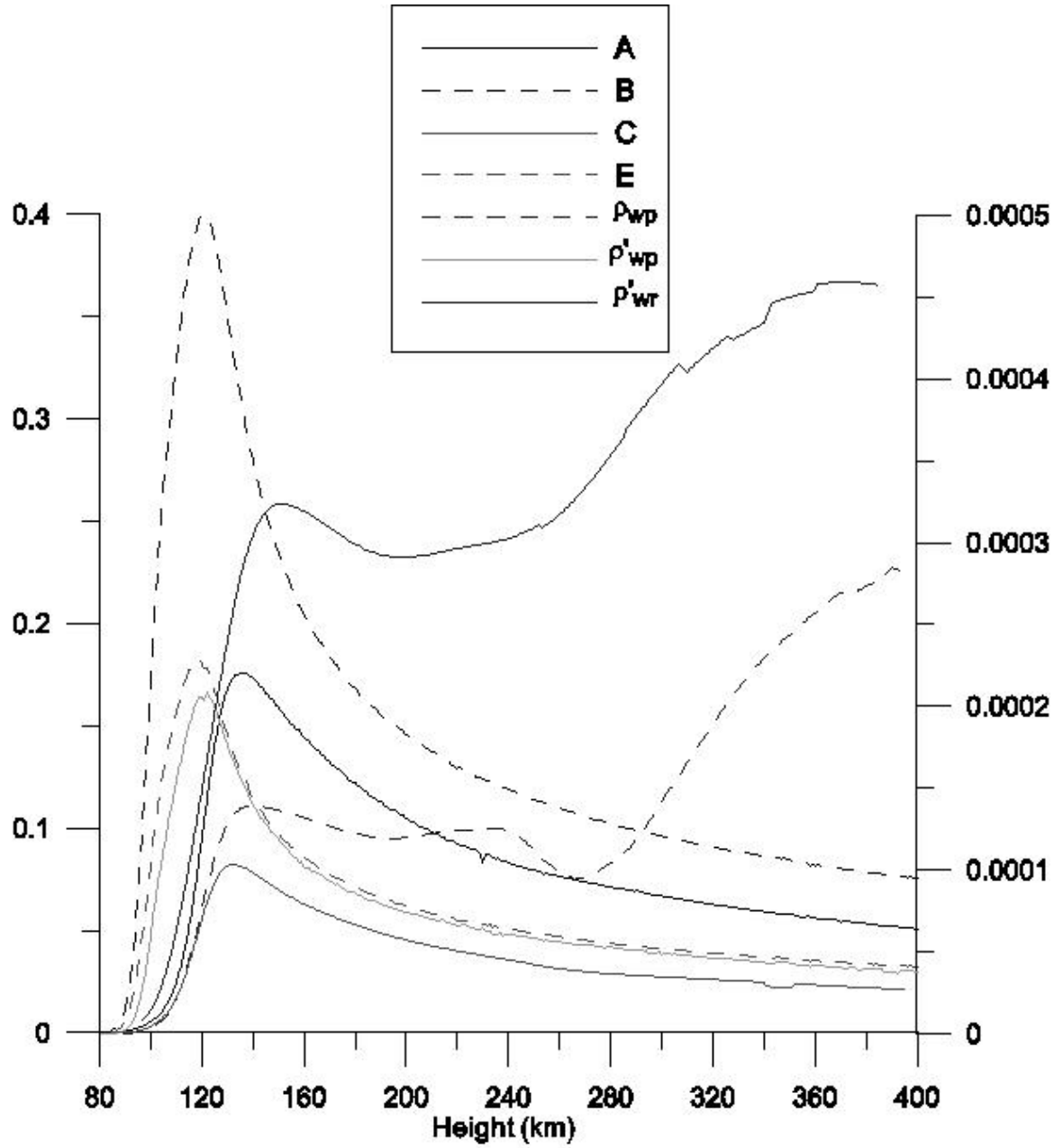

Figure 8.2 : Plot of constants used in dynamo equations Vs altitude. Right hand side scale is for A,B,C and E, while left hand side scale is for ρ_{wp} ,ρ'_{wp}, and ρ'_{wr}

The parameters A, B, C and E in units of mhos.m while the wind related parameters have units of amperes/m. Though the numerical values of these two sets of parameters appear to be very different, the terms they generate contribute to the same order of magnitude. What is more relevant here is the nature of dependence on the equatorial height of the specific field line.

It may be noted that though the parameters represent the values integrated along the field lines, each of the values gets multiplied by the ionospheric conductivity that is significant only within the dynamo region. The values are weighted heavily by segments of the field immersed in the dynamo region. A look at Figure 8.2 brings out the point well. The parameters A, B, C and E which represent Hall and Pedersen conductivities or their longitudinal derivatives multiplied by some scale heights have significant values at lower height peaking around field lines corresponding to 120 to 140 km altitude.

The wind related parameters contribute significantly even for the field lines originating at mid-latitudes. This is understandable as some of the tides considered here have much larger magnitudes at mid latitudes. This shows that tide generated potentials originating in mid latitudes are relevant for the forcing of the currents while the response is essentially due to conductivity patterns at lower latitudes. The contributions of winds, however, drop when you get to field lines at really high latitudes.

8.4.5 Solution in terms of zonal harmonics

The basic framework described in the last section presents a methodology that requires the differential equations to be solved at each longitude and the longitudinal gradients have to be determined for each longitude. For full global solution this will be tantamount to solving a 2-D partial difference equation. It is possible to simplify these calculations considerably, as we know the quiet day conductivity, tides and currents can be well described as a sum of first four

harmonics of the diurnal pattern. In terms of longitudinal harmonics, it is taking a snap shot at each UT and expressing the longitudinal variations as a sum of four harmonics.

It should be remembered that we are working in geomagnetic frame of reference and the harmonic co-efficient will be different from what they would appear to be in geographic co-ordinates. This follows from the fact that some of the latitudinal variations in the geographic coordinates will map into co-efficient of the longitudinal harmonics in the geomagnetic co-ordinate system.

The above dynamo equations (8.28) and (8.29) are differential equations and are to be solved in order to obtain the dynamo currents. Instead of solving the full two-dimensional equations, we express the electrostatic potential (Φ), the currents $(\bar{J})$, conductivities (σ_1) and (σ_2) and the zonal winds (V_r) and meridional winds (V_p) in terms of the first four harmonics of the global (360 degree) cyclic variation at each UT. This is a simple straightforward procedure and involves computing the values of all the tidal and conductivity parameters for specified geomagnetic latitude-longitude grid and then to determine the harmonic coefficient of longitude variation at each latitude grid. The tidal and conductivity model inputs are discussed in detail in chapter 6 and 7 are used to generate the values at the geographic co-ordinates corresponding latitude-longitude combination in the geomagnetic frame of reference. A Fortran program has been developed to carry out this operation.

Thus we can express,

$$\Phi(r, p) = \sum_{k=0}^{4} \{\Phi_{kc} \cos kr + \Phi_{ks} \sin kr\} \qquad (8.31)$$

$$\sigma_1(r, p) = \sum_{k=0}^{4} \{\sigma_{1kc} \cos kr + \sigma_{1ks} \sin kr\} \qquad (8.32)$$

$$\sigma_2(r,p)=\sum_{k=0}^{4}\{\sigma_{2kc}\cos kr+\sigma_{2ks}\sin kr\} \quad (8.33)$$

$$V_r(r,p)=\sum_{k=0}^{4}\{V_{rkc}\cos kr+V_{rks}\sin kr\} \quad (8.34)$$

$$V_p(r,p)=\sum_{k=0}^{4}\{V_{pkc}\cos kr+V_{pks}\sin kr\} \quad (8.35)$$

$$J_r(r,p)=\sum_{k=0}^{4}\{J_{rkc}\cos kr+J_{rks}\sin kr\} \quad (8.36)$$

$$J_p(r,p)=\sum_{k=0}^{4}\{J_{pkc}\cos kr+J_{pks}\sin kr\} \quad (8.37)$$

$$J_{wr}(r,p)=\sum_{k=0}^{4}\{J_{wrkc}\cos kr+J_{wrks}\sin kr\} \quad (8.38)$$

$$J_{wp}(r,p)=\sum_{k=0}^{4}\{J_{wpkc}\cos kr+J_{wpks}\sin kr\} \quad (8.39)$$

Since the entire field line is confined to the same geomagnetic meridian, the harmonics of $A, B, C, D, E, \rho_{wr}\rho'_{wr}, \rho_{wp}$ and ρ'_{wp} can be obtained by integrating along the field line for each of the harmonics. All these steps for the initialization step in the algorithm developed.

The prescription for writing a product of harmonic and the resultant has to be expressed in terms of the harmonics and all the coefficients for all the sine and cosine harmonics have to be separately equated to obtain eight equations corresponding to equation (8.28) and eight corresponding to equation (8.29). There are 16 equations to be considered to obtain a complete solution for the first four harmonics. In carrying out the harmonic multiplication one has to keep track of harmonic coefficients of dependent variables Φ and I. The procedure to carry out this product is described in appendix 3. It is fairly straightforward to note that 16 differential equations for the respective harmonic coefficients can be carried out quite mechanically and can be programmed without any difficulty.

Using that we can write the harmonic components of equation (8.28) in the form

$$\mathbf{R} \cdot \frac{d\boldsymbol{\varphi}}{dp} = \mathbf{S} \cdot \boldsymbol{\varphi} + \mathbf{J}_{\mathbf{wp}} - \mathbf{I} \qquad (8.40)$$

This can be inverted to get

$$\frac{d\varphi}{dp} = \mathbf{R}^{-1}\left(\mathbf{S} \cdot \varphi + \mathbf{J}_{\mathbf{wp}} - \mathbf{I}\right) \qquad (8.41)$$

Similarly, equation (8.29) can be rewritten in the form

$$\frac{d\mathbf{I}}{dp} = \mathbf{Q} \cdot \varphi + \mathbf{E} \qquad (8.42)$$

where, $\varphi = \begin{vmatrix} \phi_{c1} \\ \phi_{c2} \\ \phi_{c3} \\ \phi_{c4} \\ \phi_{s1} \\ \phi_{s2} \\ \phi_{s3} \\ \phi_{s4} \end{vmatrix}$, $\mathbf{J}_{\mathbf{wp}} = \begin{vmatrix} J_{wp\,c1} \\ J_{wp\,c2} \\ J_{wp\,c3} \\ J_{wp\,c4} \\ J_{wp\,s1} \\ J_{wp\,s2} \\ J_{wp\,s3} \\ J_{wp\,s4} \end{vmatrix}$

The matrices **R**, **S**, **I** and **E** can be defined using the procedures presented in appendix 3 and indeed can be determined once and for all at the beginning of the program for each UT hour.

Equations (8.41) and (8.42) are solved, using the procedures outlined in the last section but with the difference that the boundary conditions have to be applied for each of the four sine and cosine harmonic coefficient of **I**.

8.5 Model for short period fluctuations:

A brief reference was made in chapter 5 on the implications of the results on modelling and how model designed for high latitude geometry and applied to equatorial observations failed to explain the magnitude of phase shifts introduced by the daytime ionosphere. Recently, Federov et al [1999] developed

a more realistic model for ionospheric propagation of hydromagnetic disturbances at the low latitudes. Here we examine the treatment of Fedorov et al [1999] using low and equatorial latitudes. The model essentially valid for low inclination of the ambient field, considers a conductive layer of thickness 'l' . Let $J_0(x,z,t)$ be the current induced by the oscillating part of an external current, which is EEJ current in the equatorial region, which flows along the dip equator (Y axis). Since the field aligned electric field component, $E_{\parallel} \to 0$ when $\sigma_{\parallel} \to \infty$, we have the disturbed transverse electric field $E_{\perp}$,

$$\left(\nabla \times \nabla \times E_{\perp}\right)_{\perp} + \mu_0 \frac{\partial}{\partial t}\left(\sigma_1 E_{\perp} + \frac{\sigma_2 \left(B_0 \times E_{\perp}\right)}{B_0}\right) = -\mu_0 \frac{\partial}{\partial t} J_0$$

where B_0 is the ambient M.F lies in the XZ-plane with inclination I and μ_0 is the magnetic permeability of free space. Here Z is vertically upward and X is northward.

One of their important finding is that you can have poleward propagating compressible or gyrotropic wave generated oscillating equatorial currents. Our results with African electrojet array suggest that the phase lags between electrojet and non-electrojet stations are more consistent with the view point that the oscillations are propagating equatorward. Thus they do not represent the scenario envisaged by Fedorov et al [1999].

8.6 Summary and discussions:

The present chapter represents an attempt to place the salient results presented in the earlier chapters in a proper theoretical perspective. No attempt is made to model all the features obtained from the satellite or ground data. Instead we just present a framework that can be used in future to understand, in a quantitative manner, the longitudinal dependence of the day to day variability in the low latitude current systems. It is suggested that the simplest model, that distinguishes the positions of the dip equator from the geographic equator,

should be the first candidate to explain the strong dependence of the day to day variability on geographic location of the dip equator.

The model generated here does not attempt to examine to incorporate all the features of the geomagnetic field geometry but takes into account the effect of the location of the dip equator with the geographic equator by solving the dynamo equation in a dipole geomagnetic field geometry. While the dip equator defined by a dipole field does differ from the actual dip equator, we believe that the simplified geometry should provide sufficient insight into mechanism operating.

The methodology developed by Singh and Cole [1987] has been developed into a working model of the ionospheric current system by integrating it with the conductivity and tidal models. The emphasis in the chapter is on the development of the scheme for the computation of the currents given the tidal forcing and ionospheric conductivity. We also describe the scheme that is used to generate the harmonic structure of the global current system.

The model developed uses migratory tides computed from the classical tidal theory. The thermal inputs for the tides are generated from the Phodis package, the electron densities and the neutral densities form the IRI and MSIS models respectively. The conductivity and tides are generated from the algorithms developed in chapters 6 and 7. We find that the wind generated emf make significant contributions even on the field lines originating at relatively high latitudes. This is understandable as some of the tides considered by us have much larger magnitudes at mid latitudes. But it does show that tide generated potential originating in mid latitudes are relevant for the forcing of the currents while the response may be essentially due to conductivity patterns at lower latitudes.

The programming framework developed here offers excellent opportunity for performing variety of numerical experiments that can lead to better understanding of mechanisms responsible for the longitude dependence of Sq and electrojet current systems.

Chapter 9
Conclusions

This thesis presents a systematic study of low latitude current systems using satellite and ground observations. The overall objective of the study was to obtain the benchmark for the models of the low latitude current systems. A theoretical modelling framework was also generated to place the observational findings obtained from satellite and ground data in proper prospective. The main conclusions of present investigations along with the scope of future work are outlined below.

There are very few phenomenon in the upper atmosphere that are as sensitive to the strength and distribution of the earth' s core field as the equatorial electrojet. In **chapter 2**, we use the Oersted initial field model along with the earlier IGRF models to provide insight into the secular changes in the global patterns of the position and strength of the Equatorial Electrojet (EEJ). A northward drift in the location of the dip equator (hence the position of the axis of the EEJ) to the extent of 1.0 degrees per decade is seen around 300^0. In contrast, in the Pacific, east of Australia, there is practically no drift. It is also observed that the largest secular variation in the Cowling conductivity occurs in the South American sector with a possible 4.0% increase per decade for the same level of ionization in the E-region. The Oersted main field model does not suggest any changes or reversal of these trends. A very significant result is that the magnetic field at the dip equator need not be perpendicular to the line of zero dip and this deviation from the idealized scenario of the equatorial electrojet can result in significant contribution of the equatorial electrojet to the declination component. This is an area where considerable amount of theoretical and observational inputs is needed.

In **chapter 3**, we have shown that the magnetic field observations obtained from the Oersted satellite can form an excellent data base for studying not only the longitudinal structure of the equatorial electrojet but also the sources responsible for its variations from day to day. We have devised an objective method for identifying the signature of the EEJ and determining the parameters that define its basic structure and found that it works out very well in describing the surface manifestations of the EEJ as seen in the observatory data. The excellent correlation between the ground observations and the corresponding field computed from the deduced satellite parameters, for both the Indian and American sectors, shows the authenticity of the data and method of analysis. It should be noted that the identification of the parameters is not necessarily accurate on a pass to pass basis. However, it has been clearly brought out from the analysis that the deduced parameters can reproduce statistically consistent characteristics of the EEJ.

Our analysis was able to reproduce many of the features observed earlier using satellite magnetic measurements [cf. Onwumechili, 1997 and references therein]. Our study reveals a multi-peak longitudinal structure for the EEJ. We believe that the longitudinal structure of the EEJ cannot be explained on the basis of the conductivity distribution in the equatorial ionosphere and asymmetrical tidal forcing has to be taken into account. We do find a clear indication that the axis of the EEJ tends to move away from the dip equator towards the geographic equator as suggested by Onwumechili [1985]. More remarkably the position of the EEJ axis deduced from satellite exhibits a local time dependence similar to what has been observed on ground [Fambitkoye and Mayaud, 1976] being closest to the dip equator around noon. There is also a clear indication that the EEJ strength weakens as the axis moves away from the dip equator. These features can be seen only using satellite data because of its extensive spatial coverage.

The width of the electrojet is found to vary considerably with longitude and is as high as 6.5^0 in the American zone compared to around 2.5^0 in the 120-180^0 belt. In fact the peak in the computed EEJ signature around 270^0E is connected more with an enhancement of the width of the EEJ, as peak current (J_0) does not exhibit any peak in this region.

The most striking results obtained through the analysis, based on principal component technique are related to the day-to-day variability of the EEJ strength on ground. The analysis technique revealed many interesting features hitherto unnoticed. The first component, which contributes a little over 30% to the observed variance, could be identified with the global variation of the EEJ emanating from the day-to-day variability of the migrating tides. The second and fourth components, which account for around 15% and 10% of the variance respectively, are driven by forcing that depends on whether the location of the EEJ in that sector is in the northern or southern hemisphere. The third component provides maximum contributions wherever the geomagnetic and dip equators are sufficiently close, accounting for 12.5% of the variance. The remaining components could be associated with contribution of non-migratory tides or other unknown mechanisms. Thus the present study suggests that besides conductivity, atmospheric tidal modes play important role in defining the zonal variability of the EEJ current system.

In **chapter 4**, we have shown that the reverse EEJ signature at satellite indicates the counter electrojet. This has been achieved by examining simultaneous satellite and ground data. Whenever, the satellite is in the longitude belt of the ground station observing the CEJ, the satellite also sees the CEJ. However, the satellite does not see the CEJ if satellite and ground differ in longitude by 30^0 or more. The longitudinal width of the pre-noon CEJ is found to be never more than

3 hours. This gives insight into the longitudinal structure of the CEJ and indicates the importance of the role of non-migrating tides.

Even though the seasonal variation is sitting on the local time variation, higher percentage of CEJ occurrence recorded during morning and afternoon hours are quite consistent with earlier findings of Rastogi [1974b]. We also find that the largest occurrence of CEJ is associated with the region of weakest normal EEJ.

Statistical study shows that the longitudinal variation of the centre of the CEJ current system lies south of the dip equator for Indian sector and north of the dip equator of American sector. Thus the centre of CEJ appears to be shifted away from the dip equator towards the geographic equator in both the hemispheres. It is also seen that there is significantly greater probability of CEJ occurrence in the 300^0–330^0E longitude sector. This is the region where the magnetic field and the local dip equator contours deviate significantly from perpendicularity.

Chapter 5 brings out the features of compressible hydromagnetic waves in frequency range of 10-80 mHz, using the Oersted magnetic field data analyzed in conjunction with the ground magnetic data available with a sampling rate of 1 second. A high degree of coherence between the satellite and fixed ground oscillation is seen, despite the fact that the satellite covered a significant latitudinal distance. Even the temporal structures show a high degree of correlation over the large orbital distance. This suggests that the incident hydromagnetic waves are phase coherent over a large range of latitudes. We have also demonstrated that the phase delays experienced by the wave depend on the frequency and the ionospheric conductivity. A full fledged non-local model which takes into account the varying inclination and conductivity with latitude is required to provide the right explanation for the observed phenomenon.

Chapter 5 also examines data from West African equatorial array sampled at one minute interval to study magnetic pulsations of range 1-4 mHz. The average daytime equatorial enhancement in H component and the enhancement in D component at the fringes of the electrojet can be attributed to the equatorial ionosphere and this is consistent with earlier findings [Pathan et al., 1999, Jain and Srinivasacharya, 1975] for Indian stations. We observe that the enhancement is frequency dependent and it is larger for lower frequencies. Apart from the amplitude modulation, the phase of the received signal is also modulated by the EEJ. Thus our analysis shows that the daytime ionosphere effects are important and need to be modeled.

Chapter 6 is devoted to the studies of atmospheric tides based on classical theory of atmospheric tides. The tidal model presented in this chapter uses more recent ways of computing the heating sources based on the inputs of the public domain Phodis package. Though it does not account for the dissipative forces and does not include non-migratory tides, it is ideally suited for study of the day-to-day variability of the EEJ. The tidal model, is flexible and supports different input parameters such as temperature, pressure so that day to day variability of the tidal components and its effect on the EEJ can be studied by performing numerical experiments. The program is developed to calculate Hough modes and can be extended to calculate the non-migrating tidal components.

Chapter 7 carries out extensive study of ionospheric conductivity that plays a major role in ionospheric current system. We have developed a new model based on Pesnell et al [1993] formula for O^{+}-O collision frequency. The results obtained have been compared with earlier standard models. The present model uses more realistic ionospheric parameters (IRI, MSISE models). The comparative study reveals that the formalism and the input data set have significant influence on the height profile of conductivity. For the theoretical computations of the low latitude current systems, different conductivity models are useful in order to

study the sensitivity of current models to conductivities. We believe that our new model along with the realistic input data sets will improve the estimates of ionospheric currents in future model calculations. This chapter explores different aspects of ionospheric conductivity such as latitude, longitude, and local time dependence. This certainly will add to the understanding of ionospheric conductivity in global perspective.

In **chapter 8** an attempt to place the salient results presented in the earlier chapters in a proper theoretical perspective. No attempt is made to model all the features obtained from the satellite or ground data. Instead we just present a framework that can be used in future to understand, in a quantitative manner, the longitudinal dependence of the day-to-day variability in the low latitude current systems. It is suggested that the simplest model, that distinguishes the positions of the dip equator from the geographic equator, should be the first candidate to explain the strong dependence of the day-to-day variability on geographic location of the dip equator.

The model generated here does not attempt to incorporate all the features of the geomagnetic field geometry but takes into account the effect of the location of the dip equator with the geographic equator by solving the dynamo equation in a dipole geomagnetic field geometry. While the dip equator defined by a dipole field does differ from the actual dip equator, we believe that the simplified geometry should provide sufficient insight into mechanism operating.

The programming framework developed in this chapter offers excellent opportunity for performing variety of numerical experiments using the conductivity and tides generated from the algorithms developed in chapters 6 and 7. Such experiments can lead to better understanding of mechanisms responsible for the longitude dependence of Sq and electrojet current systems.

References:

Agu, C. E. and C. A. Onwumechili, *J. Atmos. Terr. Phys*., 43, 801-807, 1981a.

Agu, C. E. and C. A. Onwumechili, *J. Atmos. Terr. Phys*., 43, 809-816, 1981b.

Anand Rao, B.G. and R. Raghav Rao, *Space. Res*., 19,283-286, 1979.

Anderson, J. M. and L. Goldstein, *Phys. Rev.,* 100, 1037-1046, 1955.

Baker, W. G. and D. F. Martyn, *Phil. Trans. Roy. Soc. Lond,* A246, 281-294, 1953.

Banks and Kockarts, *Aeronomy: part A, Chapter 9,* Academic Press, 1973.

Bhargava, B. N. and A. Yacob, *J. Atmos. Terr. Phys.,* 35, 1253-1255, 1973.

Bhargava, B. N. and N. S. Sastri, *J. Geomag. Geoelectr.*, 31, 97-101, 1979.

Burrage, M. D., R. A. Vincent, H. G. Mayr, W. R. Skinner, N. F. Arnold, and P.B. Hays, *J.Geophys. Res.,* 101, 10,365-10,392, 1996a.

Burrage, M.D., R.A. Vincent, H.G. Mayr, W.R. Skinner, N.F. Arnold, and P.B. Hays, *J. Geophys. Res*., 101, 12,847-12,854, 1996b.

Butler, S.T. and K. A. Small, *Proc. Roy. Soc.,* A274, 91-121, 1963.

Cahill, L.J., J. Geophys. Res., 64, 489-503, 1959.

Cain J.C. and Sweney R.E., *J. Atmos. Terr. Phys.*, 35, 1231-1247, 1973.

Chandra, H., R. K. Misra and R. G. Rastogi, *Plan. Space Sci*., 19, 1497-1503, 1971.

Chandra, H., H. S. S. Sinha and R. G. Rastogi, *Earth Planet Space*,52,111-120, 2000.

Chapman, S., *A review, Nuovo Cimento, Suppl. 4, Ser. X*, 1385-1412, 1956.

Chapman, S. and R.S. Lindzen, *Atmospheric Tides, Dordrecht: Reidel Pub*., 1970.

Cohen, Y.,and J. Achache, *J. Geophys. Res.*, 95, 10783-10800, 1990.

Dalgarno, A., *J. Atmos. Terr. Phys*., 26, 939, 1964.

Davis, T.N., J. D. Stolarik, and J.P. Heppner, *J. Geophys. Res.*, 70, 5883-5894, 1965.

Doumouya. V., J. Vassal, Y. Cohen, O. Fambitakoye, M. Menvielle, *Ann. Geophy*., 16, 658-676, 1998.

Ducruix, J., V. Courtlillot and J. L. LeMouel, *J. Geophys. Res.*, 82, 335, 1977.

Ebun Oni, *J. Atmos. Terr. Phys.* , 35, 1267-1271, 1973.

Fambitkoye,O., *J. Atmos. Terr. Phys*., 35, 1265, 1973.

Fambitkoye, O. and P. N. Mayaud, *J. Atmos. Terr. Phys*., 38, 19-26, 1976.

Fambitkoye, O. and P. N. Mayaud, *J. Atmos. Terr. Phys.*, 38, 1-17, 1976.

Fedorov, E.,V. Pilipenko, V. Surkov, D.R.K. Rao and K. Yumoto, *J. Geo. Res*.,104, A3, 4329-4336, 1999.

Fejer, B. G., C. A. Gonzales, D. T. Farley, and M. C. Kelley, *J. Geophys. Res*., 84, A10, 5797-5802, 1979.

Fisher, R. I., *Statistical methods for research workers, Macmillan Publishing Co.,New York*, p189, 1970.

Forbes, J. M. and R. S. Lindzen, *J. Atmos. Terr. Phys*., 38, 897-910, 1976.

Forbes, J. M. and H. B. Garrett, *Geophy. Res. lett*., 5, 1013-1016, 1978a.

Forbes, J. M. and H. B. Garrett, *J. Atmos.Terr. Phys*., 35, 148-159, 1978b.

Forbes, J. M., *J. Geophys. Res*., 87, 5222-5240, 1982a.

Forbes, J. M., *J. Geophys. Res*., 87, 5241-5252, 1982b.

Forbush, S. E. and M. Casaverde, *Carnegie Institution of Washington Publication*, 620, 1961.

Garrett, H.B. and J. M. Forbes, *J. Atmos. Terr. Phys*., 40,657-668, 1978.

Garcia, R.R. and S. Solomon, *J. Geophy. Res., 90*, 3850-3868, 1985.

Gnanadesikan R., *Methods for statistical data analysis of multivariate observations, Joh Wiley and sons, New York*, 1977.

Gouin, P. and P. N. Mayuad, *Ann. Geophys.* 23, 41-47, 1967.

Gouin, P., *J. Atmos. Terr. Phys.*,35,1257-1264, 1973.

Groves, G.V., *J. Atmos. Terr. Phys.*, V.44, No.2, p111-121, 1982a.

Groves, G.V., *J. Atmos. Terr. Phys.*, V.44, No.3, p281-290, 1982b.

Hagan, M.E., Chang, J.L. and Avery, S.K.. *J. Geophys. Res*. 102, 16439-16452, 1997.

Hall, L. A. and H. E. Hinteregger, *J. Geophys. Res.,* 75, 6959-6965, 1970.

Harries, M.F., *J. Geophys. Res.,* 64, 983-995, 1959.

Hanuise, C., C. Mazaudier, P. Vila, M. Blanc and M. Crochet, *J. Geophys. Res.*,88,253-270,1983.

Haurwitz, B., *J. Mar. Res.,* 3, 254-267, 1940.

Hedin A. E. and G. Thuillier, *J. Geophys. Res*. 93, 5965-5971, 1988.

Henry, R. J. W. and M. B. McElroy, *Photoelectrons in planetary atmospheres, in The Atmospheres of Venus and Mars, edited by J. C. Brandt and M. B. McElroy,* pp.251-285, *Gordon and Breach, New York,* 1968.

Hesse, D., *Ann. Geophys.*, 38, 315-320, 1982.

Hines, C. O., H. G. Mayr, and C. D. Reddy, *J. Atmos. Sol. Terr. Phys.,* 59, 181-189, 1997.

Hinteregger, H. E., *Ann. Geophys.*, 26, 547-554, 1970.

Hough, S. S., *Phil. Trans. Roy. Soc. A*, 189, 201-257, 1897.

Hough, S. S., *Phil. Trans. Roy. Soc. A*, 191, 139-185, 1898.

Howard, J.N., D.E. Burch and D. Wlliams, *J. Opt. Soc. Am.,* 46, 186, 237, 242, 334, 452, 1956.

Hughes, W. J., and D. J. Southwood, *J. Geophys. Res.*, 81, p3234-3240, 1976.

Hutton, R., *J. Atmos. Terr. Phys.*,29, 1411-1427, 1967a.

Hutton, R, *J. Atmos. Terr. Phys.*, 29, 1429-1442, 1967b.

Itikawa, Y., *Planet. Space Sci.*, 19, 993-1007, 1971.

Jacchia, L. G., Smithson, *Astrophys. Obs. Spec. Rept*. No.332, 1971.

Jadhav, G. V., M. Rajaram, and R. Rajaram, *J Geodynamics,* 2001 (in press).

Jain, A.P. and K. G. Srinivasacharya, *J. Atmos. Terr. Phys.*, V.37, p.1477-1483, 1975.

James, M. E., D. Tripathi and R.G.Rastogi, Ind. J. Radio & space phys., 25, 36-43, 1996.

Johnson, D.H., *Quart. J. Roy. Meteorol. Soc.,* 81, 1-8, 1955.

Kane, R. P., *J. Atmos. Terr. Phys*., 35, 1249-1252, 1973.

Kane, R. P., *J. Geophys. Res.,* 83, 2671, 1978.

Kato, S., *J. Geoelectr.*, 8, 24-37, 1956.

Kato, S., *J. Geoelectr.*, 9, 107-115, 1957.

Kato, S., *J. Geophy. Res.*, 71, 3201-3209, 1966a.

Kato, S., *J. Geophy. Res.*, 71, 3211-3214, 1966b.

Kelvin, Lord (Thomson W.), *Proc. Roy. Soc. Edinb*., 11, 396-405, 1882.

Keneshea, T. J., R. E. Huffman and J. D. George, *Solar photoionization rate constants and ultraviolet intensities, in DNA Reaction rate Handbook*, 1972.

Kikuchi, T. and T. Araki, *J. Atmos. Terr. Phys.,* V-41, p-917-925, 1979a.

Kikuchi, T. and T. Araki, *J. Atmos. Terr. Phys.,* V-41, p-927-936, 1979b.

Kim, K.H. and K. Takahashi, *J.Geophys. Res.,* 104, p4539-4558, 1999.

Kim, K.H., K. Takahashi and B. J. Anderson, *J. Geophys. Res*.,103, p11755-11769, 1998.

Kylling, A., *Phodis, a program for calculation of photodissocitaion rates in the Earth's atmospheree, available by anonymous ftp to kaja.gi.alaska.edu, cd pub/arve'*,1995.

Labitzke, K., J. J. Barnett, and B. Edwards (eds.), *Handbook MAP 16, SCOSTEP, University of Illinois, Urbana,* 1985.

Lacis, A.A. and J.E. Hansen, J. Atmos. Sci.,31, 118, 1974.

Langel, R. A., M. Purucker and M. Rajaram, *J. Atmos. Terr. Phys*., 55, no-9, 1233-1269, 1993

Leovy, C., *J. Atmos. Sci*., 21, 238-248, 1964.

Lindzen, R. S., *J. Roy. Meteorol. Soc*., 93, 18-42, 1967a.

Lindzen, R.S., *Mon. Wea. Rev.*, 95, 441-451, 1967b.

Maeda, H., *J. Geomagn. Geoele*., 9, 86-93, 1957

Maeda, K., *Rept. Ionosph. Space Res. Japan*, 9, 148-165, 1955.

Maeda H., Kamei T., Iyemori T. and Araki T., *J. Geophys. Res. 90*, 2481-2486, 1985.

Maeda, H., Iymori T., Araki T. and Kamei T., *Geophys, Res. Lett*., 9, 243-245, 1982.

Maeda, K. and S. Kato, *Space Sci. Rev.,* 5, 57-79, 1966.

Manabe, S. and F. Moller, *Mon. Wea. Rev*., 89, 503-532, 1961.

Marriott, R. T., A. D. Richmond, and S. V. Venkateswaran, *J. Geomag. Geoelectr.*, 31, 311-340, 1979.

Mason R.G., *The equatorial electrojet in Central Pacific. Rept of the Marine Physical Laboratory of the Scripps Institute of Oceanography, San Diego 52, California, S10 Reference* 63-13, 1963.

Mason, E. A., *Planet. Space Sci*., 18, 137-144, 1970.

Matsushita, S. and W.H. Campbell, *Vol I and II, Academic Press, New York*, 1967.

Matsushita, S., Geophys. *J. R. Astron. Soc.,* 15, 109-125, 1968.

Matsushita, S., *J. Geomagn. Geoelectr*., 3, 44-46, 1951.

Mayaud, P.N., *J. Atmos. Terr. Phys*., 39, 1055-1070, 1977.

Mayaud, P. N., *Planet Space Sci.*, 24, 1049-1057, 1976.

Maynard, N.C., and L.J. Cahill, *J. Geophys. Res*.,70, 5923-5936, 1965a

Maynard, N.C., and L.J. Cahill, *J. Geophys. Res*.,70, 5975-5978,1965b.

McLandress, C., G.G. Shepherd, B.H. Solheim, *J. Geophys. Res.*, 101, 4,093-4,114, 1996a.

McLandress, C., G.G. Shepherd, B.H. Solheim, *J. Geophys. Res.*, 101, 10,441-10,453, 1996b.

Molina and Molina, *J. Geophy. Res*, vol. 91, pp 14501-14508, 1986.

Neamtarr, S. M., *J. Meteorol.*, 3, 53-56, 1946.

Nicolet, M, *J. Atmos. Terr. Phys.*, 3, 200-211, 1953.

Nicolet, M., *Planet space Sci.*, 32,1467-1468, 1984.

Nishida, A., *Geomagnetic Diagnosis of the Magnetosphere, Springer-Verlag, New York*, 1978

Oko S. O., C. A. Onwumechili and P. O. Ezema, *J. Atmos. Terr. Phys.,* v-58, no-5, 555-564, 1996.

Oldenburg, D. W., *Geophys. J.R. Astron. Soc.*, 46, 42-66, 1976.

Olsen N., Holme R., Hulot G., Sabaka, T. J., Neubert T., Toffner-Clausen L., Primdahl F., Jorgensen J., Leger J.M., Barraclough D., Bloxham J., Cain J., Constable C., Golovkov V., Jackson A., Kotze P., Langlais B., Macmillan S., Mandea M., Merayo J., Newitt L., Purucker M., Risbo T., Stampe M., Thomson A. and Voorhies C. *Geophys. Res. Letts.* 27, 3607-3610, 2000.

Olsen, N. and T. J. Sabaka, *Geophys. Res. Letts*. (communicated).

Olson, N. and Sabaka T. J., *Earth and Planetary Sciences,* 1999 (submitted).

Omidvar, K., R. Menard, and M. J. Buonsanto, *J. Atmos. Solar-Terr. Phys.*, 60, 1485-1496, 1998.

Onwumechili C.A., *J. Geomag. Geoelectr.*, 37, 11-36, 1985.

Onwumechili C.A., Netherlands. pp 627, 1997.

Onwumechili, A., *Academic press, New York*, pp. 425-507, 1967.

Onwumechili, C. A. and C. E. Agu, *Ann. Geophys.*, 38, 307-313, 1982.

Onwumechili, C. A. and C. E. Agu, *Planet Space Sci.*, 29, 627-634, 1981a.

Onwumechili, C. A. and C. E. Agu, *J. Atmos. Terr. Phys*., 43, 573-578, 1981b.

Onwumechili, C. A. and C. E. Agu, *Planet Space Sci.,* 28, 1125-1130, 1980.

Onwumechili, C. A., *The equatorial electrojet, Gordon and Breach science Publishers, Netherlands*, 1997.

Onwumechili, C.A. and P. O. Ezema, *J. Atmos. Terr. Phys*., 54, 1535-1544, 1992.

Onwumechili, C.A., *Nigerian J. Sci*., 1, 11-19, 1966a.

Onwumechili, C.A., *Geomagnetic variations in the equatorial zone; In: Physics of Geomagnetic Phenomena, Vol. 1, Chap. III-2, 4225-507, Eds. Matsushita, S. and Campbell, W.H., Academic Press, New York,* 1967.

Onwumechili, C.A., *Special publication of Annales de Geophysique*, 157-162, 1966b

Osborne, D. G., *J. Atmos. Terr. Phys*.,35, 1273-1279, 1973.

Pack, J. L. and A. V. Phelps, *J. Chem. Phys*., 44, 1870-1883, 1966.

Pack, J. L. and A. V. Phelps, *Phys. Rev., Ser*. 2, 121, 798-806, 1961.

Pathan, B.M., N.G. Kleimenova, O.V. Kozyreva, D.R.K. Rao, and R.L. Asinkar, *Earth Planets Space,* 51, 959-964, 1999

Pesnell, W. D., Omidvar K., and W. R. Hoegy, *Geophys. Res. Lett.,* 20, 1343-1346, 1993

Petit, M., *Ann. Geophys*., 24, 1-38, 1968

Rajaram M. and R. Rajaram, *Indian J. of Radio and Space Physics*,v-12, 160-168, 1983

Rangarajan G.K. and Dekka R.C, *Proc. Indian Acad. Sci. (E & P),* 100, 361-368, 1991

Rangarajan G.K., *PAGEOPH*, 143, 697- 711, 1991, 1994

Rangarajan, G. K., *Application of the linear prediction filters in equatorial electrojet studies, Proc. Indian Acad, Sci, (Earth Planet. Sci.),* 101, 329-338, 1992

Rastogi R.G., *J. Geophys. Res.*, 79, 1503-1512, 1974a

Rastogi R.G., *J. Atmos. Terr. Phys*., 36, 167-170, 1974b

Rastogi R.G., *J. Atmos. Terr. Phys.*, 24, 1031-1040, 1962

Rastogi, R. G., *The equatorial electrojet: Magnetic and Ionospheric effects' , Geomagnetism, edited by J. A. Jacobs, vol-3, chapter-7, page-461-525, Academic Press Ltd*, 1989

Rastogi R.G. and A.P. Patil, *Current science*, 55, 433-436, 1986

Rastogi, R.G., Stening, R.J., *Adv. Space Res.*, 12(6), 23,199

Ravat, D. N, and Hinze W. J., Geophys. J. Int.,113,387-398, 1993

Reddy, C. A. and C. V. Devasia, *Nature,* 273, 195-199, 1978

Reddy, C.A., *Indian J. Radio Space Phys.,* 17, 193-202, 1988

Richmond, A. D., *Geomagnetic crochets and ionospheric tidal winds, Ph. D. thesis, UCLA Dept. of Meteorology,* 1970

Richmond, A. D., J. Atmos. Terr. Phys. 35, 1083-1103, 1973

Richmond, A. D., *Report AFCRL-72-0668, ERP 421,Air Force Cambridge Res. Lab., Hanscom AFB, Bedford, Mass.*,1972

Richmond, A. D., *J. Geomag. Geoelectr.*,31,287-310,1979.

Robinson, E. A., *Multichannel time series analysis with digital computer programs, Goose Pond press, Houston, Texas*, 179, 1983

Rush, C. M. and D. Miller, *A three-dimensional ionospheric model using observed ionospheric parameters, Rep. AFCRL-73-0567, ERP 455, Air Force Cambridge Res. Lab., Hanscom AFB, Bedford, Mass.,* 1973

Salah, J. E., *Geophys. Res. Lett*. 20, 1543-1546, 1987

Sampath, S. and Sastry, T. S. G., *J. Geomagn. Geoelectr*., 31, 373-379, 1979

Sastry, N. S. and Jayaker, R.W., Ann. Geoelectr., 28, 581-591, 1972.

Sastry, T.S.G., *J. Geophys.,Res*., 73, 1789-1794, 1968.

Sastry, T.S.G.,K. Burrows, S. Sampath, J.D. Stolarik, and M.J. Usher, *Space Res.,* XVII, 409-410, 1977.

Schlapp, D. M., *J. Atmos. Terr. Phys.,* 30, 573-577, 1968

Shinohara, M., K. Yumoto, N. Hosen, A. Yoshikawa, H. Tachihara, O. Saka and T. I. Kitamura, *J. Geophys. Res*., V.103, No.A6, p.11,745-11,754, 1998

Sibert, M., *Advance in Geophysics, Vol.7, Academic Press, New York*, pp.105-182, 1961

Singh, A. and K. D. Cole, *Atmos. Terr. Phys*. 49, 529-537, 1987

Singh, A. and K. D. Cole, *J. Atmos. Terr. Phys*. 49, 539-547, 1987

Singer, S. F., Maple, E. and Bowen, W. A., *J. Geeophys. Res*., 56, 265-281, 1951.

Solberg, H., *Astrophys. Norweg,* 1, 237-340, 1936

Stallcop, J. R., H. Partridge, E. Levin, *J. Chem. Phys.*,95, 6429-6439, 1991

Stening, R.J., *Planet. Space Sci*.,16,717-728,1968.

Stening, R.J., *Adv. Space Res*.,12,(6)23-(6)32,1992.

Stening, R. J., *J. Atmos. Terr. Phys*., 57, 1117-1128, 1995

Stewart, B., *Terrestrial magnetism, Encyclopedia Britannica, 9th* edn.,1882

Storch von Hans, *Spatial patterns: EOF and CCA, in Analysis of Climatic variability, ed. H. von Storch and a. Navarra, Springer-Verlag Berlin Heidelberg*, 1999

Stubbe, P., *J. Atmos. Terr. Phys*.,30, 1965-1985, 1968

Sugiura, M. and D. J. Poros, *J. Geophys. Res*., 74, 4025-4034, 1969

Swider, W., *Rev. Geophys*., 7, 573-594, 1969

Takeda, M. and H. Maeda, *J. Geo. Res*., 85, 6895, 1980.

Takeda, M. and H. Maeda, *J. Geo. Res*., 86,5861-5867,1981.

Takeda, M., *J.Atmos. Terr.Phys.,* 44, 187, 1982.

Untiedt, J., *J. Geophys. Res*., 72, 5799-5810,1967.

Ward, W.E., J. Oberheide, M. Riese, P. Preusse, and D. Offermann, *J. Geophy. Res*., V.104, No.D13, p-16, 391-16,403, 1999.

Yacob, A., *J. Atmos. Terr. Phys.,* 39, 601, 1977.

Yamamoto, G. ,*J. Atmos. Sci*., 19, 182, 1962.

Appendix 1

Fortran program algorithm for identifying EEJ signature in the satellite data and further analysis

An automated program for the identification of equatorial electrojet in the satellite data facilitate us to handle the enormous scalar magnetic field data from the satellite measurements over a period of year. The program is written in Fortran language and tested on IRIX 4.2 system. The program contains self-documenting subroutines, which can be considered as black boxes with input and output terminals fully described.

To begin the actual program, let us comment briefly on the algorithm of the main program, which is followed by the flowchart. The raw data file, which is the input of the program, contains the information about day, UT, radius from the centre of the earth, geographic latitude, geographic longitude, local time, and observed value of total scalar magnetic field (F) by the satellite.

Firstly program converts geographic latitude into dip latitude, which is achieved by calling subroutine 'diplat'. The input for diplat includes longitude near geographic equator, date, and altitude. Here onwards, latitude is referred as dip latitude at 106 km. Next it opens the file containing Dst indices and reads appropriate Dst index for a given day and hour of a year. MAGSYN subroutine computes the main field magnetic field [Olson et al, 2001] for a given day, latitude, longitude, altitude and Dst index. Thus subtraction of IGRF from the total observed magnetic field forms a set of observed residual field as a function of latitude. The data set of latitudinal range of 20^0S to 20^0N is used to study the equatorial electrojet phenomenon.

Removal of linear trend helps in making the residual field symmetric about the dip equator. Call of subroutine 'filt', passes the data set through a low pass filter, which removes the variations of time scale less than one minute, i.e. spatial variations of order 4^0. This

smoothened data set for a given pass can be further analysed for the identification of EEJ signature.

Subroutine 'crct' takes the above data of trajectory and comments on the characteristic of the pass. This is achieved by determining the number of minima (or dip) in the latitude range of $\pm 4^0$ and maxima (or peak) within $\pm 20^0$. A minimum within $\pm\ 4^0$ can be considered as a position of the centre of the current system. Then depending on the number of minima and maxima, the type of the pass is decided as follows:

If no minimum and one maxima within $\pm\ 2^0$ is found then, the pass is considered to have CEJ event.

If one minimum and at least two maxima on either sides of minimum found, then the situation is treated as ideal EEJ situation. Those two maxima are considered as the shoulders of the signature, which are almost equidistant from the centre of the current system.

If one minimum and no maximum found, then the situation is analysed further. Third derivative contains the information about the gradient of slope, which could be attributed to the unseen peaks in the signature. The part of the profile which lies from the extremes to the points, where the slope changes can be considered out of the EEJ effect and is used further for fitting a polynomial. In case, the slope does not change, the region beyond $\pm 12^0$ can be treated as non-equatorial. Removal of fitted cubic from the residual field of trajectory is same as removal of background Sq field. Hence this improves the signature of electrojet and sometimes results in ideal EEJ signature.

If one minimum and one maximum found, then examine third derivative. Gradient in slope can be considered as an indication of second maximum on the other side of the dip.

Except the CEJ situation, the above procedure is repeated for 5 times to get better signature. Thus, once one dip and two shoulders on either side are identified, a linear trend passing through two shoulders is removed in order to bring both the shoulders to the same level.

Consequently, the identified EEJ signature is analysed further for the detailed study.

The program tries to fit Onwumechili's model for EEJ current system, which has been discussed in the chapter, into ideal EEJ and dip with one peak condition. Consider residual

magnetic field between two peaks with additional 40 points on each side of peak. Then do loop for parameters in Onwumechili's model viz., a and alpha is set up. Substantially, a and alpha determines the position of two shoulders through the use of subroutine 'fsat'. Retain those values of a and alpha for which, the position of computed shoulders at the satellite altitude and the observed peaks are very close by. Retain the values of a, alpha and the observed profile, determine another parameter K, which is directly proportional to the peak eastward current intensity (J_0) responsible for EEJ through the use of least square fit method. This is achieved by calling subroutine 'own'. The details of the least square method for Onwumechili's model are discussed in appendix 2. Least square fit also determines an additional parameter that can account for a constant baseline shift. Thus using these parameters viz., a, alpha, K and shift, a complete profile at satellite altitude is computed and find out the correlation coefficient between the observed and computed residual magnetic field at satellite height. Select those values of a and alpha, for which the correlation coefficient is largest and the variance is least. The information about day, longitude, local time, a, alpha, correlation coefficient, dip latitude of centre of the current system, width of EEJ at satellite, width of EEJ on ground, field estimated at the centre of the current system and at the dip equator is summarised in the output file.

Explanatory:

iday = daynumber of year

UT = universal time

r = radial distance from the centre of the earth

glat = geographic latitude

glong = geographic longitude

lday = local daynumber

LT = local time

F = scalar total magnetic field from satellite measurements

dip = geographic latitude of dip equator for given longitude and 106 km altitude

Figrf = main magnetic field

ΔF = residual magnetic field

cp1 = dip latitude of first peak

cp2 = dip latitude of second peak

jam = output from subroutine 'crct' , which indicates the characteristic of pass as follows

jam = -1 indicates CEJ

jam = 0 indicates no dip found

jam = 1 indicates ideal EEJ situation

jam = 2 indicates dip with one peak

jam = 3 indicates only dip present

jam = 4 indicates insufficient data

count = counter

a, alpha, K = Onwumechili's EEJ model parameters

A = base line shift

pc1 = dip latitude of first peak computed using Onwumechili's model

pc2 = dip latitude of second peak computed using Onwumechili's model

mk = dummy variable

sat(mk) = magnetic field computed at satellite altitude using Onwumechili's model

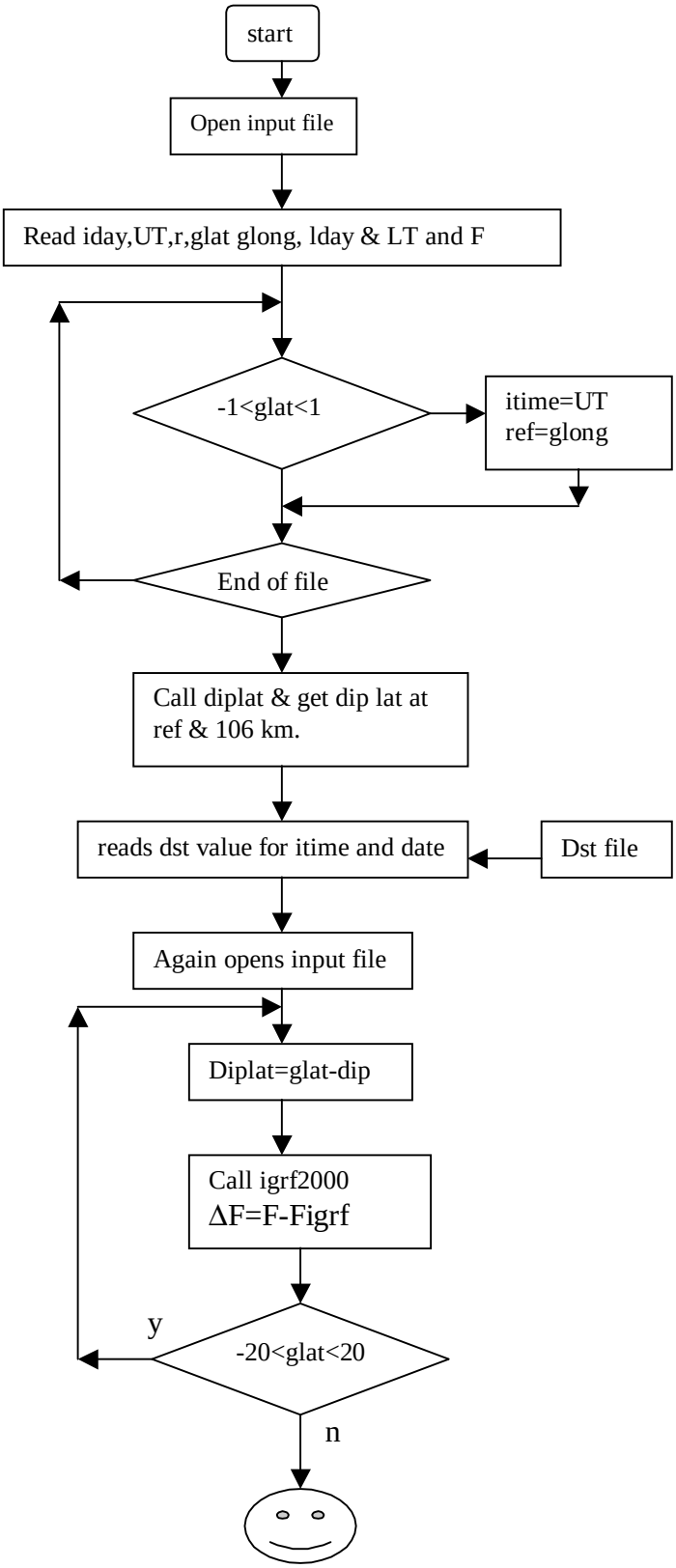
start
Open input file
Read iday,UT,r,glat glong, lday & LT and F
-1<glat<1
itime=UT
ref=glong
End of file
Call diplat & get dip lat at
ref & 106 km.
reads dst value for itime and date
Dst file
Again opens input file
Diplat=glat-dip
Call igrf2000
ΔF=F-Figrf
y
-20<glat<20
n

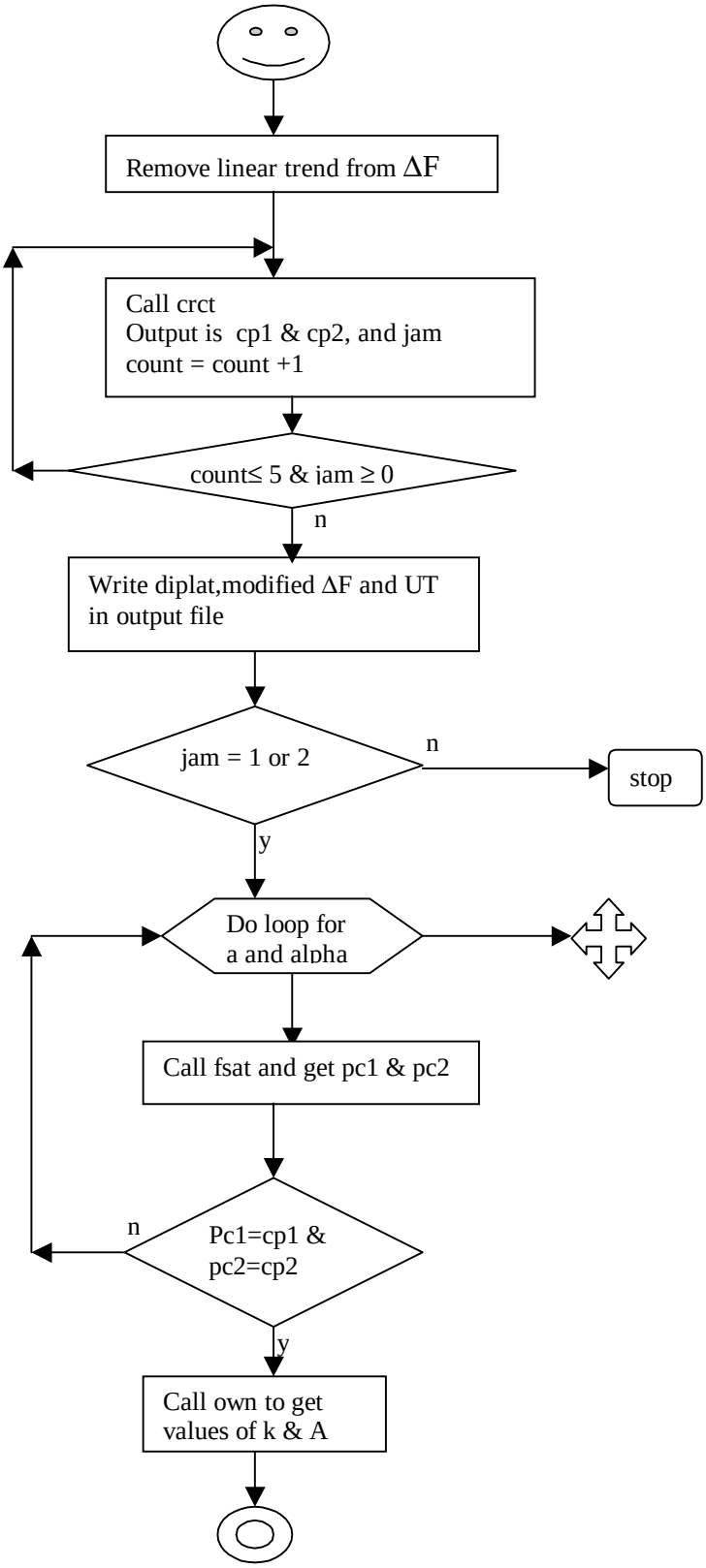
Remove linear trend from ΔF
Call crct
Output is cp1 & cp2, and jam
count = count +1
count≤ 5 & jam ≥ 0
n
Write diplat,modified ΔF and UT
in output file
jam = 1 or 2
n
stop
y
Do loop for
a and alpha
Call fsat and get pc1 & pc2
n
Pc1=cp1 &
pc2=cp2
y
Call own to get
values of k & A

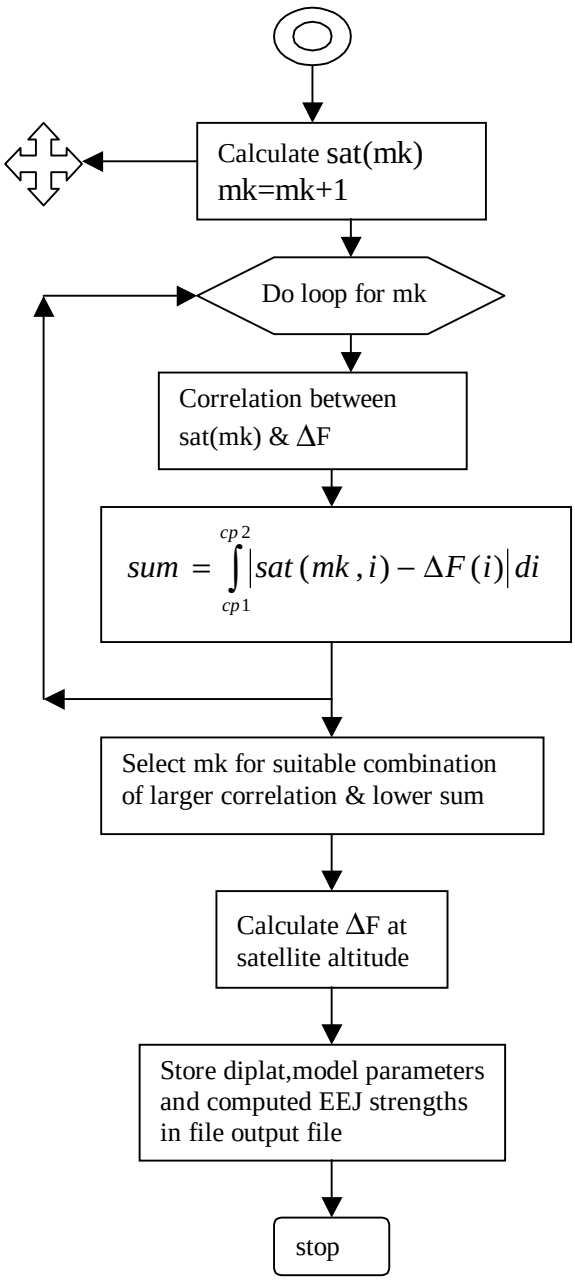
Calculate sat(mk)
mk=mk+1
Do loop for mk
Correlation between
sat(mk) & ΔF
$sum = \int_{cp1}^{cp2} |sat(mk, i) - \Delta F(i)| di$
Select mk for suitable combination
of larger correlation & lower sum
Calculate ΔF at
satellite altitude
Store diplat,model parameters
and computed EEJ strengths
in file output file
stop

Appendix: 2

Least square method

In the coordinate system with the centre of the current system is the origin and x is northward latitudinal distance, y is eastward, and z is vertically downward distance,
thin current shell equations of the magnetic fields due to equatorial electrojet are,

$$(sg \cdot z)P^4 X = \frac{1}{2} Ka\left[(v + \alpha v + 2\alpha a)(u + b)^2 + (v + \alpha v + 2a)(v + a)^2\right] \quad (1)$$

$$-(sg.x)P^4 Z = \frac{1}{2} Ka(u + b)\left[(1 + \alpha)(u + b)^2 + (v + \alpha v + 3a - \alpha a)(v + a)\right] \quad (2)$$

Where,

$$P^2 = (u + b)^2 + (v + a)^2$$
$$K = 0.2\pi J_0$$

$$u = |x| \quad and \quad v = |z|$$
$$sg \cdot x = sign\ of\ x = \frac{x}{u} \quad and$$
$$sg \cdot z = sign\ of\ z = \frac{z}{v}$$

a and *b* are latitudinal and vertical scale lengths, respectively
α is dimensionless constant controlling latitudinal distribution of current.
J_0 is the peak current intensity or the height-integrated current density at the centre of the current system and *K* is the magnetic field constant.

The variation in the total magnetic field at any point in space is written as,

$$\Delta F_{model} = \frac{X\Delta X + Z\Delta Z}{F}$$

where ΔX and ΔZ can be substituted from equation (1) & (2) and X, Z, & F is due to main field at the location of the evaluation of ΔF.

$$\therefore \Delta F_{\mathrm{mod}\,el} = \frac{Ka}{2P^4}\left\{\begin{array}{l} sgz\cdot\dfrac{Z}{F}\left[(v+\alpha v+2\alpha a)(u+b)^2+(v+\alpha v+2a)(v+a)^2\right]- \\ sgx\cdot\dfrac{X}{F}\cdot(u+b)\left[(1+\alpha)(u+b)^2+(v+\alpha v+3a-\alpha a)(v+a)\right] \end{array}\right\}$$

Variable C can replace the quantity in curly brackets,

$$\Delta F_{\mathrm{mod}\,el}(i) = \frac{Ka}{2P^4(i)}C(i)+A$$

$$\Delta F_{\mathrm{mod}\,el}(i) = K\cdot C1(i)+A$$

where $C1(i) = \dfrac{a}{2P^4(i)}C(i)$ and

A is the additional constant for the base line shift.

The following quantity *U*, estimates the square of the error involved,

$$U = \sum_{i=1}^{N}\left(F_{\mathrm{mod}\,el}(i)-F_{obs}(i)\right)^2$$

$$U = \sum_{i=1}^{N}\left(K\cdot C(i)+A-F_{obs}(i)\right)^2$$

where *N* is the total number of points.

Least square method demands *U* to be minimum,

$\therefore \dfrac{\partial U}{\partial K} = 0$ *and* $\dfrac{\partial U}{\partial A} = 0$ give rise to,

$$K = \frac{\sum_{i=1}^{N}\Delta F_{obs}(i)\cdot C(i)-\frac{1}{N}\sum_{i=1}^{N}\Delta F_{obs}(i)\sum_{i=1}^{N}C(i)}{\sum_{i=1}^{N}C^2(i)-\frac{1}{N}\sum_{i=1}^{N}C(i)\sum_{i=1}^{N}C(i)} \quad \text{and}$$

$$A = \frac{1}{N}\sum_{i=1}^{N}\Delta F_{obs}(i)-\frac{1}{N}\sum_{i=1}^{N}C(i)\cdot\frac{\sum_{i=1}^{N}\Delta F_{obs}(i)\cdot C(i)-\frac{1}{N}\sum_{i=1}^{N}\Delta F_{obs}(i)\sum_{i=1}^{N}C(i)}{\sum_{i=1}^{N}C^2(i)-\frac{1}{N}\sum_{i=1}^{N}C(i)\sum_{i=1}^{N}C(i)}$$

Appendix 3:

A Prescription for writing Product of Harmonic

We can express the parameter ψ as

$$\psi = \sum_{n=1}^{4} \left(a_n \cos nr + b_n \sin nr\right)$$

and the coefficient P as

$$P = \alpha_0 + \sum_{n=1}^{4} \left(\alpha_n \cos nr + \beta_n \sin nr\right)$$

The product $P\psi$ can be written as

$$p\varphi = [\sum_{n=1}^{4} (a_n \cos nr + b_n \sin nr)][\alpha_0 + \sum_{n=1}^{4} (\alpha_n \cos nr + \beta_n \sin nr)]$$

$$= c_0 + \sum (c_n \cos nr + d_n \sin nr)$$

In order to determine c_n and d_n, we have to expand the terms within the brackets and simplify the resultant trigonometric inequalities.

Note the following

$$a_n\alpha_m \cos nr \cos mr = \left\{\frac{1}{2}\cos(n+m)\, r + \cos(n-m)\, r\right\} a_n\alpha_n$$

$$b_n\beta_m \sin nr \sin mr = \frac{1}{2}\{\cos(n-m)r - \cos(n+m)r\} b_n\ \beta_m$$

$$\begin{bmatrix} b_n\alpha_m \\ a_m\beta_n \end{bmatrix} \sin nr \cos mr = \frac{1}{2}\{\sin(n+m)r + \sin(n-m)r\} \begin{bmatrix} b_n\alpha_m \\ a_m\beta_n \end{bmatrix}$$

Using the above inequalities, we can write various harmonics of cosine sine terms in the product. Thus,

First four harmonics coefficient of *cosine* function are,

$$C_1 = (\alpha_0 + \frac{1}{2}\alpha_2)a_1 + \frac{1}{2}(\alpha_1 + \alpha_3)a_2 + \frac{1}{2}(\alpha_2 + \alpha_4)a_3 + \frac{1}{2}(\alpha_3)a_4 +$$

$$\frac{1}{2}\beta_2 b_1 + \frac{1}{2}(\beta_1 + \beta_3)b_2 + \frac{1}{2}(\beta_2 + \beta_4)b_3 + \frac{1}{2}\beta_3 b_4$$

$$C_2 = \frac{1}{2}(\alpha_1 + \alpha_3)a_1 + (\alpha_0 + \frac{1}{2}\alpha_4)a_2 + \frac{1}{2}\alpha_1 a_3 + \frac{1}{2}\alpha_2 a_4 + \frac{1}{2}(\beta_{31} - \beta_1)b_1 + \frac{1}{2}(\beta_4)b_2 + \frac{1}{2}\beta_1 b_3 + \frac{1}{2}\beta_2 b_4$$

$$C_3 = \frac{1}{2}(\alpha_2 + \alpha_4)a_1 + \frac{1}{2}(\alpha_1)a_2 + \alpha_0 a_3 + \frac{1}{2}\alpha_1 a_4 + \frac{1}{2}(\beta_4 - \beta_2)b_1 - \frac{1}{2}(\beta_1)b_2 + \frac{1}{2}\beta_1 b_4$$

$$C_4 = \frac{1}{2}\alpha_3 a_1 + \frac{1}{2}\alpha_2 a_2 + \frac{1}{2}\alpha_1 a_3 + \alpha_0 a_4 - \frac{1}{2}\beta_3 b_1 - \frac{1}{2}\beta_2 b_2 - \frac{1}{2}\beta_1 b_3$$

and D.C. term is given by,

$$C_0 = \frac{1}{2}(\alpha_1 a_1 + \alpha_2 a_2 + \alpha_3 a_3 + \alpha_4 a_4 + \beta_1 b_1 + \beta_2 b_2 + \beta_3 b_3 + \beta_4 b_4)$$

First four harmonics coefficient of *sine* function are,

$$S_1 = \frac{1}{2}\beta_2 a_1 + \frac{1}{2}(\beta_2 - \beta_1)a_2 + \frac{1}{2}(\beta_4 - \beta_2)a_3 - \frac{1}{2}\beta_3 a_4 + \left(\alpha_0 - \frac{1}{2}\alpha_2\right)b_1 + \frac{1}{2}(\alpha_4 - \alpha_3)b_2 + \frac{1}{2}(\alpha_2 - \alpha_4)b_3 + \frac{1}{2}\alpha_3 b_4$$

$$S_2 = \frac{1}{2}(\beta_1 + \beta_3)a_1 + \frac{1}{2}\beta_4 a_2 - \frac{1}{2}\beta_1 a_3 - \frac{1}{2}\beta_2 a_4 + \frac{1}{2}(\alpha_1 - \alpha_3)b_1 + (\alpha_0 - \frac{1}{2}\alpha_4)b_2 + \frac{1}{2}\alpha_1 b_3 + \frac{1}{2}\alpha_2 b_4$$

$$S_3 = \frac{1}{2}(\beta_2 + \beta_4)a_1 + \frac{1}{2}(\beta_1)a_2 - \frac{1}{2}\beta_1 a_4 + \frac{1}{2}(\alpha_2 - \alpha_4)b_1 + \frac{1}{2}\alpha_1 b_2 + \alpha_0 b_3 + \frac{1}{2}\alpha_1 b_4$$

$$S_4 = \frac{1}{2}\beta_3 a_1 + \frac{1}{2}\beta_2 a_2 + \frac{1}{2}\beta_1 a_3 + \frac{1}{2}\alpha_3 b_1 + \frac{1}{2}\alpha_2 b_2 - \frac{1}{2}\alpha_1 b_3 + \alpha_0 b_4$$